Bubble size, gas holdup and interfacial area distributions in mechanically agitated gas-liquid reactors

Barigou, Mostafa

Award date:
1987

Awarding institution:
University of Bath

BUBBLE SIZE, GAS HOLDUP AND INTERFACIAL AREA DISTRIBUTIONS IN MECHANICALLY AGITATED GAS-LIQUID REACTORS

Submitted by

Mostafa BARIGOU

for the degree of

Doctor of Philosophy (PhD)

of

The University of BATH

April 1987

ProQuest LLC
789 East Eisenhower Parkway
P.O. Box 1346
Ann Arbor, MI 48106-1346

ABSTRACT

A 1.0 m mechanically agitated vessel apparatus for batch gas-liquid mixing has been developed for carrying out detailed gas-liquid dispersion studies. The system capability for the selection and measurement of impeller speed and power has been enhanced by interfacing it to a microcomputer. A fully submersible capillary suction probe interfaced to a high speed data acquisition system supervised by a microcomputer, has been developed for measurement of bubble size in large scale reactors. A conductivity probe technique was also developed for local gas holdup measurement and adapted to the same data acquisition system.

Using the capillary probe technique a detailed quasi-point examination of the structure of bubble size distributions in both 'coalescing' and 'non-coalescing' gas-liquid dispersions was conducted in the 1.0 m agitated tank. The bubble size distributions were found to vary widely with the liquid system used and from one region of the reactor to an other, deviating greatly from the standard Gaussian distribution. The agitator speed affects the mean bubble size to varying extents in different zones, the effects being dependent on the gas flow rate.

The local gas holdup and interfacial area were found to change appreciably with position in the dispersion. The impeller region contains a relatively large proportion of the total surface area in the tank. It is difficult to establish useful amounts of gas circulation in the region below the impeller and hence, from this point of view, high impeller clearances are not desirable.

Predictive correlations have been obtained for the total gas holdup and gassed power demand. The accuracy of the correlations was significantly improved by a systematisation of the experimental data into groups according to the impeller gas cavity regimes.

An investigation into the power dynamics of the agitator including photography of the impeller gas cavities was carried out. The power response resulting from an input disturbance in sparged gas flow rate reveals two regions. A very fast drop in power in the first region of the transient, which

accounts for the major part of the total power reduction, is followed by a much slower response in the second part of the curve. A simple first order dynamic model has been proposed to predict the first region of the transient response, which is mainly associated with the growth of large gas cavities.

ACKNOWLEDGEMENTS

The award of a Bath University scholarship is greatfully acknowledged by the author.

Sincere thanks go to Mr J. Bishop, the department's electronician, for his expert help in developing the instrumentation involved in this research.

Thanks are due to Dr A. Brucato (Visiting researcher from the University of Palermo, Italy) for his assistance in carrying out the power dynamic tests.

Finally, I record my appreciation to Dr M. Greaves for his help and his moral support at times of difficulty.

M.Barigou

April 1987

CONTENTS

Chapter 1

INTRODUCTION

Mechanically agitated gas-liquid reactors find wide application in the chemical and allied process industries. They are utilised for performing various gas-liquid operations, with physical absorption (eg. aerobic fermentation) or chemical absorption (eg. oxidation, hydrogenation, chlorination etc.). They provide large interfacial area for mass transfer, long residence times of the gas bubbles, good agitation of the liquid and good backmixing of both liquid and gas phases. They can also handle highly viscous systems and achieve adequate suspension of solid particles.

The three-dimensional turbulent gas-liquid flow in a stirred vessel has an inherently fluctuating structure of a very complex nature. This poses a difficult problem theoretically, not least in the solution of relevant equations to predict the internal flow in such a system. Understandably, therefore, the methods so far adopted for designing this type of reactor are mainly empirical. They rely on global results derived from experimental studies carried out on laboratory or pilot scale units. This design approach has seen important development since the early investigations conducted on gas-liquid mixing, and has provided satisfactory answers to a number of industrial problems. Recently, however, it has been realised that this 'global' approach has limited research potential. In contrast the distributed point of view should provide a better scientific basis for investigation and design. Thus the localised approach enables much more detailed description of the two-phase flow structure to be obtained. In this way, greater accuracy and greater reliability can be achieved in the design of industrial gas-liquid stirred vessel reactors.

This detailed understanding necessitates obtaining information on a number of local parameters among which bubble size, gas holdup and

interfacial area distributions are of paramount importance. Indeed, these parameters are interrelated and fundamental to developing a complete understanding of the basic bubble phenomena which are at the heart of the gas-liquid mixing problem. Measurement of these local properties is one of the least developed areas in this field and has remained a major challenge to researchers due to the lack of adequate measurement techniques. This research is presented as a contribution in this direction.

For convenience of presentation each area of research investigated is confined in a self contained chapter. The layout of the thesis is summarised below:

-Chapter 2: An extensive survey of the state of the art in terms of two-phase gas-liquid flow instrumentation with particular emphasis on the measurement techniques relating to bubble size, gas holdup and interfacial area.

-Chapter 3: Details of the design and construction of the 1.0 m mixing rig employed and experimental procedures for measuring agitator speed and power, and total gas holdup.

-Chapter 4: Detailed description of the capillary suction probe technique developed for bubble size measurements, and the instrumentation and data acquisition system associated with it.

-Chapter 5: The results obtained on bubble size distributions in different regions of the 1.0 m stirred vessel using the capillary probe technique are discussed.

-Chapter 6: The application of a computerised conductivity probe

technique for measurement of the local gas holdup in the 1.0 m agitated tank is described and the experimental results are discussed. Local interfacial area distributions obtained by combining point bubble size and gas holdup results are also analysed.

Chapter 7: Development of improved gas holdup and impeller power correlations based on the systematisation of experimental measurements according to impeller gas cavity regimes.

Chapter 8: An investigation into the impeller power dynamics coupled with a photographic study of the impeller gas cavities.

Chapter 9: Recommendations for future research.

Chapter 2

SURVEY OF TECHNIQUES FOR MEASUREMENT OF BUBBLE PARAMETERS IN GAS-LIQUID CONTACTORS

2.1 Introduction

Theoretical modelling of gas-liquid dispersions remains a difficult problem for researchers in this field. Bubble properties still cannot be, in general, theoretically predicted. Therefore, there is a strong need for instruments capable of detecting and measuring bubble parameters in gas-liquid contactors. Of central importance are bubble size, gas holdup and interfacial area. Over the last ten years, much effort has been devoted to the development of two-phase flow instrumentation. A wide variety of techniques have been designed, ranging from photographic methods to miniature fibre optic probes and sophisticated laser-scattering techniques. This chapter reviews the contributions in this area, with an evaluation of their scope and applicability. The techniques described fall into two main categories; Invasive techniques, including chemical and local measurement methods, and non-invasive techniques which embrace photographic, laser and radioactive methods.

2.2 Invasive techniques

2.2.1 Chemical methods

Integral values of interfacial area in gas-liquid dispersions may be obtained by absorption experiments. Many chemical systems have been proposed for the determination of interfacial area by so-called 'chemical methods' [2, 22-25]. When using a chemical method the interfacial area is calculated by means of mass transfer. This is achieved by selecting a gas-liquid system such that the absorbed gaseous component reacts chemically in the liquid phase. For instance, if an Oxygen-Sodium sulphite system is used and the reaction is carried out batchwise with respect to the liquid phase, the absorption rate can be measured directly from the change with time in the sulphite concentration. Knowledge of

the absorption rate allows calculation of the interfacial area [22]. The value obtained is often called 'effective interfacial area', indicating that it may differ from the geometrical interfacial area as measured by a physical method eg. photography. The difference between the effective interfacial area, a_{chem}, and the geometrical area, a_{geo}, may be considerable. Literature results compiled by Stichlmair [25] (Fig 2.1), demonstrate this fact for sieve-tray columns. The effective interfacial areas are generally smaller than the geometrical ones. Schumpe and Deckwer [27], and Hofer and Mersmann [25] have discussed the reasons behind this discrepancy. In the case of high mass transfer rates depletion of the absorbing component in the gas bubbles takes place. This process which is usually ignored, increases in significance with increasing enhancement factor (ratio of mass transfer in presence of a chemical reaction to that in a purely physical process) and bubble residence time, and with decreasing bubble size. This shrinking effect causes the driving force at a bubble interface to reduce to such an extent that under extreme conditions a small bubble may reach a state of equilibrium with the adjacent liquid. However, such bubbles can be detected by a physical technique and therefore will contribute to the geometrical interfacial area. Normally, the interfacial area is calculated using the measured overall conversion rate together with the assumption that the driving force is effective over all bubbles. In actual fact, bubbles of different amounts of absorbent gas are mixed at the reactor exit where the gas concentration is mainly determined by the concentration of large bubbles which undergo only a small depletion. Such depletion effects can be taken into account if the mass transfer rate is determined by integration over the whole bubble size distribution [25, 27]. Otherwise, measurements of interfacial area under conditions of high absorption rates are not valid.

Among all chemical methods the most widely used are the absorption of CO_2 in Sodium Hydroxide or in a solution of Potassium Carbonate, and the absorption of O_2 in a solution of Sodium Sulphite. These two systems, however, have been found to yield largely different values of interfacial area under similar, or even identical conditions, as shown in Fig 2.2. Of special interest are curves E1 and I2 which refer to the same bubble column. The reason for this discrepancy is that with sulphite oxidation only small depletion effects are observed. Because of the very high Henry's coefficients for mass transfer of O_2 in an aqueous solution the conversion rate is smaller. Indeed it was found that the sulphite method gives values of interfacial area which are close to the geometrical ones [27]. Midoux et al [28] have discussed the suitability of chemical methods for interfacial area measurements and noted that because of the short residence time required for the depletion effect to be negligible, the use of these techniques has been restricted to small scale units not exceeding $1\,m^3$ in volume. Hence, scale-up by the use of the chemical method seems hazardous.

At this stage it is worthwhile mentioning the experiment of Sridhar and Potter [3] in a 0.12 m stirred vessel. Using a chemical method (O_2–Na_2SO_3) and a local light attenuation technique, they found that the chemical interfacial area was 1.5-2 times that obtained using the second method. The difference was attributed to the high local mass transfer rates taking place in the impeller region. Rennie and Valentin [93] who studied mass transfer phenomena in stirred vessels using high speed photography, concluded that the impeller region contained the most 'active' surface. High shear rates and therefore high energy dissipation in the agitator zone result in high rates of surface renewal and high mass transfer coefficients. Indeed, Sridhar and Potter [3] showed that the mass transfer coefficient in the impeller region was about 50

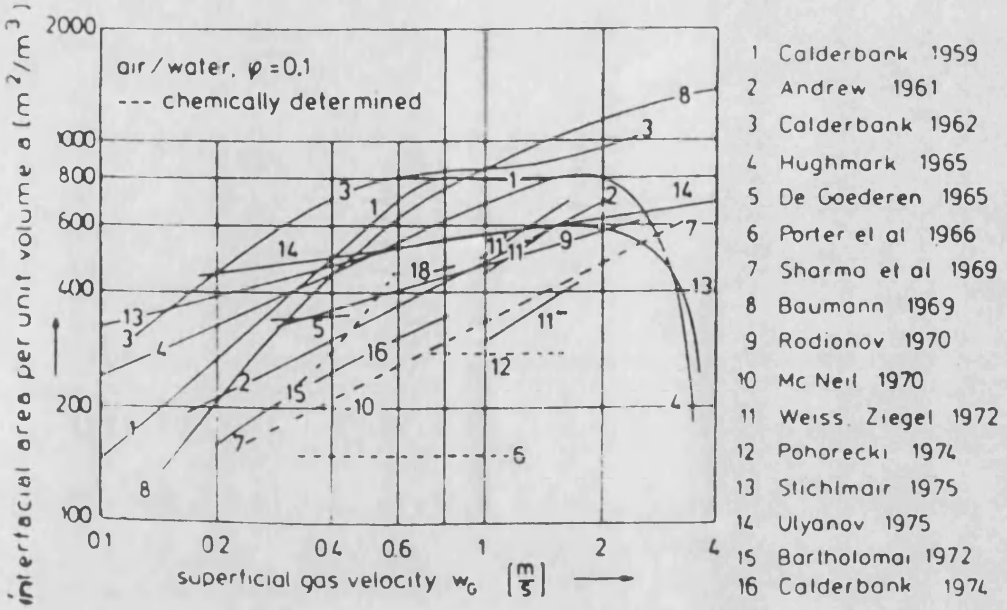

Fig 2.1 Comparison of literature results for the variation of interfacial area with superficial gas velocity [25].
—— physically determined

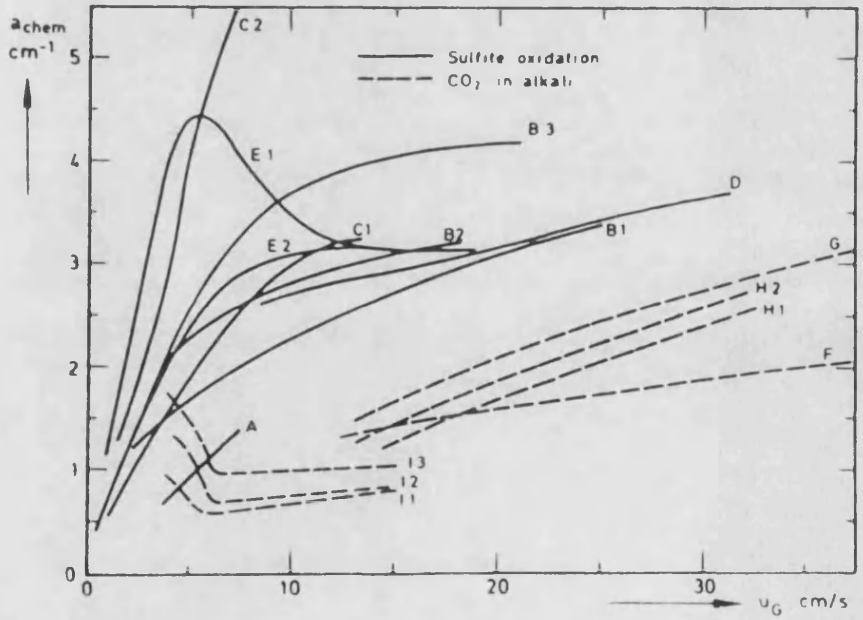

Fig 2.2 Specific interfacial area from sulfite oxidation and CO_2 absorption in alkali in bubble columns (27).

times the average coefficient in the tank. The rate of absorption is taken to be independent of the mass transfer coefficient, K_L, and hence of the hydrodynamic conditions if the enhancement factor, M, is high enough ie., $\sqrt{M} > 3$ [3]. Because of the wide variation in K_L throughout the vessel this criterion may not be met at every point in the reactor. While this effect may be limiting in mechanically agitated reactors it will be much less pronounced in packed beds and bubble columns.

From the above discussion the following remarks can be made about the use of the chemical method. The technique yields from a single measurement an overall value of the interfacial area. It is useful as a standard but there are some unresolved problems and consequently the results obtained will have to be interpreted with caution. For a particular application a suitable reaction has to be chosen with considerable care, and experimentation may be very time consuming. In many cases, the information obtained is rather specific to the conditions of the reaction, especially the ionic strength of the solution and type of ions present [23]. Also a systematic investigation of the effect of liquid properties such as viscosity and interfacial tension, on the interfacial area is very difficult since the addition of surface active or viscous components would make a new and time consuming investigation of the kinetics of the chemical reaction necessary [29].

Finally, a novel method has been proposed [9]. It involves the use of a nuclear reaction to radiate a beam of light within the dispersion. The light intensity registered by the detection system is proportional to the interfacial area. The technique seems interesting because it allows measurement of the interfacial area in organic fluids and is also applicable to continuous flow systems.

2.2.2 Light attenuation methods

This technique is based on the scattering of a light beam as it passes through a transparent dispersion, by reflection, refraction and diffraction (Fig 2.3). In its simplest form [30], a parallel beam of light is passed through the dispersion inside the gas liquid contactor. This is received by a photocell some distance away from the scattering region at the extremity of an internally blackened tube, as shown in Fig 2.4. Only the light which meets no obstruction in its path is sensed by the photocell, the scattered light being absorbed on the blackened tube. It has been shown [30] that the light attenuation ratio $\frac{I_0}{I}$ is related to the specific interfacial area, a, according to the equation:

$$\ln\frac{I_0}{I} = \frac{al}{4} \qquad (2.1)$$

where,

I_0 = incident light intensity,

I = transmitted light intensity,

l = optical path length.

This relationship is valid for transparent or opaque particles which are distributed in a sufficiently dispersed medium. This was tested by Calderbank [30] with air bubble swarms of known interfacial area in a pulsed sieve-plate column and polystyrene spheres of known sizes in a stirred vessel.

The photocell was connected to a light quantity meter and an electric timer. The timer serves to measure the time, t_0, required for the light meter to receive a given quantity of light through the continuous phase only, and the time t_d for the same quantity to be received through the dispersion. It has been shown that [30]:

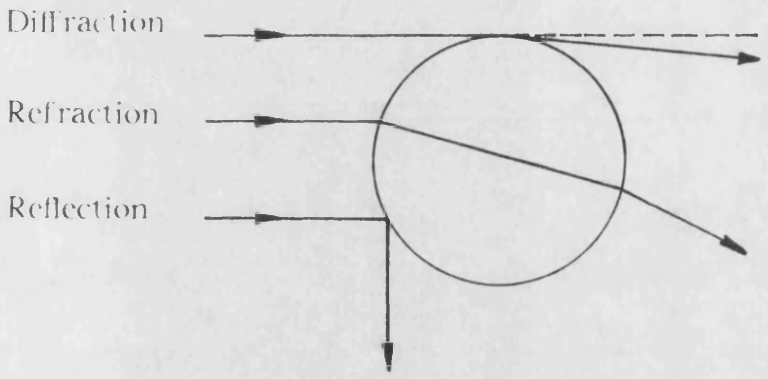

Fig 2.3 Principles of light scattering.

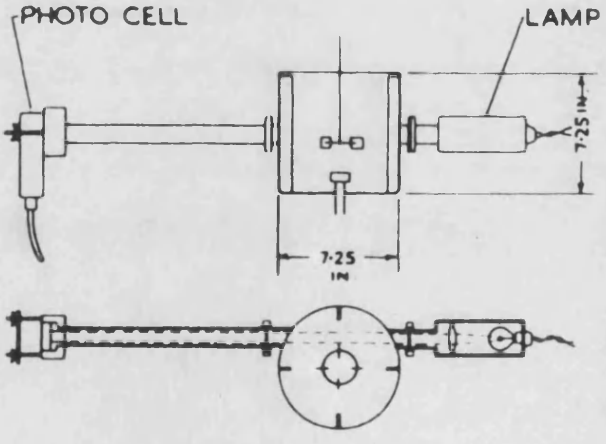

Fig 2.4 Set-up for light transmission through a stirred vessel [30].

$$\frac{I_0}{I} = \frac{t_d}{t_0}$$

Therefore, Equation (2.1) becomes:

$$\ln\frac{t_d}{t_0} = \frac{al}{4} \qquad (2.2)$$

This allows the time-average interfacial area to be determined. Although this technique was originally proposed for uniform particle sizes, it has been shown, using a numerical simulation, to be applicable to polydispersed systems [31, 32]. Experimental verification using polystyrene beads was also reported [31].

Using the above principles Calderbank [30] then developed a movable probe (Fig 2.5), which he exhaustively tested with suspensions of polystyrene and glass beads of known sizes and found it also gave results in accordance with Equation (2.1). He used it to measure interfacial area in a 40 l and a 100 l stirred vessels. This probe was an improvement on the earlier probe by Vermeulen et al [33], which needed calibration by high-speed photographs of the emulsions, on which the specific interfacial area was determined by droplet size counting (see Section 2.3.1).

Mclaughlin and Rushton [31] stated a number of conditions that must be satisfied if Equation (2.1) is to be valid. These conditions are:

1. Transparent continuous phase;
2. Random spatial particle distribution;
3. Particles must be greater than 0.10 mm in diameter;
4. Particles are subject to random orientation in the light beam;
5. Particles have no concave surfaces;
6. Light source emits an incoherent parallel light beam;
7. Light detector receives only parallel light.

Due to errors from multiple scattering in the case of dense dispersions Calderbank [30] set a limit of validity for the technique expressed as al<25 while Mclaughlin and Rushton [31] recommended a maximum value for $\frac{I_0}{I}$ equal to 10. This criterion is limiting vis-à-vis the range of interfacial area values that can be measured, especially when measurements are made from outside the contactor, since the optical path length in this case would be rather large. Landau et al [2] used the light scattering technique to measure interfacial areas in air-water and air-electrolyte solutions in a bubble column. The light source and photocell were placed outside the column. The optical path length was 0.098 m and the values of al were up to about 80. This constitutes a significant extension in the range of applicability of the method. They achieved this by developing the semi-empirical equation:

$$a = \frac{\frac{4}{l}\ln\frac{I_0}{I}}{1-f\,(al)} \qquad (2.3)$$

where,

$$f\,(al) = 1 - \frac{26.36}{al}(1-e^{-0.0583al}),$$

which accounts for the effect of multiple scattering at high values of a. Equation (2.3) was found to give values of a within a mean deviation of approximately 5% from those determined photographically. On the other hand, Lockett and Safekourdi [34] reported a linear relationship between the light attenuation ratio and the interfacial area for high levels of light scattering (al>27).

Sridhar and Potter [3] developed a fibre optic light probe, which is shown in Fig 2.6. The optical path length was 10 mm. Polystyrene beads were used to check the applicability of the light transmission

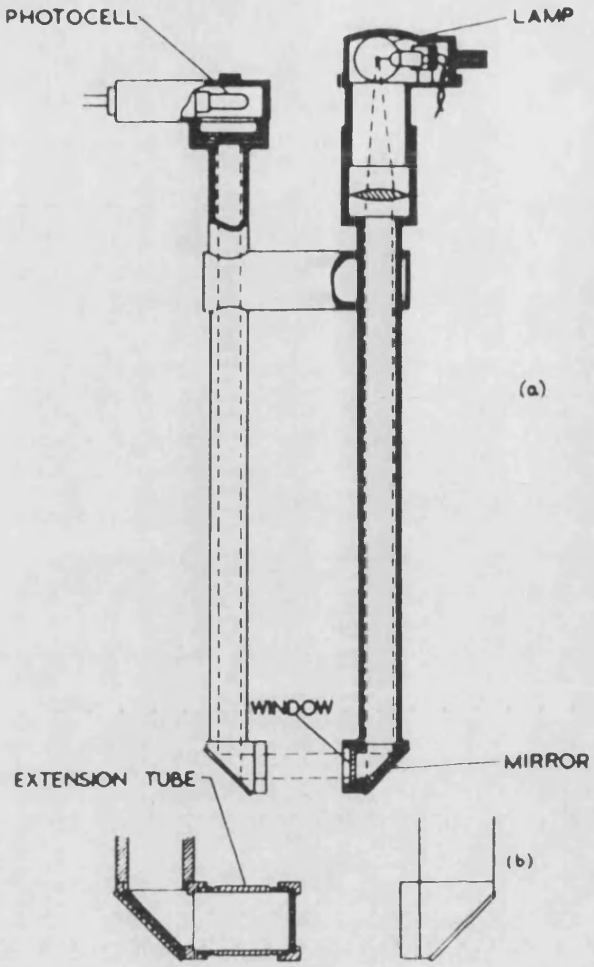

Fig 2.5 Light transmission probe of Calderbank [30].

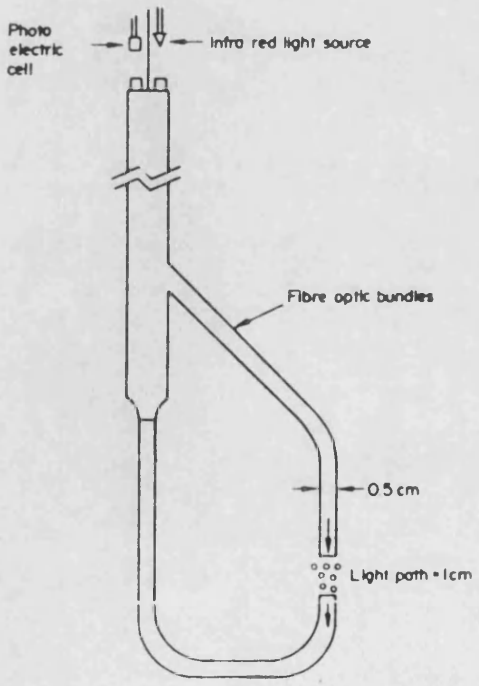

Fig 2.6 Light transmission probe of Sridhar and Potter [3].

relationship (Equation 2.1). A microprocessor was used to sample and average the output signal of the photocell at a rate of 1 KHz over a 20 second period. The probe had an improved design which made it capable of withstanding high pressures and temperatures. This probe was employed by the authors to measure interfacial areas in a 0.13 m stirred vessel for a wide range of system physical properties, at temperatures reaching 150 °C and pressures up to 10 atm. The reproducibility of the results was within 5%.

Recently Al Taweel et al [36] have extended the range of applicability of the technique up to al values of 460. This was accomplished by the use of a laser as a source of monochromatic collimated light, and a very sensitive low-bias picoammeter to measure light attenuation ratios as large as $\frac{I_0}{I}=10^8$. Using their calibration data obtained with polyvinyl toluene, Kaolin, corn and pecan pollen suspensions, they modified the relationship of Landau et al [2], Equation (2.3), and proposed the following explicit expression in a:

$$a = -\left[\frac{29.9}{l}\right]\ln\left|1-\frac{\ln\left[\frac{I_0}{I}\right]}{6.433l^{0.147}}\right| \qquad (2.4)$$

The light scattering technique was also used by Lee and Meyrick [37] and Figueiredo [38] for the measurement of point interfacial area in stirred vessels.

A technique based on the optical reflectivity or backward scattering of light from dispersions was first proposed by Calderbank et al [39]. The principle of the technique is illustrated in Figs 2.7 and 2.8. This method has not received widespread use. Like the photographic technique it only reveals information on the interfacial area near the

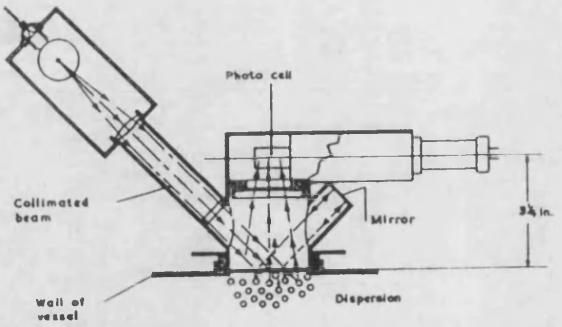

Fig 2.7 Light reflectivity probe of Calderbank et al [39].

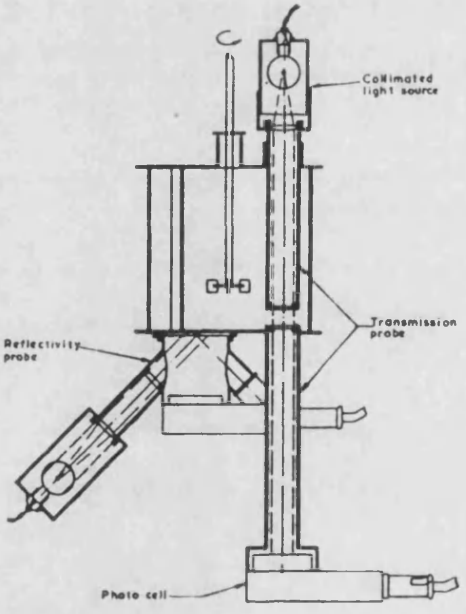

Fig 2.8 Set-up for use of light reflectivity and light transmission in a stirred vessel [39].

wall of the contactor. Hence most of the criticism made about the photographic method (see Section 2.3.1) is valid here as well.

2.2.3 Fibre optic probes

The use of fibre optic probes to detect the presence of gas bubbles in liquids is described by Danel and Delhaye [41] and by Galaup and Delhaye [42]. The working principle is based on the phenomenon of total internal reflection of light. Considering a prism of refractive index n_1 immersed in a medium of index n_2, as shown in Fig 2.9, Snell's law of light refraction gives:

$$n_1 \sin i_1 = n_2 \sin i_2$$

ie.,

$$\sin i_2 = \frac{n_1}{n_2} \sin i_1$$

It is clear, therefore, that refraction will occur if $\sin i_2 < 1$. In the case of a glass prism ($n_1 = 1.62$) and $i_1 = 45°$ there will be refraction only if $n_2 > 1.15$. Therefore, any medium with refractive index $n_2 < 1.15$ will cause total reflection of light. For instance, in the case of a two-phase air-water dispersion light will be refracted if the glass tip is immersed in water (n=1.33), and total reflection will occur if the tip is inside an air bubble (n=1.00). The transition from one mode to the other produces a step change in reflected light intensity which is used to detect the passage of a bubble interface.

Three fundamental elements constitute an optical probe:

(i) a light source: eg. micro-bulb, laser diode...

(ii) a light guide: eg. glass rod, optical fibres...

(iii) a light detector: eg. photodiode, phototransistor...

The existing optical probe designs can be classified into three main

categories according to the type of light guide used:

1. Glass rod probe (Fig 2.10):

Developed in 1969 by Miller and Mitchie [43], this probe was intended for local voidage measurement in two-phase gas-liquid systems [43, 44]. The method of calculation is shown in Fig 2.11. The instrument consists of a drawn glass rod shaped at its end in the form of a right angle cone and an optical fibre Y-junction. Light from a quartz-iodine lamp (6V, 100W) is focused on one of the branched ends of the light guide and a phototransistor (Fairchild P21) is located at the receiving end of the light guide. The sensing end is 0.3 to 0.5 mm in diameter. The authors claim that the instrument is capable of detecting small bubbles of 0.5 mm diameter. The major drawback of this system is the significant light losses, requiring the use of a high powered lamp (10 W) which prevents miniaturisation of the instrument. These losses occur in the glass rod tip of the probe because of the non-uniform surface polish as well as the joining section between the optical fibre and the glass rod.

2. Fibre bundle probe (Fig 2.12):

This instrument was designed by Hinata [45] (1972) and was used by him to determine local void fraction profiles in air-mercury flows in a pipe. Approximately one hundred fibres of 30 μm diameter having a central core and an outer cladding, are assembled in a Y-shape configuration. The index of the the fibre core is 1.62 and that of the cladding is 1.52. This arrangement prevents the leakage of light to the adjacent fibre. Therefore, the light is reflected at the boundary between the core glass and the coating glass, and is transmitted through the bent fibre by internal reflection (Fig 2.13). A glass rod, 0.5 mm in diameter, 1 mm long, itself coated with a glass of lower refractive index to prevent

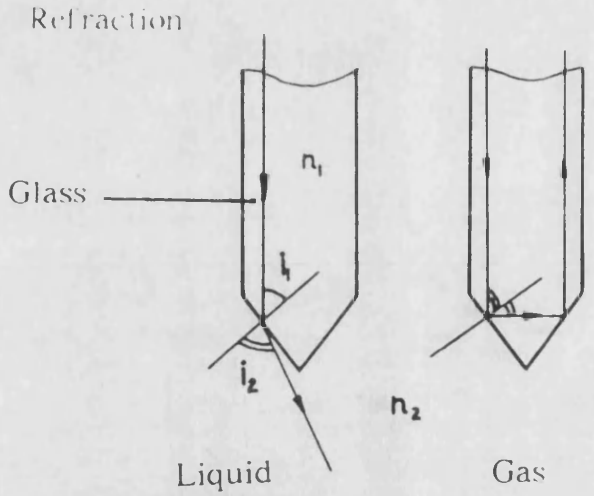

Fig 2.9 Principle of an optical phase detector

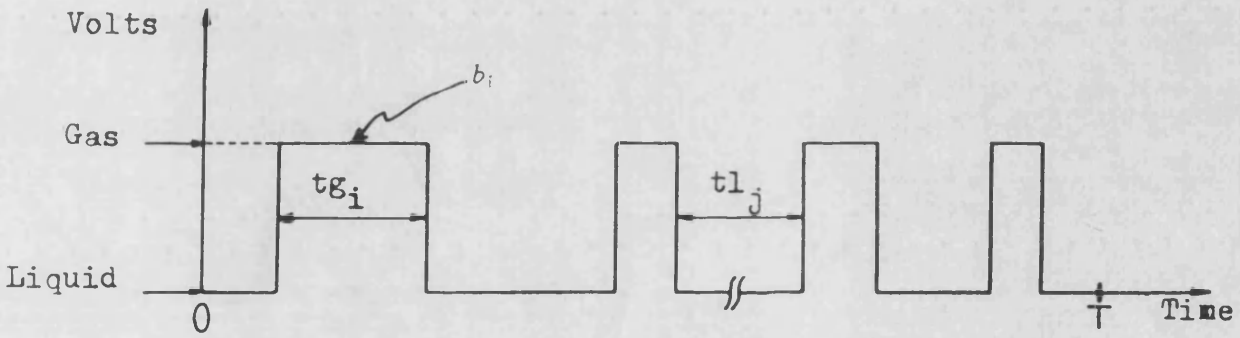

$$\epsilon = \frac{\sum t_{g\,i}}{T} \qquad n_f = \frac{\sum b_i}{T}$$

Fig 2.11 Method of calculation of gas holdup from processed probe signal.

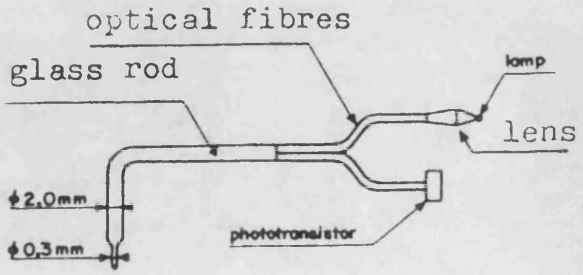

Fig 2.10 Glass rod probe of Miller and Mitchie (1969) [43].

light losses, is cemented to the tip of the fibre bundle. The end of the rod is ground and polished. The ends of the bifurcation are connected respectively to a flood light projector and a phototransistor.

The main disadvantage with this probe is the long rise and fall times of the signal in comparison with the duration of light pulses, on account of the influence of the thickness of the probe tip. The time error due to this effect was estimated to be of several milliseconds.

3. U-shaped fibre optic probe (Fig 2.14):

The original design of this probe was by Danel and Delhaye [41] (1971). The main components of the instrument are a low power dissipation lamp (300 mW), a phototransistor (Photodarlington BPX30) chosen for its good sensitivity and a single 40 μm optical fibre. The end of the probe is obtained by bending the fibre through an angle of 180 degrees, which allows a diameter of 100 μm to be achieved. The fibre is protected inside a 2 mm diameter stainless-steel tube, except for the U-shaped end. An improved version of this probe was later developed by Galaup and Delhaye [42] (1976). The size of the protective tube was reduced to 0.3 mm and the light detector was replaced by a phototransistor TIL81 (200 KHz against 20 KHz for the BPX30) associated with an amplifier integrated in the body of the probe. This system has a distinct size advantage (0.1 mm) over the glass rod and the fibre bundle systems (respectively 0.3 and 0.5 mm). It is capable of detecting bubbles down to 0.4 mm [47]. Its rise and fall times are also short, respectively 80 and 40 μs [42]. The main disadvantage of this design is its fragility. The bending of the fibre is difficult and the assembly of the instrument is delicate, and in the case of a breakage mending poses tremendous difficulties [46].

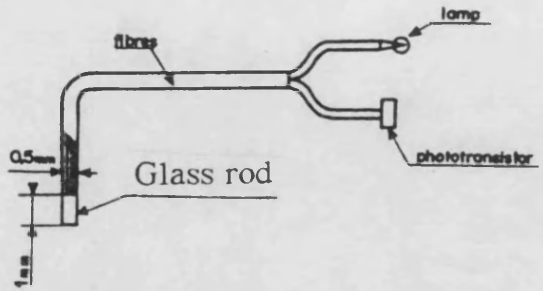

Fig 2.12 Fibre bundle probe of Hinata (1972) [45].

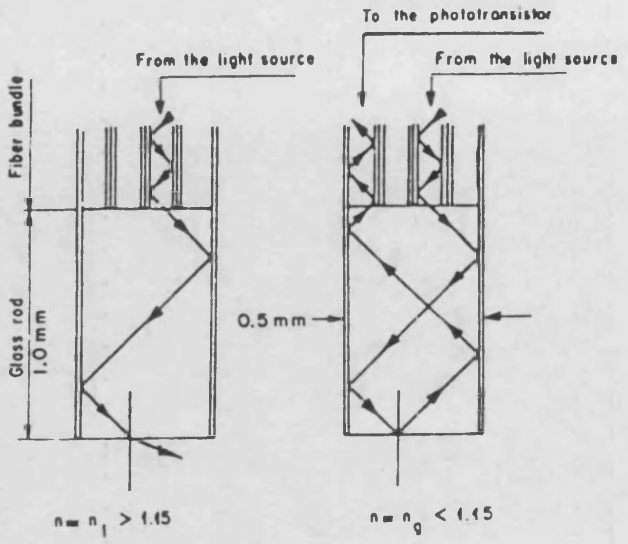

Fig 2.13 Fibre bundle (Hinata [45]).

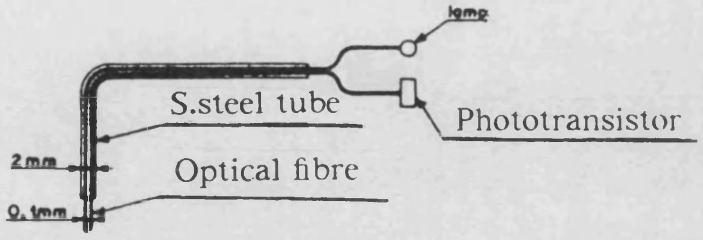

2.14 (a) Probe assembly

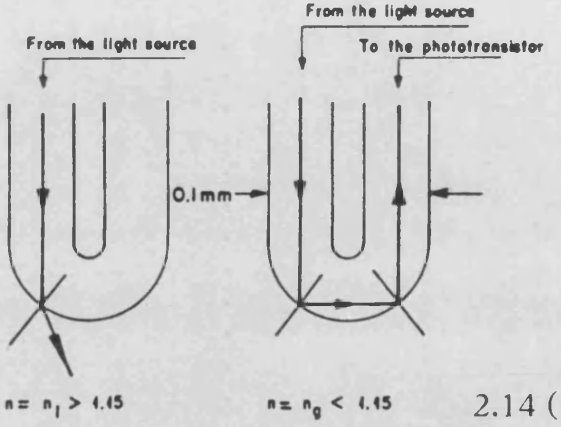

2.14 (b) Sensor tip

Fig 2.14 U-shaped probe of Danel and Delhaye (1971) [41].

A probe configuration combining features of the three designs described above has been proposed by Abuaf et al [48, 49] (Fig 2.15). The main elements consist of two 125 μm fibres inserted in a 0.5 mm O.D. stainless-steel tube. The tip of the probe is ground and polished to form an included angle of 90 degrees. The light source is a 3 V incandescent light bulb, and the photodetector is a PIN photodiode. An amplifier with a rise time of 20 μs is used to enhance the output before going into the readout device.

The signal analysis and the methods for obtaining the local information on void fraction include triggering techniques to transform the actual signal into a binary signal. A trigger level is set between the peak values of the signal to define the transition from liquid to gas and vice versa. Often the trigger level is set arbitrarily without justification. This can introduce significant errors in the measurements if the rise and fall times of the signal are important in relation to the duration of the light pulses. A typical signal delivered by the U-shaped probe is shown in Fig 2.16. Instead of obtaining a clear on-off signal during the passage of an interface, the static levels of the signal and the fluctuations caused by the passage of the bubbles varied with the void fraction. Thus, Galaup [46] used a double triggering technique where the threshold levels were determined from a calibration test against a γ-ray absorption technique, to give the same profile average of local void fraction across a pipe section. The above phenomenon which was attributed to electronic or hydrodynamic response problems [46], was investigated by Abuaf et al [48, 49] using their conical-tip probe. They found that the signal amplitude decreased with increasing bubble velocity independently of the bubble size. This was attributed to a liquid film thickness left on the probe tip, which increased with bubble velocity and, therefore, caused the decrease in the signal intensity that was observed experimentally.

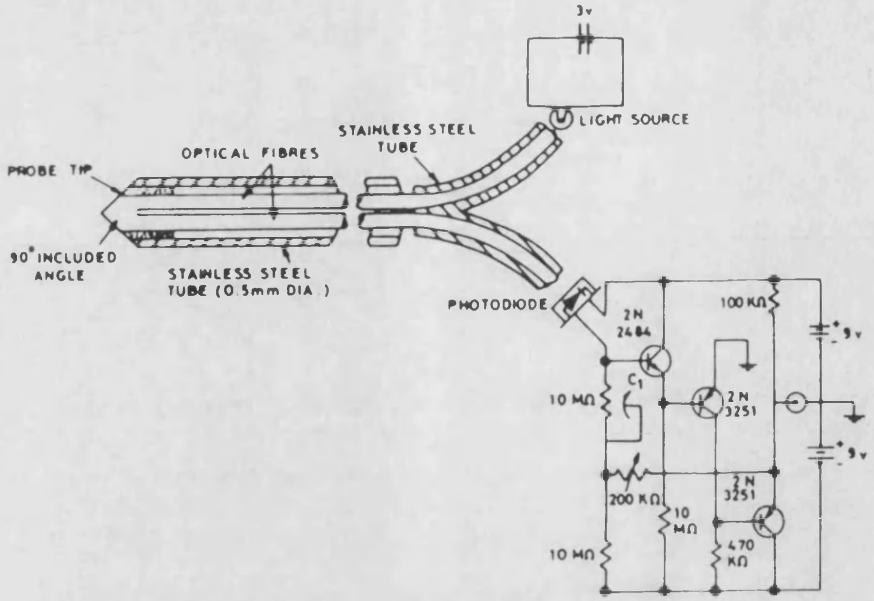

Fig 2.15 Optical probe of Abuaf et al [48,49].

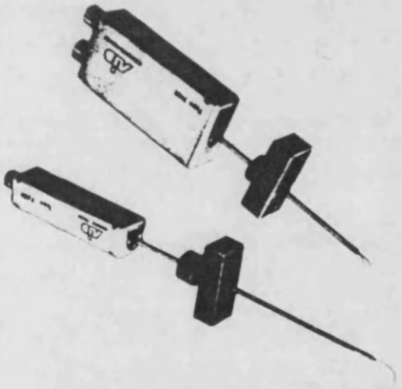

Fig 2.17 DISA U-probes (single and double).

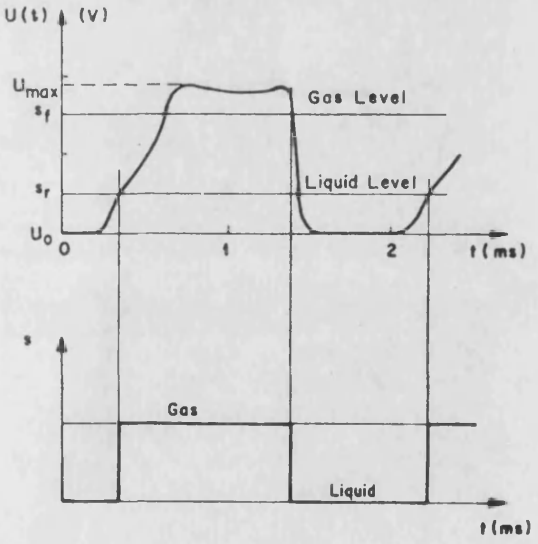

Fig 2.16 Typical optical probe signal and discrimination method [67].

They concluded that the probe is capable of measuring local bubble velocity as well as local void fraction. For velocity measurements the probe was calibrated inside a glass tube. Bubbles were injected at the lower end of the tube. The velocity of the bubble slugs was measured by means of two photodetectors just before it was detected by the probe, and correlated with the signal attenuation. For measuring local interface velocity and local specific interfacial area, Galaup and Delhaye [42] used a probe with two U-shaped sensing ends 2.3 mm apart. The interface velocity was determined from the ratio of the known probe spacing and the bubble travelling time between the two sensors, and the interfacial area, a, was obtained from:

$$a = 4\frac{n_f}{\bar{v}_b} \tag{2.5}$$

where, n_f is the bubble passage frequency and $\bar{v}_b$ is the average bubble velocity. Both this probe and the simple U-probe described above are available commercially, made by DISA (Fig 2.17). Each instrument is supplied with a phase indicator unit which powers the probe and conditions the signal. A void fraction unit is also available which can be connected to the phase indicator unit to give a direct reading of the local gas holdup [50]. The use of these probes has been restricted to two-phase flows in pipes probably because of their short length and fragility. Recently, Mann and Hackett [47] have used a DISA fibre optic probe to investigate the local statistics of approximately two-dimensional bubble clouds.

Compound optical probes have also been developed for measurement of bubble sizes and velocities in large gas-liquid contactors. The probe of Calderbank and Pereira [51] is a combination of five optical probes (Fig 2.18). Each element is made of a glass rod 0.2 mm diameter

the end of which is ground to a point. Optical fibres are used to convey the incident light from a 500 W light source and return the reflected light to a transistor photodiode supplied with an amplifier on the same chip. The signal rise time is of the order of 0.5 ms. The five sensors constitute an array in which a leading probe is symmetrically surmounted by three identical probes as shown in Fig 2.19. The fifth probe is placed on the same horizontal plane as the leading probe, at a short distance from it. An external discrimination circuit is used to select for measurement only those bubbles which strike the array of probes coaxially to give the maximum bubble height and bubble velocity. The fifth probe serves to measure the position and height of a vertical chord at a known distance from the centre line, from which the bubble shape can be deduced.

The major disadvantage of this system is its size. Only bubbles greater than 6 mm can be detected and if the fifth sensor can be disregarded bubbles down to about 3 mm can be registered. A successful bubble encounter with the probe may be a rare event, a typical experimental run in a sieve-tray froth was reported to take about 4 hours [51]. It is also doubtful whether the instrument would be strong enough to be used in highly turbulent contactors such as stirred vessels. Nevertheless, it is still an important contribution in this field. A similar probe has been used more recently by Glass and Mojtahedi [94] to investigate bubble size distributions and rise velocities in a freely-bubbling fluidised bed.

The latest version of fibre optic probes is by De Lasa et al [52]. This system consists of four 400 μm diameter U-shaped probes. The fibres are protected inside stainless-steel tubes. The radius of the U bend is approximately 0.5 mm at the tip of the probe. The light source used is

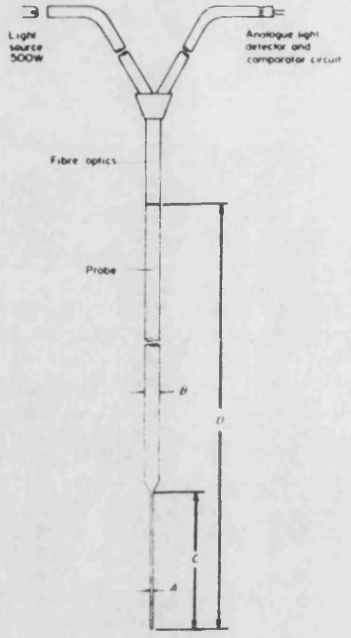

A single probe. *A*, 0.018–0.024 cm; *B*, 0.280–0.295 cm; *C*, 11.5–12.5 cm; *D*, 38–40 cm.

Fig 2.18 Light probe of Calderbank and Pereira (1977) [51].

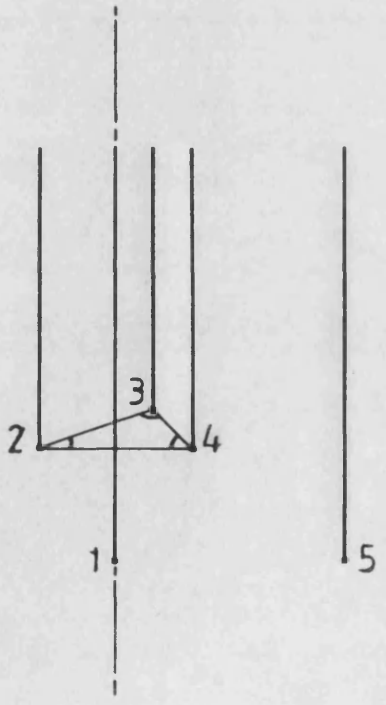

Fig 2.19 Spatial orientation of light probe elements [51].

a Helium-Neon laser beam. A microprocessor was used for data analysis.

2.2.4 Conductivity probes

The conductivity probe method, also called resistivity probe method, is based on the difference in electrical resistivity between the liquid and the gas phase. Hence, the first requirement when using a conductivity probe in two-phase flow is that the two phases have significantly different electrical conductivities. The principle of the technique is illustrated in Fig 2.20. Impedance changes due to change of phase distribution between the two electrodes produce a change in the output signal. Different positions and shapes of electrodes have been used by different workers. The tip of the measuring probe constitutes the first electrode while the second electrode may be a second probe, the metallic protecting sheath of the measuring probe or the general ground of the contactor.

Since the method was first proposed by Akagawa [53] (1963), many designs have been developed. At first these instruments were generally relatively bulky, but progress on miniaturisation was achieved when Lecroart and Porte [54] (1971) developed a probe, the sensing part of which was a tungsten wire, 20 μm in diameter (Fig 2.21). They used a direct current supply to energise the probe. This is the easiest solution and it has been adopted by other workers [14, 55-57]. In order to reduce electrochemical phenomena on the sensor, however, low voltages must be used (500 mV maximum). As a consequence the resultant electronics may become troublesome while the probe may undergo alteration due to electrochemical deposits. The other solution is the use of an alternating sinusoidal current supply. This technique has been employed by several investigators [58-61] in order to eliminate the electrochemical phenomena from damaging the sensor tip. The phase changes are then

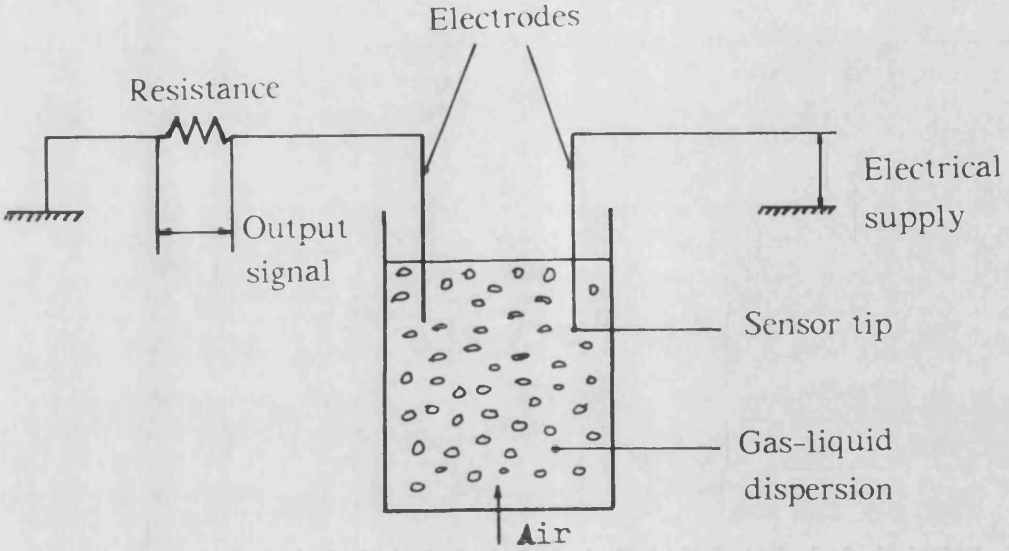

Fig 2.20 Principle of electrical resistivity method.

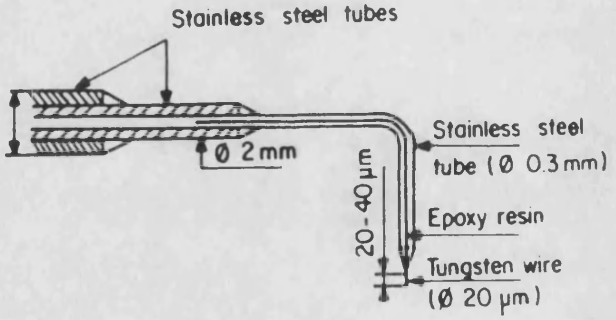

Fig 2.21 Resistivity probe of Lecroart and Porte [54].

detected by amplitude modulation of the alternating output signal. The requirement in this case is that the current frequency is significantly different from the frequency of the phase changes. An alternative solution which was adopted by Galaup [46], utilises an alternating square current waveform. Over half a period the system behaves as though it is supplied by a DC source. The supply frequency has to be lower than the signal frequency.

The signal delivered by a resistivity probe is similar to that delivered by a fibre optic probe (see Fig 2.16). The resistivity probe is often used as an alternative to the optical probe because of its simpler construction. Like the optical probe, the conductivity probe can yield information on the local gas fraction and bubble frequency in a dispersion. Double sensor probes have also been used to measure local interface velocity [55-62]. Four such probes are shown in Figs 2.22-2.25 for the sake of comparison. The probes of Buchholz and Schugerl [62], and Lewis and Davidson [61] are capable of detecting bubbles down to 0.58 and 0.5 mm respectively, while Thang and Davis [60] claimed that the minimum bubble size that could be detected was 0.1 mm, which represents a great improvement in the sensitivity of measurement. These two-electrode probes have also been considered for the measurement of local bubble size distribution. Buchholz and Schugerl [62] evaluated the bubble velocity from the time difference, Δt, between the start of the signals of the leading and the trailing electrodes and the distance, Δd, between them as:

$$v_b = \frac{\Delta d}{\Delta t} \tag{2.6}$$

and the size of the bubble was represented by its piercing depth, l_b, obtained from:

Fig 2.22 Resistivity probe of Serizawa et al (1974) [56].

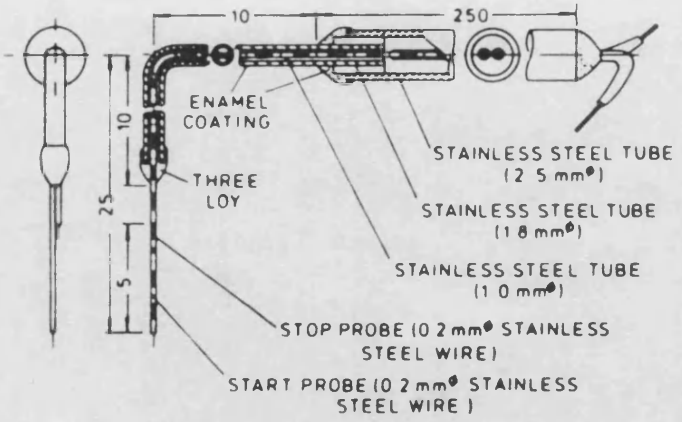

Fig 2.23 Resistivity probe of Buchholz and Schugerl (1979) [62].

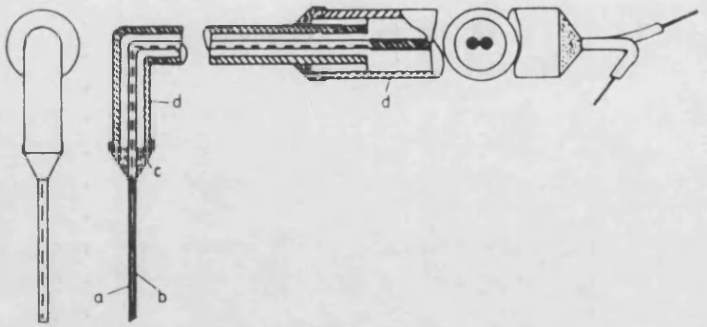

Double sensor electrical conductivity electrode. *a*: start sensor/*b*: stop sensor. Pt needles 0.08 mm in diameter insulated electrically by a sheath except for tips. Needle distance 0.1 mm. *c*: epoxy resin; *d*: stainless steel tubes

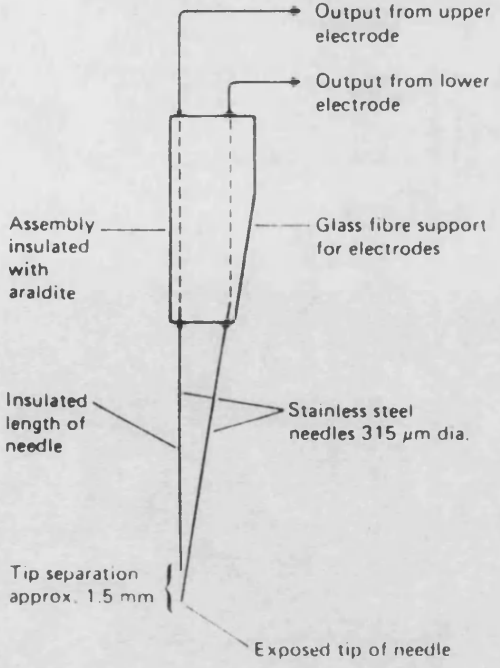

Fig 2.24 Resistivity probe of Thang and Davis (1979) [60].

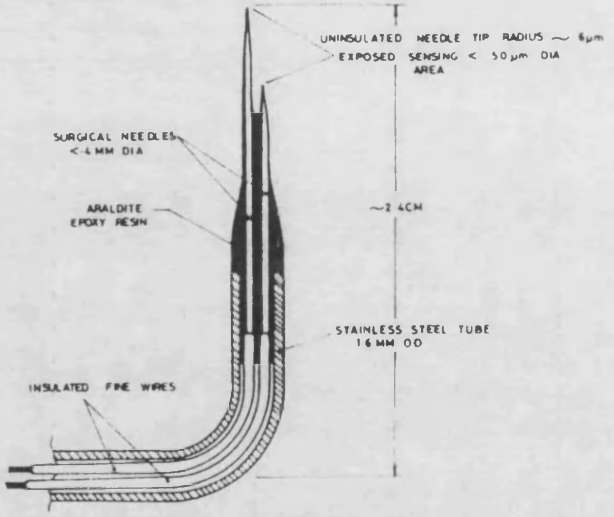

Fig 2.25 Resistivity probe of Lewis and Davidson (1983) [61].

$$l_b = v_b t_1$$

where, t_1 is the dwelling time of the leading probe in the bubble. The signals were processed in a crystal-controlled digital-computer measurement amplifier with an integrated digital-to-analog converter. They used a comparator for comparing the times t_1 and t_2 from the signals of respectively the leading and trailing needles in order to reject bubbles which are not pierced centrally. The ratio of the time values had to comply with a specified boundary value. In the case of spherical bubbles the measured chord length is equal to the diameter of the bubble. However, for bubbles with irregular shapes the measured size will deviate significantly from the true bubble size. This clearly limits the scope of application of two-point conductivity probes for bubble size measurement. In addition, using Equation (2.6) for determining the velocity especially of bubbles not centrally pierced, may lead to greater inaccuracy. This point has been examined by Steinemann and Buchholz [63] who derived the following expression which takes into account the effect of bubble curvature (see Fig 2.26):

$$v_b = \frac{2H_i}{\Delta t_1 + \Delta t_2} \tag{2.7}$$

Lewis and Davidson [61] and Lewis et al [64] used the times t_1, t_2 and t_3 stored by a microprocessor (Fig 2.27), and the known needle spacing to obtain the velocity of the front interface and that of the rear interface of the bubbles, and two measurements of the intercepted bubble chord. A maximum difference margin of $\pm 15\%$ between the measured bubble chords or velocities was set for the acceptance of a bubble, otherwise it was discarded in the subsequent analysis. Typically, 20-40% of the bubbles were, thus, rejected. The resolution of time measurement was 0.1 ms. The bubbles were assumed to be spherical and

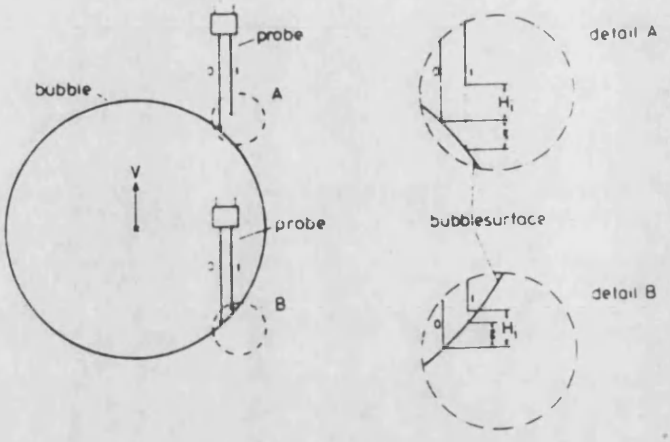

Fig 2.26 Derivation of bubble velocity taking into account effect of bubble curvature [63].

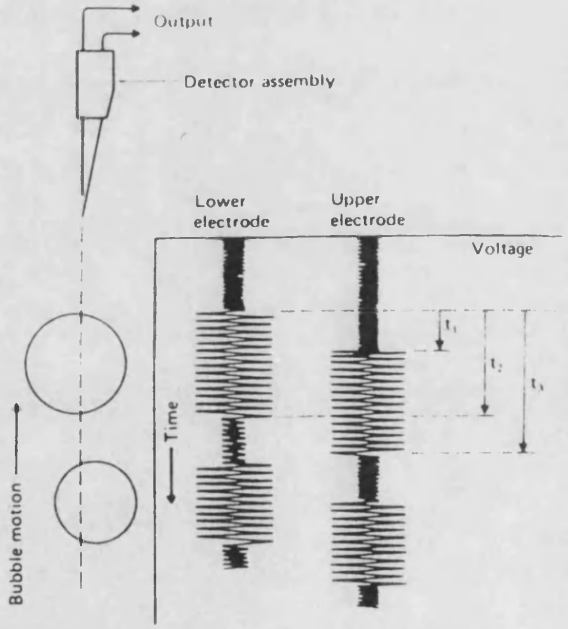

Fig 2.27 Signals from probe of Lewis and Davidson [61, 64].

an expression for the probability, P_r, of a bubble to be detected and accepted was derived:

$$P_r = \left[\frac{4}{\pi d^2}\right]\left[\frac{c^2 dc}{(d^2-c^2)^{1/2}}\right] \qquad (2.8)$$

where, c is the bubble chord length and d is the bubble diameter. The detected diameter distribution D'(d) was obtained from the measured chord frequency distribution and the probability distribution function. Since the probability of a bubble being hit by the probe is proportional to its projected area, ie., $\propto d^2$, D'(d) was weighed by d^{-2} to correct for bubbles not detected by the probe. Their results in the riser section of an air-water recirculating bubble column revealed a mean bubble diameter of 2.5-2.7 mm and a maximum bubble size of 10-15 mm for different air superficial velocities. This makes the assumption of spherical bubbles look very dubious.

A lot of uncertainties exist in the deduction of the bubble size and velocity distribution at a point in a dispersion from data yielded by two-element probe configurations because of the varying and unknown positions at which the probe contacts the bubble interfaces. In attempting to remove some of these uncertainties, Burgess and Calderbank [14] developed a three-dimensional conductivity probe with five channels (Fig 2.28) for use in sieve-tray columns and freely bubbling gas-fluidised beds. Its geometry is similar to that of the optical probe of Calderbank and Pereira [51], described in Section 2.2.3. This device was interfaced to a high speed digital computer. A typical pulse sequence generated by a single bubble as it hits the probe array is shown in Fig 2.29. A discrimination logic process allowed only those bubbles whose central axes were coincident with the probe axis to be analysed, therefore, rejecting bubbles which are off-centre. The bubble size was,

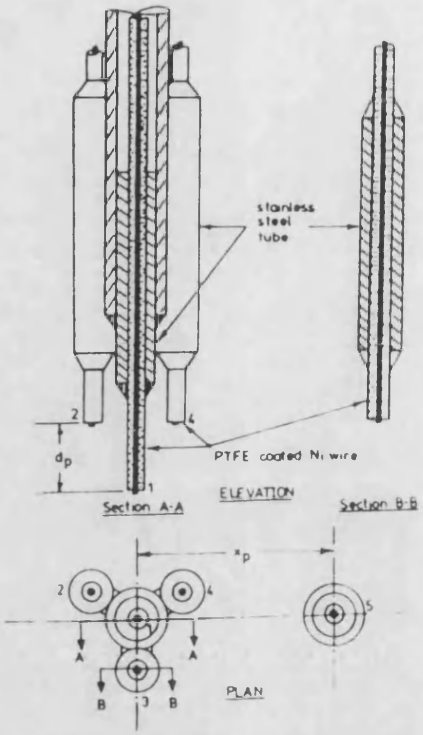

Fig 2.28 Five-point conductivity probe of Burgess and Calderbank [14].

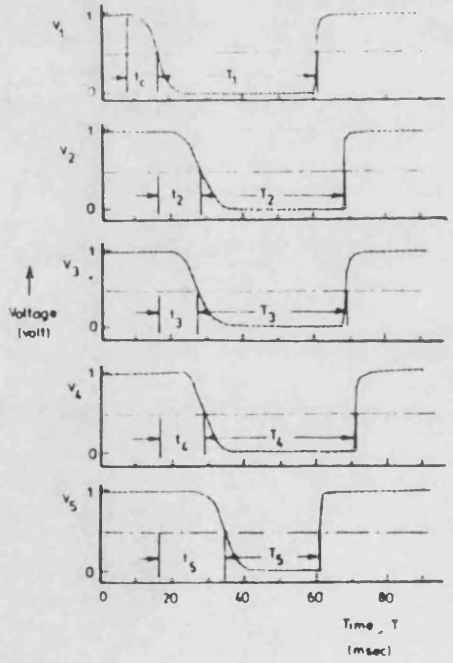

Fig 2.29 Typical pulse sequences generated by the probe when a single bubble in water rises into the probe assembly. Each point represents an instantaneous voltage sampled by the computer. The channel numbers are given by the code in Fig 2.28

thus, defined in terms of its central chord length given by:

$$l = v_b t_c$$

where the bubble velocity is obtained from:

$$v_b = \frac{3d_p}{t_2+t_3+t_4}$$

The function of the probe's fifth channel is to give information on the bubble shape by an extra vertical chord. To be detected by all five channels, a bubble must have a minimum major axis of approximately 11.7 mm. The minimum bubble size which can be detected by the four central channels is about 3 mm.

Figueiredo [38] used an identical probe to measure bubble size distributions in a stirred vessel. However, it had only the main four channels, and the probe separation had to be reduced to allow bubbles down to 0.98 mm to be detected. Successful bubble-probe encounters were rare so that a typical run took about 3 to 4 hours to obtain an average of 200 successful samples. This constitutes the main drawback of this instrument.

Much more recently, Steinemann and Buchholz [63] designed a four-point conductivity probe made of 20 μm platinum wires fused in glass (Fig 2.30). The total diameter of the probe was about 500 μm. This constitutes a major improvement in miniaturisation of these three-dimensional probes. The instrument works in a conductivity range of continuous phase from 30 to 10^5 μs/cm, which makes measurements possible in distilled water as well as in concentrated solutions. This in itself is an important achievement since all previous probes did not operate at such low conductivities. The instrument was coupled to a computer and the resolution of time measurement was 1 μs. Instead of

accepting only those bubbles which rise vertically with respect to the probe axis, diagonally rising bubbles are also measured. The time sequence generated by the four electrodes is combined with the known electrode spacings in order to describe the bubble motion including its velocity, v_b, the direction of its trajectory, ϕ, and its rise angle, θ, (Fig 2.31). An equation relating these three unknowns can be written for each pair of probe electrodes, which includes the centre channel (0) and one of the three upper channels (i=1,2,3):

$$v_b(t_{i_1}+t_{i_2}) = 2(H_i\cos\theta-\Delta_i\sin(\phi+\phi_i)\sin\theta) \qquad (2.9)$$

where t_{i_1} and t_{i_2} are respectively the time delays between channels 0 and i for the front and the rear of the bubble, other parameters being defined in Figs 2.30 and 2.31. A system of three equations has to be solved to obtain the values of v_b, ϕ and θ for each bubble detected. Using these parameters and assuming the bubbles to be ellipsoids of revolution (which includes the particular case of spherical bubbles), the mean bubble size is determined. The smallest bubble size that can be detected with this system is 1 mm. This means that bubble size distributions will be biased, a drawback which is shared to different extents by all resistivity probes described above. The accuracy of the measurements is also affected by the quality of the probe signal. This is usually characterised by a relatively slow response as the bubble is being pierced, owing to liquid thinning at the tip, followed by a relatively faster voltage change as the probe tip returns to the liquid phase. For improved accuracy the signal response should be made as fast as possible. This is usually achieved by coating the sensor tip with a hydrophobic substance eg. PTFE, Araldite, varnish. The signal obtained is transformed into a rectangular signal by means of a Schmitt trigger. A voltage level near the liquid line is usually chosen as the trigger level.

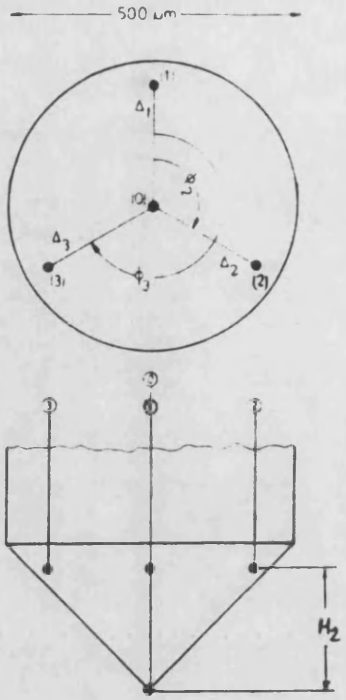

Fig 2.30 Four-point conductivity probe of Steinemann and Buchholz [63].

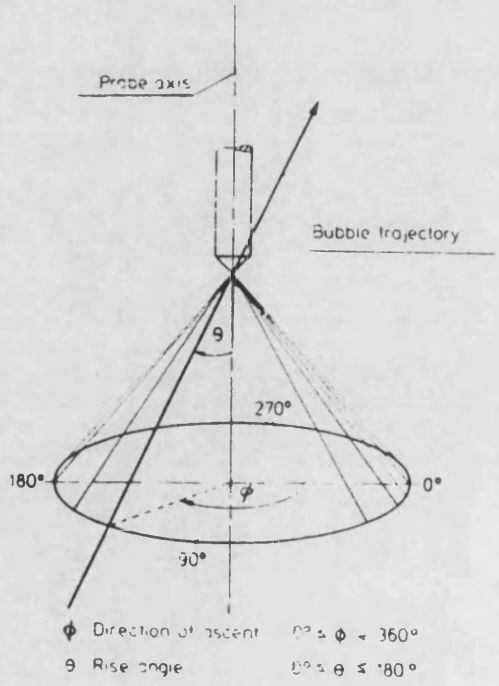

Fig. 2-31 Definition of bubble movement parameters.

2.3 Non-invasive techniques

2.3.1 Photographic methods

Flash photography was one of the first methods to be used in the study of two-phase flow and it is still often used as a check on the validity of data obtained from other measuring techniques (eg. measurement of interfacial area by a chemical method [1-3] or by an optical method [2-6]). It has been widely used to estimate bubble size distributions and interfacial area in different fields of gas-liquid contacting [7-15], eg. two-phase pipe flow, sieve-tray froths, bubble columns, stirred vessels. Hsu et al [16] have made an extensive review of photographic techniques and equipment.

Basically, the method involves taking flash photographs of the dispersion and determining the Sauter mean bubble diameter, d_{32}, from these photographs. Knowledge of the gas holdup would then allow the interfacial area to be calculated from the relation $a = 6\epsilon / d_{32}$.

Calculation of the Sauter diameter requires three-dimensional information on the geometry of the bubbles. Above a certain size, bubbles are no longer spherical and since only two-dimensional geometrical dimensions are available from the photographs, a first approach to solve the problem would be to model the shape of the bubbles. A two-parameter model in which one end of the bubble is assumed to be a hemisphere and the other end is assumed to be one-half of an ellipsoid of revolution is a popular model [17-19] because it can describe a number of different shapes, as shown in Fig 2.32, depending on the relative lengths a and b. Two equivalent diameters, d_A and d_V, can be defined for a bubble:

- Based on the projected area of the bubble, A:

$$d_A = \left| \frac{4A}{\pi} \right|^{1/2} \qquad (2.10)$$

where, A can either be directly measured or calculated if the shape of the bubble is characterised by a given model.

- Based on the bubble volume V:

$$d_V = \left| \frac{6V}{\pi} \right|^{1/3} \qquad (2.11)$$

In this case the assumption of a model is necessary. It must be emphasised that a model can only approximate the shapes of the bubbles in the dispersion. However, it cannot fit them exactly, and the uncertainty stemming from the imperfection of the model may be impossible to determine.

Although it is not always clearly stated, it seems that the use of automatic image analysers which can measure with high precision the projected areas of the bubbles, has led researchers [2] to estimate the Sauter mean bubble diameter from the equivalent diameter d_A. This approach is à priori interesting since it avoids the problem of modelling the shapes of the bubbles. By considering the model, described above, Veteau [9, 18] theoretically evaluated the error incurred in estimating the Sauter mean diameter from the equivalent diameter d_A. The error varies according to the value of the bubble shape parameter e (=a/b), as shown in Fig 2.33. For e=1 ie., for spherical bubbles the error is zero as expected. From Fig 2.33 it can be seen that the Sauter diameter is always overestimated for $e \neq 1$, and for an important range of e values ie., $0.7 < e < 1.4$, the error is within 5%.

Alternatively, the principles of stereology which relate three-dimensional parameters defining a structure to two-dimensional measurements obtained on sections of the structure, can be used to

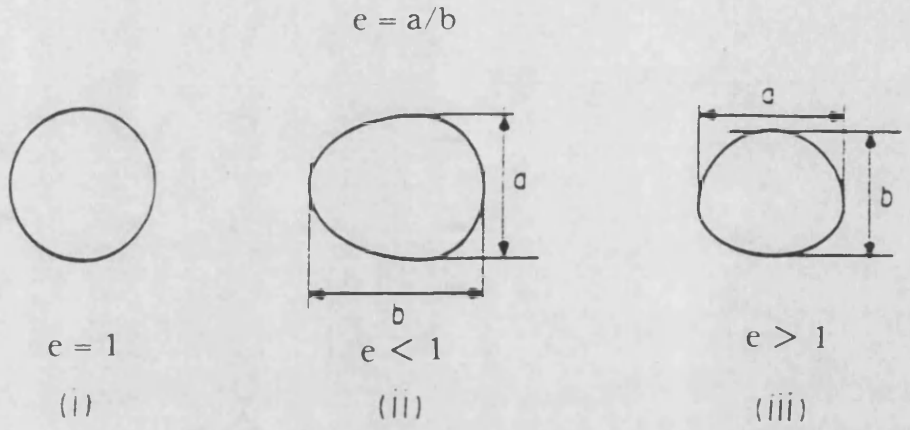

Fig 2.32 Two parameter model for bubble shapes.

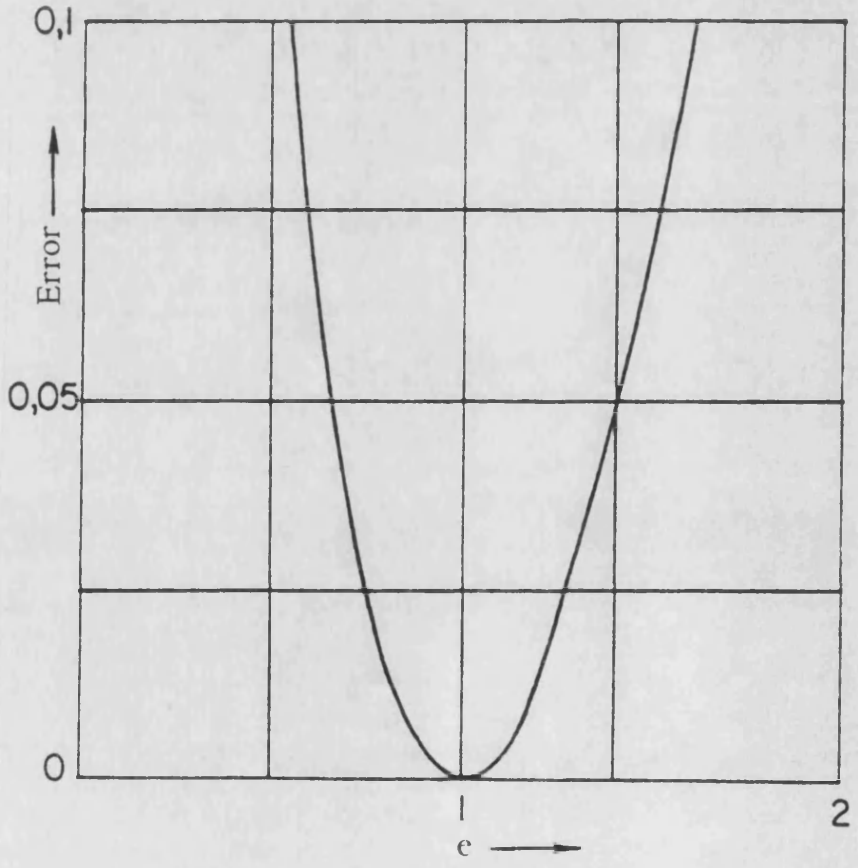

Fig 2.33 Variations of the error on d_{32} with e [9, 18].

determine the Sauter mean bubble diameter, gas holdup and interfacial area of the dispersion [20]. This method of systematic point counting consists in superimposing a square grid on the sample photograph, as shown in Fig 2.34, and counting the fraction number of grid points contained inside the projected bubble areas, P_p, and the number of intersections of the grid lines with the contours of the projections per unit length of test lines, P_l. The Sauter mean diameter, the gas holdup and interfacial area are then given respectively by:

$$d_{32} = 3\frac{P_p}{P_l} \qquad \epsilon = P_p \qquad a = 2P_l$$

This technique strictly applies for random plane sections of the structure and it is difficult to assess the error involved in applying it to photographs which are merely projections of the boundary plane of the dispersion. The method, however, was used by Calderbank and Rennie [10] for analysing photographs of bubble clouds in sieve-tray columns. Although the bubble size determined photographically seemed to be in good agreement with that obtained from optical reflectivity and γ-ray transmission measurements at high gas flow rates, the interfacial area and gas holdup were invariably lower than those deduced from the other two methods. They concluded that the bubble sample as viewed at the column wall was representative of the dispersion in the bulk of the froth, but an unrepresentative larger volume of liquid was present at the wall. Therefore, they determined the interfacial area from the gas holdup as measured by γ-ray attenuation and the photographically determined bubble size.

The photographic technique is experimentally simple, non-invasive and can be applied to both low and high viscosity systems. In addition to the quantitative information it can provide on bubble sizes, it has also

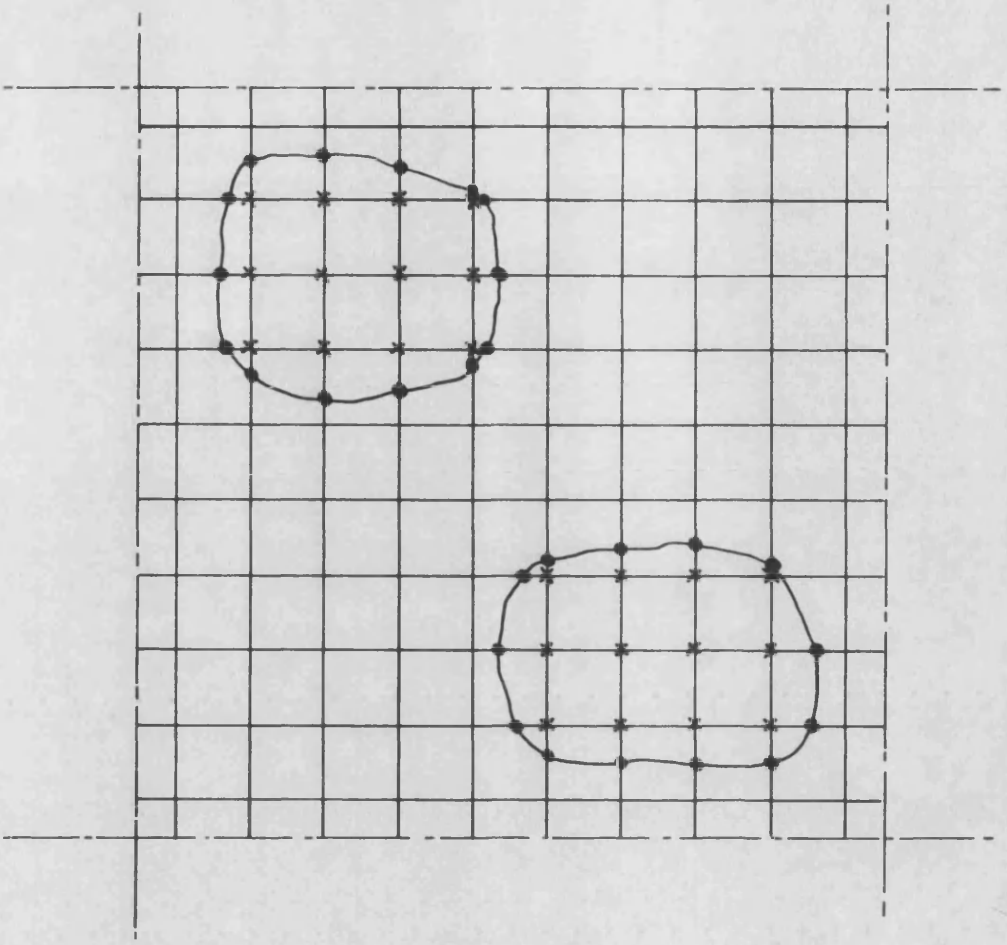

Fig 2.34 Method of systematic point counting.

eg. $P_p = \frac{24}{100}.(\times)$

$$P_l = \frac{27}{10\times10cm + 10\times10cm}.(\bullet)$$

the merit of revealing some qualitative information on the structure of dispersions such as spatial bubble distribution and bubble shapes. However, the method suffers from some handicaps which must also be borne in mind when it is used. The main drawback is whether information extracted from photographs taken through a transparent wall is representative of conditions over the entire cross-section of the dispersion. Veteau [9] measured the interfacial area in a vertical rectangular channel. The results obtained from photography were found to exceed those found using light attenuation by 30%. This difference was attributed to the smaller bubbles near the wall which are detected photographically. An equal probability of finding bubbles with different sizes on the photographs can only be achieved in the case of a narrow bubble size distribution. In the case of a broad distribution, the larger bubbles having greater rising velocities will exhibit shorter residence times in the plane of measurement, thus, resulting in truncation of the bubble size spectrum. Burgess and Calderbank [15] have shown that this effect was responsible for interfacial areas determined photographically being appreciably higher than those obtained from a chemical or a local technique in sieve-tray froths. A further disadvantage lies in the complicated evaluation process. The analysis of the photographs is time consuming and above all it is subject to inherent measurement uncertainties which may be impossible to determine. Recently Takahashi et al [21] utilised the technique to measure bubble size distributions in the region close to the impeller tip in a stirred vessel. Most of the bubbles were less than 0.2 mm with an important fraction having a diameter of 0.05 mm. Even with a 10 time magnification this would still require accurate measurement of 0.5 mm dimensions. It has been shown [9] that to obtain a reproducibility of results better than 3% at least a sample of some 300 bubbles must be analysed. Even when automatic

image analysis methods are used to speed up the processing of photographs and increase the accuracy of the measurements, the opinion of the investigator is important since he has to decide whether a particular profile present on the photograph is actually in the plane of measurement or not. Trice and Rodger [5] reported the data extracted by five different researchers from the same photographs. The maximum difference amounted to 3.5%. Azzopardi [75], on the other hand, reported much higher discrepancies going up to 17%.

2.3.2 Laser-based techniques

The principle of operation of some of the initial laser-based techniques is described by Hewitt [65, 66]. These methods which rely on the existence of Mie scattering are limited to the detection of particles less than about 150 μm [70], well below the size range encountered in most two-phase flow applications. The use of two crossed laser beams to create a field of light and dark fringes provides a means of measuring the velocity of a moving particle [72]. As a small particle crosses these fringes the scattered light will alternate in intensity between bright and dark as a fringe is crossed. A photo-multiplier tube suitably located will collect the scattered light and deliver a signal with varying amplitude. From the frequency of this signal and the fringe spacing which can be calculated from the laser light frequency and the angle between the two beams, the particle velocity is determined.

In recent years attempts have been made with the aim of adapting this technique to include simultaneous measurement of particle size. However, most of the systems proposed are only valid for small particle sizes and very low concentrations [71]. More recently, Lee and Srinivasan [73] (1982) have developed a reference-mode laser-doppler anemometer for simultaneous velocity and size measurement of large

particles in two-phase flow suspensions. The optical arrangement used is represented in Fig 2.35. The incident laser beam from a 15 mW He-Ne source is split into two beams of different intensities. The weaker beam is used as the reference beam and the stronger one as the scattering beam. After being polarised to form a 45° polarisation angle between them, the two beams are focused to the same point to form a small measuring volume (240 μm). The scattered light from the scattering beam on hitting a moving particle in the sample space is recorded together with the reference beam by a matching receiving lens along the direction of the reference beam. The resulting beam is then split into two, one in the polarisation direction of the scattering beam and the other in a direction perpendicular to it. A photo-multiplier is located to pick up the first beam which consists of the scattered beam and the component of the reference beam, which is in the same direction, whereas the second beam consisting of the reference beam component with a polarisation direction perpendicular to that of the scattering beam, is received by a photo-diode. The photo-multiplier tube produces the doppler signal for measuring the velocity whereas the signal from the photo-diode serves to measure the time for the particle to cross the reference beam, which is used in conjunction with the vertical velocity from the doppler signal to obtain the diameter of the bubble. The system was interfaced to a mini-computer for the purpose of data acquisition and processing. The technique was tested by controlled experiments using steel balls and water droplets of known sizes (1-6.4 mm). The accuracy was found to be within 2%.

Instead of a twin-laser-beam system, Semiat and Dukler [70] (1981) passed a single laser beam through a grating to produce a similar field of dark and light fringes on the other side of the grating. The effect of intersection of the laser beam by a moving transparent water drop

behind the grid is illustrated in Fig 2.36. Part of the incident rays is reflected by the drop surface, while the other part is refracted into the drop and refracted again as it leaves the drop at the other side. In the case of an air bubble the reflected rays are similarly located, but because of the inversion of refractive index, the rays diverge as they enter the bubble and diverge again as they re-enter the liquid, the end result being the same as for the drop. As the bubble moves downward, the fringes move across a vertical plane at exactly the same frequency at which they are intercepted by the bubble surface. A photodetector P_1 would give a signal having a frequency equal to the known fringe spacing divided by the unknown bubble velocity. The same result can be obtained by detecting the reflected fringes at point P_2 in a horizontal plane.

The sampling volume, here, is determined by the intersection of the laser beam with the optical line of sight of a detector through a lens system. For bubbles greater than 375 μm, the optical sample volume is the bubble volume itself. In dense dispersions, however, small diameter optical fibres can be used as a light detecting probe. While in this way, the optical sample space can be significantly reduced, the technique loses its elegant characteristic feature of being non-intrusive.

For the purpose of measuring two coordinate velocities along with the bubble size the authors employed the arrangement shown in Fig 2.37. Two gratings are rotated at a controlled speed through the laser beam. The fringe spacing and speed of rotation are selected so as to give a signal with two distinct and non-overlapping frequencies as the bubble moves through the sample space. The disks are located so that one measures the horizontal velocity while the other measures the vertical velocity of the bubble. The same photodetector is used to pick up both doppler signals which are subsequently separated by frequency filtering. A second

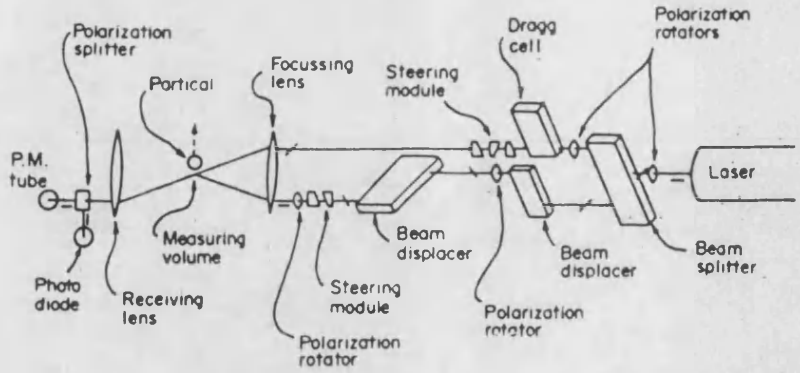

Fig 2.35 Optical arrangement of Lee and Srinivasan [73].

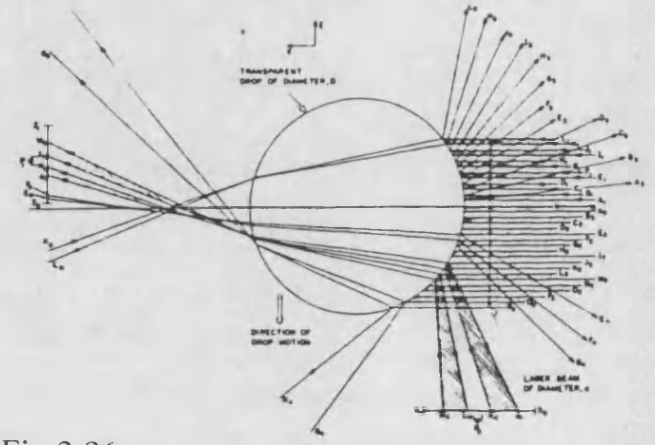

Fig 2.36 **Geometric optics for a laser beam intersecting a drop** [70]

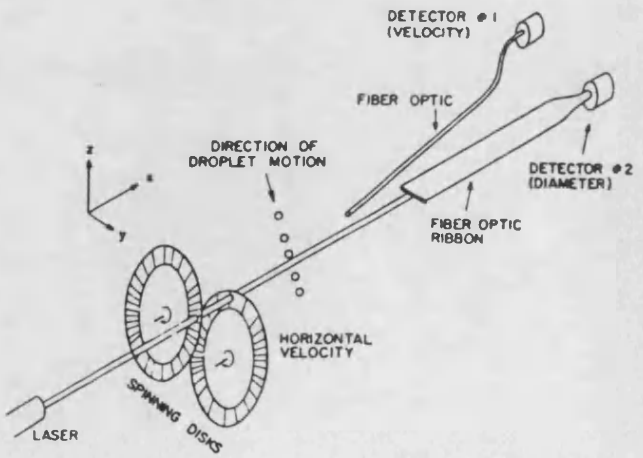

Fig 2.37 The use of rotating gratings [70].

detector is used in view of determining the particle size. Bubbles are detected as they pass in front of a narrow slot fitted with a ribbon of optical fibres which convey light to this detector. The passage time of each bubble is extracted from the signal obtained. This time is used in conjunction with the measured velocity in order to obtain the bubble diameter. The signal processing system is interfaced to a computer for data analysis. During measurements bubbles which donot give rise to a doppler signal and are only detected by the slot-beam detector, are automatically rejected.

The two laser-scattering techniques described above, like any technique that uses a passage time measurement to determine the diameter of a particle, have two major problems in common. The first one is that a chord rather than the true diameter may be measured, the effect being particularly significant for bubbles with irregular shapes. The second handicap lies in the fact that, as they stand, these techniques can be applied only to narrow dispersed systems with extremely low concentrations because of multiple particle presence in the laser beam(s) outside the sample space, which leads to a breakdown of the detection process. In order to overcome this difficulty and extend the application of such techniques to higher holdup dispersions, these methods should be designed in the form of submersible probes, which would bring them under the category of invasive techniques. Fibre optics, however, provide great potential for miniaturisation [74].

2.3.3 Radioactive absorption techniques

Attenuation of collimated Gamma-ray or X-ray beams passed through a gas-liquid dispersion, can be used to measure gas holdup. The use of these techniques has been discussed by Hewitt [65, 66]. Gamma-ray absorption is a widely used technique especially in two-phase pipe

flow [46, 67]. The absorption of a collimated beam of initial constant intensity I_0 (photons $m^{-2}s$) is described by the exponential relationship [66]:

$$I = I_0 e^{(-\mu\rho z)} \tag{2.12}$$

where μ is the mass absorption coefficient, ρ the density of the absorbing medium, and z the distance travelled through the dispersion. In applying this method, a radioactive source of γ-rays or X-rays, and a radiation detector (typically a plastic scintillator coupled to a photo-multiplier) are mounted diametrically on either side of the gas-liquid contactor. The intensities I_g and I_l recorded by the detector with the contactor, respectively, full of gas and liquid are first measured. The gas holdup is then obtained by measuring the intensity I_d transmitted through the actual dispersion [66]:

$$\epsilon = \frac{\ln I_d - \ln I_l}{\ln I_g - \ln I_l} \tag{2.13}$$

This single beam technique gives a chordal mean value of the gas holdup. To obtain a cross-sectional average value for the holdup, three alternatives are available [66]:

1. Traverse a single beam across the contactor and determine the mean cross-sectional value by some suitable integration of the chordal mean values.
2. Use a multibeam γ or X-ray system. Here, multibeams are taken from a single radioactive source [68], as shown in Fig 2.38.
3. Use a broad radiation beam, as wide as the section of the contactor. This 'one-shot' technique is described by Lottes [69].

In γ-ray measurements, two main sources of radiation are available, Caesium 137 and Thulium 170. Calderbank et al [39] used

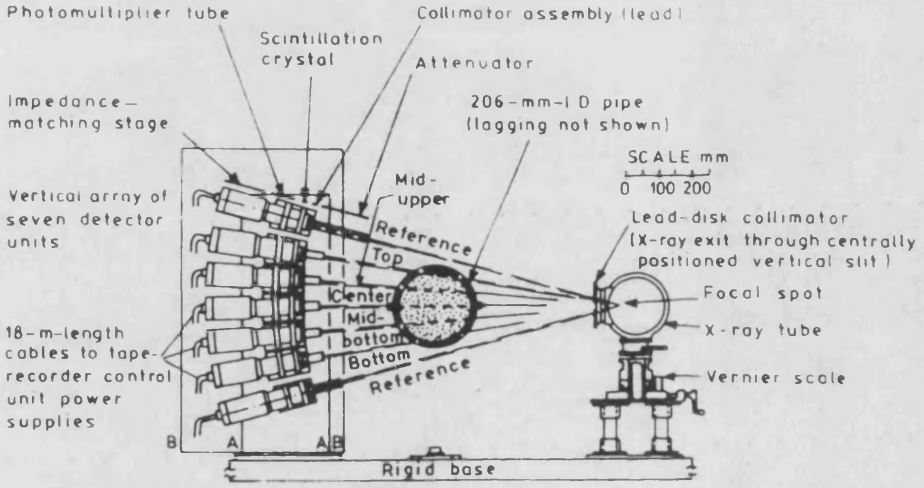

Figure 2-38 Multibeam X-ray system for determination of multiple cordal-mean void fractions (and hence general average void fraction) during a blowdown from a horizontal tube (Smith 1975)[68]

both these sources to measure the foam density in a distillation column. An automatic timer allowed the time for 10^4 counts through the empty column (t_0), through liquid-filled column (t_l) and through the dispersion (t_d), to be measured. The gas-liquid density, ρ_d, was determined from:

$$\frac{\rho_d}{\rho_l} = \frac{\ln t_0 - \ln t_d}{\ln t_0 - \ln t_l} \tag{2.14}$$

Better accuracy was achieved by the Cs 137 source than the Tm 170 source. This was due to the linear relation between $\ln I$ and density in the case of the mono-energetic Cs 137, which is not strictly valid for the multi-energetic Tm 170. Although, Thelium being the more strongly absorbed in water, gives higher sensitivity.

It is important to note that calculation of gas holdup from Equation (2.13) is only valid if the two phases are homogeneously mixed and there are no large fluctuations in the density of the mixture. In the latter case, the detector will record the mean of several exponential functions and not the exponential of the mean density [39]. In case of void orientation and/or time fluctuations, a solution is to use Cs 137 as a radiation source because its weak absorption can be approximated by a linear law which would then give [65, 66]:

$$\epsilon = \frac{I_d - I_l}{I_g - I_l} \tag{2.15}$$

However, high source strength is needed to achieve the required accuracy in this case.

An inherent source of inaccuracy in this technique is due to the random nature of the creation of photons. The standard deviation on the count rate is given by [66]:

$$\sigma = \left[\frac{R}{\tau}\right]^{1/2}$$

where τ is the counting time over which the rate R is determined. The standard deviation decreases (as a fraction of R) as both R and τ increase. The time for 10^4 counts must be observed in order to achieve 1% accuracy in the count rate from a radioactive source [39]. Other difficulties involved in the use of this technique lie in the safety problems associated with the handling of radiation.

2.4 Summary

A wide variety of measurement techniques capable of providing useful information on local and global bubble parameters in different gas-liquid contactors exist. All these methods are limited in one way or another, either in their ability to measure accurately the bubble parameter in question or in their being applicable to a sufficiently wide range of gas-liquid dispersion conditions. In recent years a noticeable trend of interest in probes capable of measuring local bubble properties has emerged because of their versatility and flexibility ie., application to a wide variety of gas-liquid flow situations. They reveal more information on the internal structure of gas-liquid dispersions than other techniques. Although they are invasive, significant progress in their miniaturisation has been achieved, therefore, reducing the flow disturbing effects. The introduction of laser systems coupled with fibre optics shows good promise in this respect. However, the problem of investigating the fluctuating structures of gas-liquid dispersions is far from being solved and hence more development is needed in the area of two-phase flow instrumentation.

Chapter 3

DESIGN OF EXPERIMENTAL EQUIPMENT AND PROCEDURES

3.1 Introduction

This chapter embodies details of the experimental arrangement and the procedures employed in this research. Section 3.2 gives a description of the general layout of the equipment and discusses the most important design features of the mixing vessel such as the sizing of the prime mover, the mechanical design of the impellers, the agitator shaft and the baffles, and the selection of appropriate shaft couplings. The techniques used for measuring agitator speed, power and total gas holdup are dealt with in Section 3.3.

3.2 Mixing apparatus : Design and layout

3.2.1 General layout of equipment

A general view of the mixing rig and the associated data acquisition and measurement system is shown in photograph 3.1. Photograph 3.2 shows the impeller shaft assembly including the torque transducer and the drive end of the motor. The air line including air filters, humidifier and flow meters, is shown in photograph 3.3, while the speed controller and the computerised impeller speed and torque supervisory system is displayed in photograph 3.4.

3.2.2 General design procedure

When designing a mixer for a given process duty, it is necessary to first specify the size of the tank and its geometry. Next, the type and size of impeller to fulfil the process requirements are specified. This enables the horsepower required to be estimated together with other special requirements such as fixed-speed operation, or adjustable variable-speed range operation. The type of prime mover needed will be determined once these criteria have been selected. Mechanical design of other

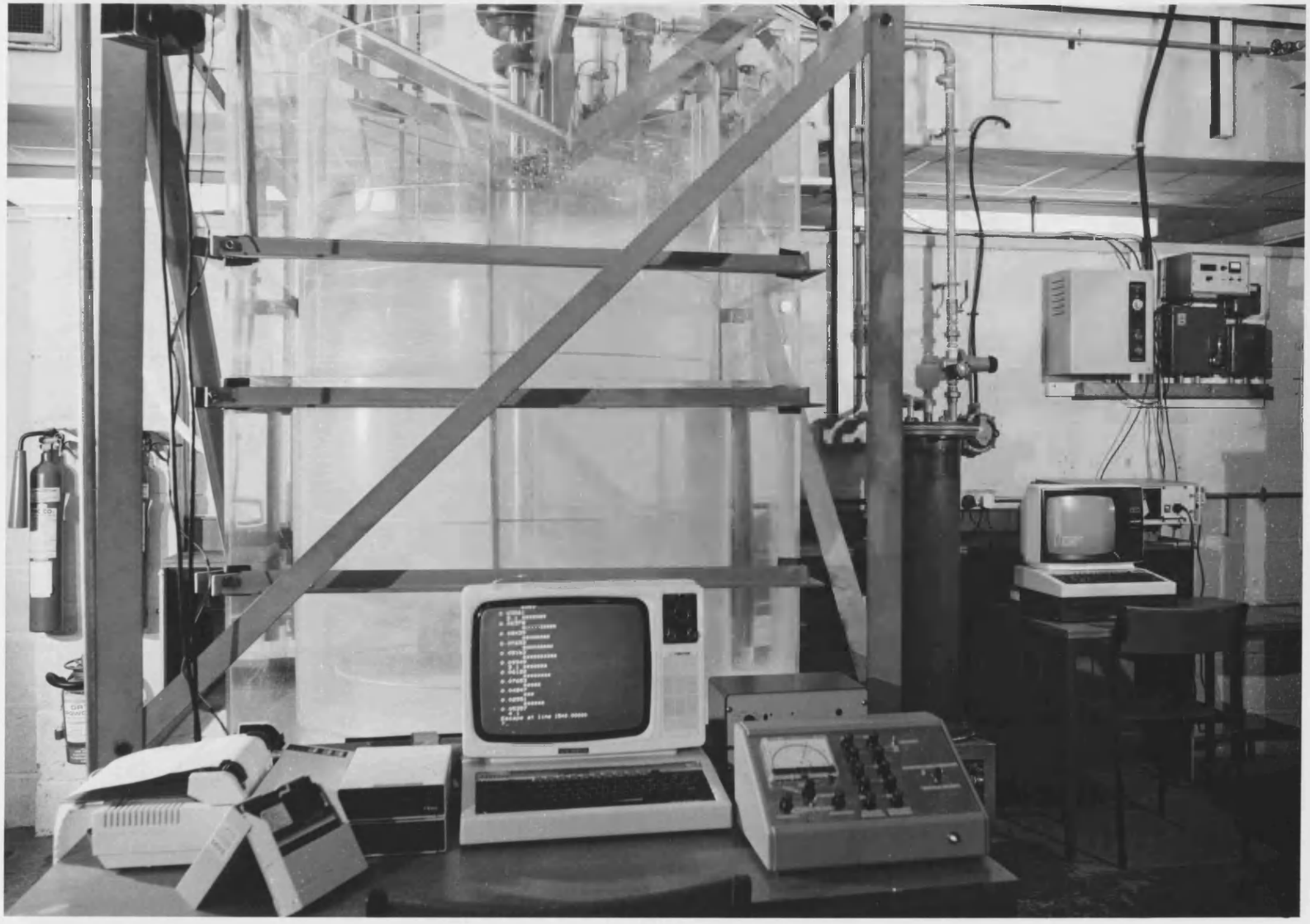

Photograph 3.I General view of mixing rig.

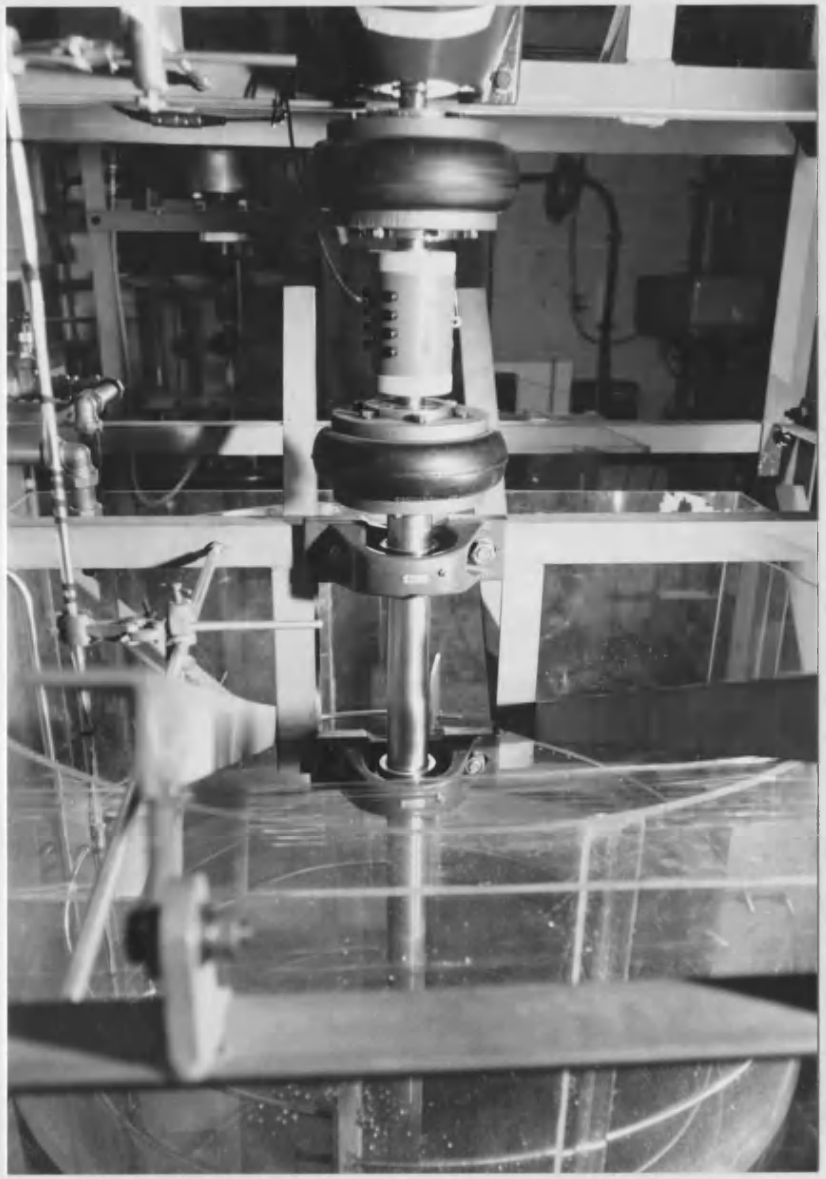

Photograph 3.2 Impeller shaft assembly.

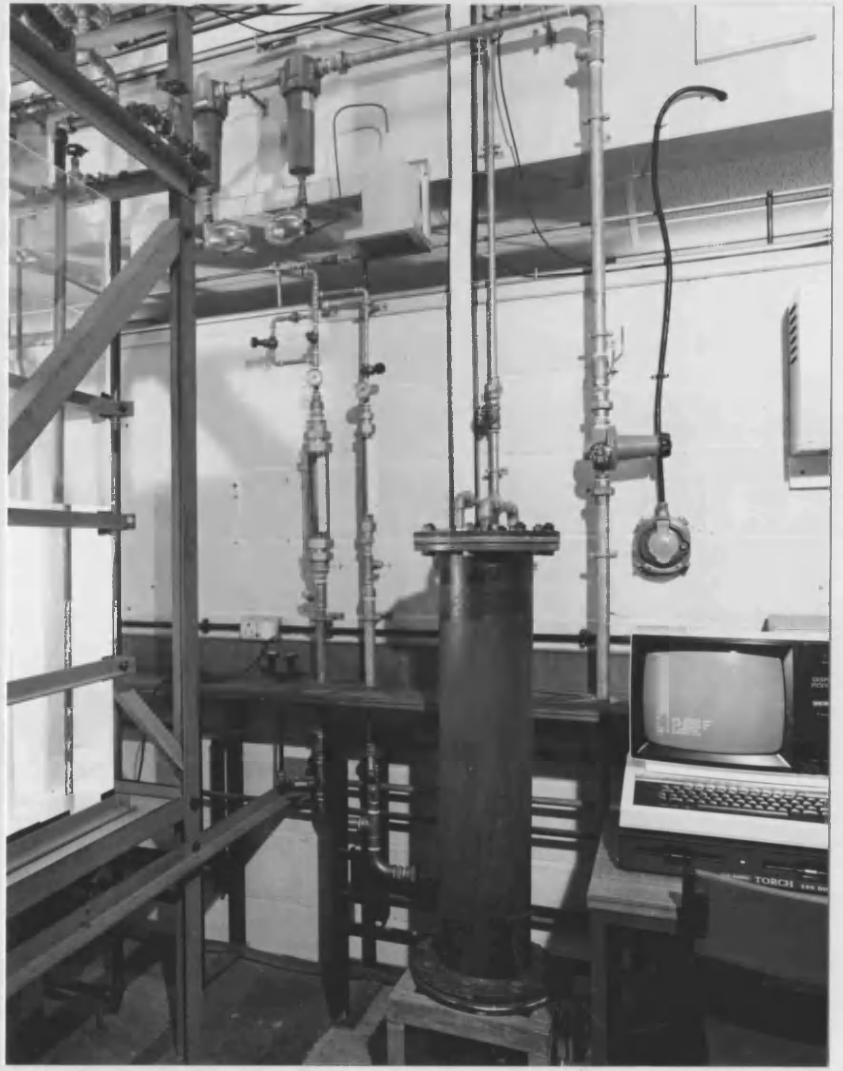

Photograph 3.3 Air line.

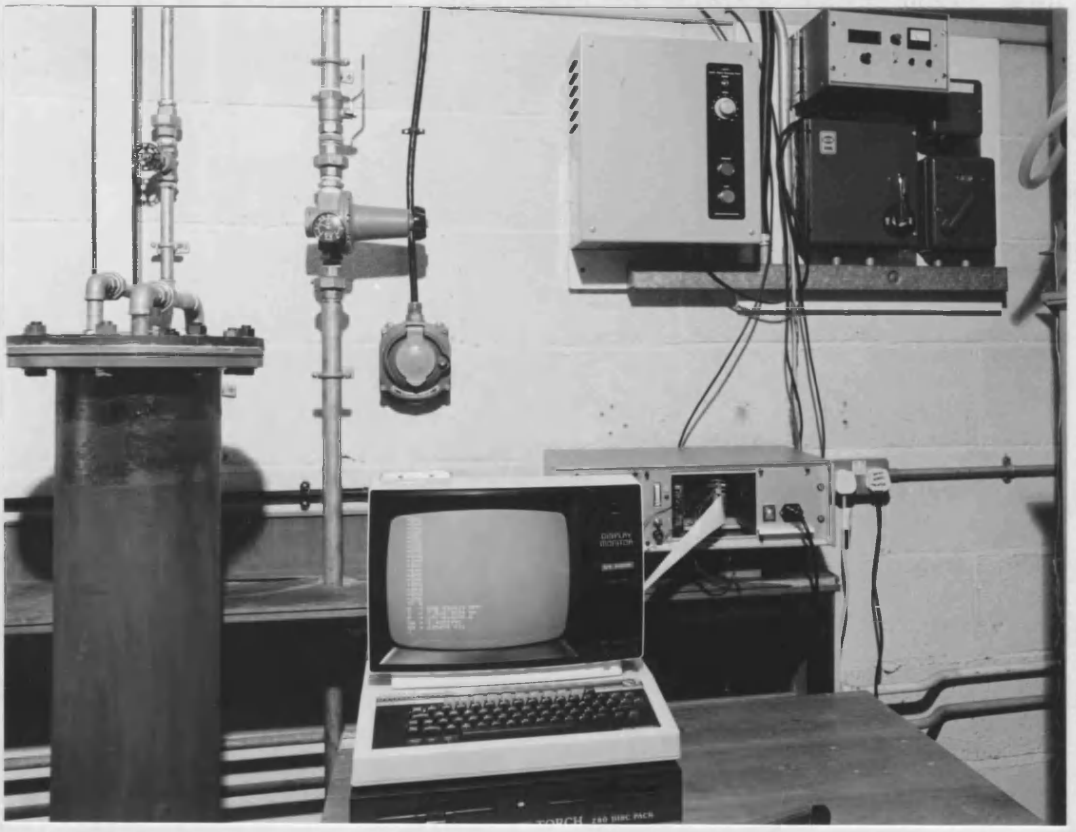

Photograph 3.4

Computerised torque and speed measurement system.

important elements of the mixing unit can then be carried out.

3.2.3 Mixing vessel

The mixing tank is a 1.0 m diameter by 1.50 m high flat-based cylinder, made of 8 mm thick perspex plate, fully baffled with four stainless-steel plates 90° apart, projecting radially inward from the wall to a distance one-tenth the vessel diameter and extending to a height of 1.25 m. It is located in a square-section perspex water-jacket which permits temperature control of the tank contents as well as light-distortion free viewing and photography through the walls. Viewing and photography are also possible through a 0.65 m diameter window in the tank-base supporting frame. A detailed diagram of the installation is given in Fig 3.1.

3.2.4 Drive motor selection

Three sizes of the well known six-blade disc turbine were adopted in this study, equivalent to impeller-to-tank diameter ratios of 1/4, 1/3 and 1/2. The impeller clearance above the base of the vessel was fixed at 0.25 m ie., T/4. This was shown by Nienow et al [76] to provide good dispersion of gas.

It is well appreciated that an impeller draws significantly less power under gassed conditions than under ungassed conditions. For a six-blade disc turbine operating in a fully baffled tank, the ratio of the two horsepowers is about 0.5. An industrial gas-liquid mixer may be required to fulfil just one specific task, therefore, the drive unit should be selected to meet this particular task because oversizing the prime mover would lead to unnecessary capital expense. However, a safety system which in the event of loss of gas flow would either slow down the mixer or completely disengage the impeller should be incorporated in

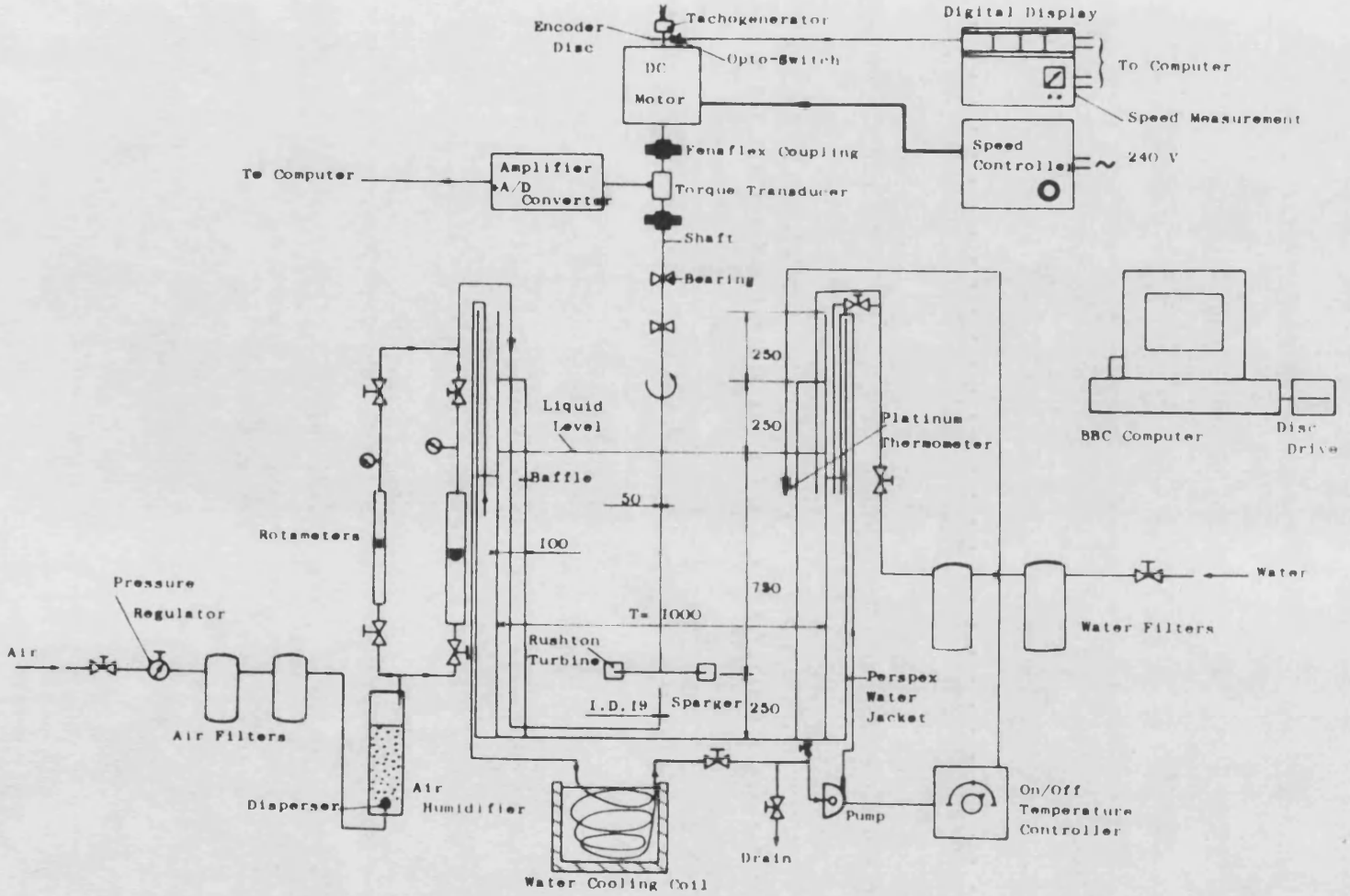

Fig 3.I General layout of the mixing rig.

the installation. A research system on the other hand, is usually a multipurpose facility and therefore, would be expected to operate safely under gassed or ungassed conditions, being subjected to various levels of loadings in the speed range considered. One of the essential features of a multipurpose experimental rig is a wide speed range and sufficient power capability so that a range of impeller sizes and fluid viscosities can be used. Also, the sensitivity of power to small changes in speed, necessitates continuous speed regulation under varying loads. The speed range should be selected to allow operation at different turbulence levels ie., from low to high levels of agitation. Holland and Chapman [77] expressed the different levels of agitation in terms of agitator tip speed as follows:

Low agitation 2.540–3.302 m/s,

Medium agitation 3.302–4.064 m/s,

High agitation 4.064–5.588 m/s.

For the present system the speed range was selected to contain the above tip speed range for the three impeller sizes employed. Then, taking into account this range of agitator tip speeds use was made of the published power number data versus Reynolds numbers to estimate the maximum power required. In this aspect, it is worthwhile mentioning the manual by Advani [78], which contains a large set of useful tables of computed horsepower values for five different turbine designs of various sizes at a wide range of speeds and liquid viscosities.

Finally, once the essential requirements of the drive are determined, a suitable electric motor has to be selected with regard to available standard sizes, flexibility of the machine, its cooling capability, quality of speed control, ease of installation and cost. A 5.5 KW DC geared motor having adjustable speed over a 21:1 range (0.42-8.77 rev/s)

was selected to power this mixing unit. High accuracy of speed control, better than ±0.1% of full speed throughout the speed range, is achieved by means of a Tacho Feedback controller through a tachogenerator fitted at the non-drive end of the motor. Details of the motor and controller are given in Appendix A.

3.2.5 Impeller design

The turbines used were made of 316 stainless steel and had six welded-on flat blades. They were hub mounted on the shaft with a rectangular key and three set screws at 120°. The general design with proportions of blade width and length is shown in Fig 3.2.

3.2.5.1 Blade design

The impeller should have blades strong enough to be able to withstand the maximum bending stress that can be caused by the tangential forces imposed on them by the fluid flow. The bending moment resulting from the shaft torque can be shown to have an effective radius equal to 0.402D [79]. Using this relationship, a simple analysis of the stress applied to the blade yields the following equation for the material thickness, t_b, [79]:

$$t_b = \left[2.27 \frac{T_s}{n_b W \sigma}\right]^{1/2} \qquad (3.1)$$

where,

T_s = maximum torque applied,

n_b = number of impeller blades,

W = width of blade,

σ = allowable working stress for the blade metal. For a six blade standard turbine, as used here, the equation becomes:

$$t_b = \left| 1.89 \frac{T_s}{D\sigma} \right|^{1/2} \tag{3.2}$$

The final value of the metal thickness had to be selected to correspond with a standard available plate thickness. In this case it was 1/8 inch ie., 3.18 mm.

3.2.5.2 Hub design

A simple and rational way is to use a hub with the same torque transmission capability as the shaft. This method is also recommended by Leedom and Parker [79]. From a simple stress analysis [80], an implicit equation is obtained which relates the internal diameter of the hub to its outer diameter as follows:

$$d_o = \left| \frac{16 T_s f_c d_o}{\pi \tau} + d_i^4 \right|^{0.25} \tag{3.3}$$

where,

d_i = internal hub diameter,

d_o = outer hub diameter,

τ = allowable shear stress for the material,

f_c = stress concentration factor,

T_s = shaft torque.

The stress concentration factor, f_c, is incorporated to allow for the effect of the keyway and the set screws. The above equation can be solved to give the exact value of d_o only when the value of d_i ie., the shaft diameter, has been determined. This will give the minimum hub thickness required which may have to be increased to allow for welding and also to give enough set-screw length. Some recommended standard hub dimensions are given by Uhl and Gray [79]. The dimensions of the hubs used here are displayed in Table 3.1 together with all other

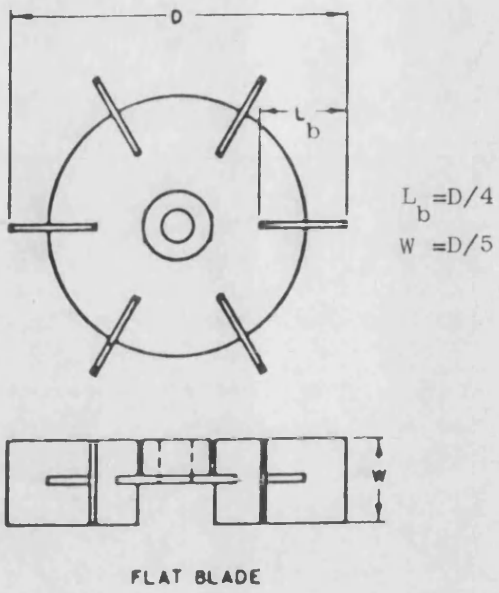

Fig 3.2 General design of Rushton turbines used.

Table 3.1 Turbine dimensions

D	Disc		blade			Hub			Key	Set
	d	T_d	L_b	W	t_b	d_i	L_h	d_o	Size	Screw
250	188	3.18	62.50	50.00	3.18	50.00	75.00	80.00	$\frac{5}{8}" \times \frac{7}{16}"$	M12
333	250	3.18	83.30	66.60	3.18	50.00	75.00	80.00	$\frac{5}{8}" \times \frac{7}{16}"$	M12
500	375	4.76	125.00	100.00	4.76	50.00	75.00	95.00	$\frac{5}{8}" \times \frac{7}{16}"$	M12

Dimensions in mm except where indicated otherwise

impeller dimensions.

3.2.6 Shaft design

3.2.6.1 Design requirements

The shaft is a vital element of the mixer and care should be devoted to its mechanical design especially when dealing with large scale units, as often it is a major limiting factor of the performance of the system. Its main function is to transmit the torque from the drive to the impeller. However, it must also be stiff enough to withstand the bending moment imposed on it by the lateral hydraulic forces acting on the agitator. Equally important, the shaft and impeller must have their first natural frequency of vibration far from the range of operational speeds. Axial forces due to the weight of the shaft and impeller are generally insignificant in the design of the shaft whereas out-of-balance forces can be minimised by dynamic balancing of the shaft and impeller, small machining tolerances and good alignment of the impeller with the shaft. Typically, turbine agitators have a cantilevered shaft ie., with no steady bearing at the bottom. This is one more reason why care must be exercised in its sizing.

3.2.6.2 Design procedure

The design of the shaft consists of the two following main steps:

- Computing the shaft diameter which fulfils the requirements of torque transmission and resistance to bending from the hydraulic force.
- Determining if the first critical speed of the shaft and impeller is reasonably far from the operating speeds.

(i) Strength criterion

Fig 3.3(a) shows the main shaft loads for the mixer configuration

used. These stresses created by the impeller torque and fluid force result in a combined shear stress and a tensile stress (Fig 3.3(b)). The maximum bending moment is obtained as the product of the resultant hydraulic force F_h and the distance from the impeller to the first bearing, L, ie., $M = F_h L$. This hydraulic force is caused by the fluid turbulence and has a random magnitude and direction. It is difficult to determine theoretically and consequently, it is usually measured on a laboratory model [81-83] and correlated with the appropriate dimensionless groups so that using similarity principles the results can be applied to the actual system. For turbine agitators Ramsey et al [84] quote a correlation for this hydraulic force in terms of shaft torque and impeller diameter as:

$$F_h = 0.0679\left(\frac{T_s b}{D}\right) \tag{3.4}$$

where b is a service factor which is taken to be 1.0 if the impeller does not run at the liquid surface for long periods but higher if this is the case or if the shaft may be subjected to shock loadings, although no further details are given by the authors. In our case b was taken to be 1.5.

The minimum diameter of the shaft will be the greater of the two values d_s and d_t calculated from the following relationships [85] to meet respectively the allowable shear stress τ or the allowable tensile stress σ of the shaft metal:

$$d_s^3 = \frac{16\sqrt{T_s^2+M^2}}{\pi\tau} \tag{3.5}$$

$$d_t^3 = \frac{16(M+\sqrt{T_s^2+M^2})}{\pi\sigma} \tag{3.6}$$

For this system the maximum rated torque for the drive is 100 Nm and

the maximum bending moment would be equal to:

$$M = \frac{0.0679 \times 100 \times 1.5}{0.25} = 40.72\ Nm$$

The recommended values [84] for the shear stress limit and tensile stress limit for stainless steel type 316 are respectively $41.40 \times 10^6\ Nm^{-2}$ and $55.2 \times 10^6\ Nm^{-2}$. Substituting for τ and σ in the above equations gives:

$$d_s = 23.68\ mm \qquad d_t = 23.94\ mm$$

If the motor is overloaded or the impeller jams suddenly the torque developed in the shaft before the overload protection cuts out will be no more than 2.00 times the maximum rated torque. Using this value the new values for the shaft diameter are:

$$d_s = 29.84\ mm \qquad d_t = 30.16\ mm$$

(ii) Critical speed criterion

As the speed of a rotating shaft system is increased it may tend to whirl or vibrate strongly in a traverse direction. When the speed of the shaft resonates with one of the natural frequencies of the system, the shaft deflection becomes so large that mechanical failure will follow. It is usually recommended [84] that the shaft should not run within ±35% of its first critical speed, and preferably, it should not be this close.

Referring to Fig 3.4, the static deflection due to the shaft weight is given by [85]:

$$\Delta = \frac{W_s L^3}{8EI} \tag{3.7}$$

The static deflection due to the impeller weight is given by [85]:

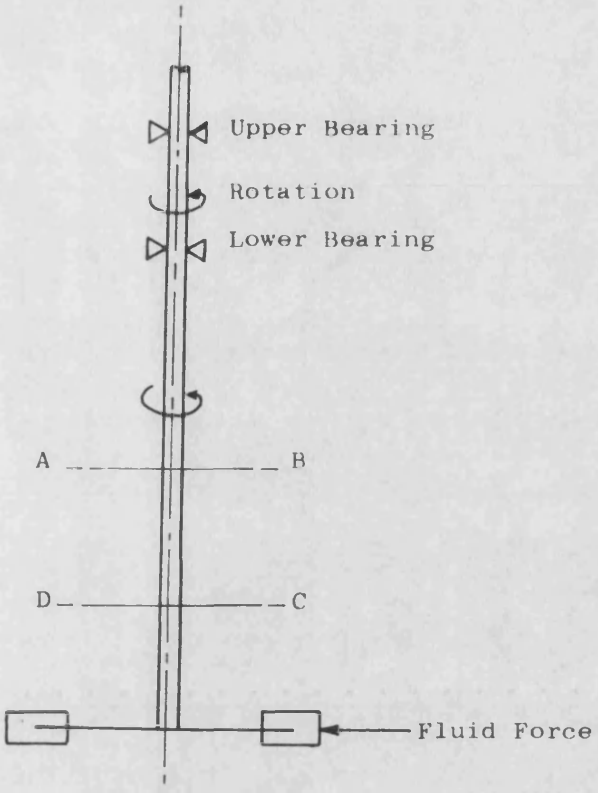

Fig 3.3 (a) Main loads on shaft.

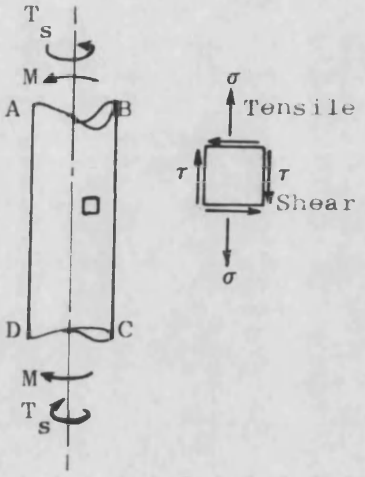

Fig 3.3 (b) Stresses on shaft.

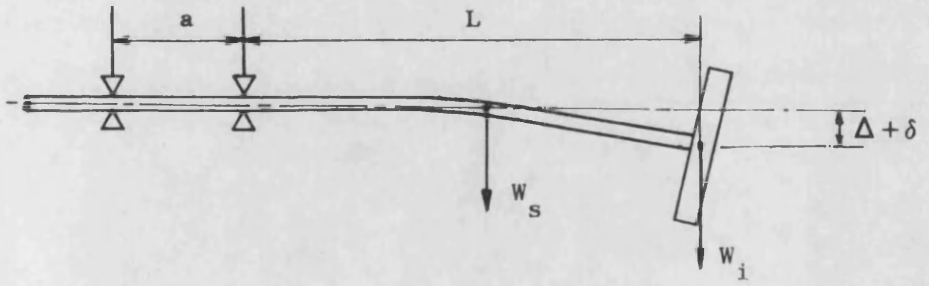

Fig 3.4 Free body diagram of a cantilevered shaft agitator.

$$\delta = \frac{W_i L^3}{3EI} \tag{3.8}$$

where,

E = modulus of elasticity of shaft material,

I = second moment of area of shaft,

W_s = shaft weight,

W_i = impeller weight,

L = overhung shaft length.

The first critical speed of the system is obtained from [85]:

$$N_{cr} = \frac{30}{\left[\delta + \frac{\Delta}{1.27}\right]^{1/2}} \tag{3.9}$$

where δ and Δ are in m and N_{cr} is in rpm. This formula assumes that the shaft is a built-in cantilever. In practice, however, the flexibility of the portion of shaft between the support bearings would lower the critical speed of the system. A bearing span factor f_B is therefore introduced to account for this effect. Hence, the correct critical speed is given by [79]:

$$N'_{cr} = N_{cr} \times f_B \tag{3.10}$$

where,

$$f_B = \left[\frac{L}{L+a}\right]^{1/2}$$

For the calculation of N'_{cr} the weight of the largest impeller is used because it gives the lowest, ie., the worst critical speed.

Data: $W_s = 151.2\ N$, $W_i = 106.4\ N$, $L = 1\ m$, $a = 0.22\ m$,

$$E = 200\times10^{9}\ Nm^{-2},\quad I = \frac{\pi d_t^{4}}{64}.$$

From Table 3.2 it is clear that to satisfy the criterion that the maximum speed of the system should be less than 65% of the first critical speed, the shaft diameter will have to be increased to 50 mm.

The shaft and the impellers used were dynamically balanced and machined to small tolerances in order to keep out-of-balance forces down to a minimum. The result was a very steady rotation of the agitator assembly with no apparent vibrations. Support of the shaft was provided by two rigidly mounted self-aligning pillow-block ball bearing units, 50 mm in diameter.

3.2.7 Shaft couplings

The choice of appropriate shaft couplings requires careful consideration. Because a strain gauge transducer had to be incorporated between the shaft and the drive unit for torque measurements, two couplings were needed; These were of Fenaflex type (Appendix A). They incorporate a flexible tyre and provide a high degree of vibration damping, shock load protection and accommodation of mis-alignment. The flexibility of the couplings was also desirable because otherwise bending moments caused by any mis-alignment would be added to the torques measured and hence causing errors in power measurements.

3.2.8 Design of baffle plates

The baffles are used to prevent vortex formation and hence are subject to a fluid force. This force is distributed over the immersed length of the baffle but it is not known exactly how. There are different load distributions which can be assumed, the simplest of which is a uniform distribution of the fluid force over the immersed length of the

Table 3.2 Critical speed for different shaft diameters

d_t (mm)	Δ (mm)	δ (mm)	N_{cr} (rpm)	f_B (-)	N'_{cr} (rpm)	N_{max}/N'_{cr} (N_{max}=526rpm)
35	1.28	2.41	513	0.905	464	1.13
40	0.75	1.41	671	0.905	607	0.87
45	0.47	0.88	849	0.905	768	0.68
50	0.31	0.58	1045	0.905	946	0.56

baffle. In this case, the maximum deflection, δ_p, in the plate is related to its thickness, B_t, as [80]:

$$\delta_p = \frac{W a_p^3}{L_p E B_p B_t^3}(3a_p^2 - 7L_p a_p + 4L_p^2) \qquad (3.11)$$

where,

W = load/unit length,

E = modulus of elasticity of plate material,

L_p = total length of plate,

a_p = immersed length of plate,

B_p = width of plate,

B_t = thickness of plate.

Therefore, the thickness of the baffle plate can be obtained for a given maximum permissible deflection. The load required to produce collapse of such a plate by excessive plastic deflection can be estimated from [80]:

$$W_u = \beta \sigma_y B_t^2 \qquad (3.12)$$

where,

β = constant depending on width/length of plate,

σ_y = yield stress of plate material.

However, because of the uncertainty in the way the force is distributed over the baffle, a more conservative method is usually used [79]. This assumes that the full torque developed by the agitator is resisted by a force applied in the middle longitudinal plane of the baffle (Fig 3.5). Therefore, each two opposite baffles will resist half the torque and hence the force F_b will be given by:

$$F_b = \frac{T_s}{2(T - B_p)} \qquad (3.13)$$

The maximum bending moment acting on the plate occurs at the point of

application of the force, Fig 3.6, and is given by:

$$M_b = \frac{F_b a_p b_p}{L_p} \tag{3.14}$$

and from basic stress theory:

$$\frac{\sigma}{M_b} = \frac{6}{B_p B_t^2}$$

where σ is the design tensile stress of the plate material. Hence, the baffle plate thickness is given by:

$$B_t = \left[\frac{T_s}{2(T - B_p)} \times \frac{a_p b_p}{L_p} \times \frac{6}{\sigma B_p} \right]^{1/2} \tag{3.15}$$

Data: $T_s = 100\ Nm$, $T = 1\ m$, $B_p = 0.1\ m$, $a_p = 0.25\ m$,

$L_p = 1.25\ m$, $\sigma = 55.2 \times 10^6\ Nm^{-2}$.

whence,

$B_t = 3.48\ mm$

The thickness of the baffle plates which were made of stainless steel type 316, was taken to be 4.76 *mm* which is the next upper standard plate thickness to the value calculated above.

The fluid force applied on the baffles is periodic in nature and has frequency, n_F, equal to the product of impeller speed, n, and number of impeller blades, n_b:

$n_F = 6n$

The natural frequency of vibration of the baffles should, therefore, not coincide with the force frequency. The maximum deflection of a baffle plate is given by [80]:

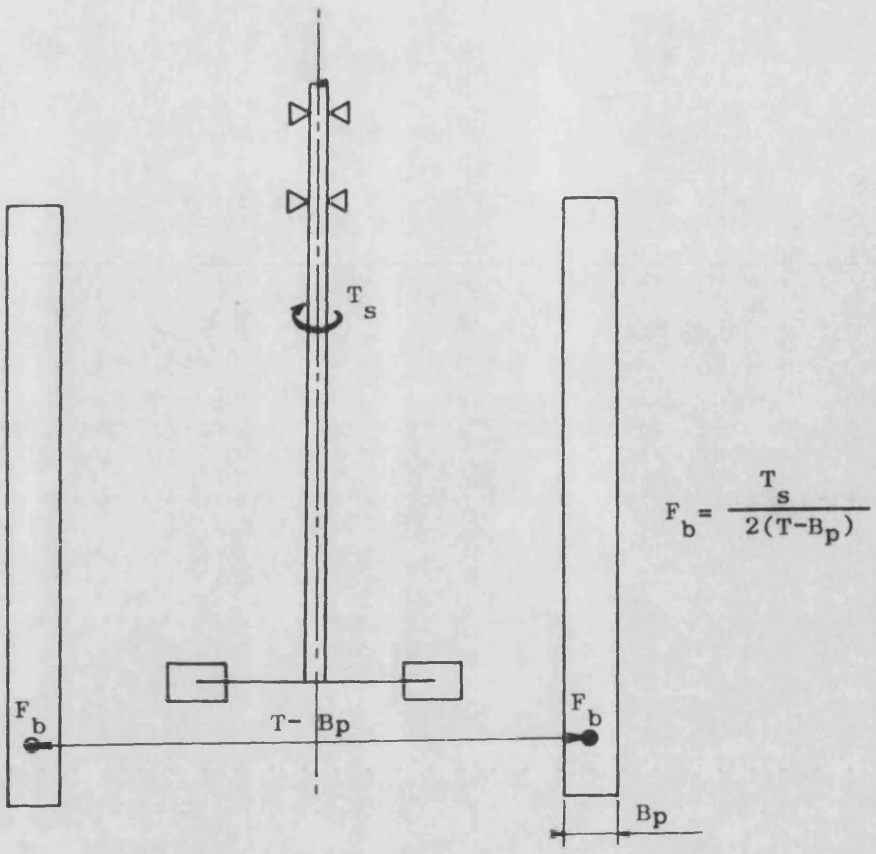

Fig 3.5 Force exerted on baffles.

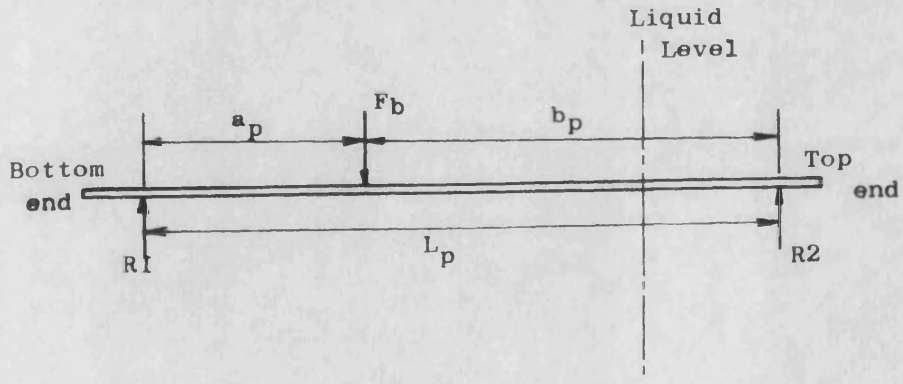

Fig 3.6 Forces exerted on baffle plate.

$$\delta_b = \frac{5\omega L'^4}{384EI} \tag{3.16}$$

where,

ω = weight of baffle per unit length,

L' = length between supports,

E = modulus of elasticity of plate material,

$I = B_p B_t^3/12$,

and the natural frequency of vibration is obtained from [85]:

$$n_c = \frac{1}{2\sqrt{\delta_b/1.27}} \tag{3.17}$$

Data: $\omega = 36.65\ N/m$, $L' = 1.05\ m$, $E = 200\times10^9\ Nm^{-2}$, $I = 8.99\times10^{-10} m^4$.

This gave a natural frequency of 9.91 Hz which is within the operating range of blade passing frequency (2.50-52.60 Hz). Therefore, two more supports were added along the length of the baffles at equal spacing, which raised the natural frequency to 89.20 Hz, well outside the operating range.

3.2.9 Air line and sparging unit

Compressed air from the laboratory air line was passed through a set of purifying filters before being moisture-saturated in a humidifier. The air pressure was reduced to the operating value by means of a pressure regulator and the flow rate was adjusted with needle valves and metered with calibrated rotameters. The air was then introduced at the centre of the tank base below the impeller through a single orifice stainless-steel tube of 19 mm diameter, rigidly attached to the side of a baffle. This is the simplest sparger arrangement that can be used and there does not seem to be any advantage in using a more complicated arrangement such as a ring sparger or a set of single orifices [86].

The maximum stable air-flow rate available from the laboratory air line was $6.87\times10^{-3}\ m^3/s$ corresponding to 0.523 vvm and to a superficial air velocity of $8.74\times10^{-3}\ m/s$. Slightly higher air flow rates up to $8.33\times10^{-3}\ m^3/s$ could be obtained but only for short periods of time, therefore, they were not used in experiments that required a stable flow rate for long periods of time.

3.2.10 Liquid media

The system is supplied with mains water or water softened by weak ion-exchange resin (<20 ppm), through a dual set of sediment removing filters. For all experiments softened water was used instead of tap water because of the excessive scaling deposition (precipitated Calcium and Magnesium salt) that was experienced with the latter due to its high Calcium hardness (average 313 ppm). The physical properties of the soft water were at 18 °C:

$\rho = 999\ Kg/m^3$,

$\mu = 1.0\times10^{-3}\ Nsm^{-2}$,

$\sigma = 70.99\times10^{-3}\ N/m$.

Sodium Chloride solutions of 0.15M were also used as a 'non-coalescing' medium. The salt used was of general purpose grade. The changes in the above physical properties were negligible at this concentration.

Control of the dispersion temperature is provided through an on/off temperature controller, a platinum thermometer immersed in the vessel and a pump circulating water in the perspex jacket through an external cooling coil. However, temperature control was not found to be necessary since the temperature remained stable at 18 ± 1 °C inside the tank when monitored over a period of a few hours of continuous operation. An explanation for this is that most of the heat generated by the mixing is carried away by the air flowing through the dispersion and

also because of the large surfaces available for heat transfer. However, with more viscous fluids the case may be different.

3.3 Measurement techniques

3.3.1 Torque measurement

A torque transducer mounted between the motor and the impeller shaft was used for measuring the agitation torque (Photo. 3.2). Torque is transmitted to a high tensile steel shaft to which is attached a network of resistance-foil strain gauges. These are covered by the rotor tube which carries a set of four silver sliprings wired to the four terminals of the fully-active strain-gauge network. The very small angular deflection of the torque shaft, resulting from the torsional shear stress, causes a change in the electrical output signal from the bridge circuit, Which is directly proportional to the transmitted torque. The specifications of the sensor are given in Appendix A.

The instrumentation associated with the sensor consists of a fixed gain front-end amplifier, followed by a suitable gain amplifier with four manually switched ranges. The excitation supply to the transducer is 40 V DC and the 3 dB bandwidth for the system is greater than 10 KHz. The 2 V full-scale output is connected to a 12 bit dual-slope integrating A/D converter under the control of the host BBC microcomputer (Appendix A). The integration period is 40 msec., giving good rejection of 50/100 Hz noise. Recorded samples of the torque signal are shown in Fig 3.7.

The total torque measured by the transducer is given by:

$$T_m = T_f + T_i \tag{3.18}$$

where,

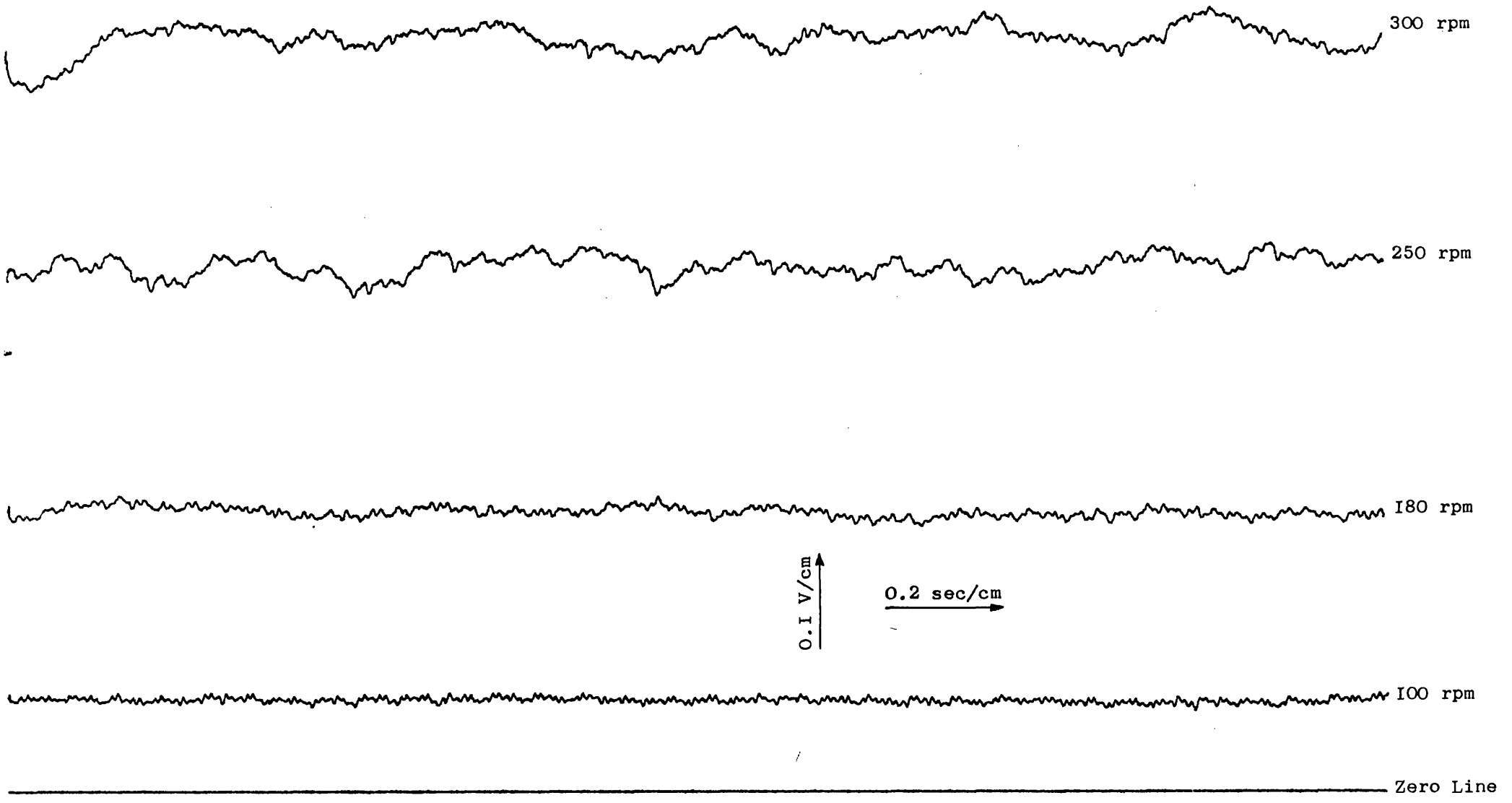

Fig 3.7 Samples of torque signal (steady state Q=0, D/T=1/3, water).

T_f = friction torque,

T_i = torque exerted by the fluid on the impeller.

The friction torque T_f was measured under a dry run for each impeller at each operating speed and subtracted from the total measured value in order to obtain the net value of the agitation torque. The friction torque was found to vary linearly with the rotational speed as shown in Fig 3.8, its value representing a few percent of the total measured ungassed torque at low speeds and dropping sharply with increasing speed down to less than one percent (Fig 3.9). The friction torques were always reproducible to within ±8%, whereas the reproducibility of impeller torques was less than 5%. The maximum error from the transducer calibration is quoted by the manufacturer to be ±0.1% of the full working torque ie., ±0.14 Nm over the full speed range.

As already described in Section 3.2, the motor is supplied with a tachogenerator connected to its shaft, which provides feedback of the shaft speed. For the purpose of speed measurement, an optical transducer was interposed between the motor and the tachogenerator as illustrated in Fig 3.10. This consists of a thin hard Nickel quality encoder disc with 120 radial slots, mounted on the tachogenerator shaft, and an optical switch assembly fixed to the motor body, capable of detecting the passage of the slots. The output of the optical switch is therefore 120 pulses per revolution of motor shaft. A second output of one pulse per revolution is provided by a single 'index' slot cut into the edge of the disc and read by a second opto-switch. This constitutes an independent check on the speed measurement given by the first opto-switch. Fig 3.11 represents schematically the speed transducer and Fig 3.12 is a functional diagram of the system.

Fig 3.9 Ratio of Friction Torque to Measured Ungassed Torque

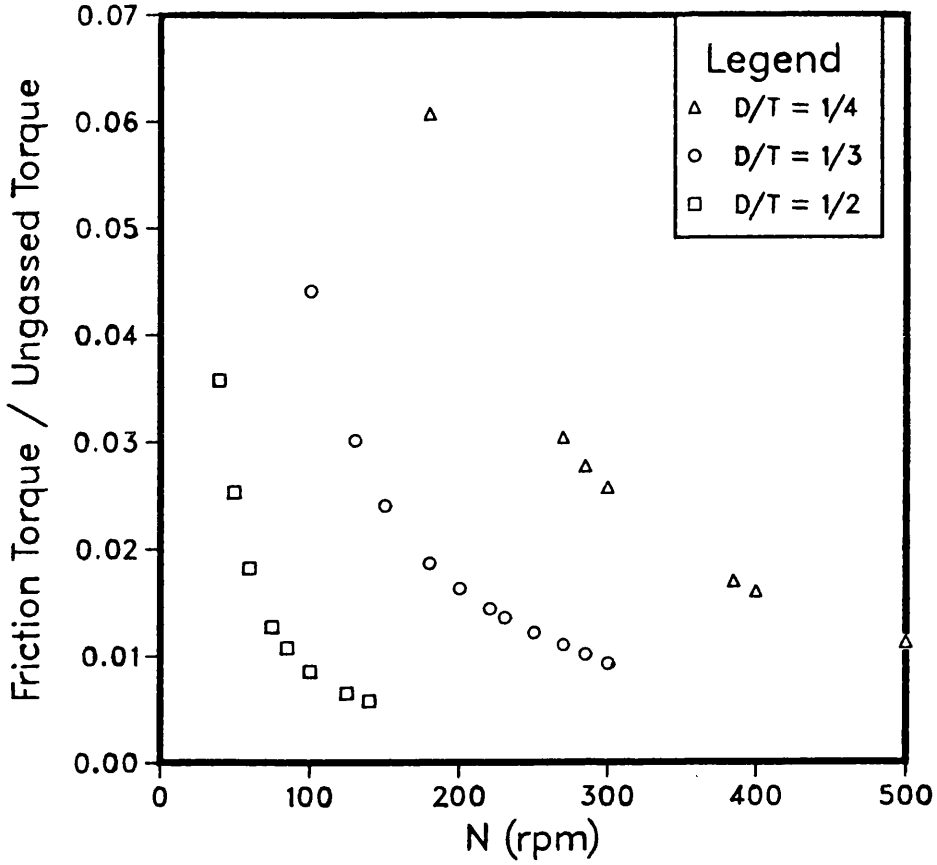

Fig 3.8 Friction Torque vs Impeller Speed

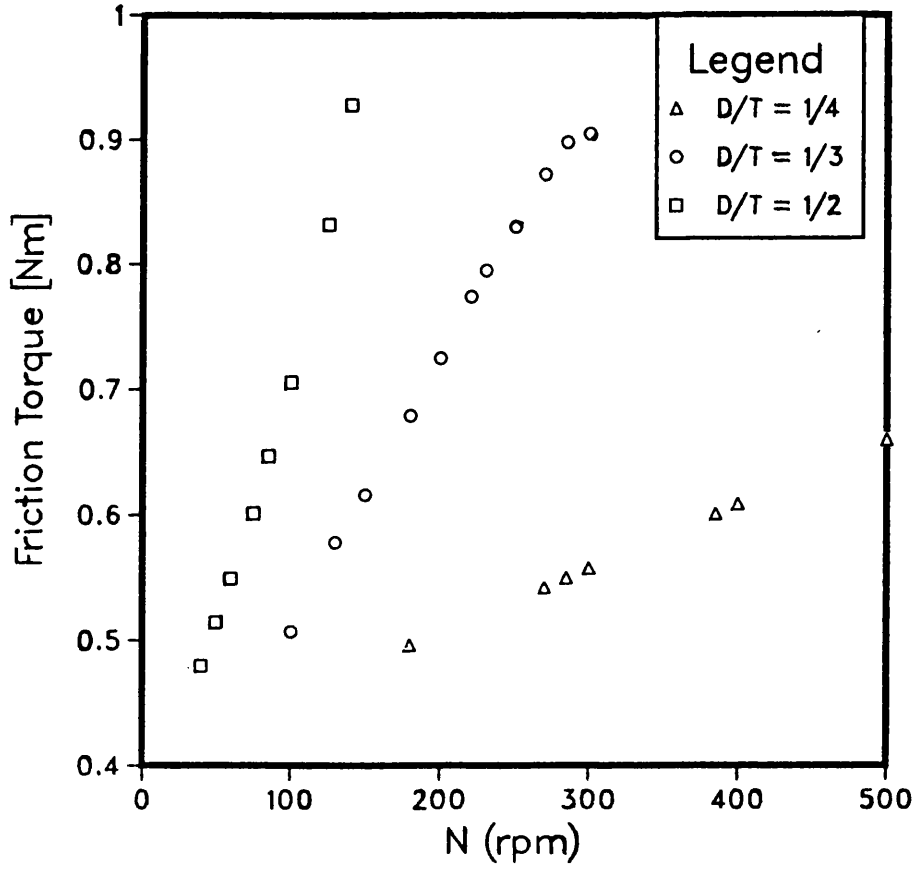

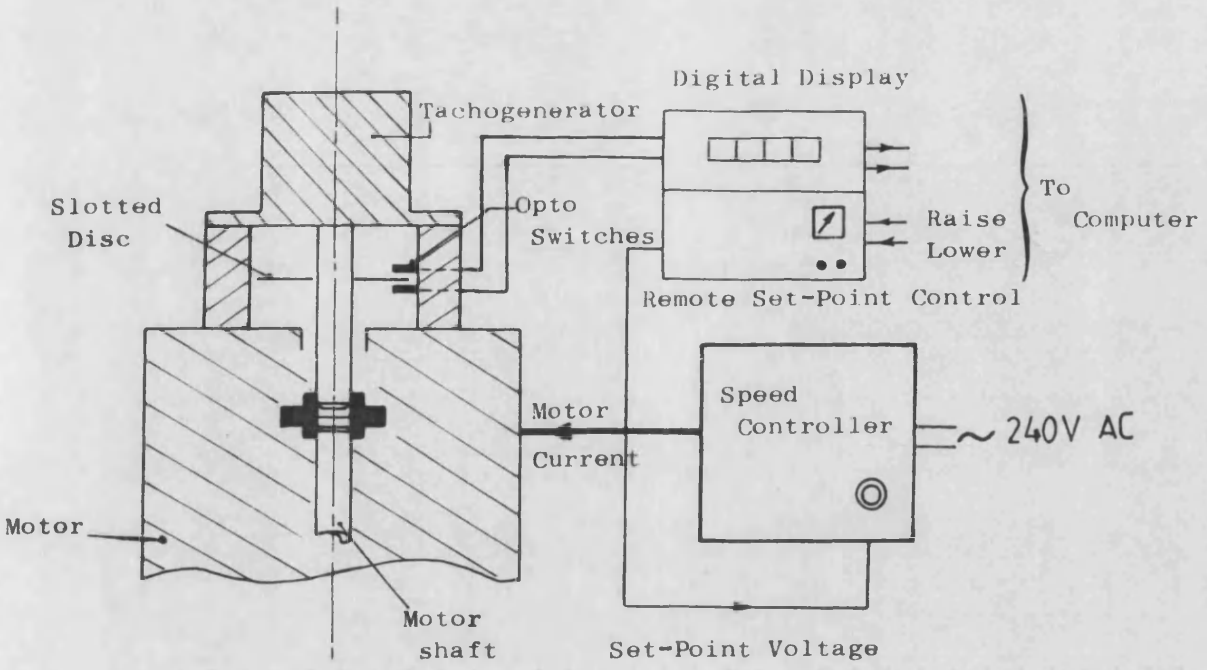

Fig 3.IO Speed control and measurement set-up.

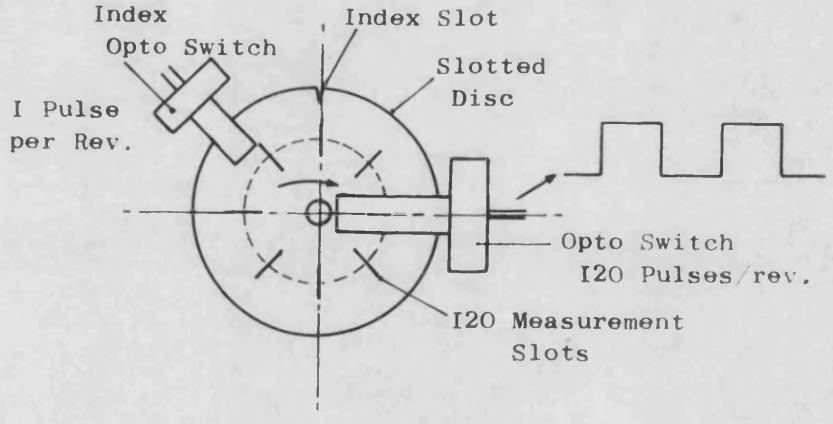

Fig 3.II Speed transducer.

The manual speed setting and display consists of a simple frequency counter arrangement. Pulses from the transducer are counted over a fixed period of either 0.5 sec. or 5 sec., giving a display of the motor speed in rpm with a resolution of 1 and 0.1 rpm respectively. Therefore, for low speeds the 5 sec. measurement time period was used whereas for high speeds the 0.5 sec. period was used.

As illustrated in Fig 3.13, for automatic speed measurement by computer, the transducer pulses are first fed to a divide-by-128 circuit. The output of this circuit is therefore high for 64 pulses and low for the following 64 pulses. When high, the output from a 50 KHz oscillator is fed to the counter pin of a VIA (Versatile Interface Adaptor) integrated circuit internal to the computer. On the high-to-low transition of the driver output, the 50 Hz oscillator is disconnected and an interrupt to the computer is generated. The interrupt service routine then stores the content of the VIA counter register in memory and prepares the VIA for the reset period measurement. In order to retrieve the current value of the shaft speed, a machine code routine called 'getspeed' is invoked. This simply returns the current stored counter value. From this value, the shaft speed can be deduced by simple arithmetic.

3.3.2 Remote (automatic) speed set-point control

The Fenner motor speed controller is provided with manual set-point control only. The set point is derived from a potentiometer mounted on the front panel. Modifications to the unit involved removing the potentiometer and replacing it with a remotely controllable voltage source. This consists of a low drift integrator circuit (ramp generator) with two digital inputs, one to raise the set point and one to lower it. For manual control, two push buttons are provided on the front panel, together with an analogue voltmeter indicating the set point. For drift-

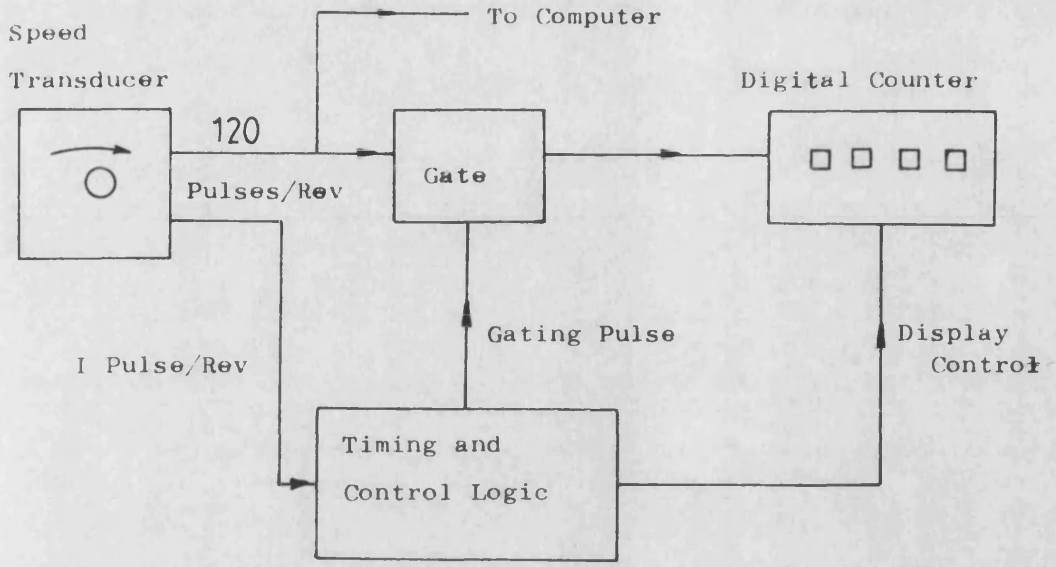

Fig 3.I2 Speed measurement and display logic.

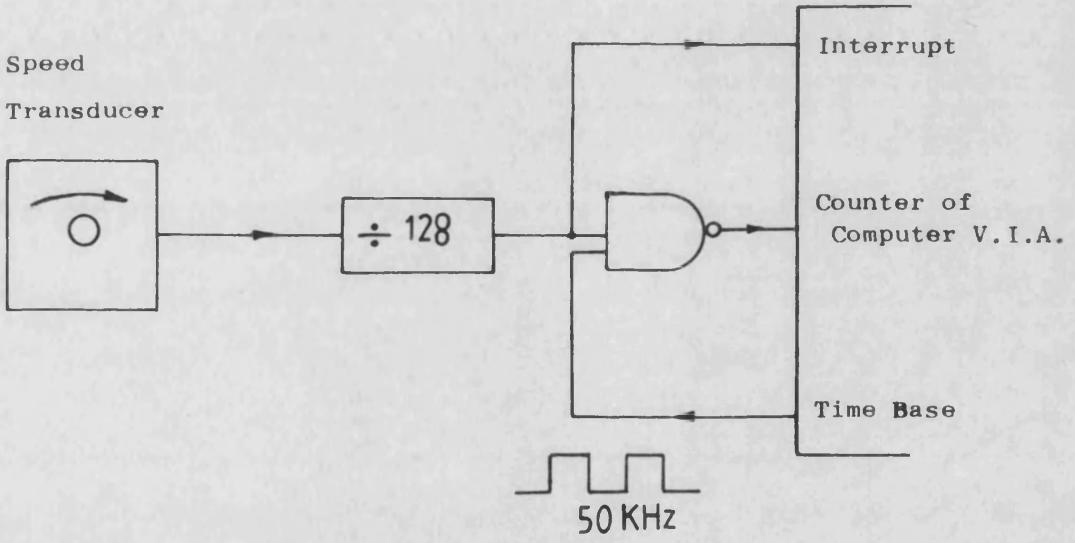

Fig 3.I3 Computerised speed measurement.

free operation, a rotary potentiometer on the front panel may be switched in. The circuit is arranged so that on switch-on, the set point assumes the value set on the rotary potentiometer, which is normally zero.

The output from this device will, over a period of many minutes, drift away from its set value. Occasional adjustment is therefore necessary, and this is easily performed by the microcomputer, which is also used to set the motor speed to a value input at the keyboard. Knowing the ramp speed, $\frac{dV}{dt}$, of the voltage source and assuming the set point is zero, it is possible to calculate the time necessary to apply the raise-set-point signal in order to reach the required value. The shaft speed may be then measured and corrective action taken if necessary.

3.3.3 Power measurement

3.3.3.1 Mechanical power

The net power input to the dispersion by the agitator was calculated by:

$$P = \frac{2\pi}{60} T_i N \tag{3.19}$$

The computer programme used for power measurement is given in Appendix B together with a description of its major constituent routines.

3.3.3.2 Sparged gas power

The gas sparged in a mixing vessel transmits energy to the liquid on expanding and rising to the surface. This energy contributes to the power dissipation in the vessel and should be taken into account especially at low impeller speeds where it can constitute a significant percentage of the total power. This aeration power can be estimated from

the equation of Lehrer [87]:

$$P_a = \dot{m}\left[0.06\frac{u_0^2}{2} + RT\ln\left[1+\frac{\rho g}{P_s}(H - H_0)\right]\right] \qquad (3.20)$$

where,

$\dot{m}$ = mass flow rate of gas,

u_0 = gas velocity at sparger exit,

R = gas constant (286.7 KJ/Kg°K),

T = temperature (291°K),

H = liquid height (1.0 m),

H_0 = sparger height (18 mm),

P_s = pressure at the dispersion surface,

ρ = liquid density.

The first term of the equation represents the kinetic energy contribution and the second term the isothermal expansion energy of the gas. Calculations showed, however, that the kinetic energy term contribution was negligible. Therefore, the above equation was simplified and reduced to:

$$P_a = 7647Q \qquad (3.21)$$

where Q is the volumetric air flow rate.

3.3.4 Overall gas holdup measurement

The overall gas holdup, ϵ, was evaluated by observing the rise in the level of the dispersion surface under aerated conditions and dividing this rise in the level by the total aerated height of the dispersion. For the purpose of level measurement a capacitance sensing probe was used. The body of the probe consists of a 3.18 mm diameter brass rod, 254 mm long, which acts as an electrode forming a capacitance between itself and

the surrounding material. This capacitance changes as the height of the liquid in the vessel changes. The electrode was insulated with a 1.59 mm thick PTFE sheath. The level probe was used with a fast response capacitance to current 'Robertshaw Skil' transmitter (100 msec.) which produced a standard 4-20 mA DC current output signal (Appendix A). The probe was calibrated by adding known volumes of water to a cylinder and relating the changes in liquid level to the corresponding changes in the output signal of the transmitter. A linear relationship was found in the form:

$$H = CV + D \tag{3.22}$$

where,

H = liquid height (cm)

V = output signal (Volts)

C , D = calibration constants

Under agitation conditions fluctuations in the level occurred in the vessel. Therefore, the signal from the probe was sampled and averaged using a Macsym II microprocessor (appendix A) for a period of 5 seconds at a frequency of 1 KHz. The level probe was positioned in the middle plane between two baffles. The height of the dispersion varied along the radius of the tank, therefore, five measurements at five equally spaced radial positions were made and an average value taken to represent the mean dispersion level. An ideal method would be to average the level of the dispersion over a 90° sector as shown in Fig 3.14. However, this procedure is very time consuming. The level without aeration was measured without agitation. Reproducibility of holdup values was better than 4%.

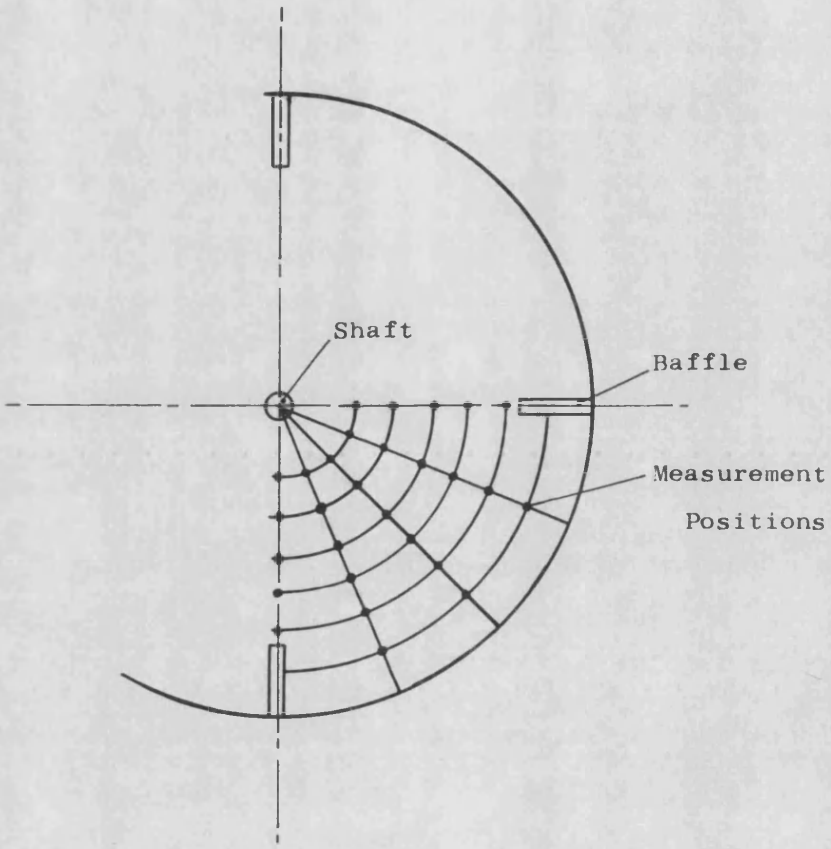

Fig 3.I4 Ideal method for determining average level rise in an agitated tank.

3.3.5 Local gas holdup measurement

A conductivity probe has been developed for local holdup measurement. The probe is interfaced to a microcomputer for the purpose of data acquisition and processing. The technique is fully described in Chapter 6.

3.3.6 Bubble size measurement

A suction probe technique for bubble size measurement has been developed. It involves continuous sampling of the gas liquid dispersion through a glass capillary tube. The bubbles are measured using light-emitting diode and phototransistor detectors. A high speed microcomputer is used to control the probe operation. The technique is described in detail in Chapter 4.

Chapter 4

CAPILLARY SUCTION PROBE TECHNIQUE FOR BUBBLE SIZE MEASUREMENT

4.1 Introduction

This chapter gives a detailed description of the capillary suction probe developed for bubble size measurement, and the instrumentation associated with it. The design and operation of the bubble detection device and the high speed data acquisition system are described. Some aspects of two-phase flow inside the capillary are discussed as well as details of the probe calibration procedure.

4.2 General principle of the technique

The method uses a vacuum to continuously withdraw a small stream of gas-liquid dispersion through a precision thick-walled glass capillary tube. Inside the capillary gas bubbles are transformed into slugs. Photodetectors mounted on the tube are used to detect the bubble slugs, producing a binary-waveform type signal. On-line computer analysis of this signal enables information on the size of the bubbles to be obtained automatically.

4.3 Instrumentation

4.3.1 Suction probe

The bubble suction probe is a short length of precision thick-walled glass capillary tubing with a funnel-shaped inlet. The dimensions of the glass probe are given in Fig 4.1, and the essential features of the instrument are described below.

4.3.1.1 Detector locations

Two flats were cut on the tube in order to position the photodetectors. The use of such flats served to reduce the bulk of the instrument, as well as offering a stable support for the detectors and

improved light transmission through the tube. The detectors were secured on the tube using a clear type of silicone rubber (type 732-RTV manufactured by Dow Corning). In addition to its cleanliness it provided very good adhesion to the glass.

The detector pairs were positioned close to each other at an interval distance of approximately 3.4 mm. This short distance was found to be important in the analysis of the signals from the two channels. Because of the complexity of the two-phase flow inside the capillary (see Section 4.5.2), a greater interval between the detectors would make cross-correlation between the two channels more difficult. The light sources were placed on opposite sides of the tube to avoid any risk of light refracted from one light beam being detected by the other detector, which would give rise to spurious signals.

4.3.1.2 Capillary diameter

The choice of a suitable capillary size for bubble measurement is essentially a function of the smallest bubble to be detected. Bubbles much smaller than the capillary diameter are not transformed into slugs and, therefore, give rise to signal pulses which are not of sufficient amplitude and width to be reliably measured. Bubbles slightly smaller than the capillary can still transform into short slugs because of the liquid film surrounding the slug. This reduces the effective cross section area of the tube slightly.

The probe used had a 0.39 mm internal diameter. It was carefully checked by measuring a slug of triple distilled mercury, inside the capillary, using a travelling microscope. The minimum bubble size detected was 0.30 mm approximately. Reducing the capillary size further was found to cause excessive bubble breakage inside the tube in

addition to it being very prone to blockage from the smallest contamination present in the dispersion. In any case, the error incurred in the measurements by rejecting these small bubbles would be negligible. For example, 900 bubbles of diameter 0.1 mm would give the same interfacial area as one bubble 3 mm in diameter.

4.3.1.3 Probe tip geometry

The shape of the probe tip was found to be important vis-a-vis bubble sampling. In a bubble swarm, bubbles arriving at the point of sampling can collide with the edge of the probe tip. Depending on the angle of collision, the impact can cause the bubble to break if the tip edge is too sharp, as illustrated in Fig 4.2. Therefore, a search for a suitable probe tip geometry was carried out. The set-up used for this purpose is represented in Fig 4.3. The probe was positioned inside a 'two-dimensional' perspex cell and a variety of mono-size bubble streams generated by different size nozzles were directed at the tip. A detection system consisting of an infra-red light source and phototransistor was used to count the bubbles released by the nozzle. A 'Gould' frequency counter coupled to the detector allowed automatic measurement of the frequency of bubble generation, and by collecting a large number of bubbles in an inverted precision burette over a known period of time, the mean bubble size in the stream could be determined.

It was found that bubbles with radii smaller than the radius of curvature of the tip edge did not break on impact. However, larger bubbles were prone to breakage at sharp angles of collision. In its original form the probe had the tip shown in Fig 4.4(a). In addition to bubble breakage at the edge of the inlet, this probe had a short funnel entrance which did not allow a gradual transition of the bubble velocity from that in the dispersion to the suction velocity inside the capillary.

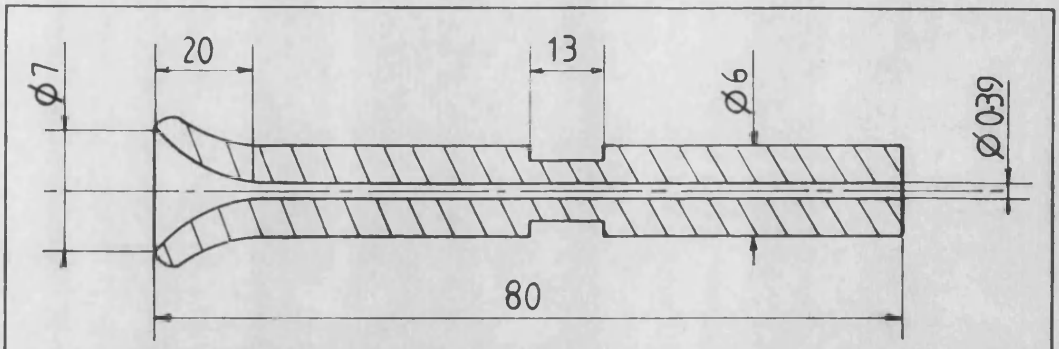

Fig 4.1 Glass Capillary probe (all dimensions in mm).

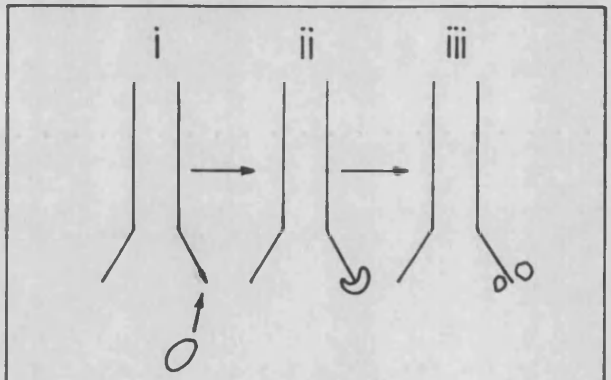

Fig 4.2 Bubble breaking on hitting outer edge of probe Tip.

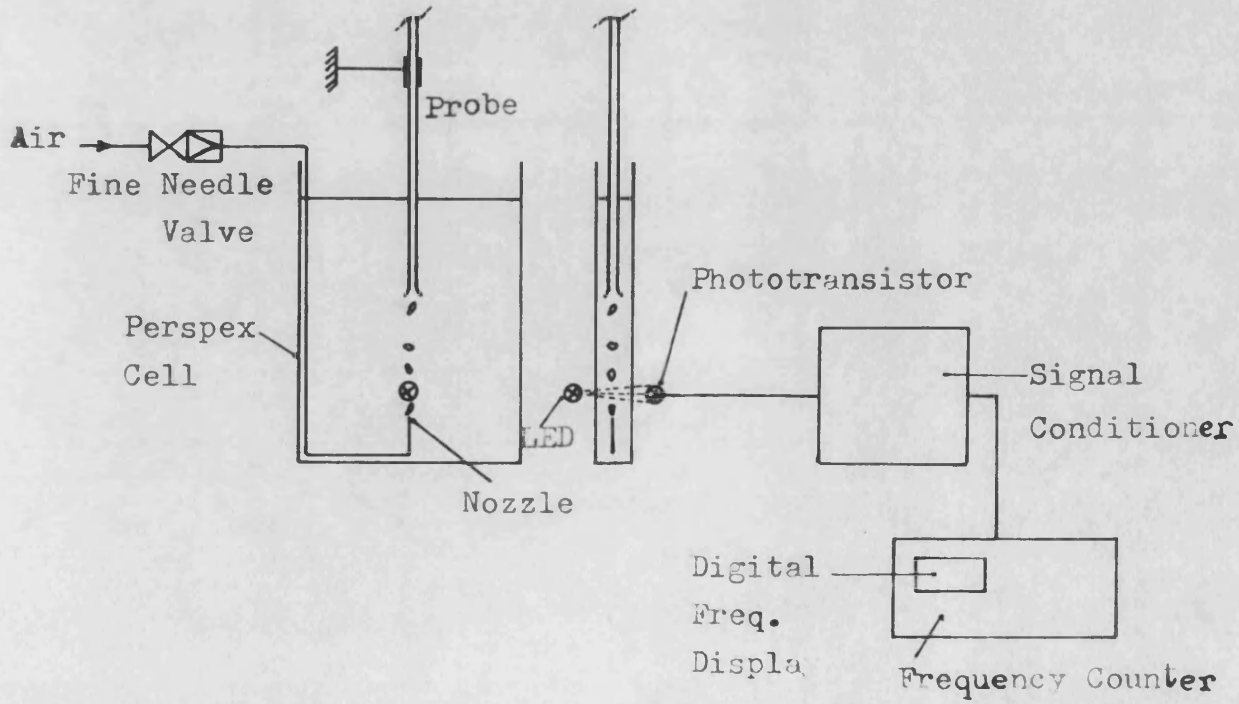

Fig 4.3 Set-up for probe testing.

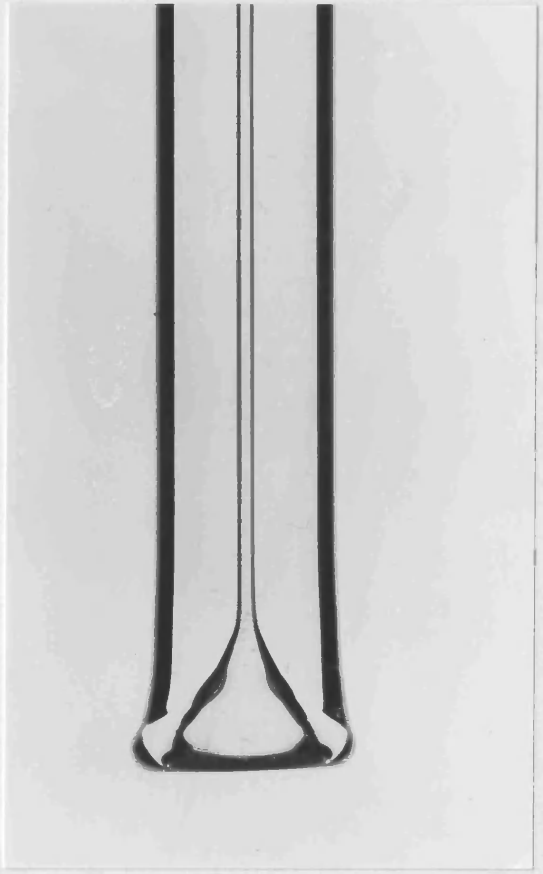

Fig 4.4 (a)

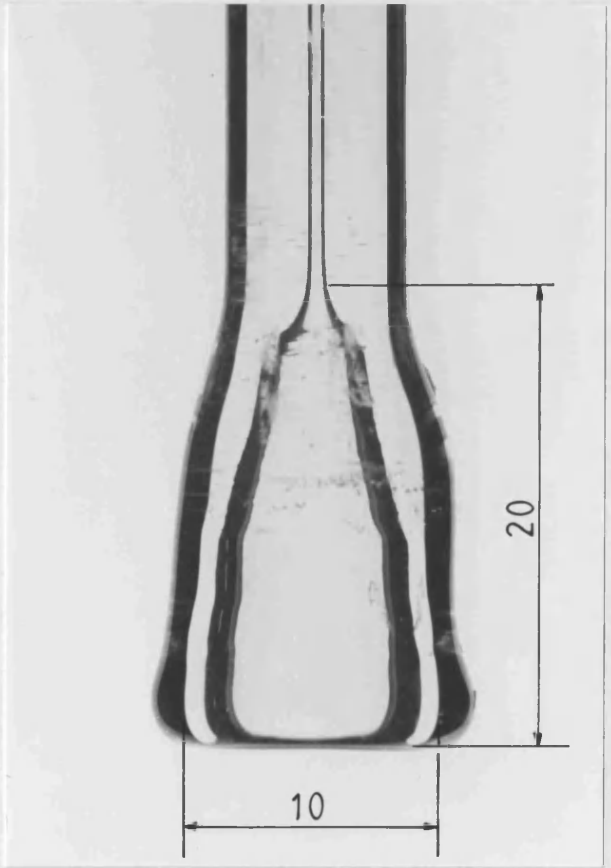

Fig 4.4 (b)

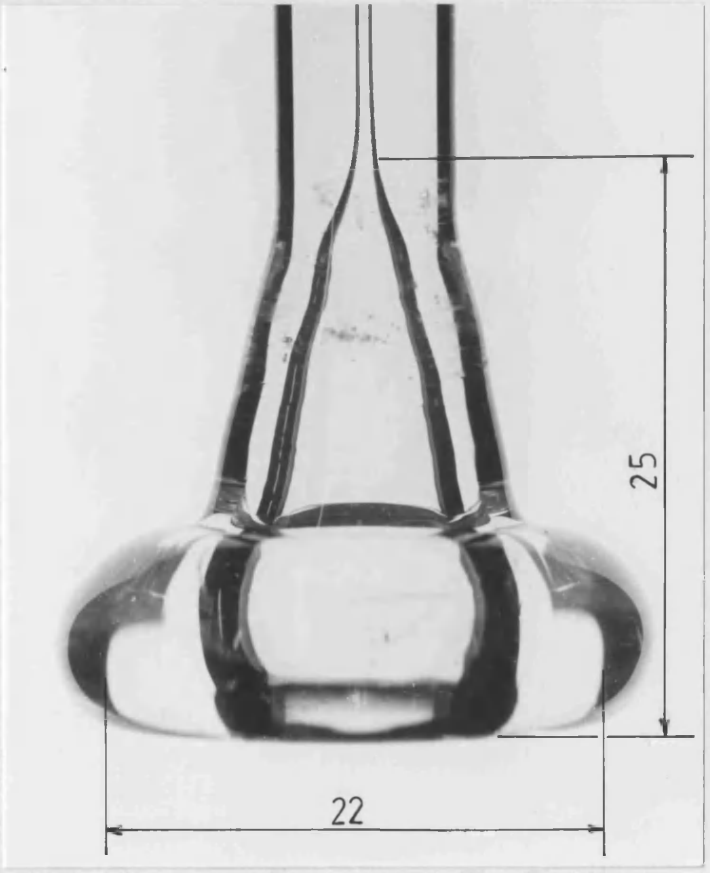

Fig 4.4 (c)

Fig 4.4 Different probe tip shapes.
(Dimensions mm)

This resulted in bubbles splitting at the entrance to the capillary. The shape shown in Fig 4.4(b) was found to limit breakage to bubbles larger than 5 mm approximately. Larger bubbles of about 6 mm in diameter were tested and found to split on hitting the probe tip edge but only at one particular angle. In a stirred vessel, such large bubbles are a rare event and the likelihood of them hitting the probe tip at this angle would be very small.

It was found that in order to suppress bubble breakage the geometry of Fig 4.4(c) would have to be adopted. This configuration, however, presents two disadvantages; First, the relatively large size of the tip greatly disturbs the sampling process. This was tested in a bubble swarm produced in the 'two-dimensional' cell and the performance of this tip shape is compared in Fig 4.5, to that of Fig 4.4(b). Clearly, the configuration of Fig 4.4(b) has a much better performance as far as flow pattern disturbance is concerned, than that of Fig 4.4(c). The other drawback of the latter shape is that the inner diameter of the tip inlet has to be made larger in order to achieve the outer profile. This in turn increases the size of the sampling zone, which causes multi-bubble sampling ie., the measured bubble is the result of coalescence of a number of small bubbles. Hence, the tip geometry of Fig 4.4(b) was chosen as the optimum configuration.

4.3.1.4 Fully submersible probe

For application in large vessels, the probe was designed to be fully submersible. This was achieved by locating the glass capillary inside a length of stainless-steel tube, leaving the tip exposed, as shown in Fig 4.6. The bubble detection assembly was sealed by immersing the leading end of the tube in a solution of waterproof silicone rubber (9161-RTV). Once set, this gave effective sealing and firm support for the glass tube.

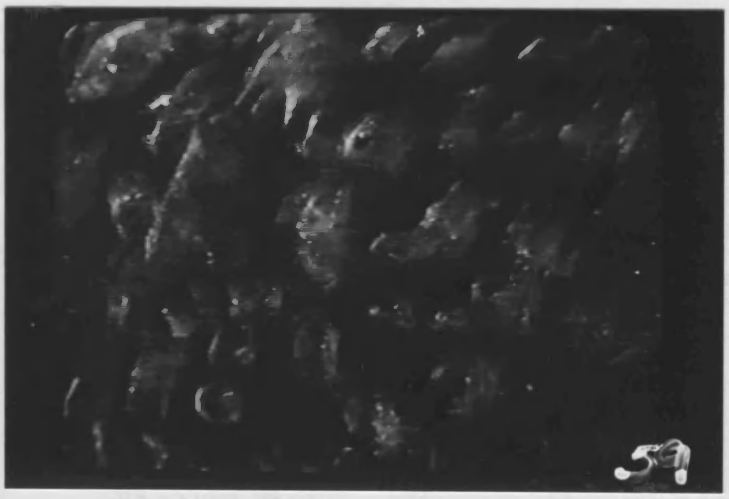

Fig 4.5 (a) Undisturbed bubble swarm in 'two-dimensional' cell.

Fig 4.5 (b) No significant disturbance caused by probe tip of Fig 4.4 (b).

Fig 4.5 (c) Significant disturbance caused by probe tip of Fig 4.4 (c).

Fig 4.5 Comparison of behaviour of different probe tips in a bubble swarm (see Fig 4.4).

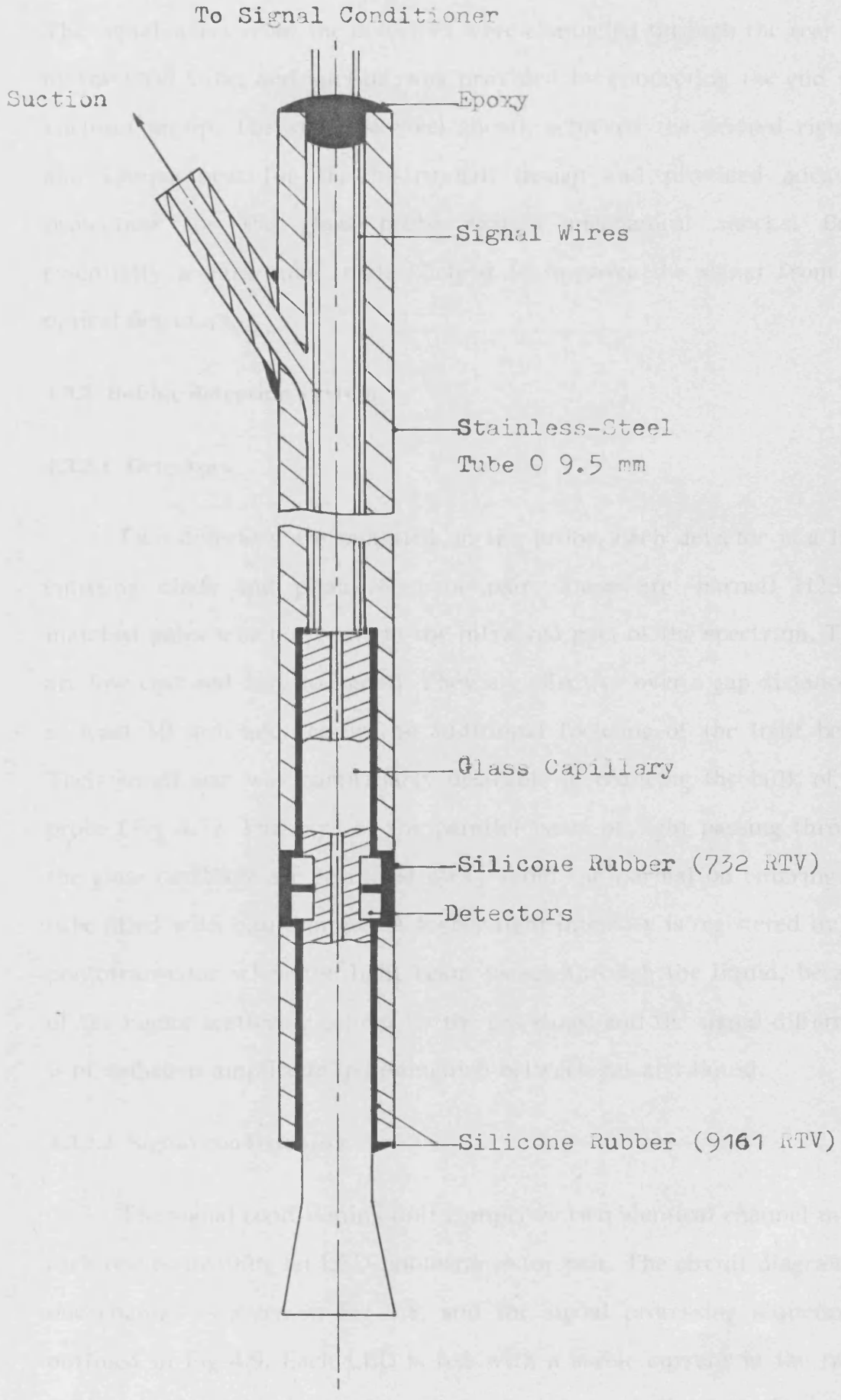

Fig 4.6 Fully submersible probe.

The signal wires from the detectors were channeled through the rear end of the steel tube, and suction was provided by connecting the end to a vacuum pump. The stainless-steel sheath achieved the desired rigidity and compactness for the instrument design and provided adequate protection for the glass probe against mechanical shocks. Being essentially a dark tube it also helped to improve the signal from the optical detectors.

4.3.2 Bubble detection system

4.3.2.1 Detectors

Two detectors are mounted on the probe. Each detector is a light emitting diode and phototransistor pair. These are 'Farnell H23A1' matched pairs which operate in the infra-red part of the spectrum. They are low cost and easy to install. They are effective over a gap distance of at least 10 mm and require no additional focusing of the light beam. Their small size was particularly desirable in reducing the bulk of the probe (Fig 4.7). The rays of the parallel beam of light passing through the glass capillary are refracted away from the normal on entering the tube filled with liquid or gas. A higher light intensity is registered by the phototransistor when the light beam passes through the liquid, because of the higher scattering caused by the gas slugs, and the signal difference is of sufficient amplitude to distinguish between gas and liquid.

4.3.2.2 Signal conditioning

The signal conditioning unit comprises two identical channel units, each one controlling an LED-phototransistor pair. The circuit diagram of one channel is given in Fig 4.8, and the signal processing sequence is outlined in Fig 4.9. Each LED is fed with a stable current in the range 0-30 mA adjustable from the system control panel, Fig 4.10. The value

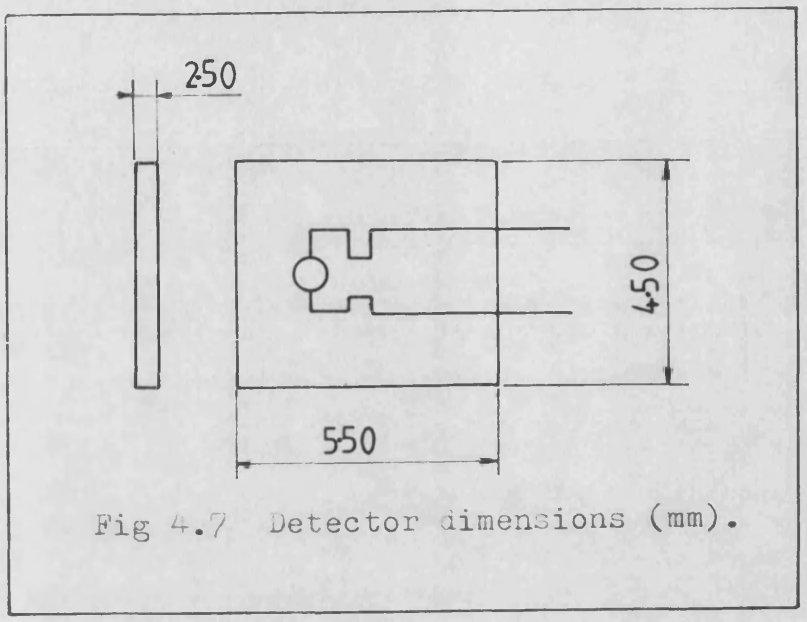

Fig 4.7 Detector dimensions (mm).

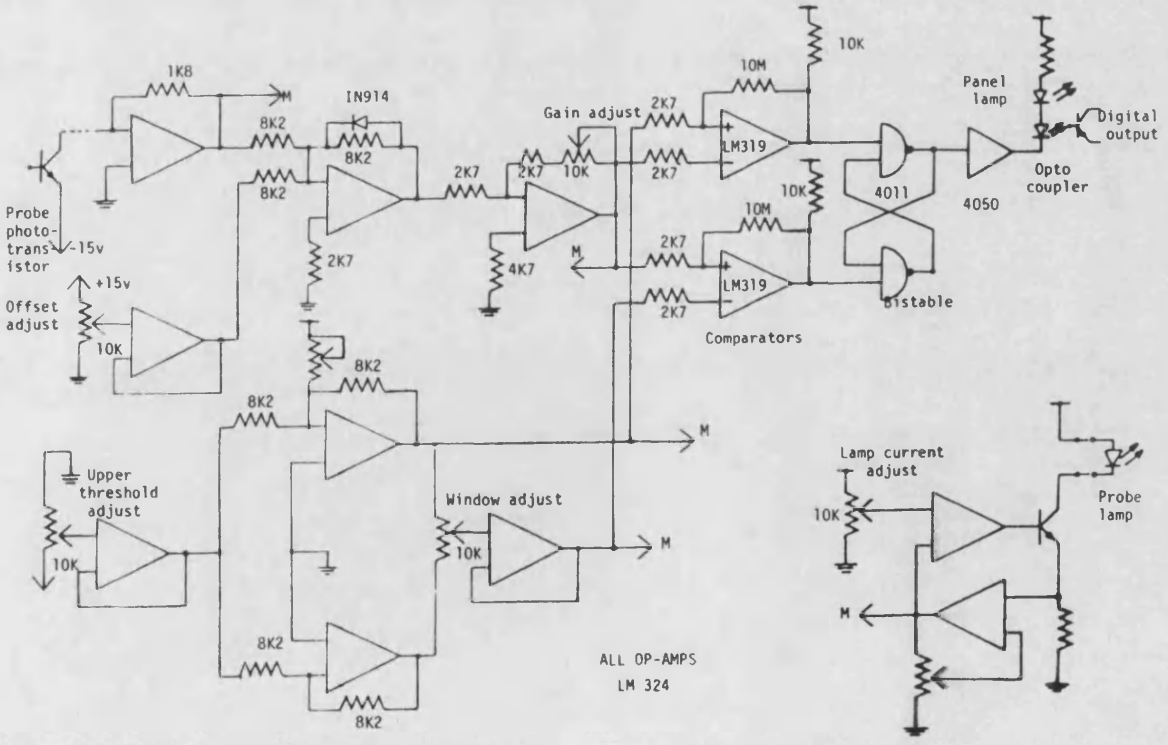

Fig 4.8 Probe signal conditioning (one channel).

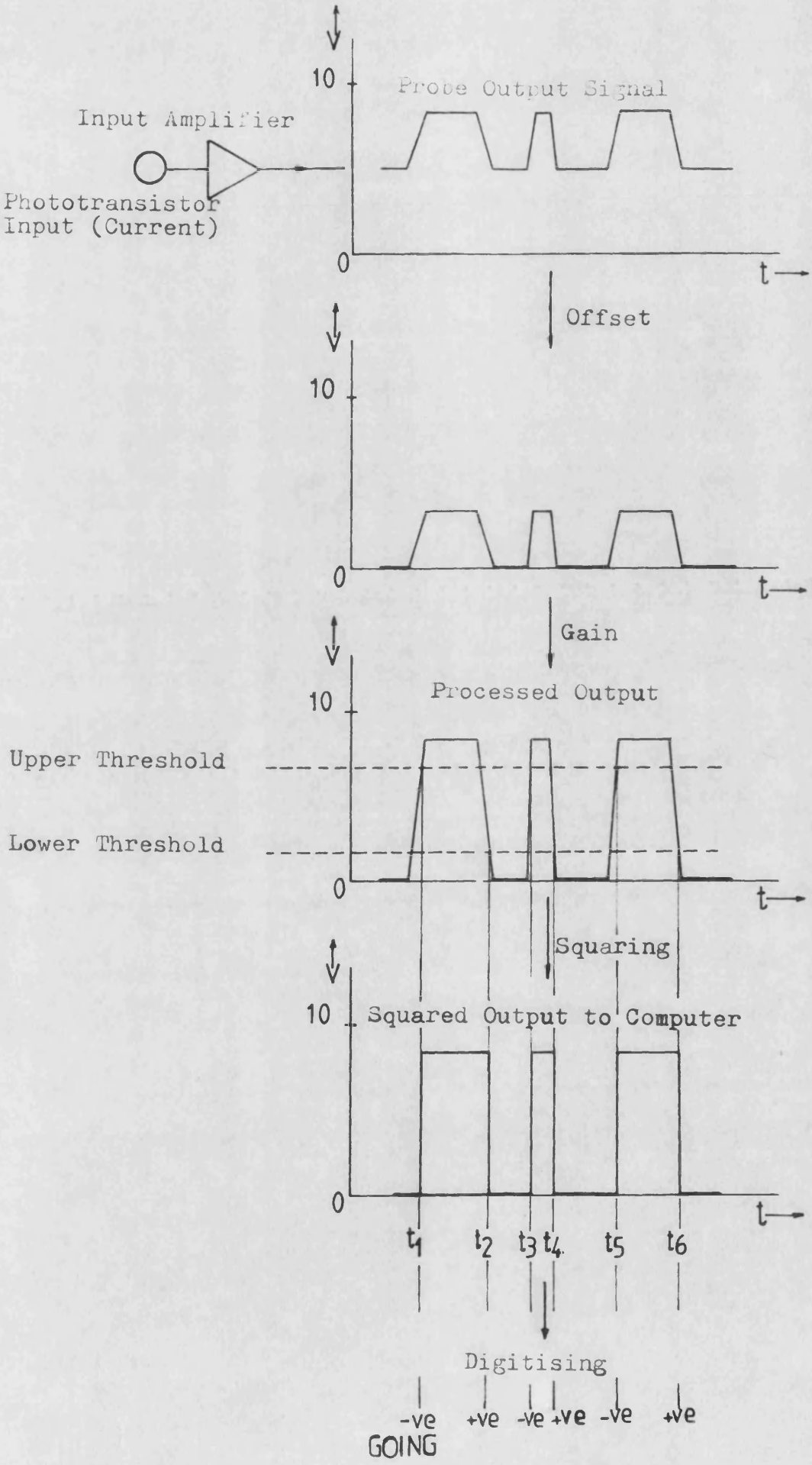

Fig 4.9 Signal processing sequence.

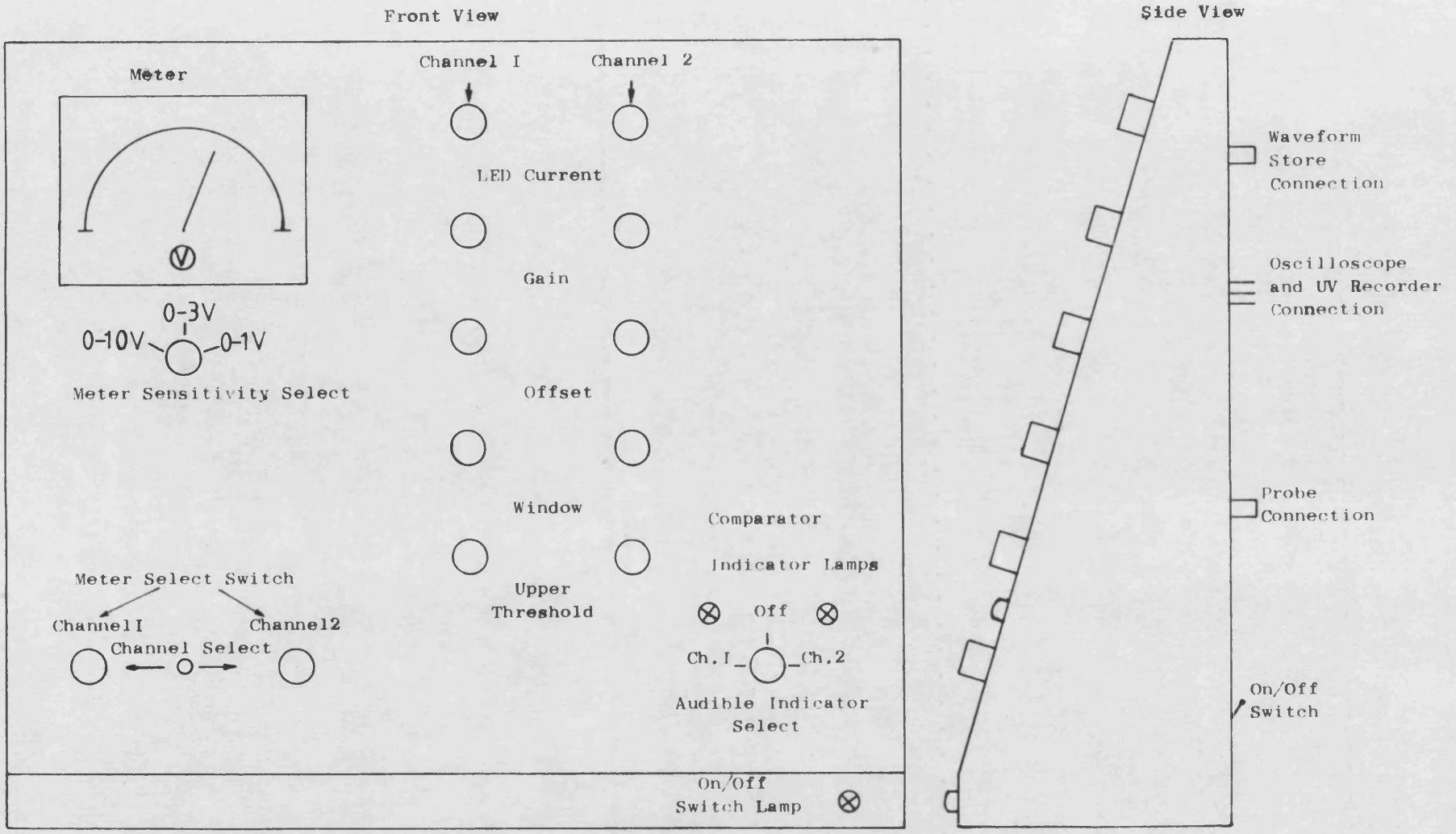

Fig 4.IO Control pannel of capillary probe.

of the current can be measured on the panel meter with the meter select switch in the appropriate position. The phototransistor is connected to a bootstrap current-voltage converter circuit. The voltage output of this circuit is proportional to the current passed by the phototransistor with a constant bias of 15 Volts applied:

$$V_0 = 1.8\times10^{-3} I_c$$

where,

V_0 = output voltage,

I_c = phototransistor collector output.

This voltage may be displayed on the panel meter for setting-up purposes. V_0 is then applied to an offset-gain block. Firstly, a voltage of 0-10 V may be subtracted from V_0, then a gain of 1 to 5 may be applied to the difference signal. The output of the offset-gain block may be displayed on the panel meter. Gain and offset are continuously adjustable from the panel.

The output of the offset-gain block is fed to a variable hysteresis comparator circuit.This consists of two comparators, for an upper and a lower switching levels, and a bistable. The upper switching level is controlled from the front panel and can be read on the meter when required. The lower threshold is arranged to track the upper one, the voltage difference between them being adjustable from the 'window' switch on the control panel with the help of the meter. In practice, because of the short switching time of the detectors (100 μs), the position of these trigger levels was not found to be critical as far as time measurements were concerned. Therefore, they were adjusted fairly close to the liquid-level voltage line in order to avoid the detection of occasional spikes in the signal that could either be due to the bubble carrying a small liquid droplet with it or to the surrounding liquid film trying to penetrate the bubble. The rare spikes that were of enough

amplitude to be still detected were subsequently numerically filtered. Lamps on the panel indicate the state of the output from the comparators. In addition, an audible indicator can be connected to either comparator output when necessary for setting-up purposes. These indicators also help to monitor the operation of the probe during experimental runs.

4.4 Data acquisition system

4.4.1 Design and development

The design of such a system evolved through different stages which ultimately, led to the system used here. In its early form the operation of data collection and processing was supervised by a Macsym II microprocessor (Appendix A), [92]. The signal output from the probe was fed, after conditioning, directly to the microprocessor through the analog input interface card contained in the machine's own ADIO (Analog Digital Input Output) bus. Continuous high frequency sampling of the signal was carried out and the signal voltage values collected were stored in the computer memory for subsequent processing, as illustrated in Fig 4.11.

This system presented serious handicaps. Because of the relatively slow speed of the Basic programming language it could only cater for one detector channel and, therefore, it was impossible to sample from the two channels simultaneously without losing vital information. The second disadvantage was that although some 64 Kbytes of memory space was devoted to the data storage, only a relatively short sample of the signal could be stored at a time. In addition, this considerable amount of data required a fairly long processing time.

An interrupt-driven system was then designed to work under the control of a BBC microcomputer (Appendix A). The presence of an assembler in this machine allowed the use of machine code programming and therefore simultaneous sampling from the two channels was made possible. This system is described in Appendix C. The hardware was simple, consisting of two VIA chips and a few LSTTL chips. The method of data acquisition was improved so that instead of the continuous high frequency sampling of the signal only the times corresponding to changes of phase state were recorded (Fig 4.12). This resulted in a considerably more efficient use of the computer memory and a substantial reduction in processing time. Furthermore, the software control of data collection was incorporated into a ROM (Read Only Memory), leaving the maximum amount of computer memory space for data. This was then readily available for analysis by the Basic-software package running on the computer using standard array-referencing statements. Because the computer memory was available both to the data acquisition system and the computer analysis programme, simultaneous processing of the data was possible. It was envisaged that part of the computer memory would be set aside for use as a first-in-first-out (FIFO) buffer. The interrupt system would supply data to the buffer as they occurred, and the Basic programme would be able concurrently to read the data from the buffer in the order in which they were collected.

Unfortunately, the system did not perform to expectation. Although the elapsed time was measured to a resolution of 10 μs, the time required to respond to each input level change was of the order of milliseconds. It was thought at first that this would be acceptable, but input data rates in practice turned out to be much faster than anticipated, so that signal level changes were effectively lost, making it often difficult to correlate the two channels. The system did, however,

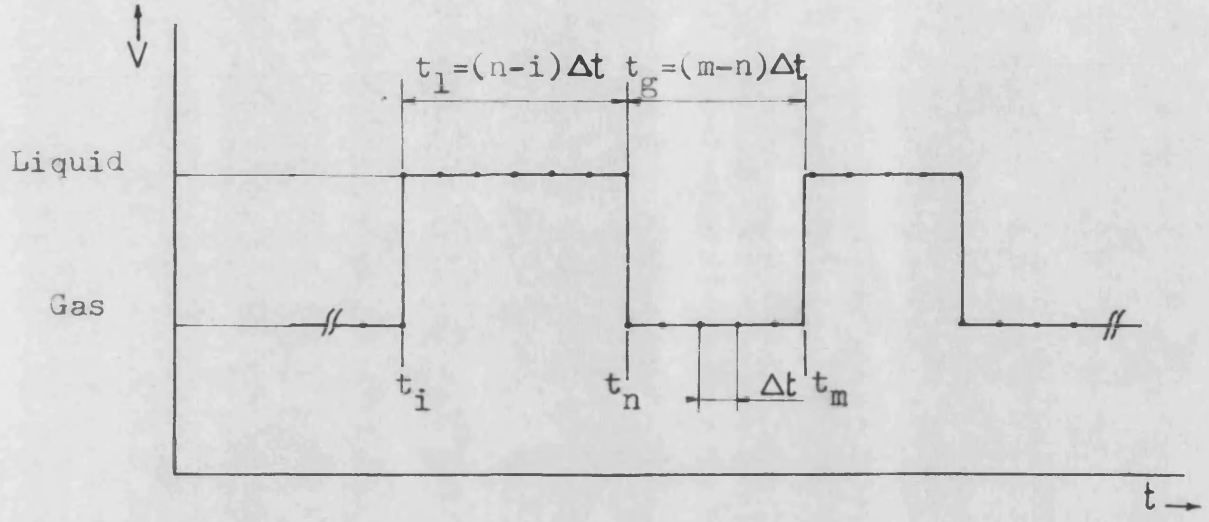

Fig 4.11 High frequency sampling of probe signal.

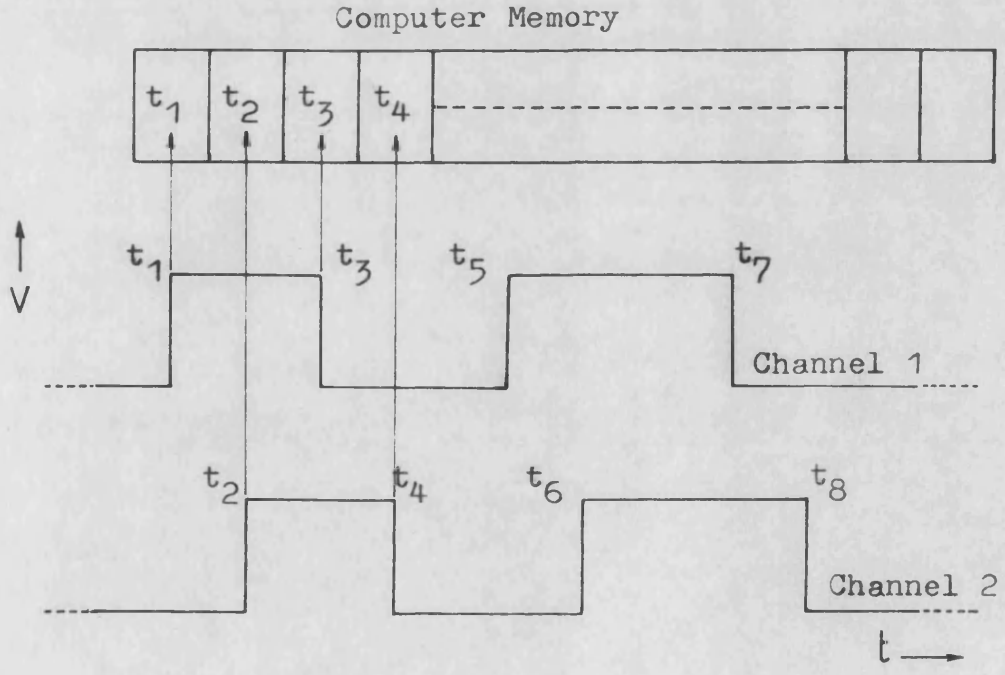

Fig 4.12 Time recording of phase state changes.

give good results with signals that exhibited low or moderate rates of phase state changes. Ideally, an external FIFO buffer was required, fast enough to respond to the input data. This would form an external 'queue' of data available to the computer main programme which through fast machine code routines could be made to process them at a rate equal to or greater than the average rate of data input. Then, the buffer only has to cope with fluctuations in input data rate and can be made sufficiently large so that it would never completely fill in practice. Under these conditions, sampling periods could be of practically unlimited length. The essential features of this proposed system are briefly outlined in Appendix C.

However, because of the amount of time and labour that the development of such a scheme would take, a compromise system, described below, which makes use of an external two-channel binary waveform store, was eventually built. This was successful and can serve as the basis for the design of a true FIFO system.

4.4.2 Two-channel binary waveform store

This apparatus was connected to the comparator output from the signal conditioner via an opto-coupler to minimise ground loops. It is capable of storing two independent binary waveforms in solid-state memory with a time resolution of 10 μs. This freed completely the computer memory for subsequent data analysis tasks such as signal reconstruction, post-mortem signal conditioning, auto- and cross-correlation, numerical filtering, spectral analysis etc.. Fig 4.13 gives a functional block diagram of this high-speed event logger. The timing of the apparatus is controlled by the master clock which, when enabled, generates a 100 KHz square wave signal (Fig 4.14). This square wave is fed to the input control logic and the elapsed-time counter. The memory

array consists of 8192×32–*bit* words. Each word is used to store an event in the following way: the last significant 28 bits hold the contents of the elapsed-time counter at the time the event occurred. The most significant 4 bits are provided by the input control logic and give information about the event ie., the channel(s) on which the event(s) occurred and the polarity of the change(s) of state (Fig 4.15). The polarity of an event is said to be positive if the change is from liquid to gas, and negative if the transition is from gas to liquid.

The address counter holds the current memory address and is incremented automatically after each memory write operation. The sample-select logic is used to determine the memory size required for the current sampling operation. All or part of the available 8192 words may be used, selectable sizes being of the form 2^{7+n}, $n = 0$ *to* 6. The shift register is used during data retrieval by the microcomputer, providing a convenient intermediate storage and interface.

4.4.3 Sampling process

When a sample is required, the microcomputer first produces a reset pulse. This sets the memory address counter and the elapsed-time counter to zero, and sets up the input control logic to detect the next negative-going input change ie., bubble nose interface. The computer then enables the master clock signal. This edge is also used to increment the elapsed-time counter (Fig 4.14). The new input samples are compared with the preceding samples by the input control logic. If a change of state in either or both of the inputs is detected, the input control logic initiates a write pulse, which first stores data concerning the event in the memory word pointed to by the address counter, then increments the address counter to point to the next available memory word. If the selected memory space is now full, the sample-select logic will disable

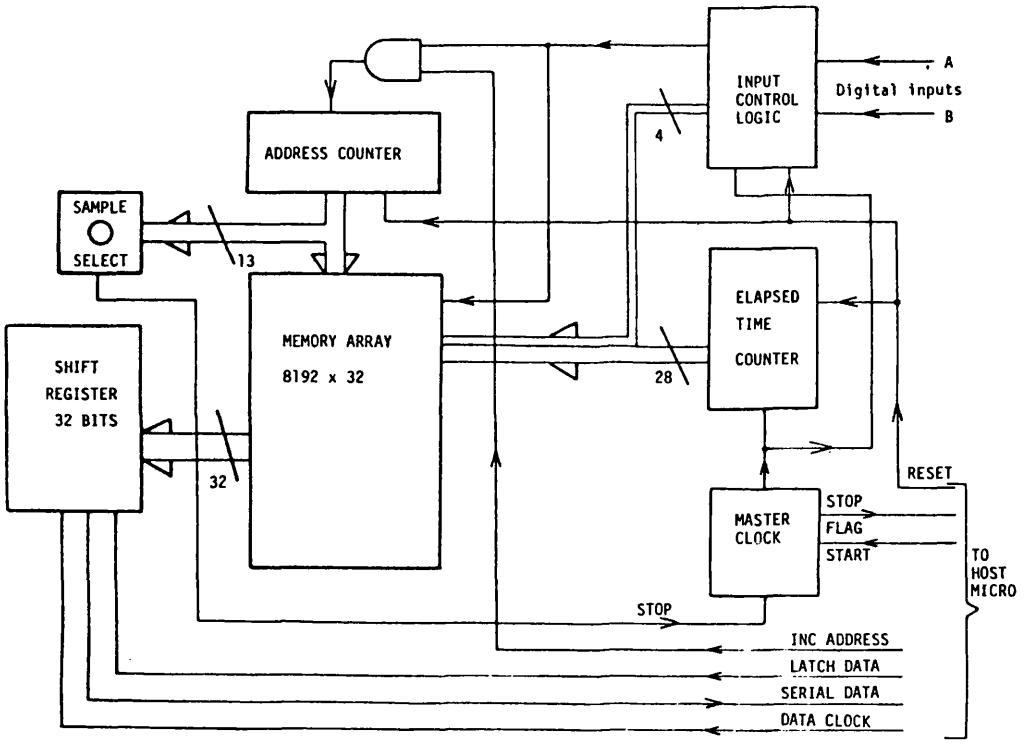

Fig 4.13 High Speed Two-Channel Event Logger.

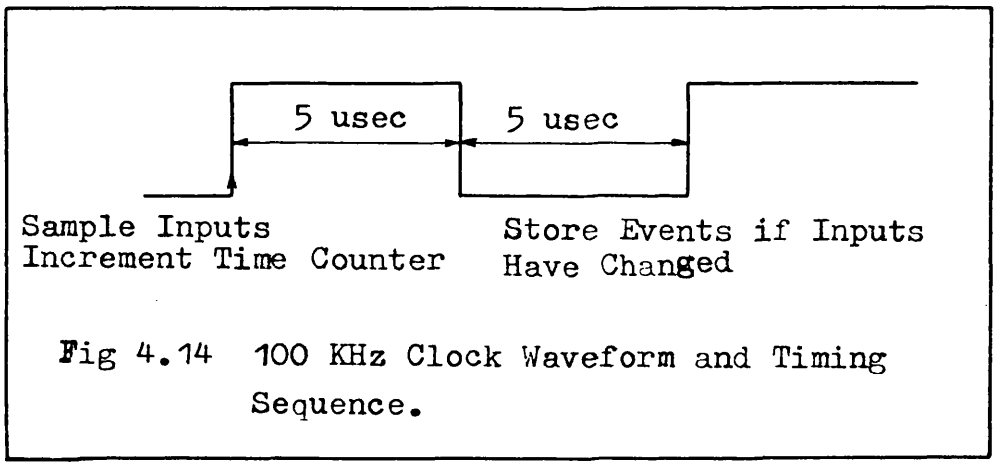

Fig 4.14 100 KHz Clock Waveform and Timing Sequence.

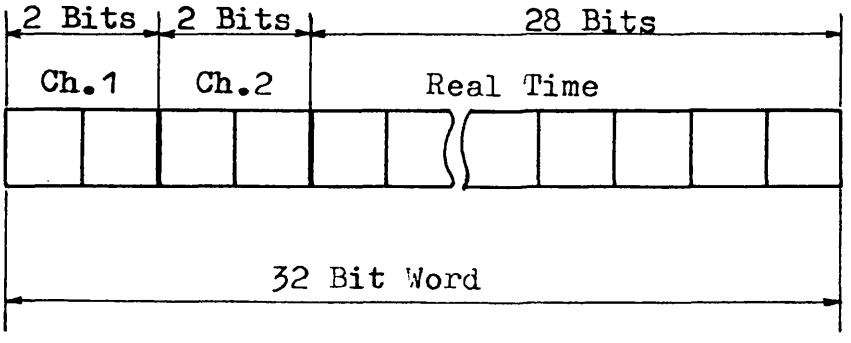

Fig 4.15 Memory Word Organisation.

the master clock, inhibiting any further sampling and inform the host computer of the situation, otherwise sampling will continue as above.

4.4.4 Data retrieval

The address counter is reset to zero by the microcomputer. A latch-data pulse is then generated by the microcomputer which stores the current (zeroth) memory word in the shift register. The register contents are then shifted out by the microcomputer as four 8-bit bytes. Finally, the computer generates an increment-address pulse to point the address counter to the next available memory word. The process is repeated until the memory-full flag is set, indicating that the available data have been retrieved.

A software package was written and used for the control of the sampling operation and the subsequent data retrieval and on-line analysis. This is given in Appendix B with a description of its major routines. The use of machine code routines allowed fast data processing. Typically, a sample of 8192 words of data was analysed and results printed in about three minutes.

4.5 Bubble size determination

4.5.1 Ideal case

For an ideal cylindrical slug occupying the whole cross-section of the capillary and moving at constant velocity U_b, the length of the slug, l_b, can be calculated from:

$$l_b = U_b T_b \tag{4.1}$$

as shown in Fig 4.16(a). The slug volume, V_b, will then be given by:

$$V_b = \frac{\pi}{4} l_b d_c^2 \qquad (4.2)$$

4.5.2 Real case

The shape of an actual slug differs from the ideal cylindrical shape because of it convex ends (Fig 4.16(b)). Additionally, it is also well known that the slug does not fill the whole cross-section of the tube. The bubble is in fact surrounded by a thin liquid film which may occupy a significant fraction of the capillary cross-section [88-90]. In addition, the motion of the bubble slugs was found to be quite different from that of constant velocity. By using a short capillary tube carrying detector pairs at different locations along its length, the motion of different bubble slugs was observed.

First of all it was found, as expected, that the detection time varied with the bubble size and suction pressure applied to the capillary. The detection time being longer for larger slugs, and for all slugs it decreased with increasing suction pressures. For a given bubble size, the detection time was different at different positions along the tube, the magnitude of the difference being dependent on the slug size, as shown in Fig 4.17. Also, the tail velocity of a bubble slug was found to be different from the nose velocity. For larger bubbles the tail velocity is greatest whereas for smaller bubbles the nose velocity is slightly higher than the tail velocity. This difference between nose and tail velocities shows that bubble slugs are not regions of constant pressure as would be the case if the flow regime in the capillary were dynamically stable ie., stable slug flow regime [90]. Indeed, because of the short length of the tube the end effects are important and the assumption of dynamic stability as made by Suo [91] in his model of two-phase flow in long capillary tubes, is no longer valid in this case. Only for those small

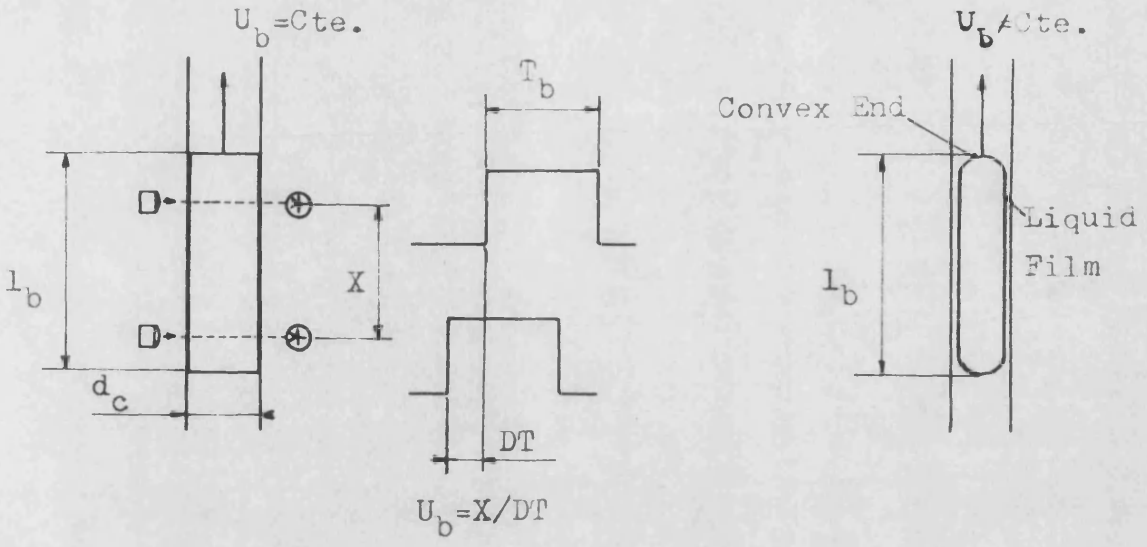

Fig 4.16 (a) Ideal Case

Fig 4.16 (b) Real Case

Fig 4.16 Bubble Flow in Capillary.

Fig 4.17 Variation of Bubble Detection Time with Bubble Size and Detector Position

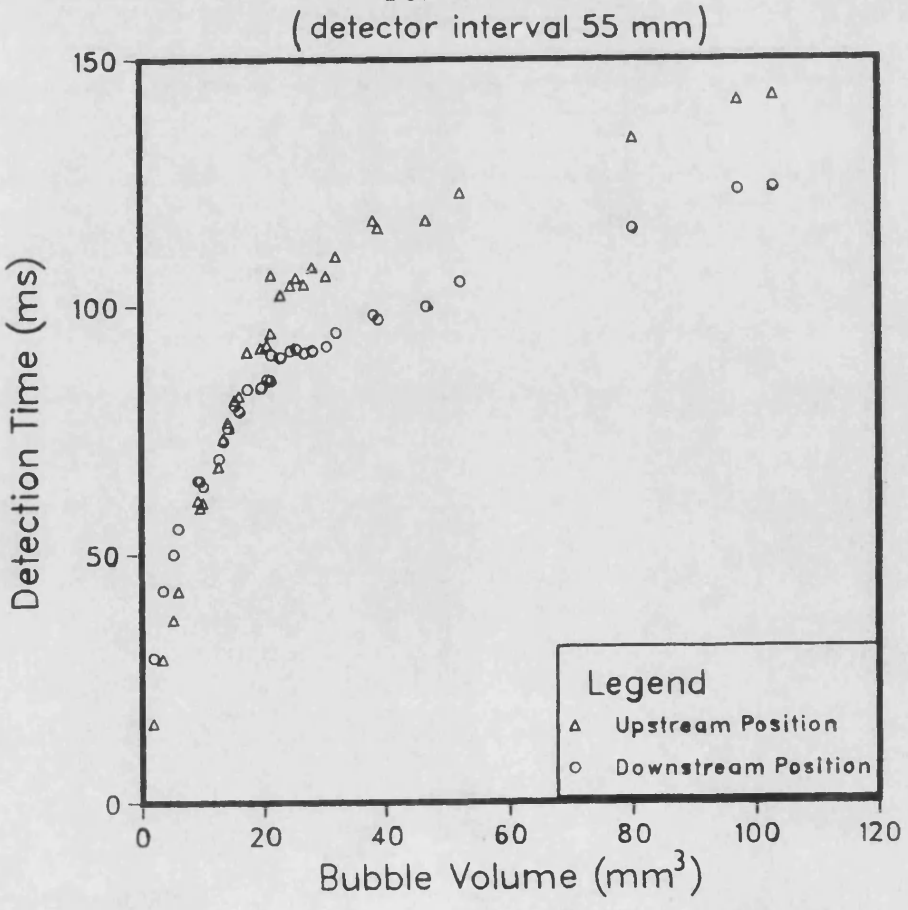

bubble slugs whose length is short relative to the tube length, is the difference between the two velocities small. This is because the pressure at the front of the slug is slightly lower than the back pressure and the flow can be said to be a quasi-slug flow. However, for larger slugs the flow is annular. This can be easily understood by comparing the length of bubble slugs with the length of the tube, as shown in Fig 4.18.

Another important fact is that because of the pressure gradient inside the tube, the gas slugs are subject to an expansion effect, and therefore the volume of the bubbles measured inside the tube will be different, to some extent, from the true volume of the bubbles in the dispersion. Hence, it can be concluded from all these observations that gas-liquid flow inside short capillaries is very complex and deviates significantly from that of a stable slug-flow regime as observed in long capillary tubes [90, 91]. Therefore, in order to take the above factors into account a direct calibration of the probe was necessary.

4.6 Probe calibration

4.6.1 Calibration procedure

A precision micrometer needle syringe was used to inject a range of bubbles with accurately known volumes in the inlet of the capillary, at a fixed suction pressure. The output signals generated by these bubbles were analysed and correlated to the bubble volumes. Two different methods of correlation were considered. The first method makes use of one single detector; The bubble detection time is directly correlated with the bubble size (Fig 4.19). The second technique uses both detectors to measure the bubble detection time and bubble nose velocity. These two parameters are then correlated with the bubble size (Fig 4.20). The two methods are evaluated, below, according to their ability in minimising

Fig 4.18 Comparison of Bubble Slug Lengths With Length of Capillary

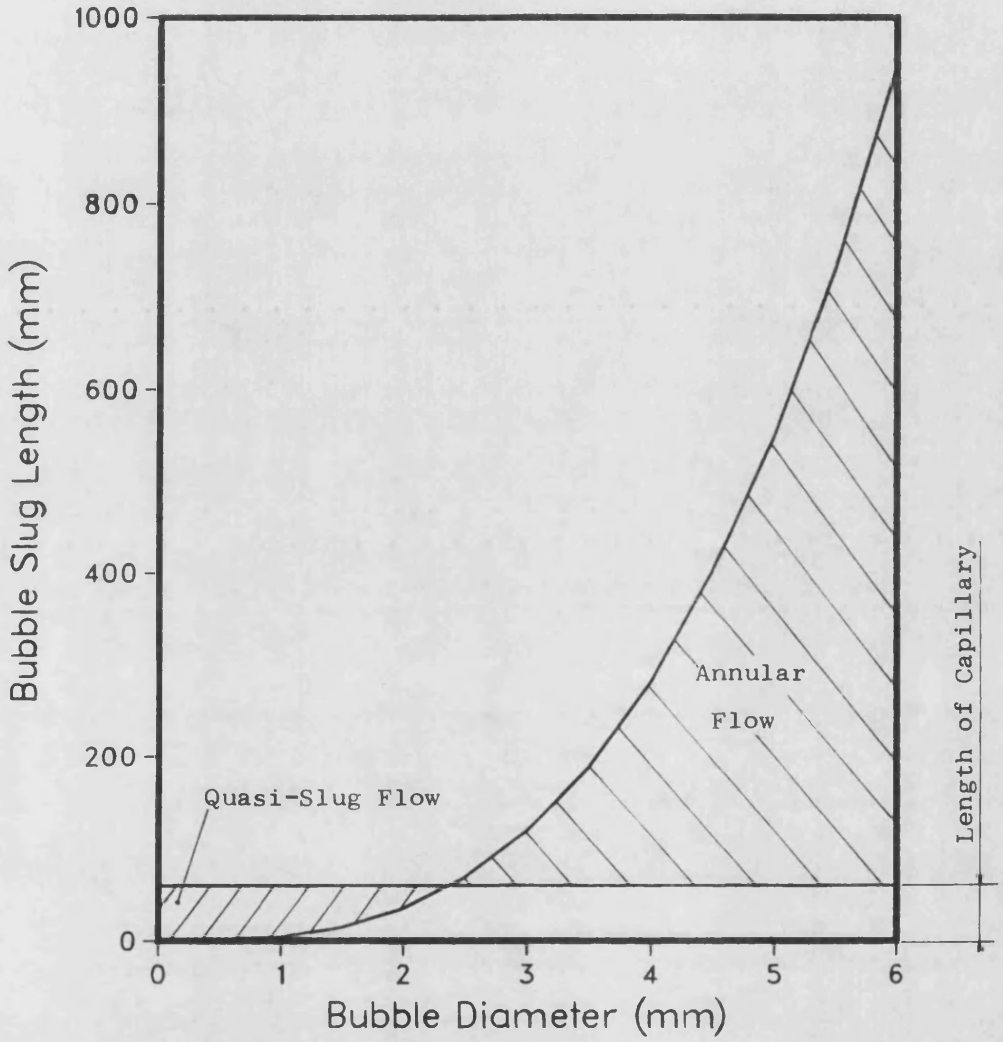

Fig 4.19 One-Detector System Calibration

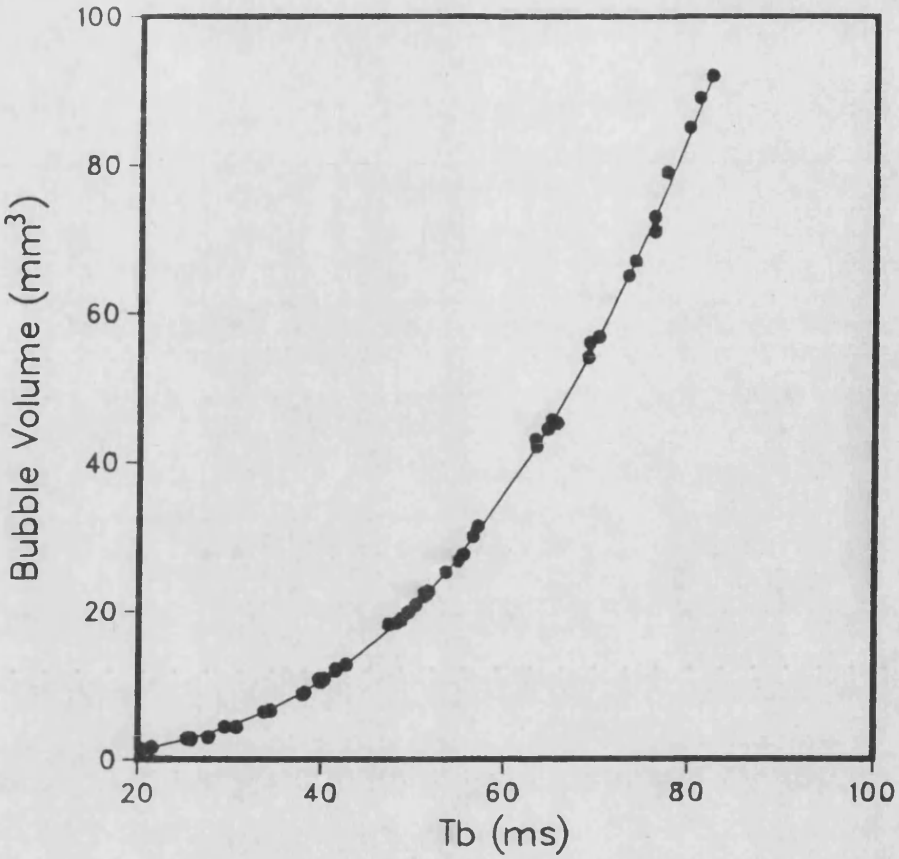

Fig 4.20 Two-Detector System Calibration

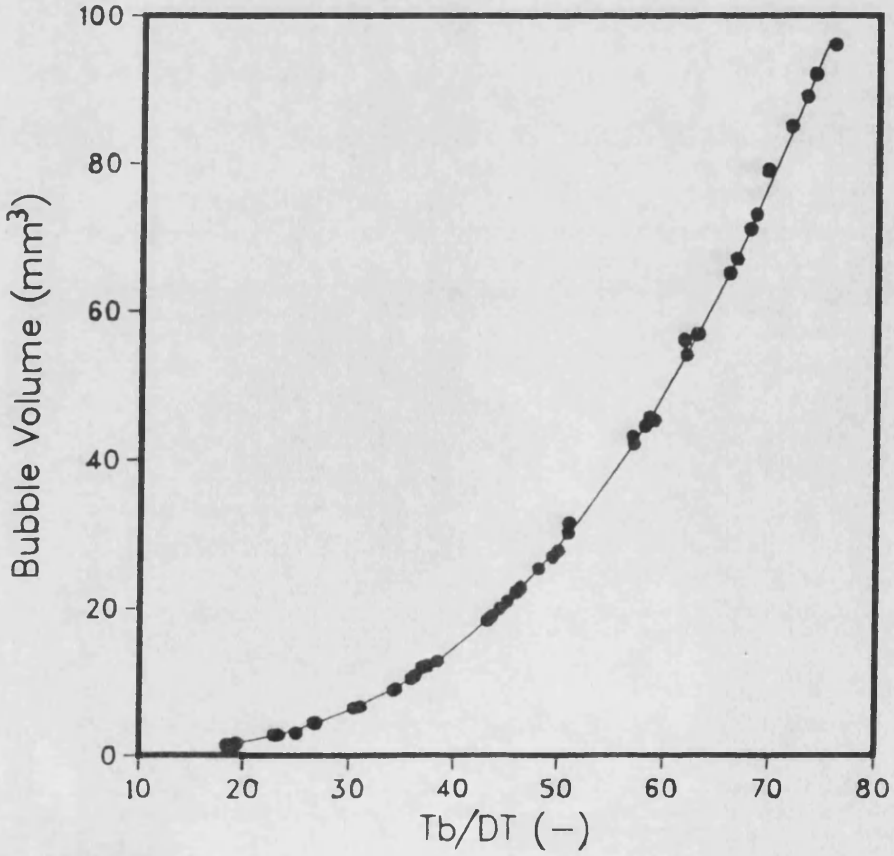

measurement errors that are likely to arise from the calibration.

4.6.2 Error sources

The calibration of the probe is achieved by measuring single isolated bubbles injected from the syringe at a fixed suction pressure. In this mode the calibration is specific to the mean suction velocity used. However, when sampling from a dispersion fluctuations in bubble slug velocity can occur. These deviations from the calibration velocity can be caused by the two main effects:

(i) Any significant contamination of the capillary may cause a reduction in slug velocity. Under conditions of severe contamination the effect can be important. This is why the capillary should be regularly cleaned. Prior to taking measurements, the tube was always cleaned with Chromic acid and thoroughly rinsed with double distilled water. In order to help detect the moment at which contamination starts to build up inside the tube during experiments, the factor $m = \frac{U_b - U_s}{U_b}$, is calculated periodically by the software programme which controls the sampling operation, where:

U_b = bubble slug velocity under actual sampling conditions,

U_s = liquid velocity measured under contamination-free conditions at the same suction pressure.

From the calibration data which is obtained under contamination-free conditions an estimate of the minimum value of m is obtained. When, during measurements the value of m is found to fall below this value repeatedly, sampling is automatically stopped, the computer emits a warning sound and a message to this effect is displayed on the VDU screen. Cleaning of the probe is then carried out.

(ii) When a series of bubble slugs are moving inside a capillary tube, bubbles close to each other interact. The trailing slug is accelerated by the wake of the leading one whereas the leading slug is accelerated by the expansion of the trailing one. As observed by Greaves and Kobbacy [92], the largest axial interaction occurs when the two successive bubbles are of different size, the trailing one being the larger of the two. The possibility of bubble trains occurring inside the capillary is restricted to small bubbles only, when using a short length of tube. Coexistence of parts of two large bubbles, one entering the tube and the other leaving it, or a small bubble followed by the leading interface of a large bubble are also likely possibilities. The effect of bubble interaction was checked using the set-up of Fig 4.3. Bubbles were generated at different frequencies, starting from a low frequency where only a single isolated bubble is sampled at a time, to higher frequencies where more than a bubble or parts of two bubbles coexist inside the tube at the same time. All variations in bubble slug velocity were found to be within 8% of that of a single bubble travelling interaction-free inside the capillary.

4.6.3 Evaluation of the one-detector and the two-detector techniques

The detection time of a bubble is a function of its velocity. Consequently, any changes in the velocity will be reflected in the measured values of its detection time and travelling time between the two detectors. These velocity changes were found to affect bubble size measurements differently according to whether one detector or two detectors were used.

To simulate these bubble velocity changes, a bubble having a diameter of 3.62 mm was injected into the capillary and its velocity was varied by altering the suction pressure. For each value of bubble velocity the calibration equation for the one-detector and the two-detector

techniques were used to calculate the diameter of the bubble, and the error between this value and the true value of the diameter was computed for each one of the two methods.

For the one-detector method the calibration model is of the form:

$$V_b \propto T_b^3$$

and the error on the diameter is given by:

$$E_{1D} = \frac{T_{be}}{T_{bc}} - 1 \qquad (4.3)$$

where, the indices c and e refer respectively to calibration velocity conditions and experimental velocity conditions.

For the two-detector system the calibration model is of the form:

$$V_b \propto \left[\frac{T_b}{DT}\right]^3$$

and the error on the diameter is given by:

$$E_{2D} = \left[\frac{T_{be}}{DT_e}\right]\left[\frac{DT_c}{T_{bc}}\right] - 1 \qquad (4.4)$$

The values of E_{1D} and E_{2D} are plotted against the velocity ratio U_e/U_c in Fig 4.21, where:

U_c = calibration velocity,

U_e = experimental velocity.

The first remark that can be made from Fig 4.21 is that the errors given by the two techniques are of opposite sign for the same value of velocity ratio. This means that, at the same condition, one method overestimates the bubble diameter, while the other method underestimates it. The important remark, however, is that the one-

Fig 4.21 Error Curves for 1–Detector and 2–Detector Systems

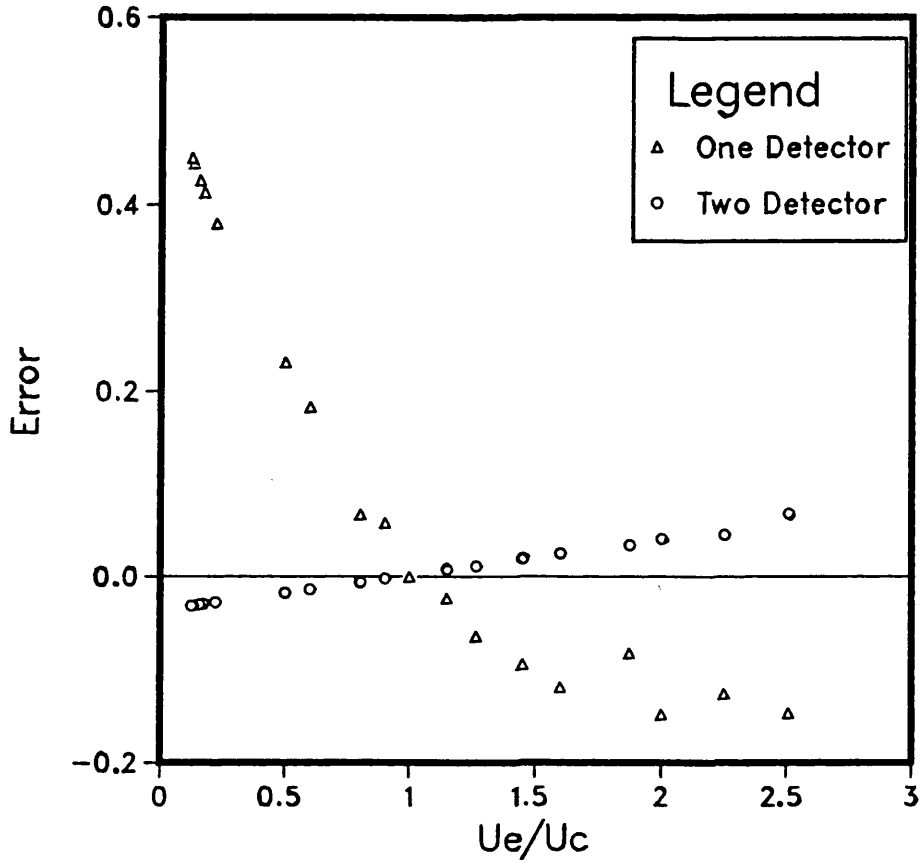

detector system gives rise to considerably higher errors than the two-detector system. Indeed, the error curve of the one-detector system is of an exponential nature whereas that of the two-detector technique is of a linear nature with a small slope. The low sensitivity of the two-detector system to velocity fluctuations is expected since the velocity of the bubble is incorporated in the calibration equation:

$$V_b = f\left(\frac{T_b}{DT}\right) \text{ or } f'(U_b T_b)$$

When the velocity changes, the quantities T_b and DT are both affected in the same way ie., they both increase or decrease and therefore, any consequent changes in the ratio T_b/DT are significantly damped. The one-detector system, on the other hand, measures the quantity T_b only, and this reflects any changes in the bubble velocity. In other words, the one-detector model intrinsically assumes that the bubble slug velocity does not deviate from the calibration value during measurements. Hence, the two-detector method was selected to be used for bubble measurements.

Chapter 5

BUBBLE SIZE DISTRIBUTIONS

5.1 Introduction

Measurement of bubble size remains one of the most challenging problems in the field of gas-liquid contacting in mechanically agitated reactors. Being perhaps the least developed area, literature on the subject is scarce. Most of the available information on bubble size has been evaluated in terms of an average global bubble diameter. This is derived from estimates of total gas holdup and interfacial area, and not from detailed pointwise investigation of the internal dispersion structure [22, 30, 37]. The reason for this lack of progress has been the absence of adequate measurement techniques. It is only in recent years that serious attempts have been made to independently measure bubble size in stirred vessels, in particular those of Figueiredo [38] and Greaves and Kobbacy [92]. Figueiredo used a four electrode conductivity probe to measure the local bubble size in a 0.91 m tank. Only five points were investigated. The logic controlling the measurement process selects only the bubbles that hit the four electrodes of the probe squarely. The method proved, therefore, to be very slow since a successful bubble-probe encounter was a rare event. A typical run consequently required up to 4 hours to collect a sample of 200 bubbles. The bubble selection feature of the method could also introduce an unknown amount of statistical bias in the sampling process. In addition, only bubbles as small as 0.98 mm could be detected by the probe. Greaves and Kobbacy [92] utilised a cruder version of the capillary suction probe technique adopted here. Their measurements relate to a small scale vessel (0.20 m).

In this Chapter the capillary suction probe technique developed (Chapter 4) is used to measure the local bubble size in the 1.0 m stirred tank. Different regions of the vessel have been examined. These are the mid-plane between two adjacent baffles, the vertical plane coinciding

with the baffles, the vicinity of a baffle plate and the impeller discharge stream. The bulk of the measurements was obtained for air-softened water. The effect of electrolytes was also investigated.

5.2 Bubble sampling process

In order to understand the process of bubble withdrawal from a gas-liquid dispersion with the suction probe, sampling from a chain of bubbles was observed using the arrangement described in Section 4.3 (Fig 4.3). A normal sampling operation is shown in the photographic sequence of Fig 5.1. This demonstrates the case where the probe is almost perfectly aligned with the bubble trajectory. In fact, this condition of 'perfect' alignment was found to be a necessary requirement for a bubble to be sampled by the probe. By alignment, it is meant that the bubble trajectory must coincide with the axis of the tube, or at least cross the sampling zone bounded by the periphery of the probe entrance, as illustrated in Fig 5.2. The case when the bubble trajectory does not align with the probe axis but which passes through the sampling zone is demonstrated in the sequence of Fig 5.3. The bubble is seen to hit the inner surface of the probe funnel before it is sucked in. A small deviation from this trajectory, in any direction, causes the bubble to collide with the edge of the probe tip, thus avoiding capture, as shown in Fig 5.4, or simply by-pass the probe inlet entirely, as in Fig 5.5. This demonstrates that the sampling zone does not extend beyond the immediate periphery of the probe tip entrance, and furthermore, the flow disturbance caused by the effect of suction is insignificant and does not cause any preferential bubble attraction towards the probe inlet from the surrounding flow field. This fact was found to be valid regardless of the suction rate through the capillary. Therefore, a high suction rate (4.5 m/s) was preferred in order to prevent the risk of bubble accumulation

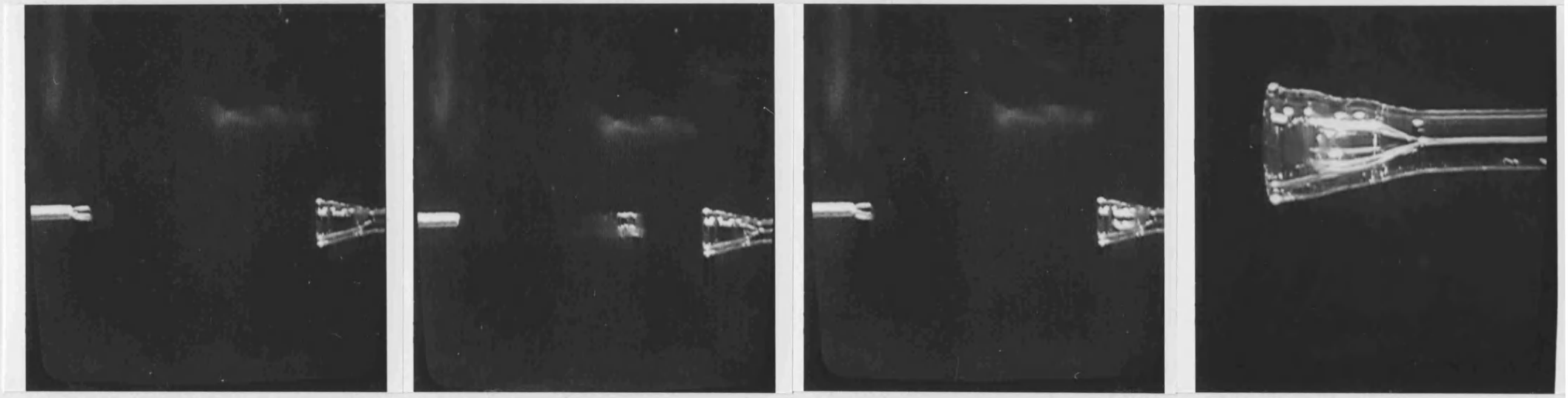

Time ⟶

Fig 5.I Photographic sequence of normal sampling operation.

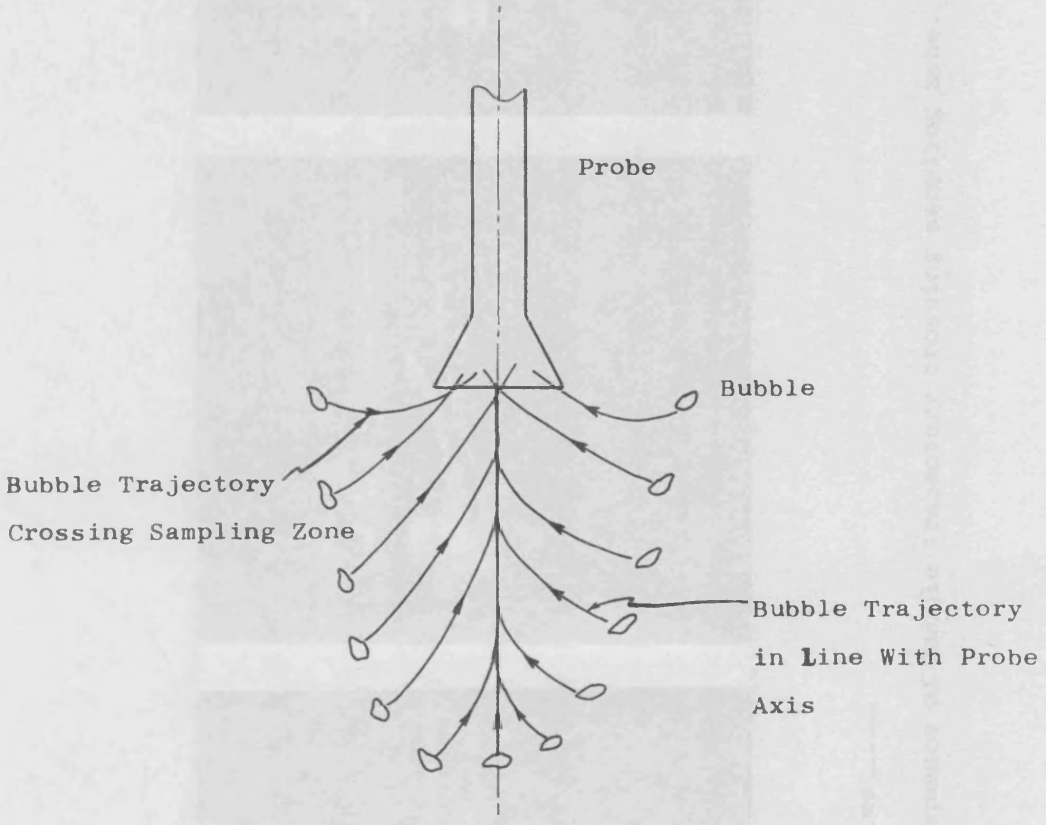

Fig 5.2 Trajectories of bubbles sampled by suction probe.

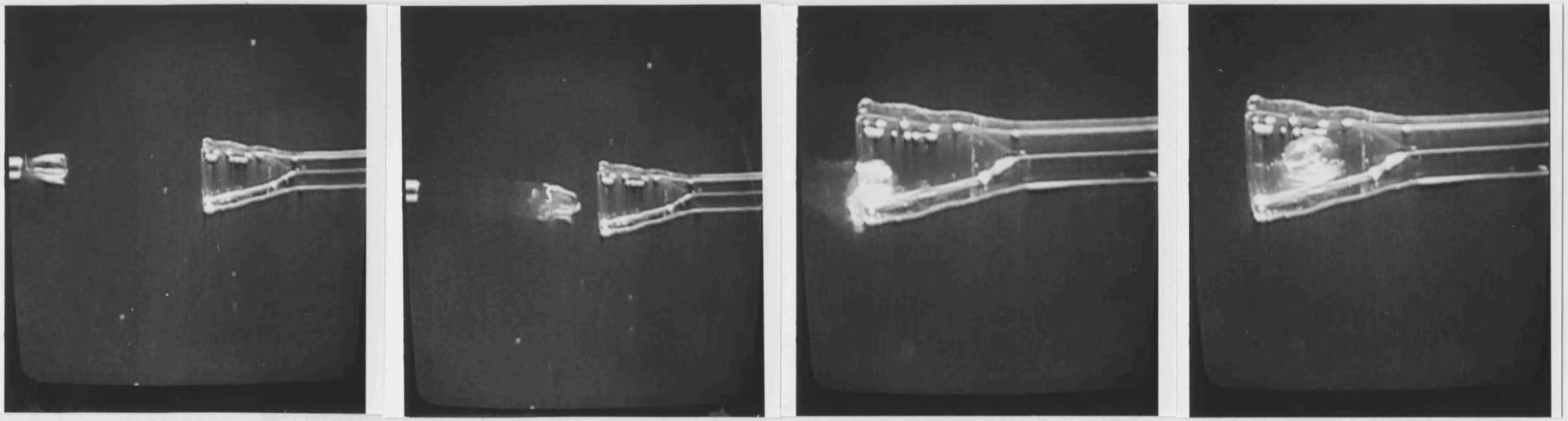

Time ——→

Fig 5.3 Photographic sequence of bubble trajectory crossing sampling zone.

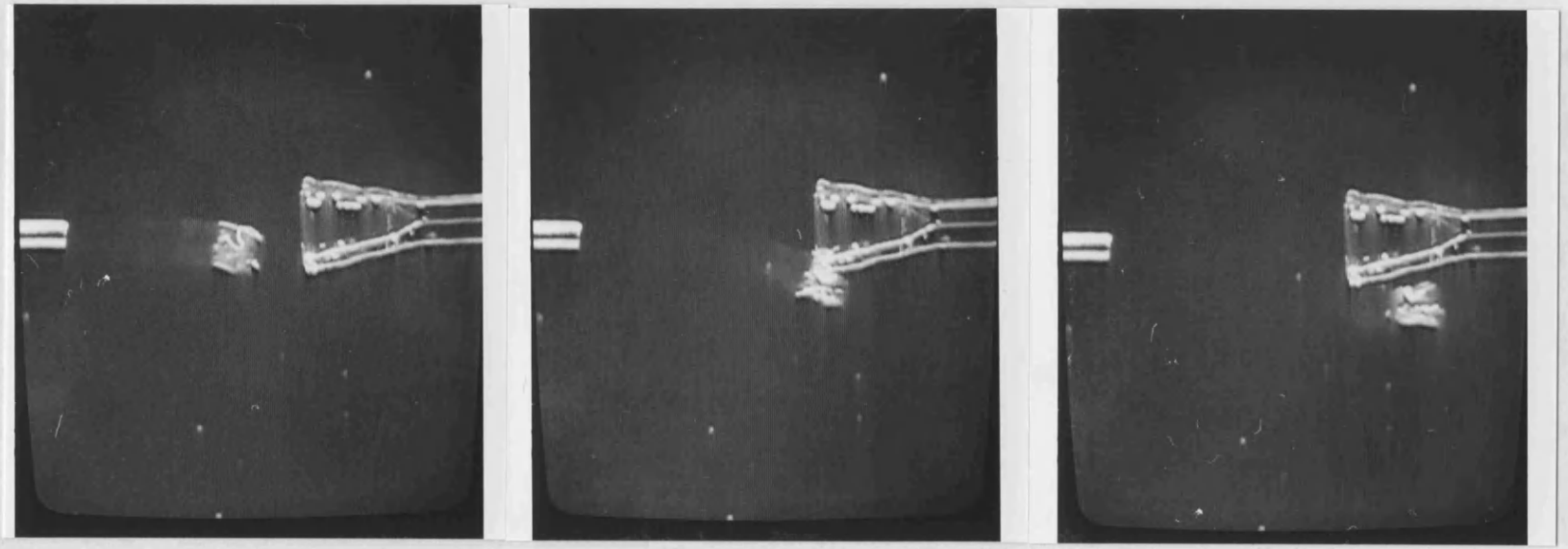

Time ⟶

Fig 5.4 Photographic sequence of bubble hitting probe tip and escaping unsampled.

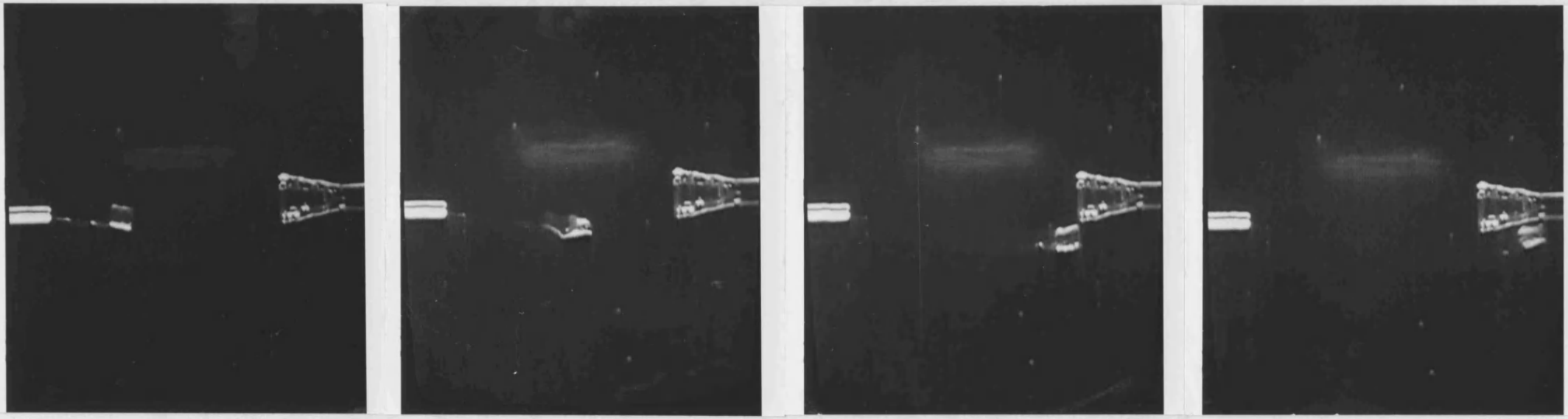

Time ⟶

Fig 5.5 Photographic sequence of bubble by-passing probe inlet.

at the probe entrance.

5.3 Experimental procedure

Measurements of bubble size were carried out using the agitated reactor unit described in Chapter 3. The experimental set-up is shown in Photograph 3.1 and is illustrated schematically in Fig 5.6. A vacuum pump was used to withdraw the bubble dispersion samples through the capillary probe *via* an air-water separator. The capillary was cleaned with Chromic acid and thoroughly rinsed with double distilled water prior to taking measurements. The probe was then positioned inside the vessel at the desired location. After the gas-liquid dispersion was judged to have reached steady-state, the sampling process was initiated from the host computer by simply running the control programme. The total period of sampling was always selected to give a statistically acceptable sample of bubbles, mainly around 500 bubbles. The same software analysed the acquired data and the results were printed on-line.

5.4 Range of experiments

Different regions of the 1.0 m reactor were explored. These were the mid-plane between two adjacent baffles, the plane coinciding with the baffles and the leeward and windward sides of a baffle. These measurements included positions in the bulk of the tank, the impeller mid-plane and also the lower part of the vessel below the agitator. The impeller discharge stream was later explored in more detail at a large number of points. In each case measurements were repeated at different agitation speeds and gas flow rates. Agitation was provided by a 0.333 m Rushton Turbine placed at 0.25 m above the tank base. The bulk of the results was obtained using softened water for the continuous phase and air for the dispersed phase (see Sections 3.2.9, 3.2.10). This represents a

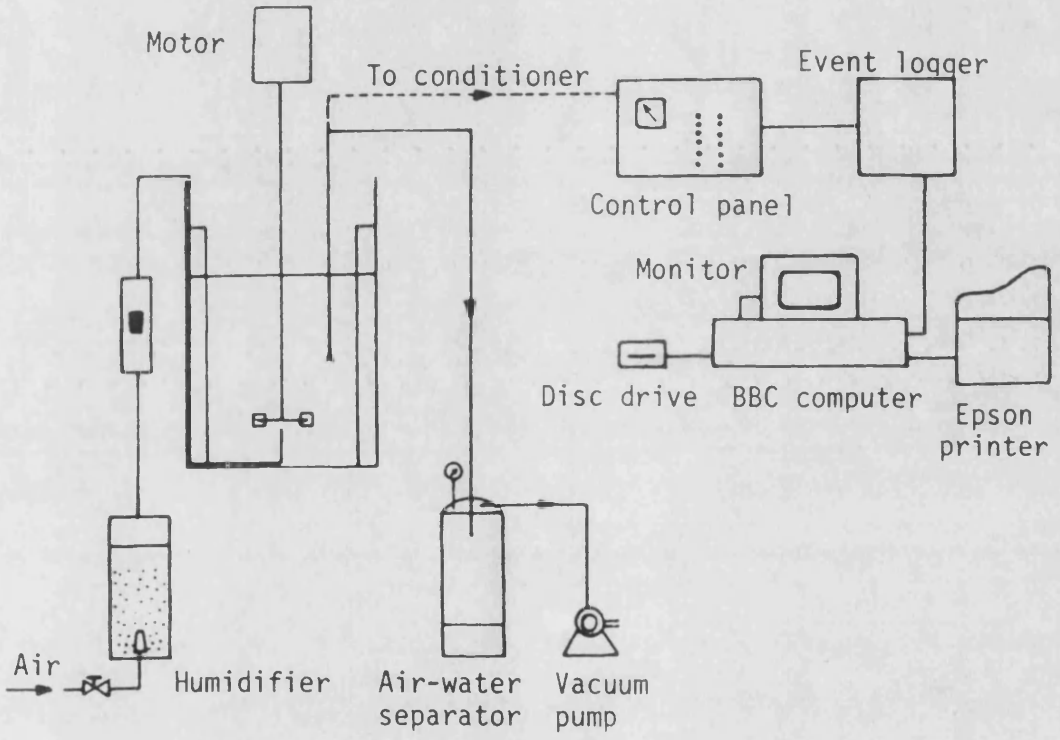

Fig 5.6 Experimental set-up for bubble size measurement.

'pure' system. The effect of the presence of impurities in the water was also investigated by using a 0.15M Sodium Chloride solution.

5.5 Results and discussion

5.5.1 Definition of statistical parameters

The statistics for each local bubble size distribution were calculated on-line from the actual sample population data, which was then grouped into histograms. The number of size classes was chosen to be large enough so as to lose as little information as possible. The different statistical parameters used are defined as follows:

(1) Mean bubble diameter d_{10}:

$$d_{10} = \frac{\sum_{i=1}^{i=n_b} d_{b_i}}{n_b} \tag{5.1}$$

where, d_b is the bubble equivalent spherical diameter and n_b is the total number of bubbles in the sample.

(2) Sauter mean bubble diameter d_{32}:

$$d_{32} = \frac{\sum_{i=1}^{i=n_b} d_{b_i}^{3}}{\sum_{i=1}^{i=n_b} d_{b_i}^{2}} \tag{5.2}$$

(3) Standard deviation σ:

$$\sigma^2 = \frac{\sum_{i=1}^{i=n_b} (d_{b_i} - d_{10}^{2})}{(n_b - 1)} \tag{5.3}$$

(4) Coefficient of variation C_v:

This coefficient gives a measure of the spread of a distribution relative to its mean, and is calculated from:

$$C_v = \frac{\sigma}{\bar{d}_{10}} \qquad (5.4)$$

Overall values of the mean diameter, $\bar{d}_{10}$, and the Sauter mean bubble diameter, $\bar{d}_{32}$, which represent a particular region of the dispersion in the mixing tank are calculated from the sum of all the measured local bubble size distributions in that region.

5.5.2 Reproducibility of results

An important measure of any experimental technique concerns the reproducibility of the results. This was checked under all agitation conditions employed in the experimental runs. Very good reproducibility of measurements was obtained, as demonstrated in Figs 5.7(a-b), for the case of two successive samples taken at the same position. Under all conditions used, the reproducibility error on the Sauter mean bubble diameter was never found to exceed the range 0-6%. Fig 5.8(a-b) represents a different test of reproducibility, wherein, two measurements were performed using the same liquid under identical agitation conditions, but taken three days apart. The liquid was left exposed to the atmosphere during this period. Although the precision of measurement is still good, somewhat larger deviations are observed in this case between the two distributions. These differences are attributed to the difficulty in preserving a constant level of cleanliness of the system in an engineering environment. Consequently, the liquid load was frequently renewed and the reactor was cleaned regularly and kept covered throughout the experimental runs. It is also important to point out that in the design of the mixing system only high grade stainless-steel and natural-grade clear plastics were used for any mechanical parts or surfaces that came in contact with the liquid phase used in the reactor, in order to minimise the risks of contamination.

Fig5·7(a) Reproducibility of Measurements (successive runs)

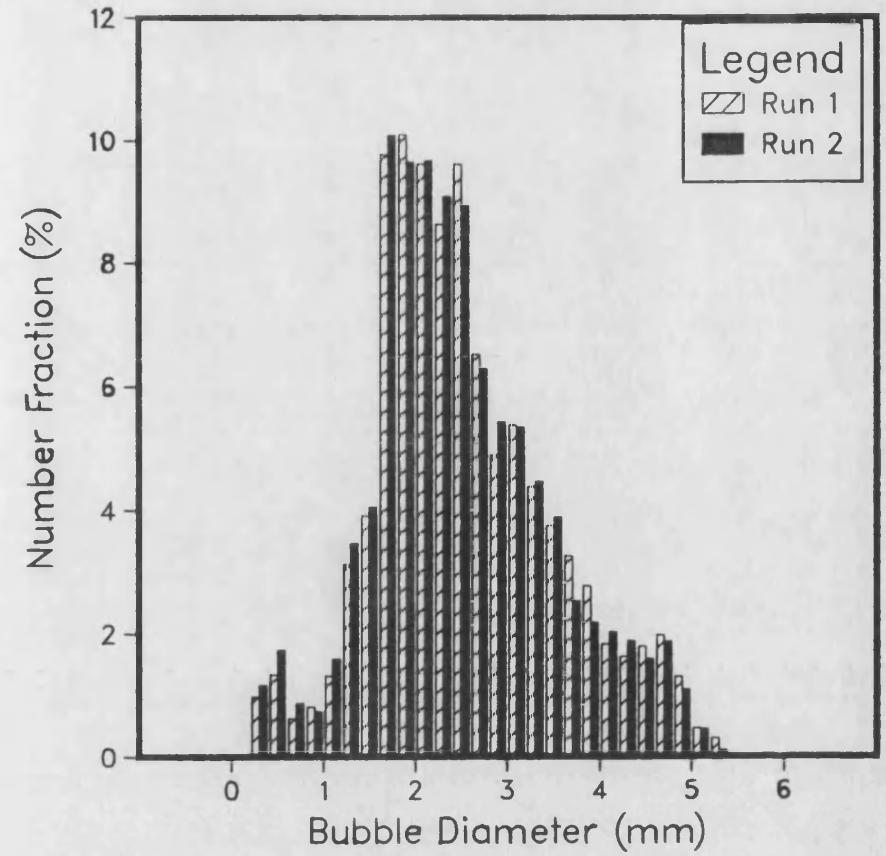

Run I	Run
n_b=614	n_b=614
d_{32}=3.26	d_{32}=3.20
d_{10}=2.54	d_{10}=2.49
C_v=0.398	C_v=0.405

Fig5·7(b) Reproducibility of Measurements (successive runs)

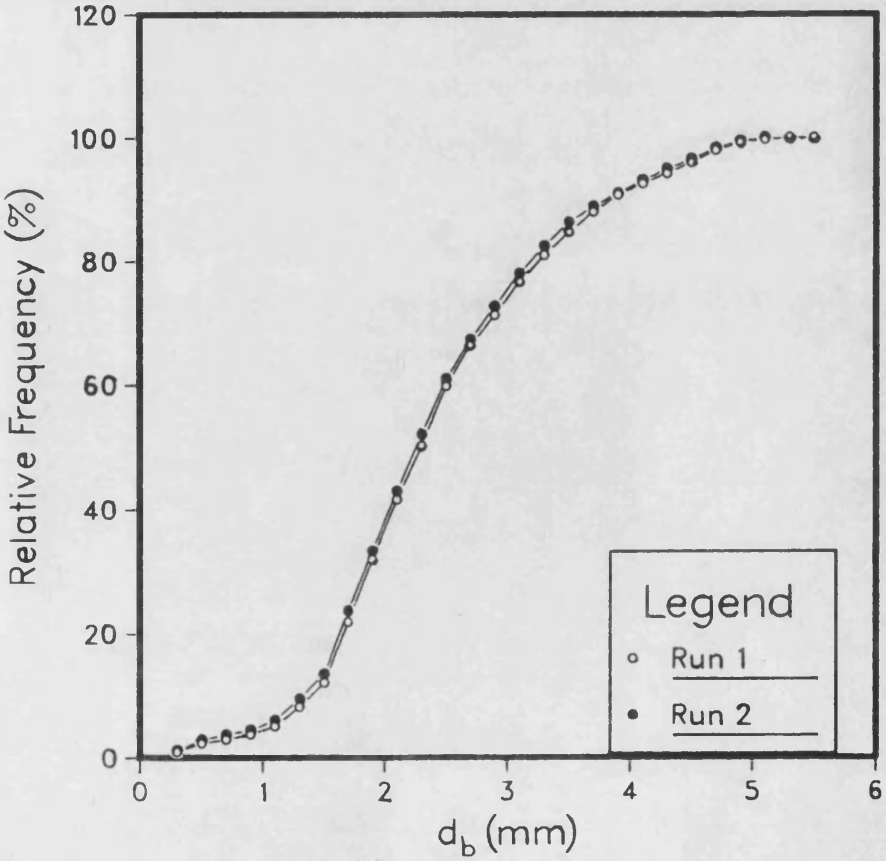

Fig58(a) Reproducibility of Measurements
(runs taken 3 days apart)

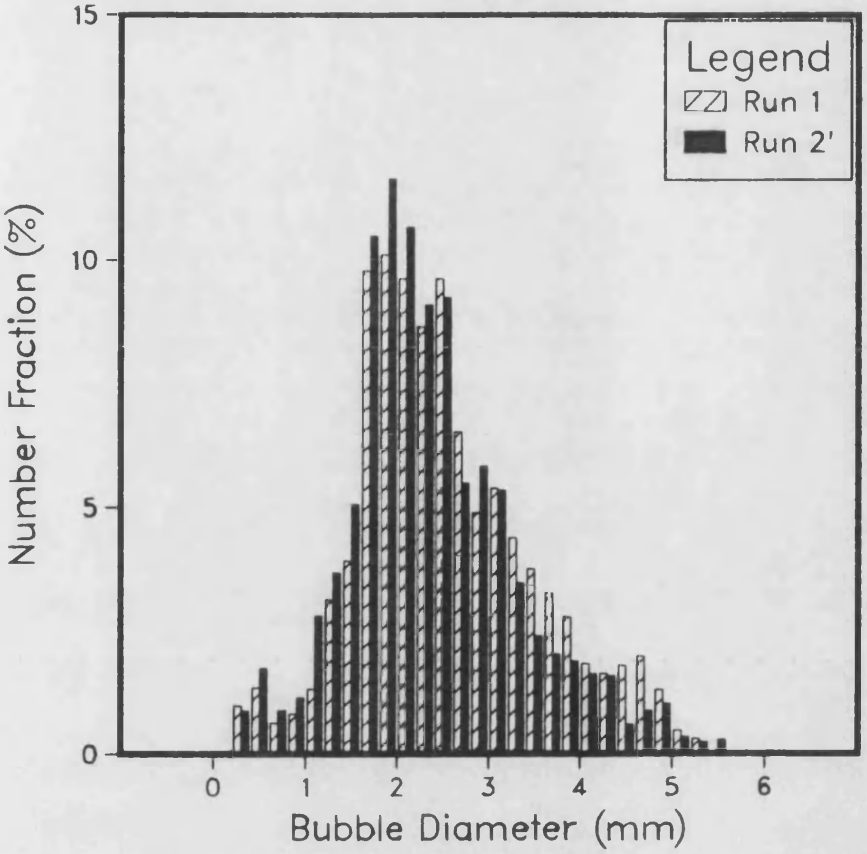

Run I	Run 2'
η_b=614	η_b=614
d_{32}=3.26	d_{32}=3.07mm
d_{IO}=2.54	d_{IO}=2.36mm
C_v=0.398	C_v=0.4IO

Fig58(b) Reproducibility of Measurements
(runs taken 3 days apart)

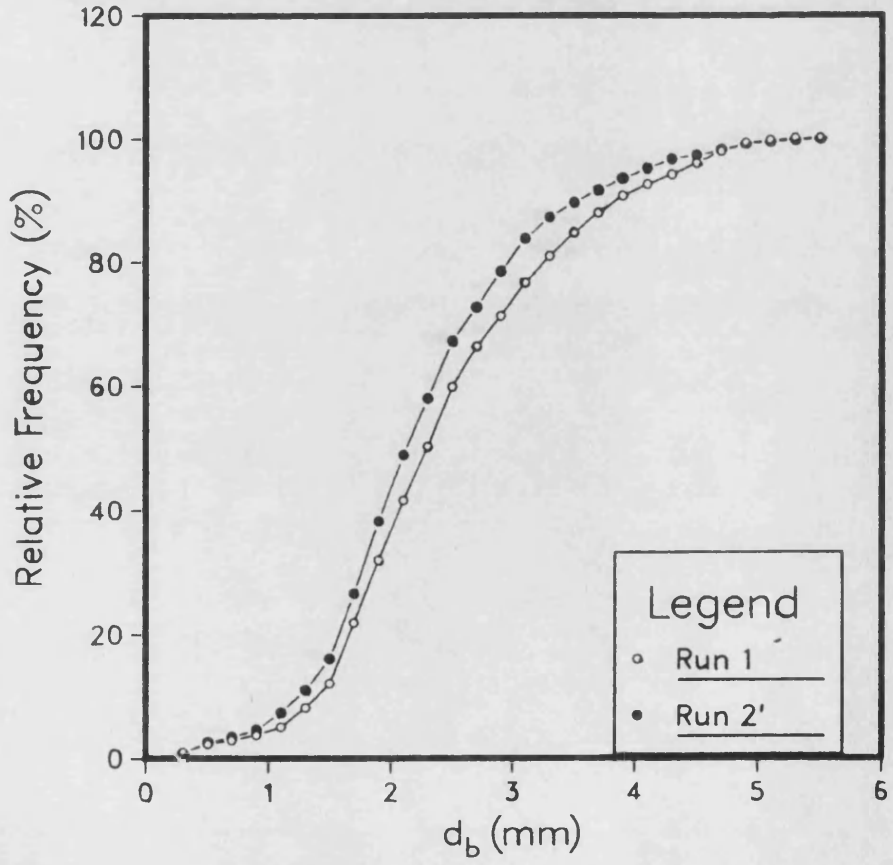

5.5.3 Bubble size in mid-plane between two baffles

Measurements in the mid-plane between two adjacent baffles were carried out at 22 locations, as shown in Fig 5.9. The spatial distributions of the point Sauter mean bubble diameter are given in Fig 5.10. For the purpose of discussion, the grid can be divided into three main regions. These are the bulk of the tank above the impeller, the impeller zone and the region below it.

5.5.3.1 Variation of Sauter mean bubble diameter

(i) Impeller region

The smallest bubble size in the reactor is found in the impeller region and, in particular, at the position closest to the impeller tip. This is due to the high level of turbulence generated in this zone, which causes high rates of bubble breakage. The effect of agitator speed is to reduce the bubble size at this location under all conditions. At other positions in the same plane, the bubble size is considerably higher, indicating that high rates of bubble coalescence occur in the impeller discharge stream. The effect of N on the local bubble size is complicated and there is no systematic trend. This is characteristic of a non-homogeneous turbulence field in this zone. The effect of N on the overall mean bubble size is represented in Fig 5.11. At the lowest gas rate, the result of increasing the speed is a sharp fall in the overall Sauter diameter. As Q increases, the slope of this trend reduces until, at the highest gas load used, the overall effect of N becomes negligible. From this behaviour it appears that, whereas at low values of Q bubble breakage is chiefly responsible for determining the mean bubble size, bubble coalescence becomes increasingly important as Q increases, due to the higher bubble density. At constant speed (N=180 rpm), the outcome of increasing the gas flow

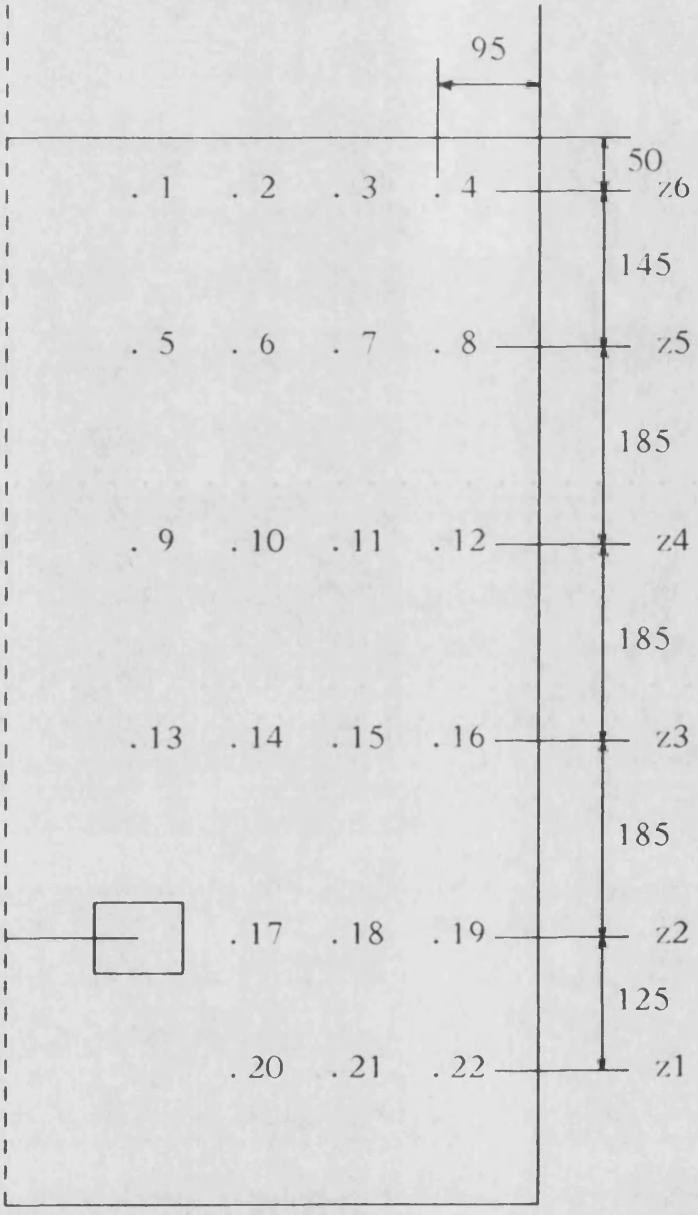

Fig 5.9 Measurement positions in mid-plane between two baffles (Dimensions in mm).

Fig 5.10 Spatial distributions of Sauter bubble diameter in air-water (mm).

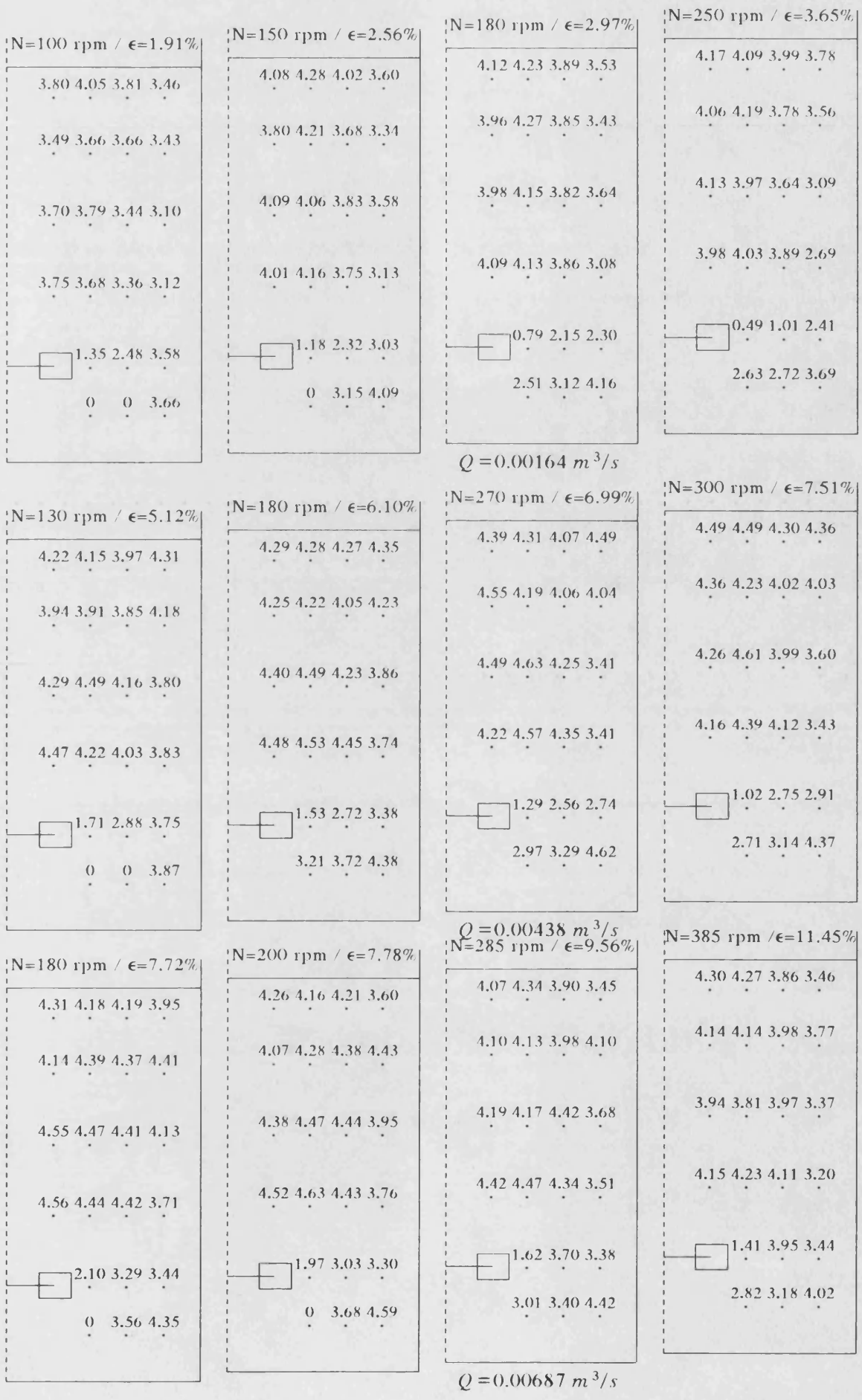

Fig5·11 Effect of N and Q on Bubble Size in Impeller Region

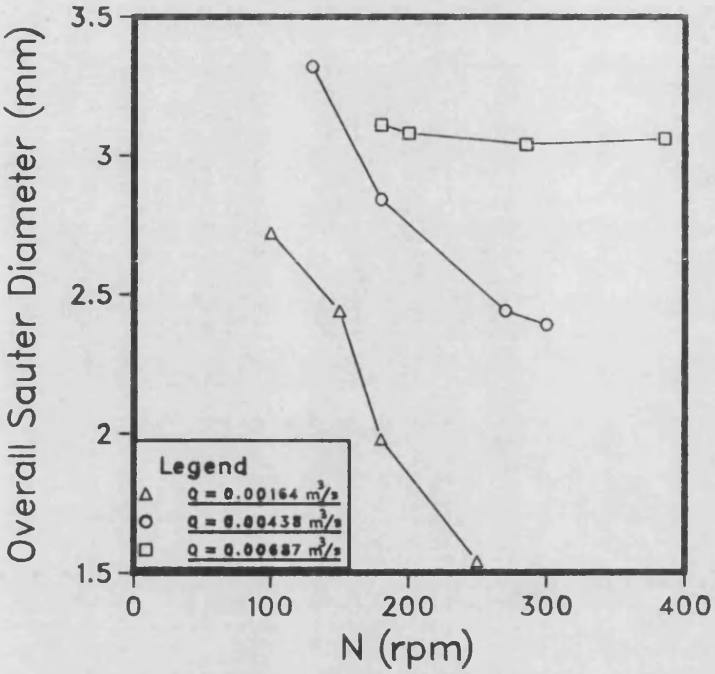

Fig5·12 Effect of N and Q on Bubble Size in Region Below Impeller

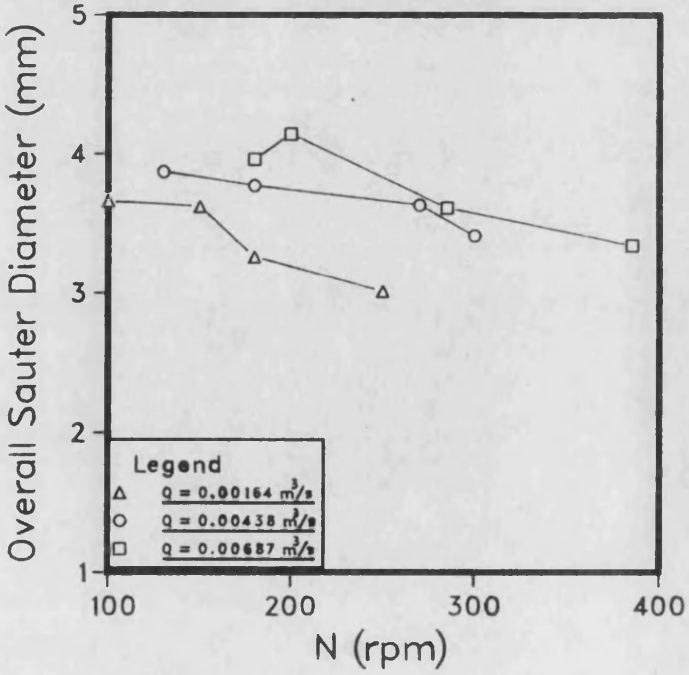

rate is to increase the bubble size. This is a consequence of two major factors. Firstly, an increase in Q reduces the level of turbulence in the agitated fluid, by reducing the mechanical power dissipation through the growth of the gas cavities behind the turbine blades, and also by dampening the velocity fluctuations in the fluid. The micro-scale structure of the turbulence field is, thus, affected in such a way that the turbulent energy acting to disrupt the bubbles is weakened. Secondly, the bubble density increases because of the greater gas holdup, and this leads to higher rates of bubble collision and coalescence.

At 180 rpm the increase in overall Sauter diameter, $\bar{d}_{32}$, to the increase in Q is three times greater between the lowest and medium values of Q than between the medium and highest values. This is understandable when one considers the corresponding changes occurring in the gas cavity structure. When Q is first raised from the lowest rate to the medium rate, the gas cavity configuration (see Chapter 8), alters from six vortex cavities to six large cavities, causing a 41% decrease in total gassed power, P_{gt}. This represents a dramatic change in the hydrodynamic field around the impeller, resulting in a significant change in the bubble size. Increasing the gas input to the highest rate does not alter the shape of the gas cavities, but it does cause a slight increase in size (Chapter 8). This results in a 5% drop in total power, which is not sufficient to significantly affect the bubble size.

The bubble size in the impeller discharge stream is studied in more detail in Section 5.5.6 below. Here, the region is explored using a much finer measurement grid.

(ii) Region below impeller

In the region below the impeller, the central zone is void of bubbles at low agitation speeds. These flow conditions correspond to the start of circulation in the lower part of the vessel, but the circulation loop is not complete. However, as the agitator speed is increased, the lower liquid circulation loop enlarges causing more gas to be dispersed in this area. The bubble size is quite large compared with that in the impeller plane, due to weaker turbulence. Consequently, the principal factor determining bubble size in this region seems to be coalescence. In the radial direction, the bubble diameter rises towards the tank wall because, as will be seen in Chapter 6, of the increasing bubble density and gas holdup, which promote bubble collision and coalescence. The effect of impeller speed and gas flow rate can be deduced from Fig 5.12. Increasing N has only a small reducing effect on the mean bubble size, which seems to diminish even more at higher gas rates. Similar to the impeller plane, the result of increasing Q at constant speed (N=180 rpm), is a 16% increase in $\bar{d}_{32}$ between the lowest and the medium gas loads, but only a 5% increase between the medium and the highest gas rates employed.

(iii) Bulk region

The effect of agitator speed on the overall Sauter diameter for the bulk section of the tank was found to be insignificant. This is in agreement with the findings of Figueiredo [38]. It appears, therefore, that in this region the effect of increased turbulence through enhanced stirring is balanced by an increase in bubble coalescence due to the rise in gas holdup. This leads to a dynamic equilibrium in this region of the dispersion. Increasing Q (N=180 rpm) causes an increase of 9.8% in $\bar{d}_{32}$ from the lowest to the intermediate gas rate. This condition, as mentioned above, corresponds to 41% reduction in power and a doubling

of the overall gas holdup. Increasing Q to the highest value introduces no appreciable change in $\bar{d}_{32}$. Only a slight drop in power (5%) was registered in this case with ϵ rising by only 27%.

In the central core region of the bulk no large variations in the Sauter diameter values with spatial position are observed. However, appreciable differences do exist in most cases between the values at positions in the segment near to the tank wall and those in the segment near the shaft. Those near the shaft are generally significantly higher. The difference is more pronounced at lower positions in the bulk. For instance, at $Q = 1.64 \times 10^{-3}\, m^3/s$ and N=250 rpm, the difference in Sauter diameter is 10-14-34-48%, respectively, for successive planes in the downwards direction. The segment near the wall corresponds to the upward flowing section of the circulation loop whereas the segment near the shaft represents its downward flowing branch. As will be seen in Chapter 6, the gas holdup in the latter region is substantially higher than in the former, implying more coalescence, whence the difference in the bubble sizes. The maximum range of variation of d_{32} with position in the bulk section of the reactor widens with speed for a given value of Q, and above full gas dispersion is generally greater than 30%. On the other hand, considering the distributions of the bubble number mean diameter (d_{10}), the range of variation was found to be within 50 to 100%. The degree of variation with position can be measured by a coefficient of variation (Equation 5.4) for the spatial distribution of diameter values. The coefficient values computed for the distributions of d_{10} were found to be approximately twice those for the distributions of d_{32}. This discrepancy stems from the mathematical definition of these two diameters, and their respective ability to represent a given bubble size distribution. d_{32} is a very useful parameter and is used because it is directly related to the interfacial area and the gas holdup ($a = 6\epsilon/d_{32}$).

However, it does not reveal all of the information about the bubble size distribution. In order to acquire a detailed and complete picture of the internal structure of the gas-liquid dispersion, in addition to the mean bubble parameters usually used, the actual local bubble size distributions should also be considered. This has important implications for the calculation of mass transfer rates. As already explained in Section 2.2.1, when using the chemical method to measure the global gas-liquid interfacial area, its value is usually calculated using the measured overall absorption rate together with the assumption that the mean driving force is effective over all bubbles. In actual fact, small bubbles may exhibit zero driving force in situations of high mass transfer rates and long residence times, thus leading to large underestimation of a. There is an increasing realisation therefore, that the mass transfer rate should be integrated over all bubble sizes in the distribution, and not simply calculated from a mean bubble diameter (eg. $\bar{d}_{32}$) [25, 27]. Consequently, the actual bubble size distributions are of great importance.

5.5.3.2 Local bubble size distributions

(i) Effect of impeller speed

The histograms in Figs 5.13 and 5.14 represent the spherical bubble diameter distributions derived from the samples collected at the measurement positions of Fig 5.9, at two different agitation speeds. Wide differences exist between the distributions from one region to an other throughout the tank. At N=100 rpm, the distributions near the impeller exhibit positive skewness and are positioned at the left hand of the bubble spectrum. The shift towards larger bubbles increases with radial distance, a sign that coalescence of the small bubbles generated by the impeller is taking place as they move away from the high shear region

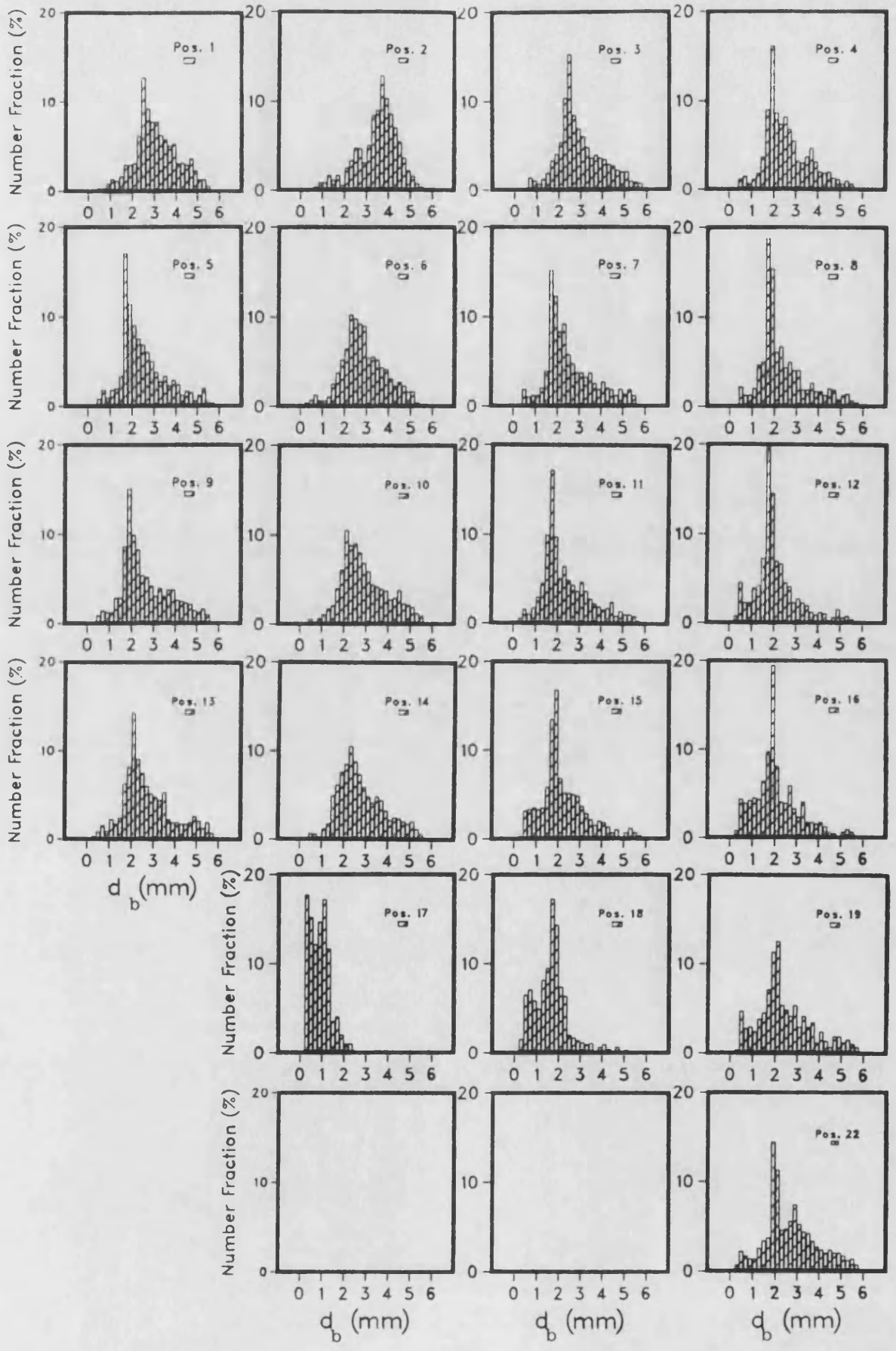

Fig 5.I3 Local bubble size distributions (Air-Water)
N=I00 rpm, Q=0.00I64 m^3/s, ϵ=I.9I%.
Mid-plane

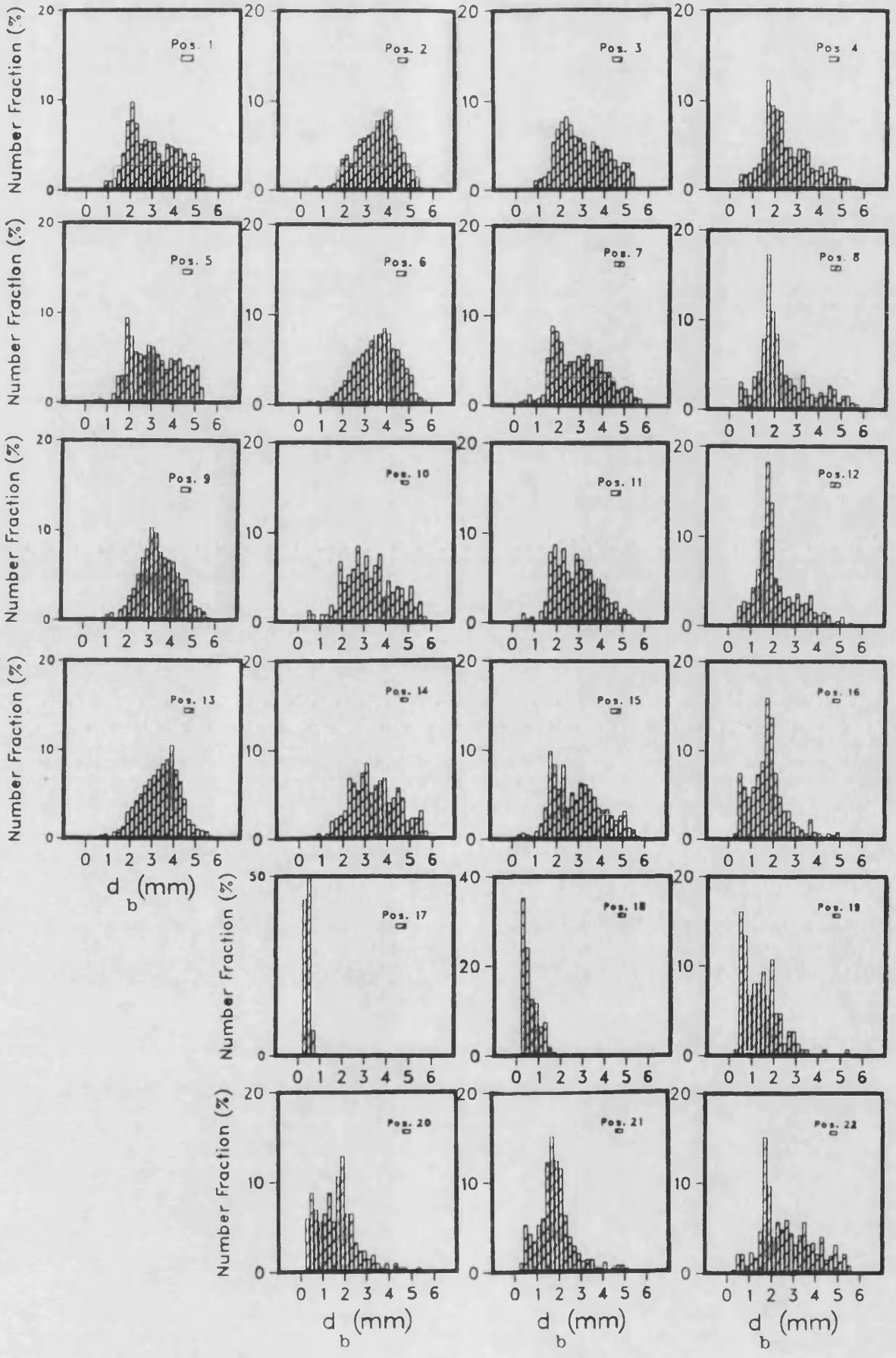

Fig 5.I4 Local bubble size distributions (Air-water)
N=250 rpm, Q=0.00I64 m^3/s, ϵ=3.65%.
Mid-plane

near the blades towards the wall of the tank. Decreasing turbulence in the same direction [143] also leads to less bubble breakage. At the higher speed of 250 rpm, the shift in the distributions towards the lower end of the spectrum is much more pronounced. At the two positions near the agitator most of the bubbles are less than 0.5 mm. Takahashi et al [21] used photography to measure bubble sizes, at extremely low gas input rates (0.0025-0.01 vvm) and very low power inputs ($0.05-0.16 KW/m^3$), around the surface of the vortex gas cavity of a Rushton turbine in a 0.61 m vessel. They obtained distributions of similar shape to the present ones. Kawecki at al [148] who estimated photographically the bubble size distribution by means of a small square column connected to the tank at the impeller level, reported distributions which were much more symmetrical in form. This shows that their distributions were affected by appreciable coalescence of the bubbles whilst residing in the connecting channel.

Below the impeller the distributions are positively skewed, but at the location near the wall where coalescence is believed to be important, the histograms are much more symmetrical. Under all conditions, the effect of increasing N was found to consist in a shift of the distributions at the inner positions to smaller diameters. Near the wall, there is first an increase in the mean (d_{10}), but at high speeds (250 rpm), as the liquid circulation becomes more intense, this effect is reversed. However, the distribution retains a similar shape.

At 100 rpm, the distributions in the bulk of the tank are mainly positively skewed. The shape of the distributions is different from one region of the bulk to an other. At this flow condition, the tank is behaving almost like a bubble column where the bubbles are seen to rise through the liquid in vertical streams with little recirculation taking

place. Furthermore, since the gas holdup is low and there is little coalescence, the difference between the distributions is much more pronounced in the radial direction than in the vertical direction. Increasing N to 250 rpm, increases the symmetry of the distributions, thus producing slightly more uniformity in the local bubble size. However, in the segment close to the boundary of the reactor, their form remains largely unaffected, with an essentially constant mean and reduced peak value. The large difference in the form of these distributions with respect to those near the shaft is notable. The latter distributions contain greater proportions of large bubbles.

Clearly, most of the distributions in the tank deviate markedly from a standard normal distribution, especially those in the agitator region. Since they all vary with position and agitation conditions it is not practical to fit a separate theoretical distribution to each one of them.

(ii) Effect of gas flow rate

The effect of increasing the gas flow rate at constant gassed power dissipation, on the local bubble size distributions can be deduced from the histograms in Figs 5.15 and 5.14. The total specific gassed power in both cases is 2.00 KW/m^3.

In the impeller region, the positive skewness of the distributions is significantly increased. The peak value is also considerably reduced, particularly at the two positions closest to the agitator, leading to a greater number fraction of large bubbles. This signifies bubble coalescence taking place in the impeller stream due to higher gas holdup (see also Chapter 6). The presence of increased amounts of gas phase can, as mentioned in Section 5.5.3.1(i) above, act to dampen the turbulence intensity in this zone. Both the macro-scale and the micro-scale eddies

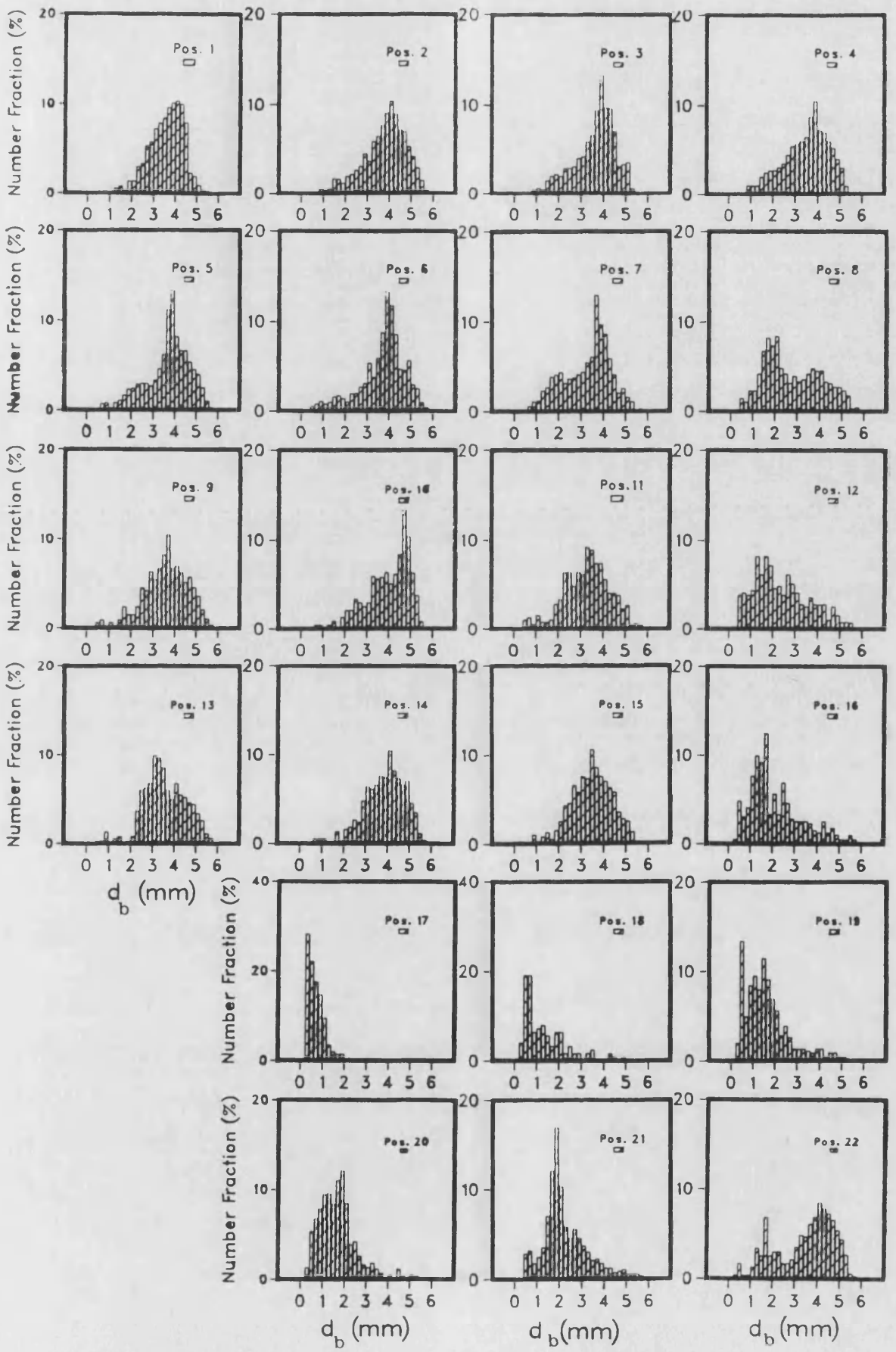

Fig 5.I5 Local bubble size distributions (Air-water)
N=300 rpm, Q=0.00438 m^3/s, ϵ=7.5I%.
Mid-plane

are affected. However, it is the small eddies which are effective in breaking the bubbles whereas the large eddies are only responsible for their physical transport and distribution. Notably, also, is the difference between the gas cavity structure behind the agitator blades. At the lower gas rate, the cavities are of a vortex nature, whereas at the higher gas rate they are of the clinging type (Chapter 8). The bubbles generated by the latter are likely to be larger.

Below the impeller level, a large difference in the distributions occurs only at the position near the wall, where its shape becomes bimodal. The other distributions remain largely unaffected.

The distributions near the wall in the bulk of the reactor are subjected to appreciable flattening and a greater spread towards the higher end of the spectrum. At other positions, the symmetry of the histograms is reduced as most are shifted to the right owing to the greater proportion of large bubbles arising from coalescence.

5.5.4 Bubble size in baffle plane

In the few studies that exist on the internal structure of the gas-liquid dispersion in agitated reactors, efforts have always been concentrated on the r (radial) and the z (vertical) directions. The θ (angular) coordinate is not usually considered. It was thought, here, worthwhile to investigate the bubble size in a different plane from the 45° plane thus far explored. The baffle plane (0°) was considered to be an interesting section of the reactor. Measurements in this plane were made at the same locations as for the mid-plane, except the six positions near the wall which coincided with the baffle plate. This was done for one gas rate and 3 impeller speeds. The matrix of the d_{32} values obtained is exhibited in Fig 5.16.

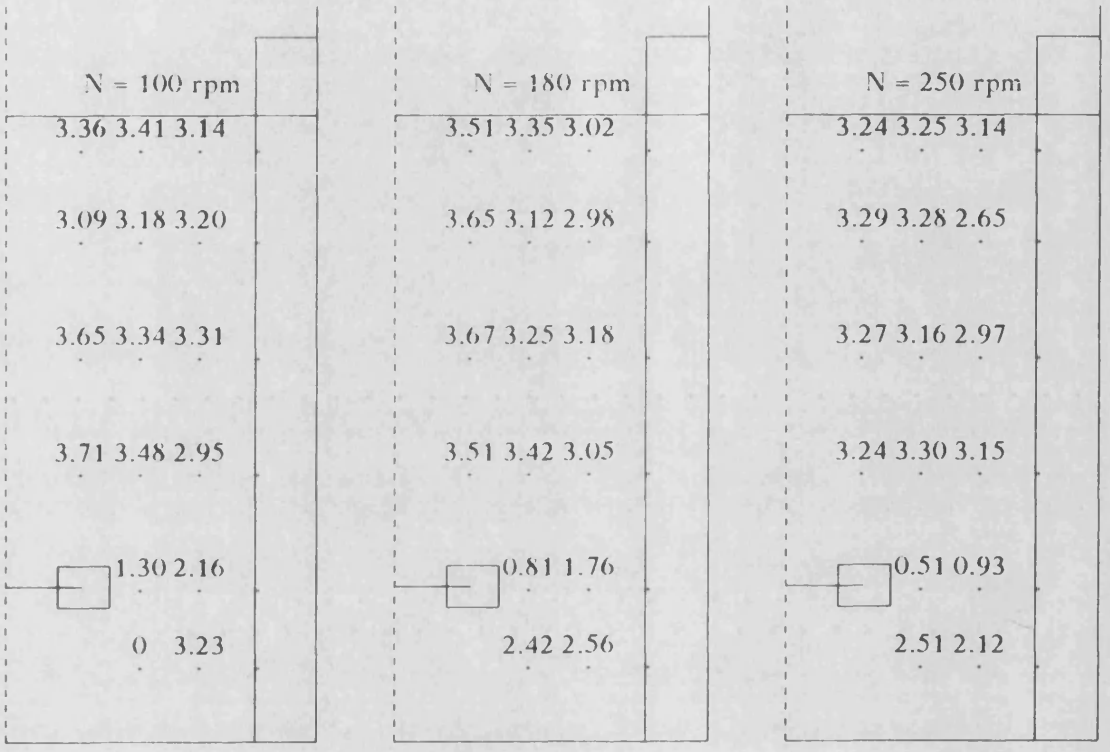

Fig 5.16 Spatial distributions of Sauter bubble diameter in baffle plane (mm).

($Q = 1.64\times10^{-3}\ m^3/s$)

The effect of stirrer speed in the bulk region of the baffle plane is negligible. The intensification of turbulence caused by increase in power dissipation, which favours bubble breakage, is balanced by a simultaneous increase in bubble coalescence due to increase in gas holdup. Below the impeller, the reduction in $\bar{d}_{32}$ values is more important, but the greatest effect occurs in the impeller plane, 25% and 44% successively from the lowest to the highest speeds.

Comparing this matrix of bubble diameters with those corresponding to the same points in the mid-plane (Fig 5.10), shows that, overall, a finer dispersion exists in the baffle plane. In the upper part of the tank, the discrepancy in the overall Sauter diameter for this section of the reactor with respect to the mid-plane, is significant and increases with the rotational speed, from 10% at 100 rpm to 21% at 250 rpm. This rising trend indicates that even larger differences may be expected at higher agitation speeds, or higher power inputs. At position 17 near the tip of the turbine blade, there is negligible difference between the mean bubble sizes in the two planes considered. At position 18 in the same plane, however, the bubble size in the baffle plane is appreciably lower. The region below the impeller also witnesses significant reduction in the mean bubble size.

Considering the two planes as a whole, the value of $\bar{d}_{32}$ in the baffle plane is smaller than the value in the mid-plane by 10 to 23% from the lowest to the highest speed employed. Assuming that the gas holdup is the same in the two planes, the interfacial area would be correspondingly higher in the baffle plane by 11 to 30%. It is also interesting to note that at the lowest speed, the inward circulation of gas from the wall has reached position 21 in this plane, whereas in the mid-plane, the gas is still confined to the zone near the wall. The baffles serve

to break the rotational vortex motion of the liquid and direct the flow in the tank more axially. Consequently, the circulation both in the upper part and the lower part of the contactor is expected to be more intense in the baffle region.

The local bubble size distributions in the baffle plane at 250 rpm are displayed in Fig 5.17. A comparison with the corresponding distributions in the mid-plane (Fig 5.14) reveals considerable difference in their forms. It is most pronounced in the bulk region of the dispersion. The baffles create a different and more intense turbulence flow field in this section, which affects the distribution of bubble size. By adding together all of the local distributions, overall distributions were constructed for the two planes and are compared in Fig 5.18. The number of large bubbles is smaller in the baffle plane, and correspondingly there are more small bubbles. This is made clearer in Fig 5.19, where the corresponding cumulative distributions are plotted. The baffle plane curve lies above the mid-plane curve by a substantial margin, demonstrating the extra fineness of the dispersion in the baffle plane.

5.5.5 Bubble size near a baffle

The bubble size was measured on both the windward and the leeward sides of a baffle at different liquid depths, as shown in Fig 5.20. The positions explored were along a vertical line 35 mm away from the baffle plate, in its middle plane.

The vertical variation of the point Sauter diameter on both sides of the baffle are exhibited in Fig 5.21. There, the bubble size varies considerably with liquid depth, the variations being more pronounced on the windward side of the baffle. This is expressed by the much higher

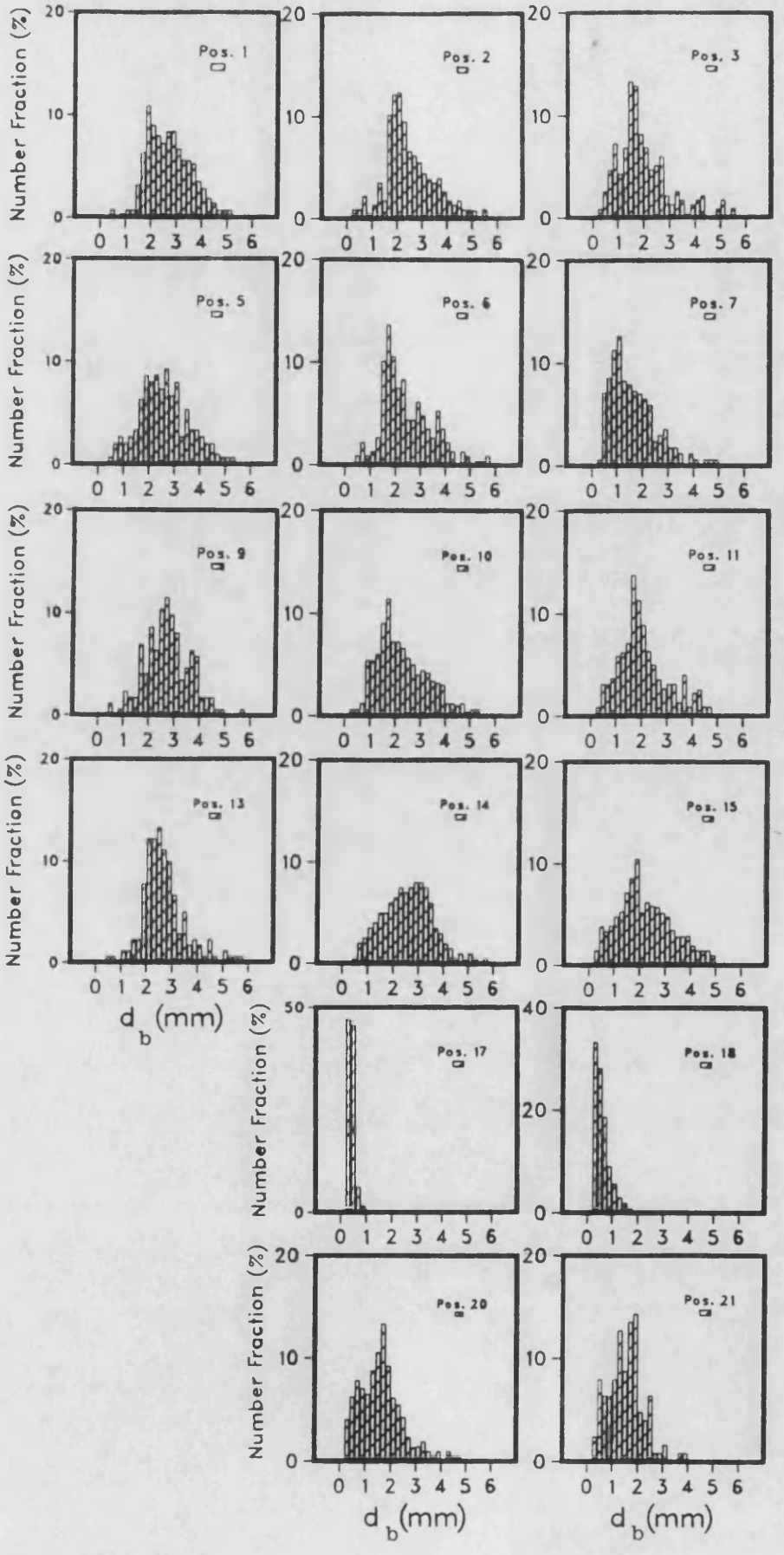

Fig 5.I7 Local bubble size distributions (Air-water)
N=250 rpm, Q=0.00164 m^3/s.
Baffle plane

Fig 5-18 Overall Bubble Size Distributions in Mid–Plane and Baffle Plane

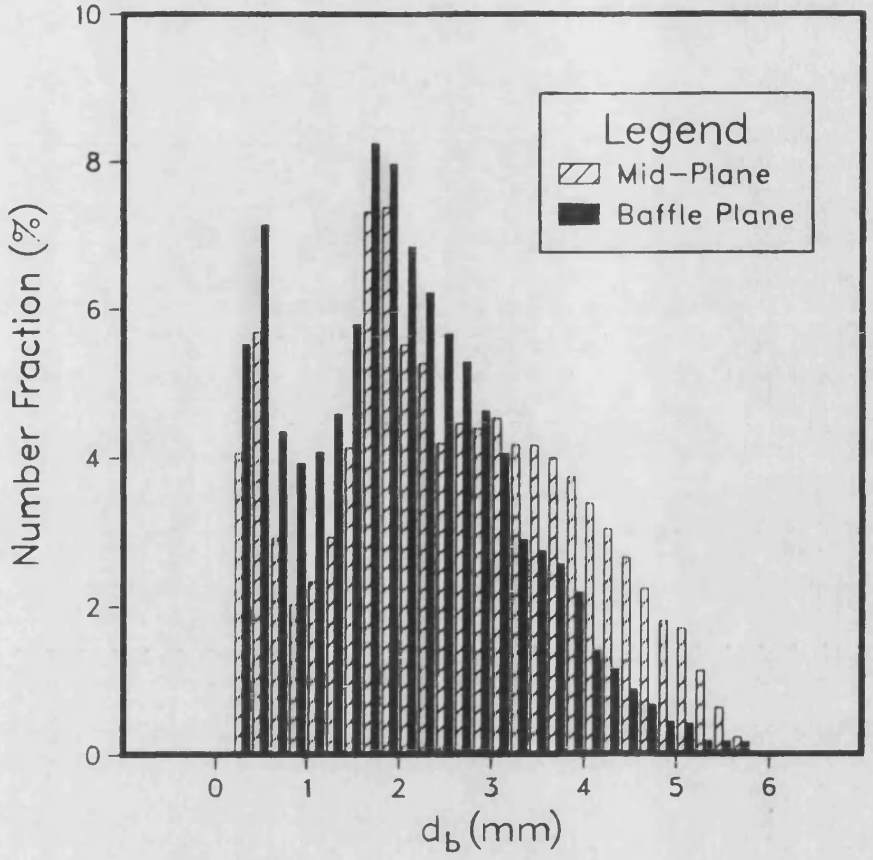

Fig5-19 Cumulative Frequency Distributions for Mid–Plane and Baffle Plane

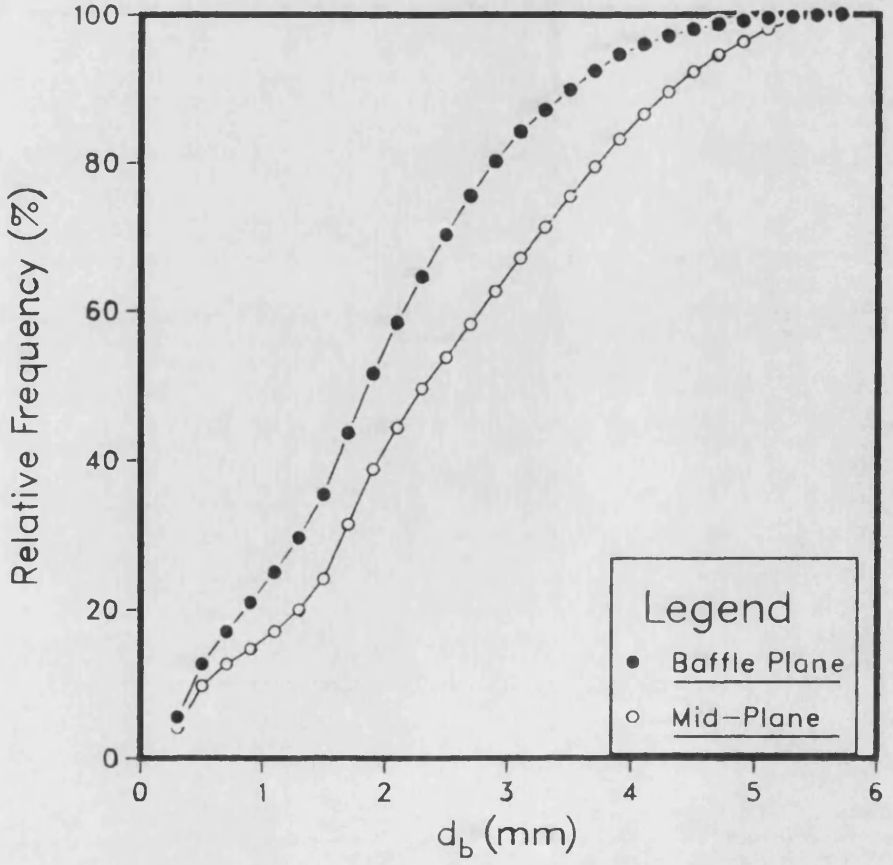

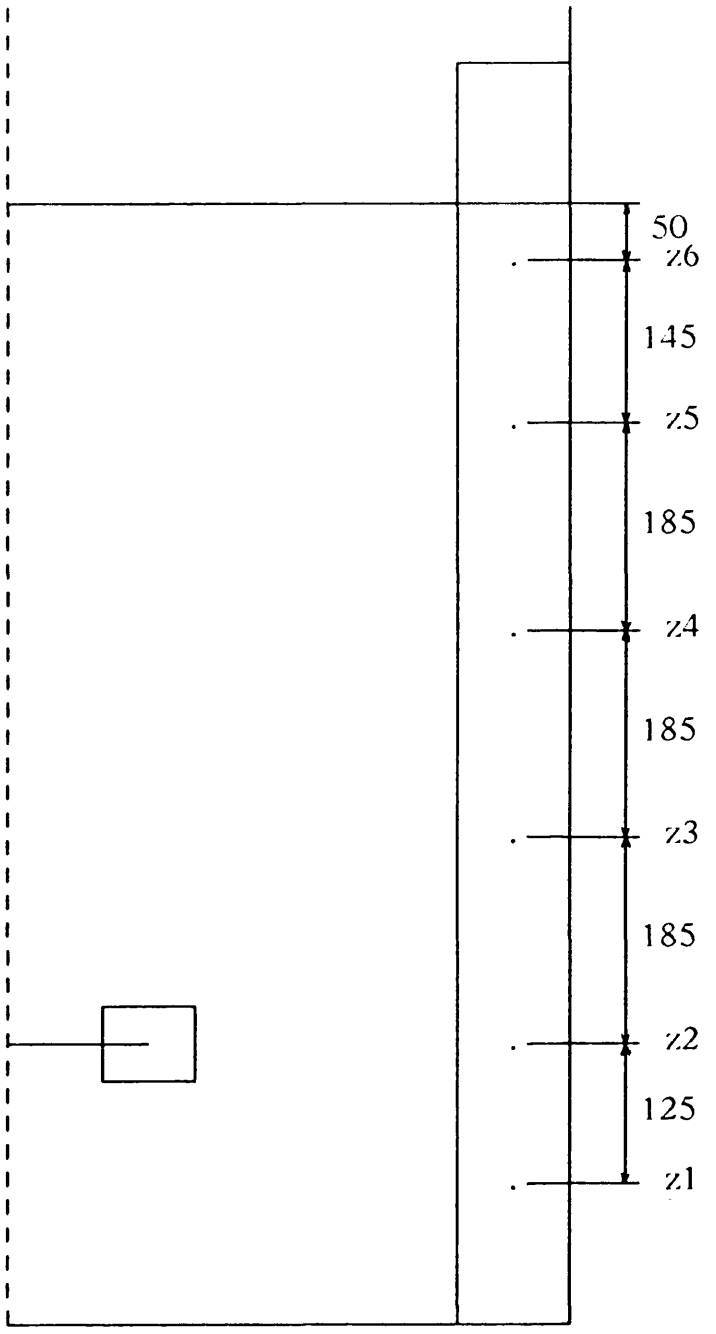

Fig 5.20 Measurement positions upstream and downstream of a baffle (Dimensions in mm).

Fig 5.21 Variation of Sauter Diameter Near a Baffle

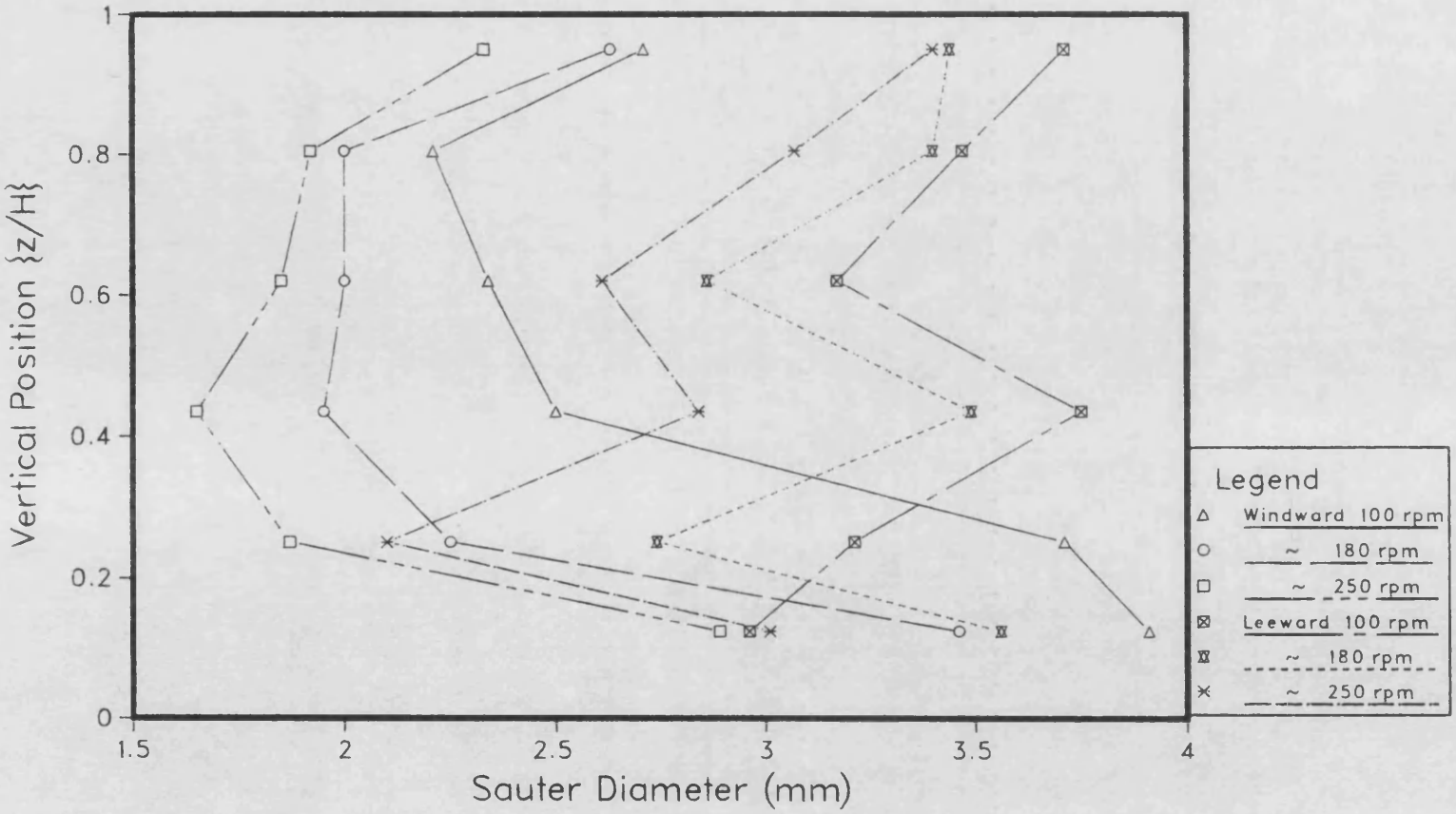

coefficients of variation, C_v, of the spatial distributions of the d_{32} values on the front side, as shown in Fig 5.22. The overall values of the Sauter diameter on each side of the baffle are plotted against the agitation speed in Fig 5.23, whence it can be concluded that, overall, increasing impeller speed leads to a significant reduction in the mean bubble size in the vicinity of the baffle. The general effect is, however, more pronounced on the windward side. The decrease in bubble diameter achieved on the leeward side, by increasing N from 100 to 180 rpm, is not significant. However, appreciable reduction takes place on the front side. An additional 39% increase in speed produces a sharper decline in the $\bar{d}_{32}$ trend behind the baffle, whereas a reduction in the slope is caused at the front. These effects are considered to be due to enhanced turbulence at the rear of the baffle and, in turn, more bubble breakage, and increased bubble density at the front, leading to more bubble coalescence. Thus, the two trends become approximately parallel indicating that further increases in agitation speed will produce similar reductions in $\bar{d}_{32}$, on either side of the baffle plate.

A pointwise examination (Fig 5.21) reveals that the most significant effect of increasing impeller speed occurs at points z1 and z3, which are near the impeller mid-plane position (z1), due to the stronger turbulent field in this region of the stirred tank.

Fig 5.22 demonstrates that, for a given speed, the spread of the distribution of the d_{32} values, as measured by C_v, is larger on the windward side. However, as N increases more dispersion takes place behind the baffle with more uniformity developing in the front zone. This results in the two regions converging towards a similar state of dispersion at high agitation speeds.

Fig 5.22 Coefficient of Variation vs Impeller Speed

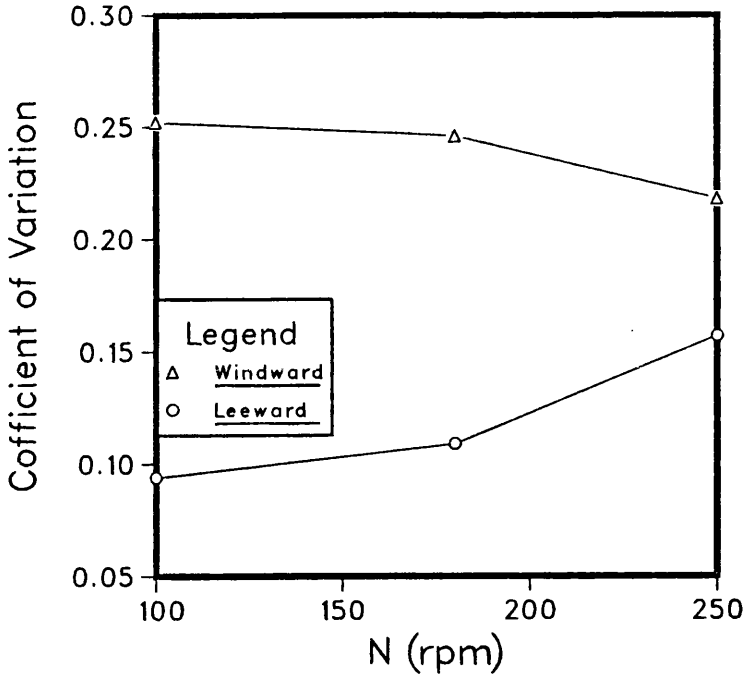

Fig 5.23 Overall Sauter Diameter vs Impeller Speed in Baffle Region

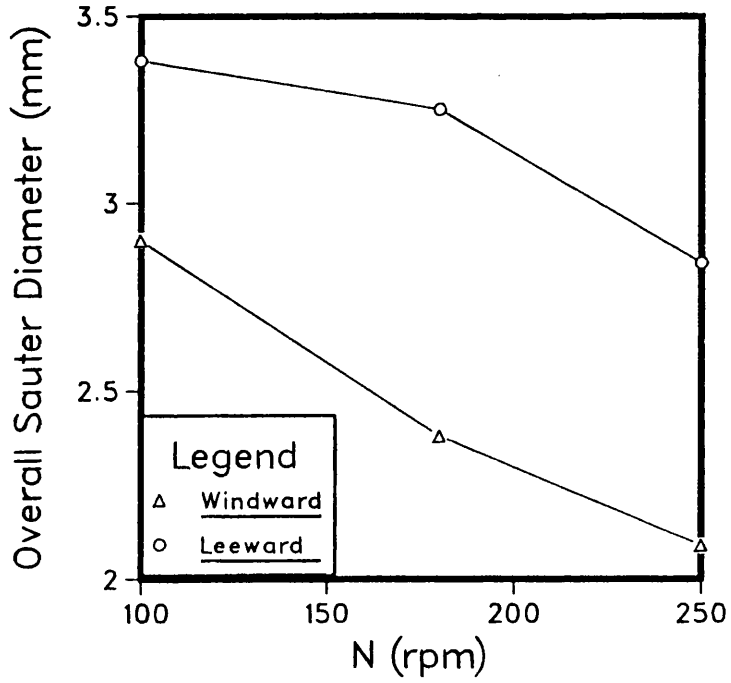

Considering the profiles in Fig 5.21, at virtually every point the bubble size at the front is significantly smaller than that at the corresponding location behind the baffle, the exception being at positions z1 below the impeller plane. For the two highest speeds the difference between the two bubble sizes is small, and for the lowest speed the bubble size is in fact lower at the back of the baffle. This is also true for position z2, in the impeller plane. The windward side of the baffle, which is directly opposed to the motion of the rotating liquid vortex, and which serves to break this vortex, is therefore a region of high turbulence. The turbulent eddies with their shearing action act to reduce the bubble size on the front-side of the baffle. The baffles, by opposing the tangential vortex, cause the flow to be directed more axially near the tank wall. Indeed, visual observation through the transparent wall of the tank showed that in the windward zone of the baffle, bubbles have markedly high rising velocities above the impeller plane and high downward velocities below it. On the other hand, the leeward side of the baffle is a relatively quiescent zone where the bubble velocities are fairly low even at high agitation speeds. Whereas near the impeller plane velocities appeared to be moderate, in the upper part of the vessel bubble rising velocities were so low that bubbles appeared to be almost in free suspension. This stagnation behind the baffles does not promote mixing, especially when dealing with highly viscous systems. This is the reason why industrial stirred reactors often have their baffle plates positioned a small distance away from the wall, in order to allow the fluid to circulate behind them and hence, enhance mixing in this region. On balance, coalescence at the rear of a baffle would, therefore, be expected to play a leading role over bubble breakage in determining the bubble sizes in this region, and hence, the mean bubble size is higher than that at the front side. The existence of significant coalescence on the leeward side

of the baffles, is supported by the photographic evidence presented by Valentin [142]. The exception at point z1 below the agitator plane, at the lowest speed of 100 rpm, can be explained in the following way. At this level of agitation, bubble recirculation in the lower half of the tank has just started. The bubble velocities are low in this region, and the bubble density on the leeward side of the baffle is considerably lower than that on the windward side. This latter phenomenon was observed visually and confirmed by the fact that it took a much longer time, to collect an equal size sample of bubbles in the rear region of the baffle. Consequently, the higher bubble density and moderately low velocities at this agitation speed, cause higher coalescence at position z1 on the front side, resulting in a larger bubble size.

5.5.6 Bubble size in turbine discharge stream

5.5.6.1 Mechanism of bubble generation by a turbine

In studying the mechanical gas-liquid dispersion process in a stirred tank, the impeller region is of major importance. Indeed, it is there that the bubble generation takes place, and that most of the mass transfer has been shown to occur [3, 93]. The investigations of Van't Riet and Smith [129], first shed light on the fundamental mechanism of bubble formation from the impeller. They reported a random closure of the cavity tips from which the bubbles are produced within a pair of trailing vortices. This put an end to the earlier assumed picture of the agitator pumping radially a mixture of gas and liquid. Photographs taken in this work (see Chapter 8), indicated that bubbles are dispersed from the irregularly shaped envelopes of the cavities, although most of the dispersion seemed to occur from the wakes of the liquid vortices shed outwards from the ends of the cavities. Similar observations have also been reported recently by Takahashi et al [21]. This process of bubble

generation makes the gas cavities act like a 'gas mixing reservoir' where old recirculated gas mixes with fresh gas sparged into the impeller. Bubbles detaching from the cavities are carried by the liquid flow through an intensely turbulent, radially discharged stream. They are subsequently distributed throughout the less fluctuating bulk of the tank by the circulating fluid, with some gas being vented at the surface.

5.5.6.2 Variation of Sauter mean bubble diameter

A fine quasi-point exploration of the turbine discharge stream was conducted in the mid-plane between two adjacent baffles. The area between the impeller tip and the tank wall was divided into a $30 \times 30\ mm^2$ network of squares, as depicted in Fig 5.24. The total number of measurement points was, thus, equal to 63. The measurement grid extended, vertically, 1.3 blade widths on either side of the horizontal edges of the turbine blades, and radially well inside the baffle region. The point Sauter diameter values obtained are displayed in Figs 5.25(a-c), for the conditions investigated.

The curves in Fig 5.26, represent the variation with height of the average Sauter diameter value for each horizontal plane in the measurement grid, at the three rotational speeds used. The profiles exhibit considerable variations with height, and a minimum at the agitator plane level. The curves are not symmetrical about the impeller plane since for equidistant sections the average $\bar{d}_{32}$ values below the impeller are always appreciably higher than those above it. Increasing the agitation speed causes the curves to shift towards lower values whilst preserving a similar shape. The most significant reduction in the average bubble size occurs at the impeller level.

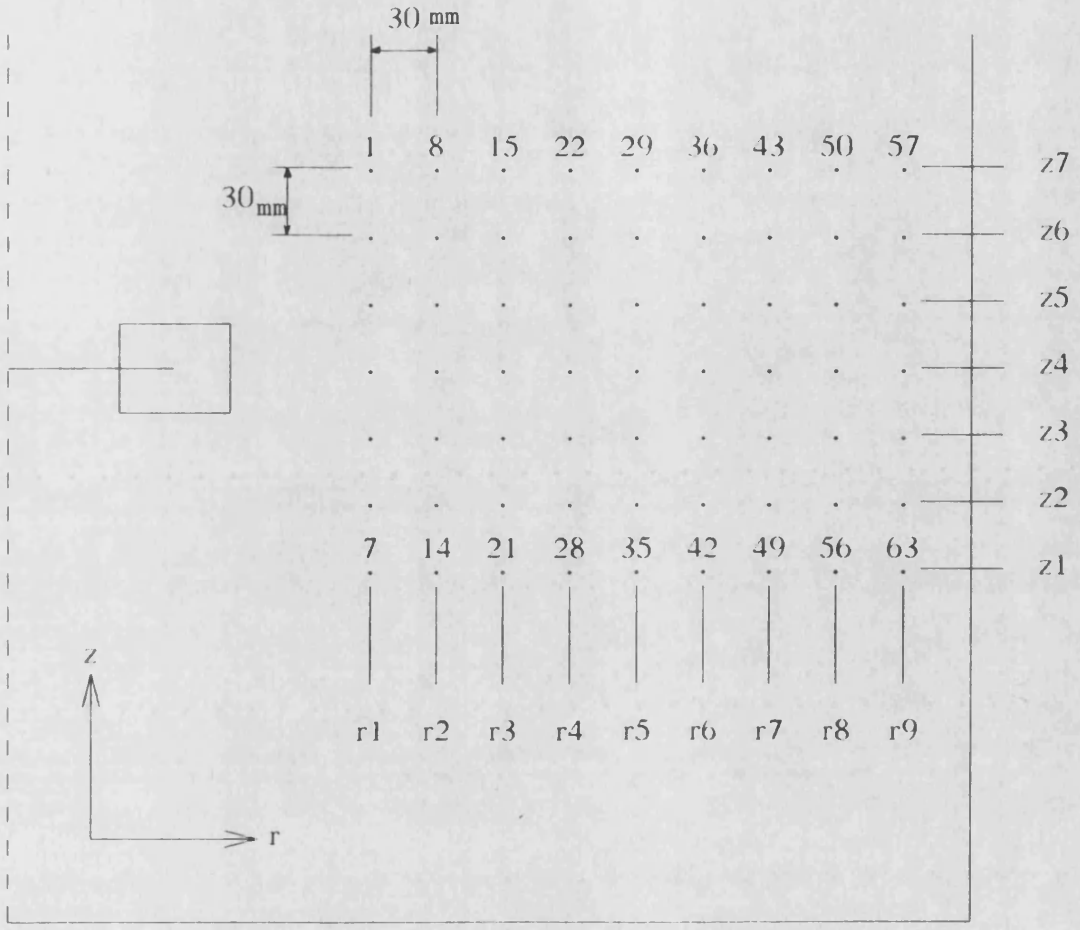

Fig 5.24 Measurement positions in impeller discharge stream.

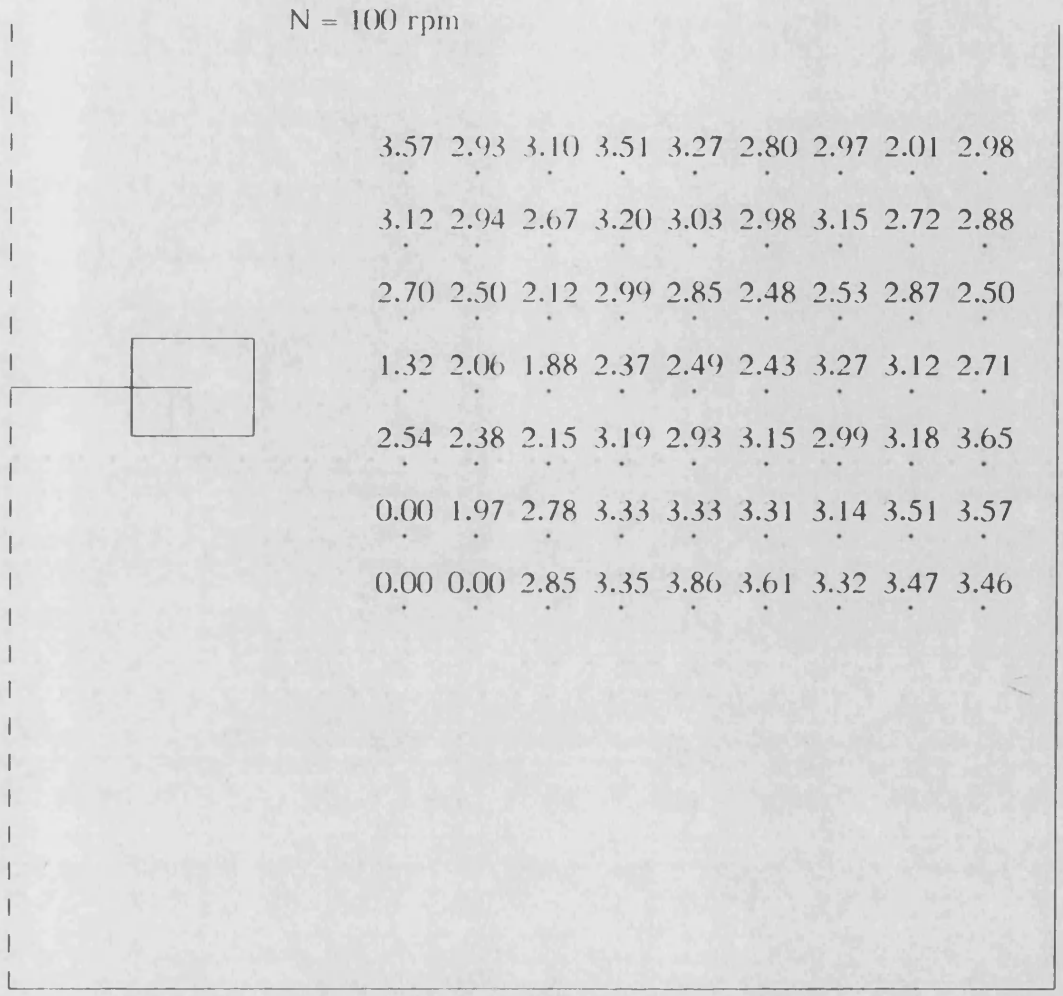

Fig 5.25 (a) Spatial distributions of Sauter bubble diameter in impeller discharge stream (air-water).

($Q = 1.64\times10^{-3}\ m^3/s$)

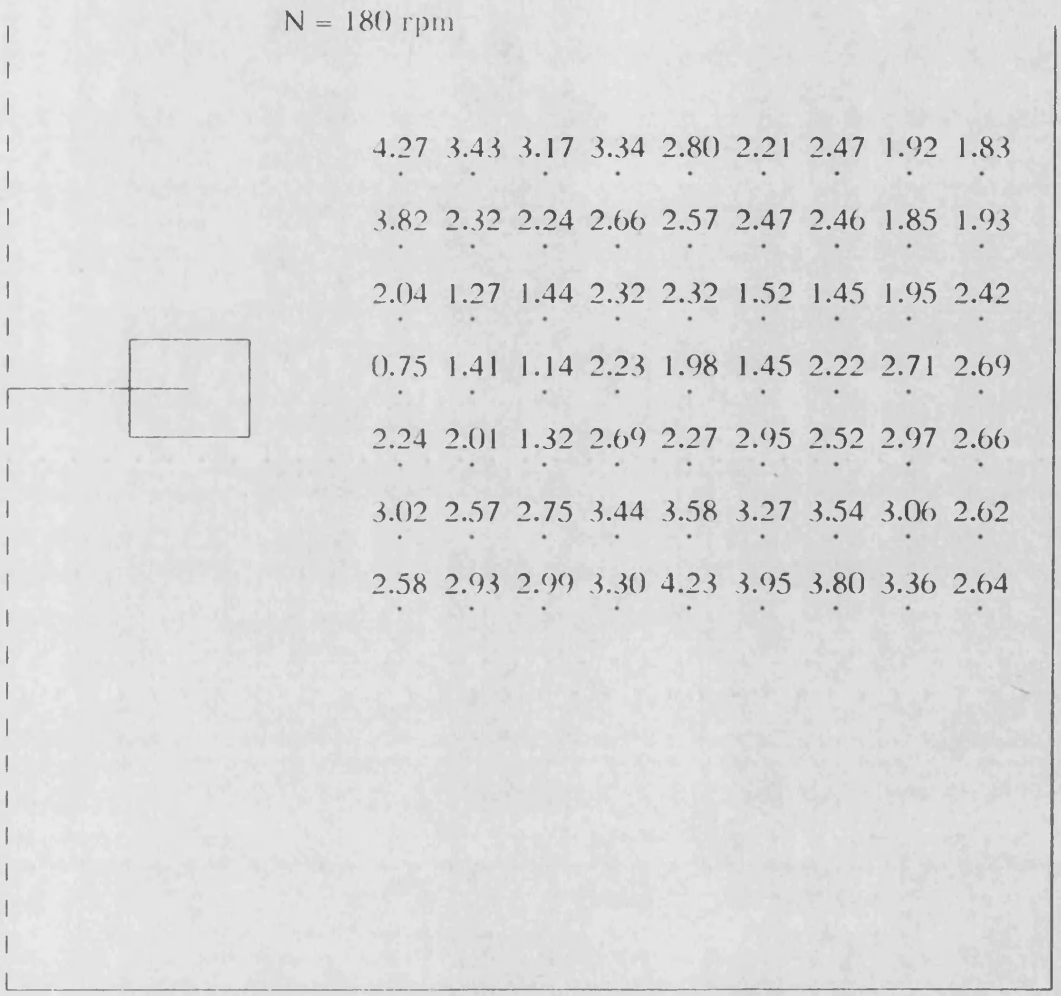

Fig 5.25 (b) Spatial distributions of Sauter bubble diameter in impeller discharge stream (air-water).

($Q = 1.64\times10^{-3}\ m^3/s$)

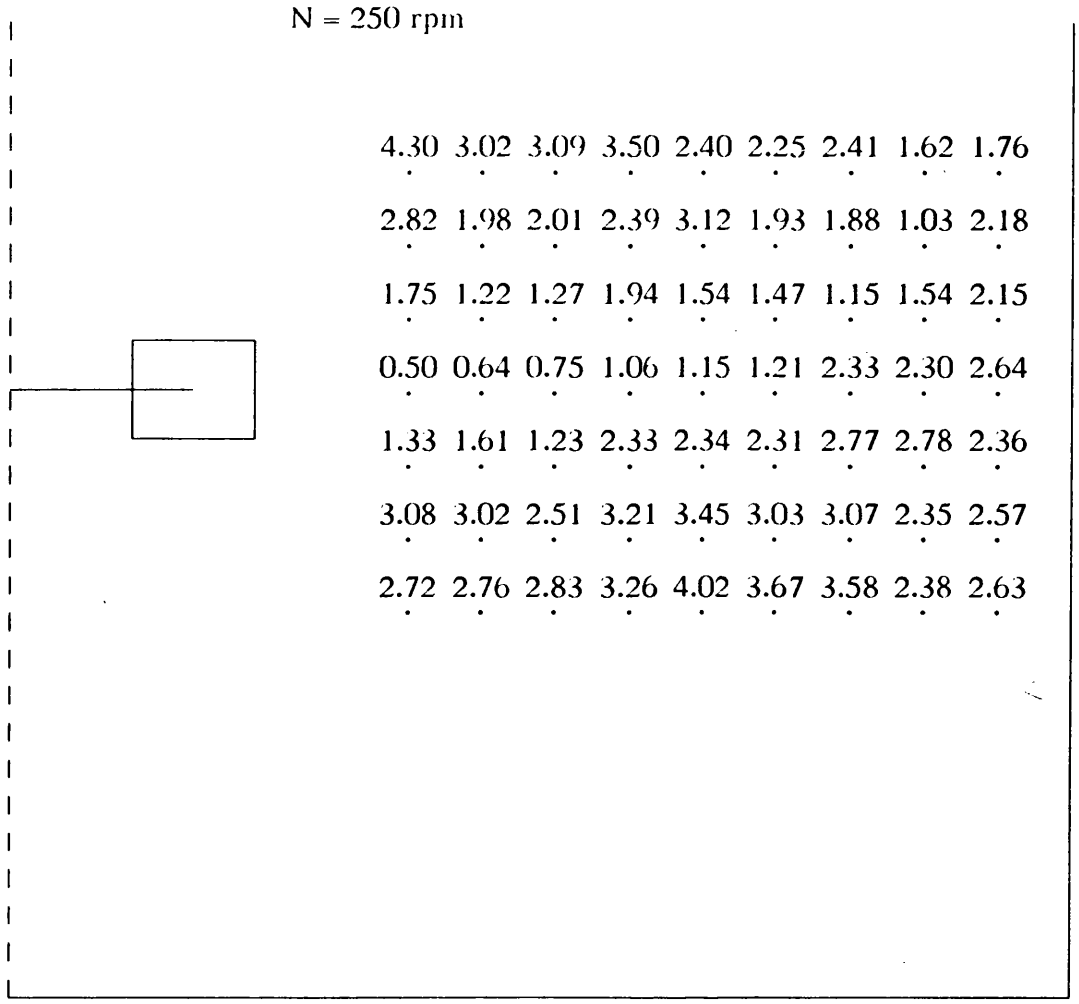

Fig 5.25 (c) Spatial distributions of Sauter bubble diameter in impeller discharge stream (air-water).

($Q = 1.64 \times 10^{-3}\ m^3/s$)

Fig5.26 Mean Sauter–Diameter Vertical Distributions

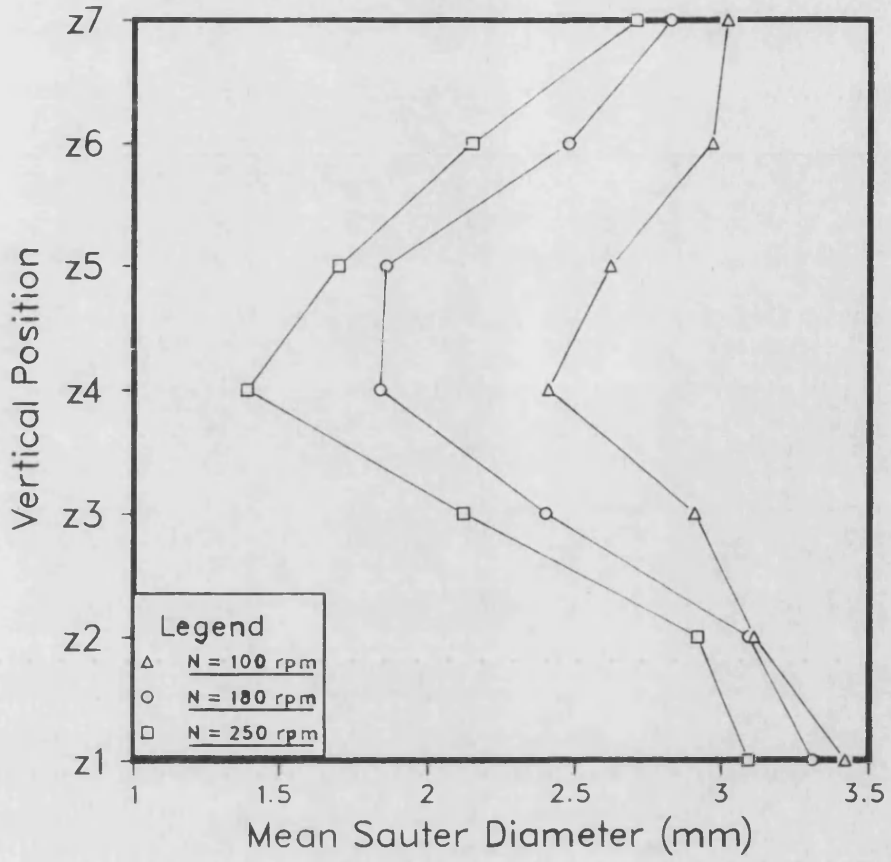

Fig5.27 Mean Sauter–Diameter Radial Distributions

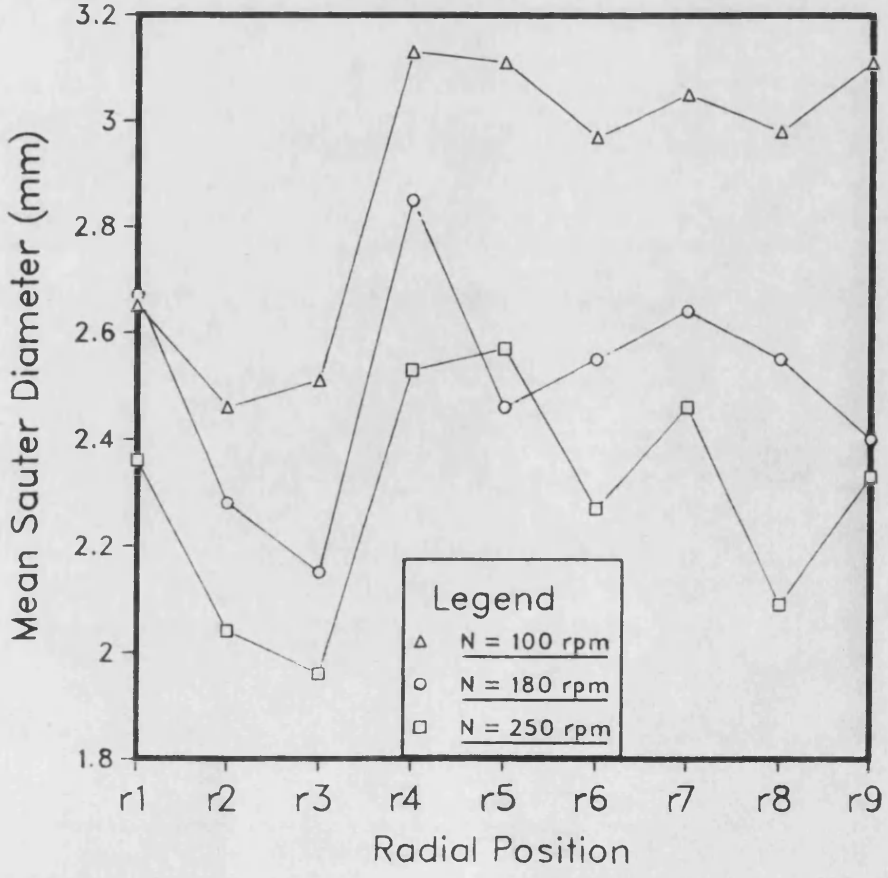

The variation of the average Sauter diameter for each vertical plane with radial position is depicted in Fig 5.27. The trends at the three different speeds are similar and lie one below the other in the order of increasing stirrer speed. The average $\bar{d}_{32}$ first decreases slightly with radial distance up to a point coinciding approximately with the central radius. Then it rises significantly and peaks at a radius which is almost exactly 2/3 the distance from the centre of the vessel to the wall. Beyond this position some fluctuations take place with a basically decreasing trend towards the tank wall.

In each radial section the amount of variation in the point bubble size with vertical position can be expressed in terms of a coefficient of variation C_v. This coefficient varies strongly with radial distance, as can be seen in Fig 5.28. For each speed, C_v exhibits a fluctuating dependence on r. However, the underlying trend represents a decrease in C_v with increasing r, which indicates that, overall, the amount of variation in the point d_{32} in each vertical section reduces with radial distance. In other words, vertical planes near the impeller have a higher spread in the spatial distribution of the local d_{32} values. This is emphasised for N=250 rpm. It is also worth noting that the C_v values increase, for a given radial plane, with stirrer speed ie., more dispersion takes place at higher agitation speeds, except at the position nearest to the wall where the speed effect is negligible.

Similarly, the extent of bubble size variation in each horizontal plane of the grid is represented by a C_v value. The trends obtained in Fig 5.29, demonstrate considerable variation with height. The profiles are very similar for the three agitation speeds used, and exhibit a maximum at the impeller plane. The effect of increasing N is mainly translated into a shift of the curves towards higher C_v values ie., enhanced spread in the

Fig5-28 Coefficient of Variation vs Radial Position

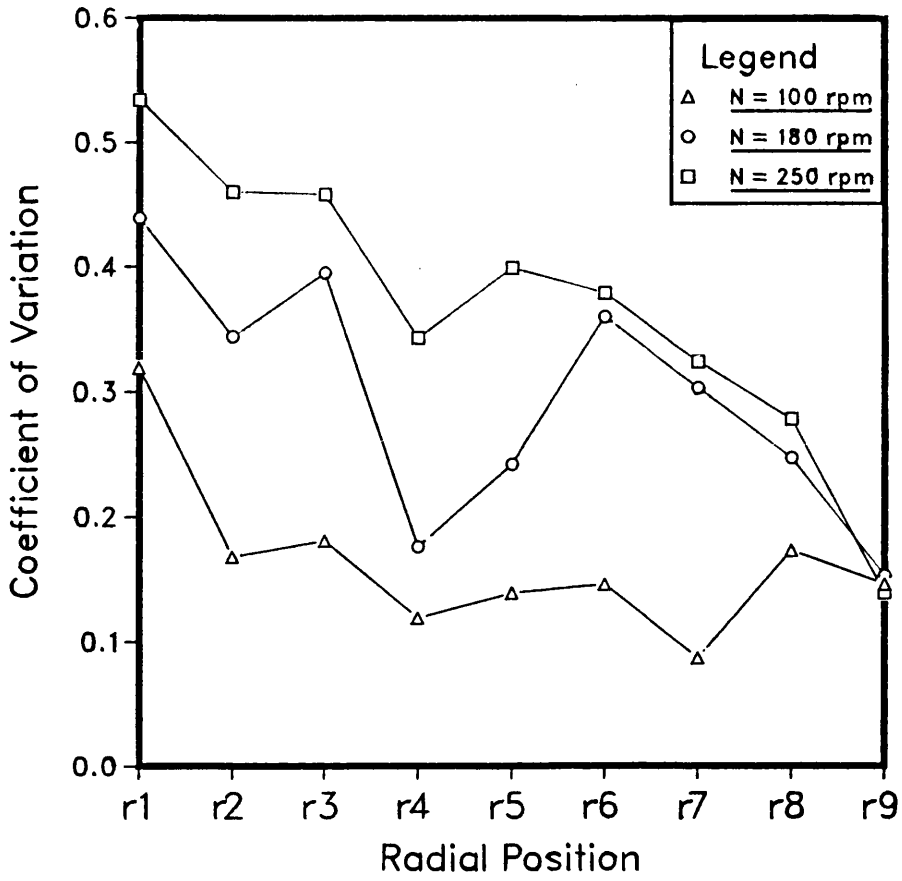

Fig5-29 Coefficient of Variation vs Vertical Position

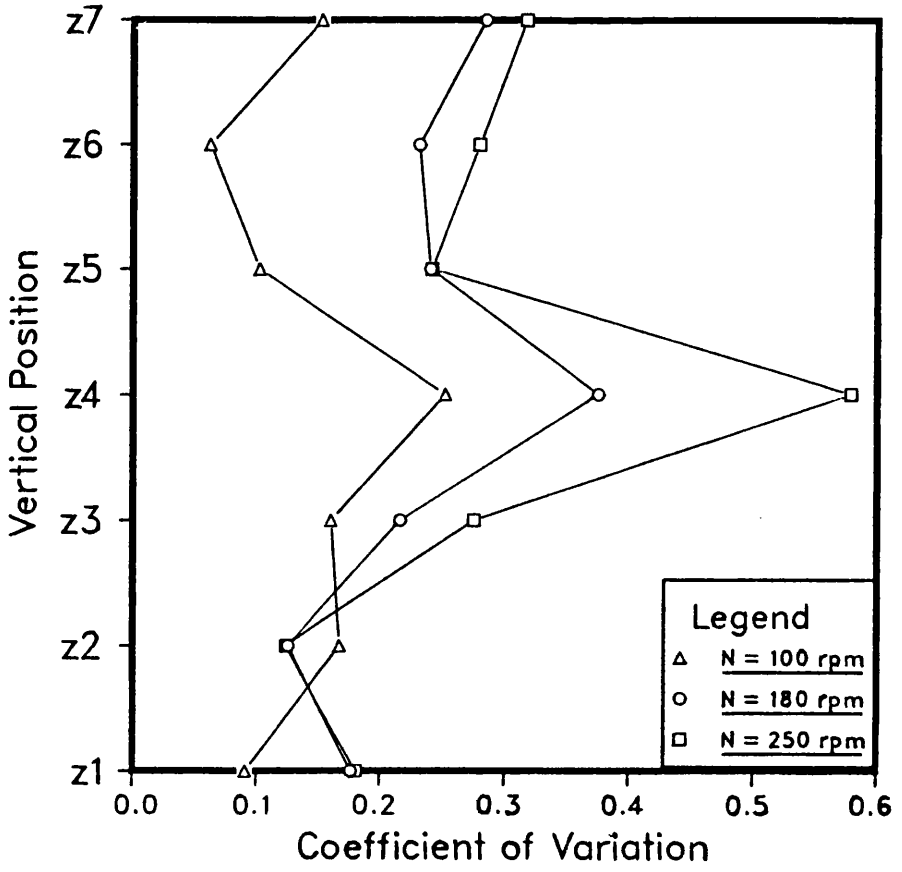

d_{32} distribution, with the maximum becoming sharper.

At positions 6, 7 and 14 no bubbles are detected at N=100 rpm, and only a few bubbles were detected at position 13. At this speed the flow near the impeller is mainly radial and tangential, and the axial liquid velocity component is too weak to push bubbles down below the agitator. Also at this stage the effect of flow inducement is important and, bubbles are swept away towards the wall. Further downstream, as the effect of the baffles progressively increases, the stream starts to diverge in the axial direction, and bubbles begin to circulate in the lower part of the vessel.

The spatial distribution of bubble sizes is highly non-uniform in the impeller stream. This is consistent with the fact that the turbulence in the agitator stream deviates greatly from homogeneity as found by Nishikawa et al [144], and by Harvey and Greaves [145, 146]. This non-uniformity in the spatial bubble size distribution, as measured by its overall coefficient of variation, increases considerably with speed. This is because of the increase in turbulence and gas holdup which, respectively, lead to higher rates of bubble breakage, bubble collision and coalescence. Considering radial and vertical distributions, the vertical distributions show higher variations than the radial distributions. Indeed, Van't Riet [136] observed strong variations of turbulence intensity with vertical distance in the impeller stream.

The vertical distributions are represented in Fig 5.30, for the conditions investigated. Considering the vertical plane r1, near the impeller tip, at all three speeds the curves exhibit similar trends, with the widest bubble size variation of all distributions in the stream. The minimum at the impeller level indicates that this is the most turbulent horizontal plane in the grid. Similar trends are observed at radii r2, r3

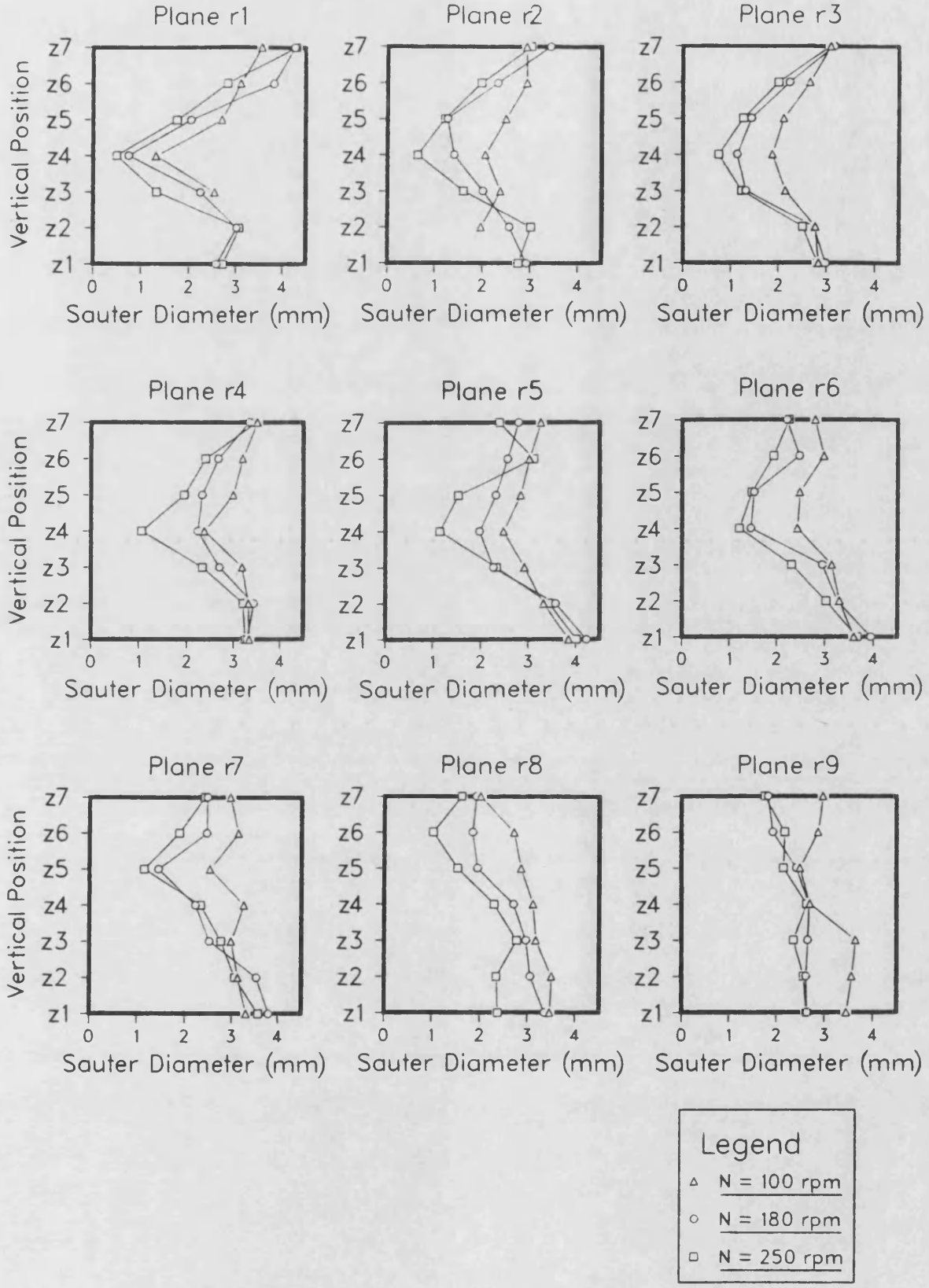

Fig 5.30 Vertical distributions of Sauter bubble diameter in impeller discharge stream
$Q=0.00164\ m^3/s$

and r4. Starting from r5, the distributions begin to exhibit fluctuations and become gradually flatter with increasing radius. These remarks are consistent with those of Bertrand et al [147], who found that the turbulence intensity profiles presented a maximum at the impeller plane of symmetry. Okamoto et al [143] also reported that the highest values of energy dissipation exist in the agitator plane, with a decreasing trend towards the wall. Although their observations are related to single-phase liquid flow, qualitatively at least, they ought to hold for the case of a gas-liquid mixture.

The radial d_{32} distributions are presented in Fig 5.31. Their trends are more complicated than those of the vertical distributions. Notable is the impeller level plane (z4) which presents a consistently increasing trend towards the wall, evidencing the occurrence of bubble coalescence in this direction.

5.5.7 Effect of ionic solution

It is a well known fact that the degree of purity of the fluid system affects the bubble size in a gas-liquid dispersion. Even small quantities of impurities present in the system can have a substantial effect. The small changes induced in the physical properties of the solution, including the surface tension, are not important enough to influence the bubble disruption process in a turbulent gas-liquid dispersion. Thus, the principal action of the impurities is to retard bubble coalescence with the consequence that small bubbles, once they are formed, tend to preserve their individual indentities. This results in a comparatively smaller mean bubble size in the contactor. In many industrial applications the liquids used tend to be coalescence suppressing, although usually they are not totally coalescence inhibiting. In order to simulate this type of system, a 0.15M Sodium Chloride

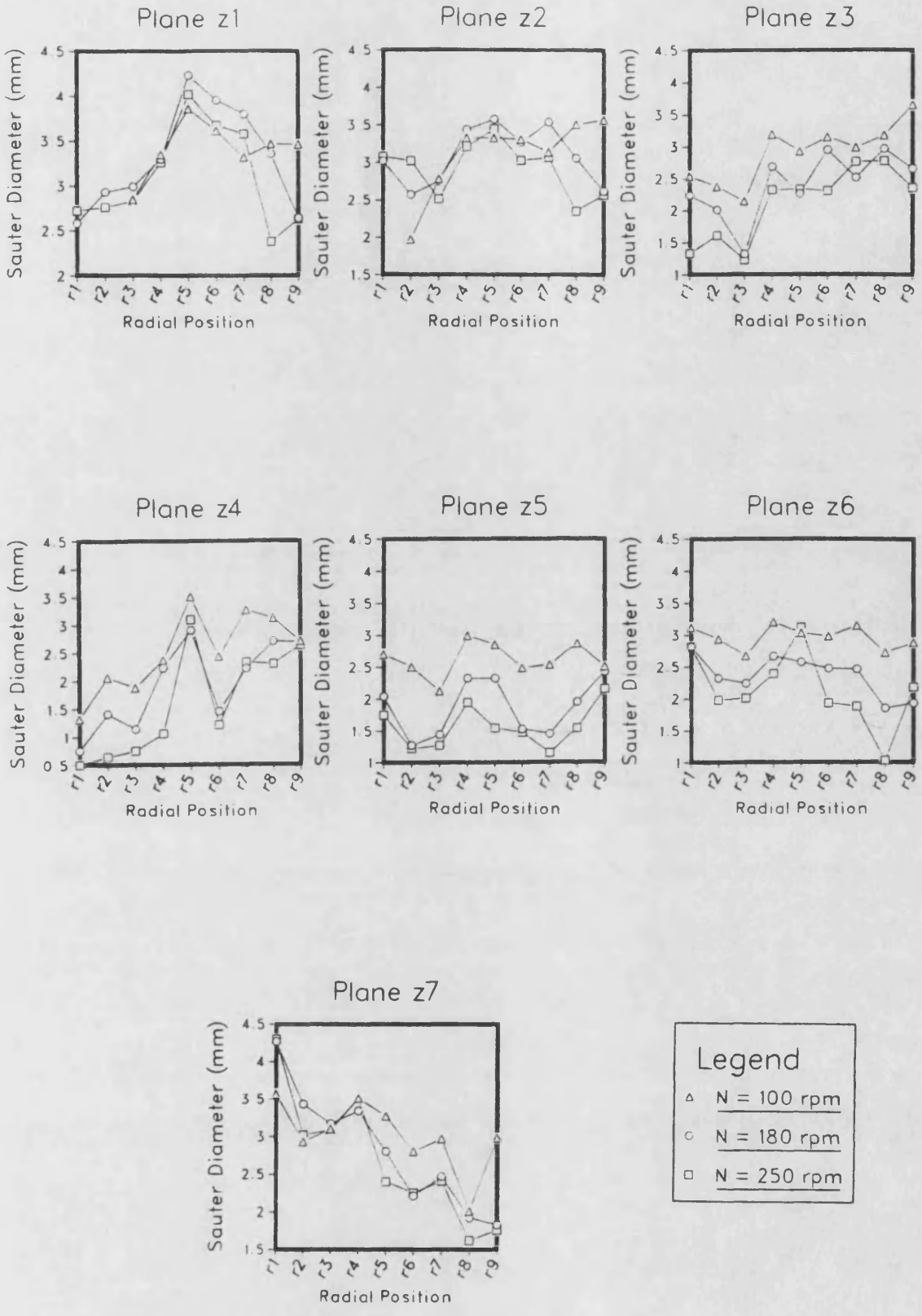

Fig 5.3I Radial distributions of Sauter bubble diameter in impeller discharge stream
$Q=0.00164\ m^3/s$

solution was employed. Point measurements were made in the mid-plane between two baffles using the same grid (Fig 5.9) as for the air-water dispersion. The d_{32} values are presented in Fig 5.32 for the conditions employed.

Overall, finer and more uniform dispersions were produced. The reduction in the representative mean Sauter diameter for the whole matrix depends on the mixing conditions but is within the range 22-34%. Large increases in the total gas holdup were generated especially at high speeds (up to 69%). These reductions in bubble size and increases in gas holdup will be shown later (Chapter 6) to produce large increases in interfacial area. Invariably, at position 17 near the impeller shearing edge the difference between the Sauter diameter for the ionic and water systems is small. This clearly shows that bubble breakage is much more important than coalescence in this region. Circulation in the lower half of the vessel appears to start at lower impeller speeds in the salt solution compared to water. This is deduced from the fact that at the lowest speeds (100, 130 rpm) bubbles were detected at position 21 below the impeller in the ionic system, whereas this was not the case for water. This early circulation is due to the fact that the bubbles are smaller in the salt solution and, thus, have lower rising velocities. Consequently, they are more easily entrained by the downward circulating liquid.

The effect of increasing N on the overall Sauter diameter in the upper part of the tank is insignificant. In the agitator stream and the lower zone of the vessel, however, the reducing effect is substantial as shown in Figs 5.33 and 5.34, respectively. There, it can also be seen that increasing Q at constant speed causes a significant rise in the mean bubble diameter. For instance, at 180 rpm $\bar{d}_{32}$ increases by 33% below the agitator and by 60% in the turbine discharge stream. There is also a 26%

Fig 5.32 Spatial distributions of Sauter bubble diameter in air-0.15M NaCl (mm).

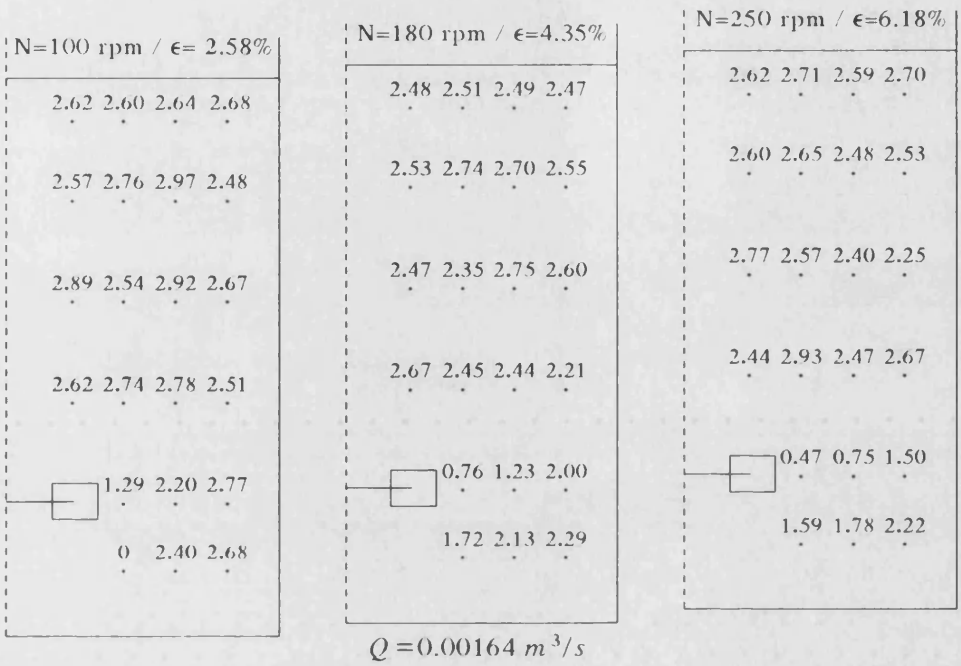

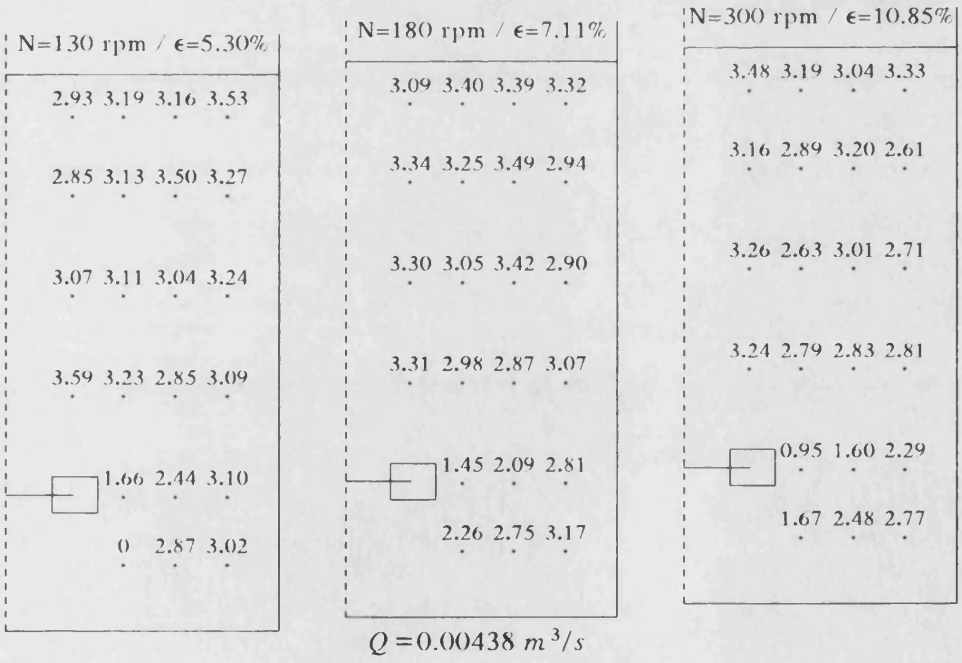

Fig5.33 Effect of N and Q on Bubble Size in Impeller Region, in Ionic Solution

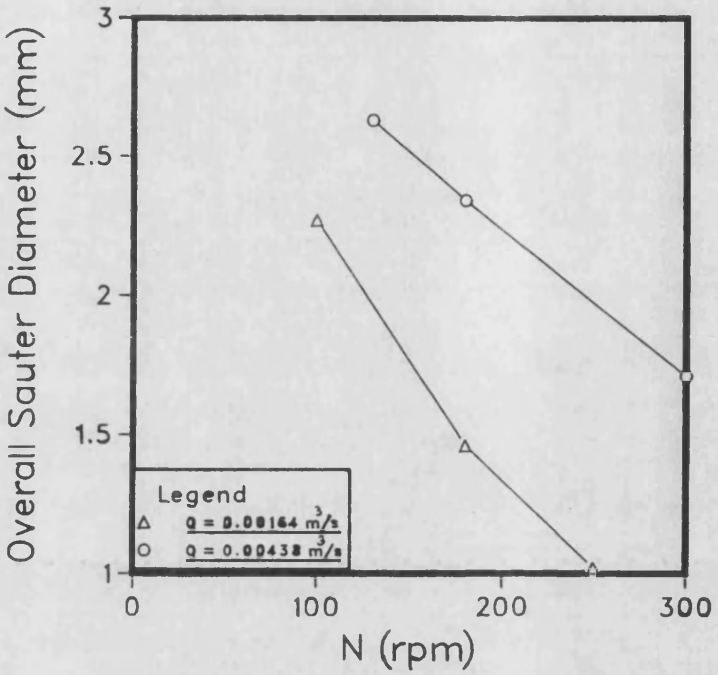

Fig5.34 Effect of N and Q on Bubble Size Below Impeller Region, in Ionic Solution

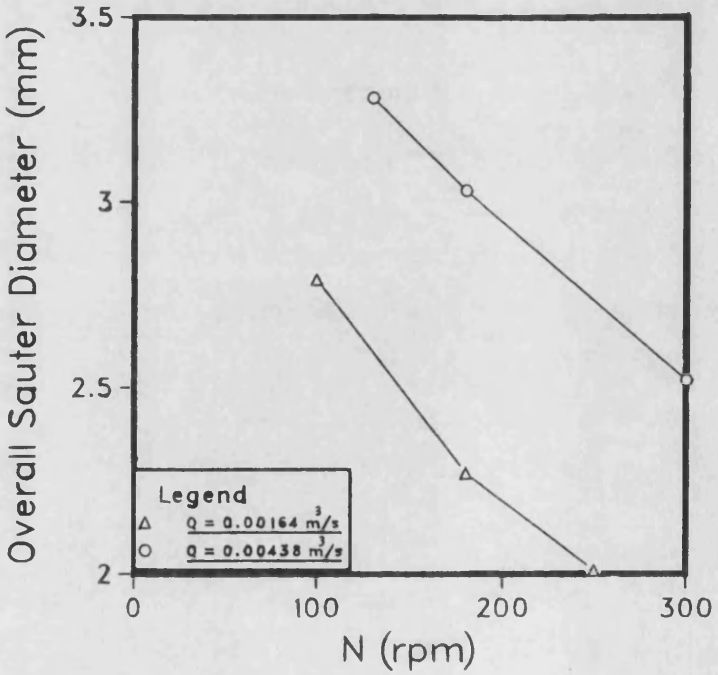

rise in the bulk.

The point bubble size distributions generated for N=250 rpm and $Q = 1.64 \times 10^{-3}\ m^3/s$, are presented in Fig 5.35. All of the distributions are based at the left end of the spectrum and are positively skewed. They are completely different from the corresponding distributions obtained for water (Fig 5.14). Considering the bulk region of the reactor, the histograms are not identical in form. However, they do exhibit a close similarity, which demonstrates the large degree of uniformity introduced by the ionic solution in the dispersion. The spread of these distributions compared with those for the water is considerably reduced, and is therefore evidence of greatly reduced bubble coalescence. However, it still remains relatively wide indicating, as may be expected, that the coalescence inhibition at this moderate salt concentration is not total. In fact, higher concentrations up to 0.50M were tested and found to produce very small bubbles. The signal pulses generated from the photodetectors by these bubbles were too small to be analysed satisfactorily. One solution to this problem would have been to reduce the size of the capillary so as to allow the bubbles to transform into proper slugs and thereby enable a satisfactory detection. However, decreasing the capillary size would cause excessive bubble breakage inside the probe and, therefore, would make the signal analysis more complicated. Also, with a very fine capillary (a 0.1 mm diam. capillary would have been needed) probe blockages by any contamination or dirt in the solution, however small, would be a major problem.

In the agitator plane the ionic distributions have their means shifted to the lower end of the bubble size range and, compared to their corresponding water distributions they have significantly lower spreads and a much higher proportion of small bubbles. Similar observations

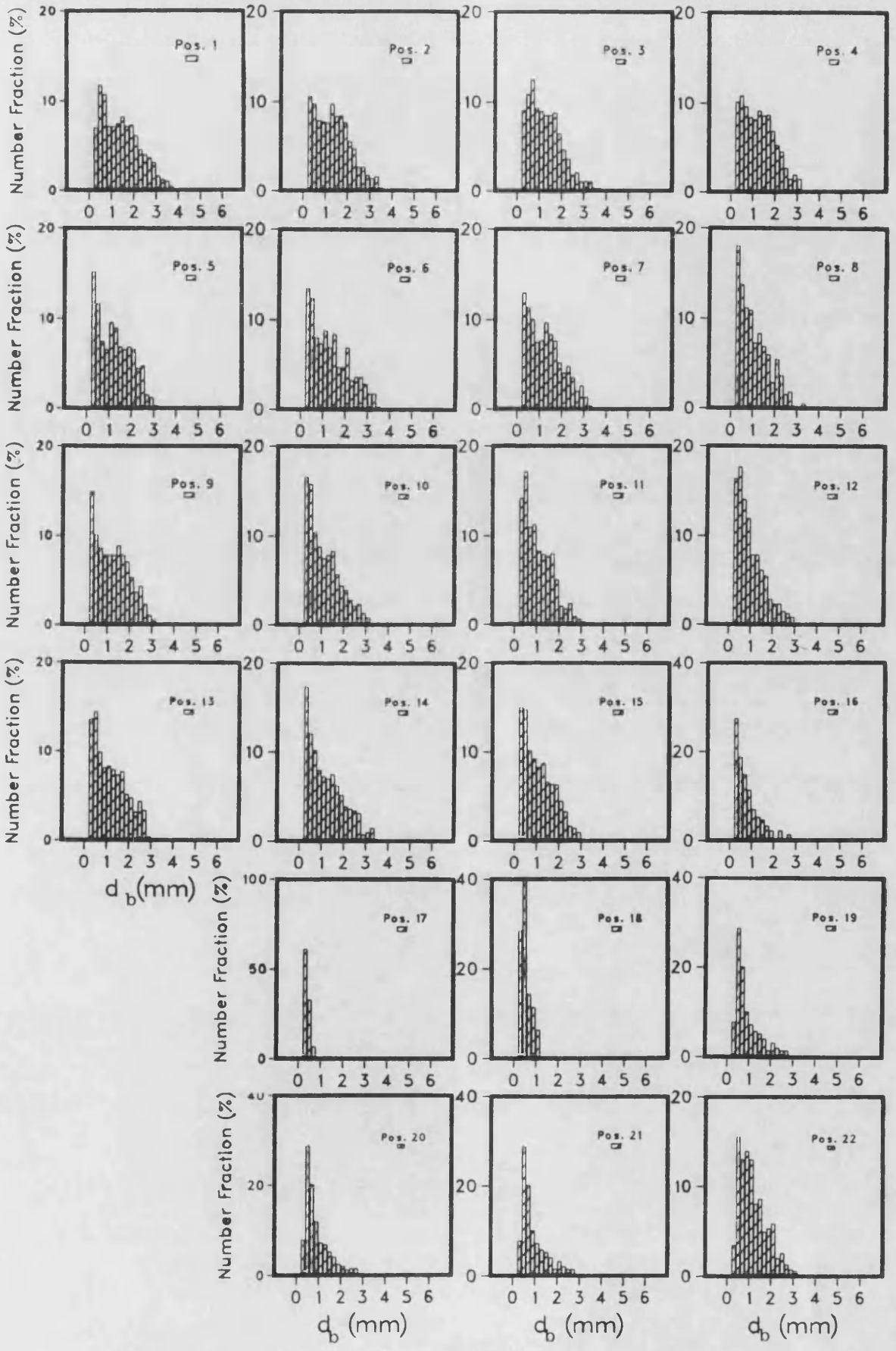

Fig 5.35 Local bubble size distributions (Air-O.I5M NaCl)
N=250 rpm, Q=O.OOI64 m^3/s, ϵ=6.I8%.
Mid-plane

can be made about the distributions below the impeller.

Overall bubble size distributions were constructed for water and salt solution, by adding together in each case all of the 22 local distributions. These distributions are compared in Fig 5.36, to reveal the effect of the ionic system on the gas-liquid dispersion in the reactor as a whole. The two distributions are markedly different. The mean bubble size in the electrolyte system is considerably smaller than in water. The difference in $\bar{d}_{10}$ is 54%, and in $\bar{d}_{32}$ it is 35%. The corresponding cumulative frequency distributions are also presented in Fig 5.37. There is a wide difference in the trends. Over half the bubble population has a diameter less than 1 mm in the electrolyte gas-liquid dispersion, and less than 1.5% have diameters greater than 3 mm.

Simulation of the above discrete distributions by the normal distribution was attempted. The distributions, as expected, were found to be nonnormal and particularly so the ionic distribution. Several other continuous statistical distributions were tested. From these theoretical distributions, the Weibull distribution was found to fit the air-water bubble size distribution best. The probability density function of this distribution is given by:

$$f(x) = \frac{\alpha x^{\alpha-1} e^{-(x/\beta)^{\alpha}}}{\beta^{\alpha}} \qquad (5.5)$$

with x = d_b, $\alpha = 2$ and $\beta = 3$. The fit is shown in Fig 5.38.

The air-electrolyte bubble size distribution was well approximated by the exponential distribution, which has the following probability density function:

Fig5-36 Effect of Ionic Solution on Overall Bubble Size Distribution

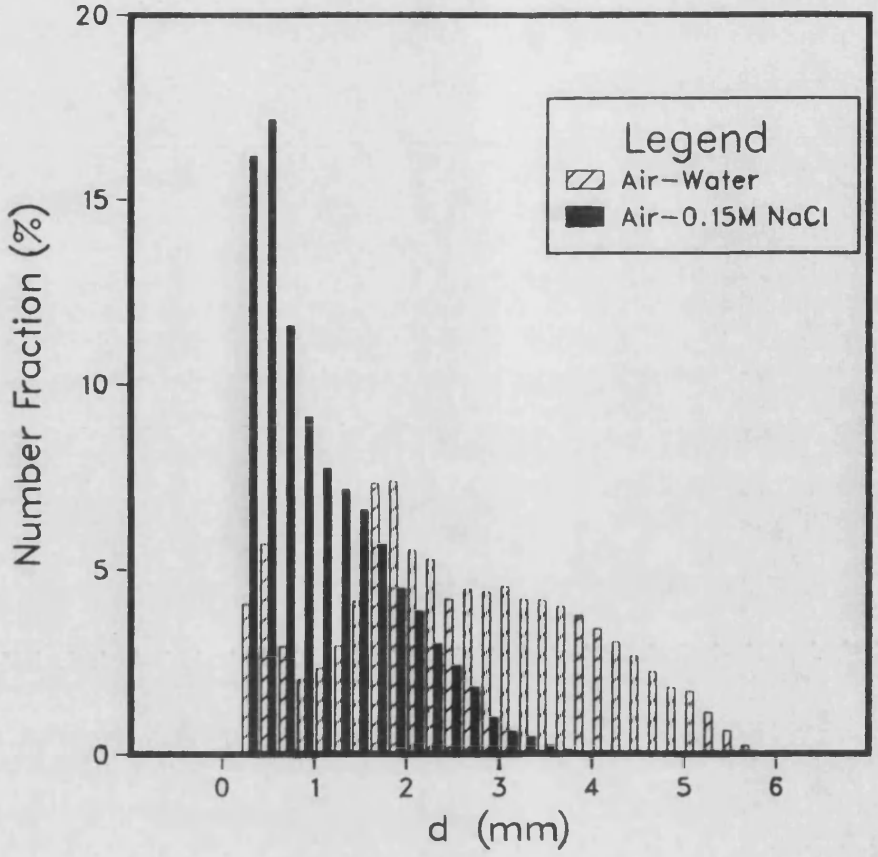

Fig5-37 Effect of Ionic Solution on Overall Bubble Size Distribution

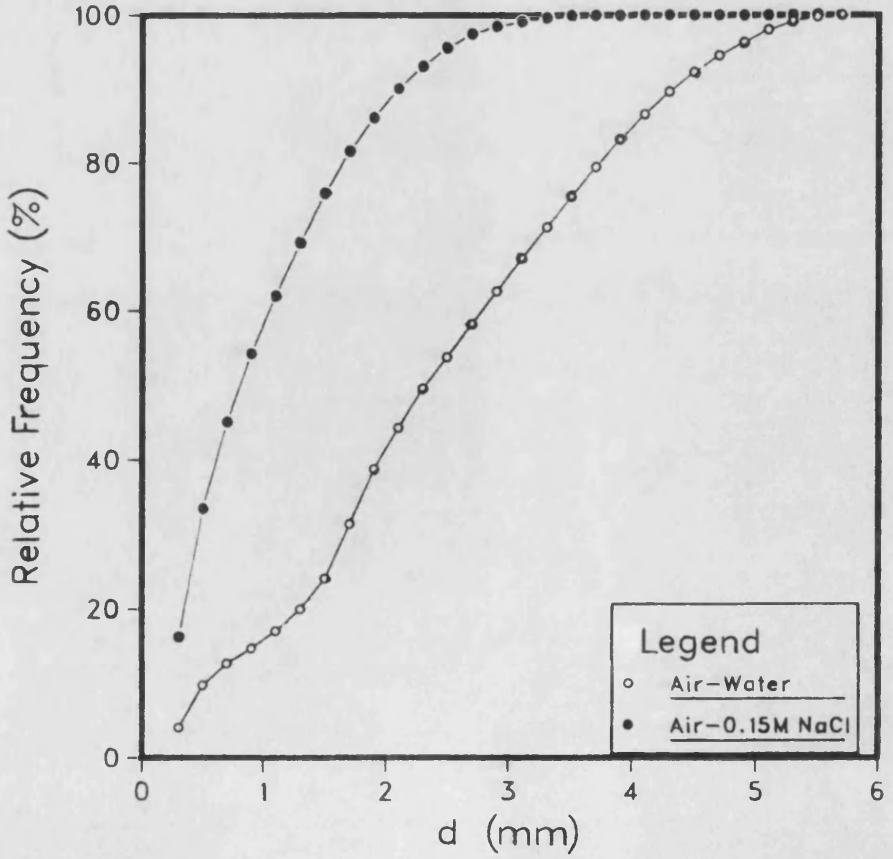

Fig5.38 Functional Form of Overall Bubble Size Distribution

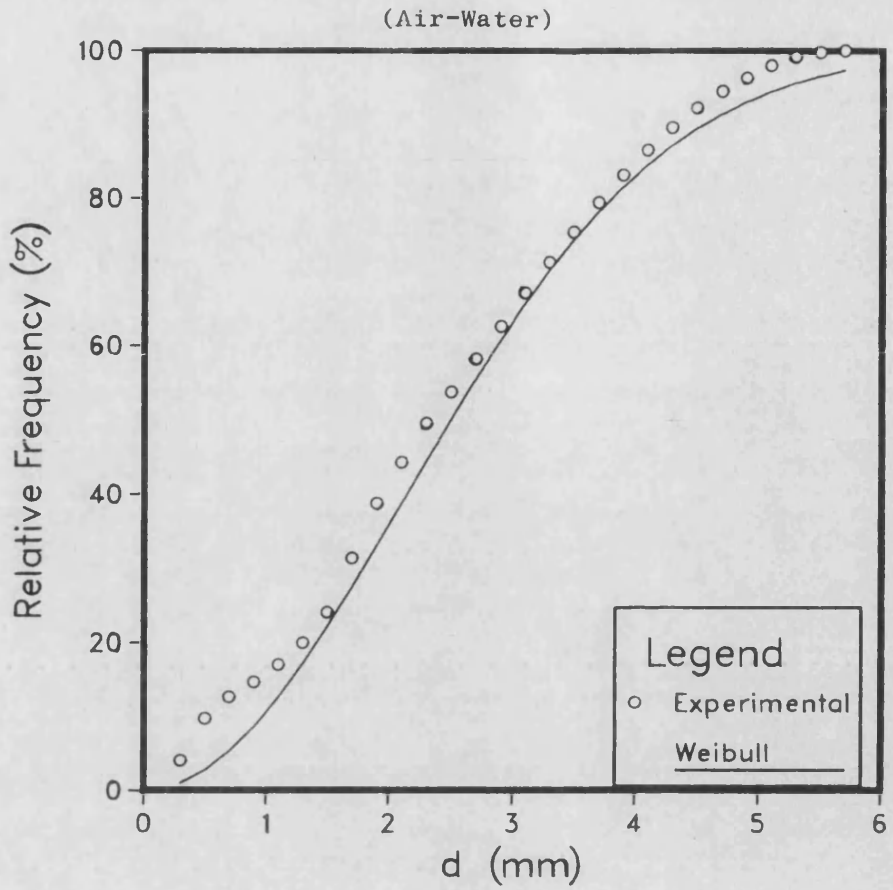

Fig5.39 Functional Form of Overall Bubble Size Distribution

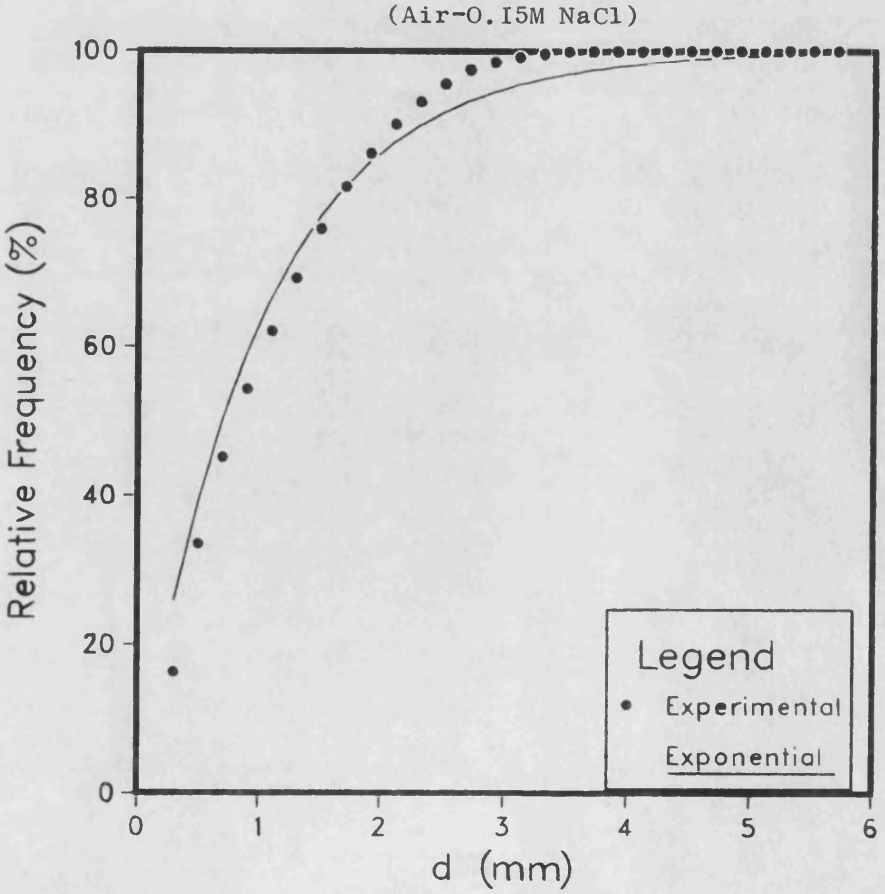

$$f(x) = \frac{1}{\beta} e^{-x/\beta} \qquad (5.6)$$

where β is equal to 1. The fit of this function to the experimental distribution is presented in Fig 5.39.

5.6 Conclusions

- The fully submersible capillary suction probe technique developed for use in large stirred reactors, has been successfully used to carry out, for the first time, a detailed quasi-point investigation of the structure of bubble size distributions in 'coalescing' and 'non-coalescing' gas-liquid dispersions in a 1.0 m tank. The probe was interfaced to a high speed data acquisition system supervised by a microcomputer to allow storage of large amounts of data and fast on-line processing.

- The bubble size distributions were found to vary widely from one region of the reactor to an other, deviating considerably from the standard normal distribution. The effect of increasing the agitation speed is to shift the distributions towards the lower end of the spectrum, whereas an increase in gas flow rate has the opposite effect.

- Increasing the impeller speed causes a sharp drop in the mean bubble size in the impeller zone at low gas flow rates. At high gas rates, however, the effect becomes insignificant, evidence of important rates of bubble coalescence. This is supported by the substantial increase in mean bubble size that results from an increase in Q. In the upper and lower parts of the vessel the effects of N and Q remain generally small, indicating that in these regions an equilibrium exists between the two competing processes which determine the mean bubble size in the reactor ie., bubble breakage and coalescence.

- The mean bubble size in the vertical plane coinciding with the baffles is appreciably smaller than that in the mid-plane between two baffles. Large differences exist between the respective local bubble size distributions in the two planes. The overall cumulative bubble size distribution in the baffle plane lies above that of the mid-plane by a considerable margin.

- The leeward side of a baffle shows a more pronounced variation of the bubble size with liquid depth than the windward side. The leeward side is a relatively quiescent zone which promotes bubble coalescence.

- The impeller discharge stream was explored using a high resolution measurement grid. The spatial bubble size distribution showed strong nonuniformity. The vertical distributions of the Sauter bubble diameter have a parabolic shape which gradually flattens towards the wall of the tank.

- The use of a 0.15M NaCl solution produced considerable bubble coalescence retardation which was reflected in a substantial drop in the bubble size. The local bubble size distributions obtained were situated at the left end of the bubble spectrum and were very different from the corresponding water distributions. The overall distributions for the whole dispersions of water and ionic solution were well approximated by a Weibull distribution and an exponential distribution, respectively.

Chapter 6

LOCAL GAS HOLDUP AND INTERFACIAL AREA DISTRIBUTIONS

6.1 Introduction

Information on the spatial distribution of the total gas holdup is necessary for a complete appreciation of the internal processes in a gas-liquid stirred reactor. In this Chapter, the application of a computerised conductivity probe technique for the measurement of local gas holdup is described. Measurements were made in the 1.0 m stirred tank. These are discussed and compared with existing data in the literature. Combining these holdup distributions with point bubble size results provides the local gas-liquid interfacial area distributions.

6.2 Local gas holdup

6.2.1 Capillary suction probe

The possibility of measuring local gas holdup simultaneously with local bubble size using the capillary suction probe technique was investigated. The point holdup values were calculated from the total volume of the gas bubbles sampled and the liquid volume concurrently collected. The holdup values thus obtained were found to be too high to be acceptable. A well defined flow situation was used to investigate this phenomenon. The arrangement used consisted of the cell in Fig 4.3. The probe was positioned inside the cell and sampling was conducted from a chain of mono-size bubbles. The liquid flow rate through the tube was varied by changing the suction pressure, while the bubble frequency in the gas stream was kept constant. The measured holdup was found to be highly dependent on the liquid flow rate. The higher this rate the lower the holdup estimate. Therefore, it became clear that the reason for the overestimation of gas holdup obtained was due to the fact that the liquid volume collected was greatly underestimated. As the gas flow rate through the tube increases this volume of liquid reduces further, since

the liquid flow rate remains constant during the sampling process. The liquid flow rate through the capillary is also highly dependent on its diameter. One solution which was tested, consisted of increasing the size of the tube in order to allow more liquid to be collected. However, this led to a large underestimation of the volume of gas sampled since all bubbles smaller than the tube diameter could not be detected. This caused an underestimation of the gas holdup. In any case, even when the capillary size is increased it is not obvious how to correct the liquid rate, since it will depend, as already mentioned, on the actual gas flow rate. In a dispersion, this varies from point to point. At this stage it was decided to adopt a different technique for point holdup measurement, and a conductivity probe was developed for this purpose.

6.2.2 Conductivity probe

The principle of operation of a conductivity probe has already been described in Section 2.2.4. The probe used here consisted of a single stainless-steel wire 125 μm diameter located in a 0.3 mm diameter stainless-steel hypodermic tube, as represented schematically in Fig 6.1. The detection end of the instrument had a progressively tapering profile achieved by means of different diameter stainless-steel tubes, firmly joined and sealed with Epoxy resin. The tapering profile was desirable in order to minimise flow disturbance near the sensor tip. The probe head electrical assembly, which was located inside the body of the probe, consisted of two four-arm resistive bridge circuits with one side of each bridge common to both circuits for reasons of space economy (Fig 6.2). This, therefore, caters for two probe sensors so that the instrument can in future be easily extended to a double sensor probe to permit simultaneous measurement of bubble velocity. This was the original intention. However, the construction of a two-element probe proved to

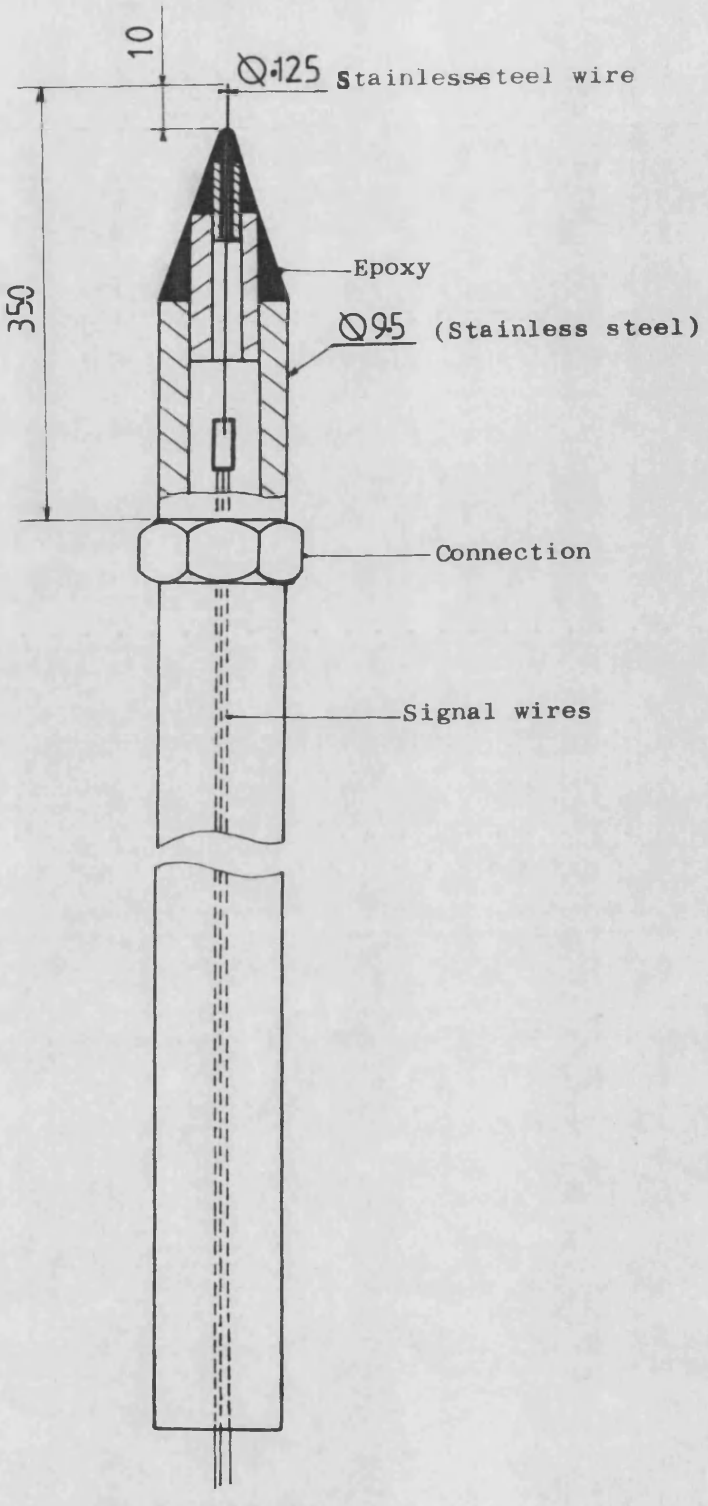

Fig 6.I Conductivity probe.
(Dimensions mm)

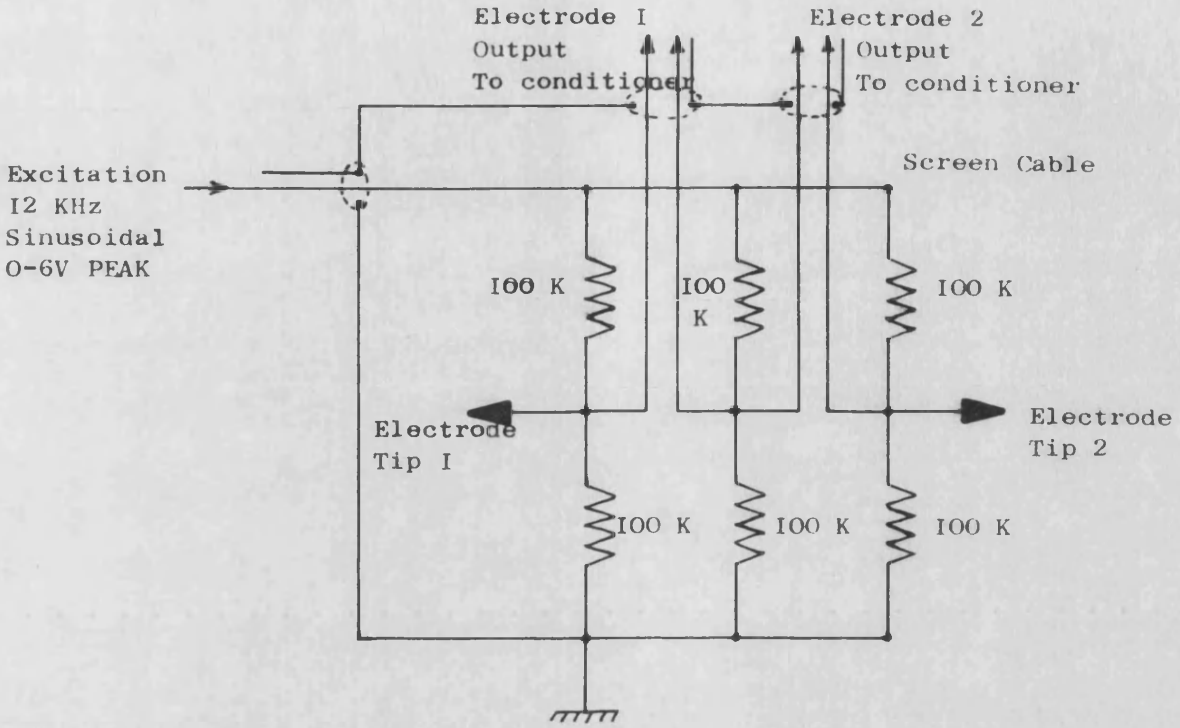

Fig 6.2 Conductivity probe head assembly (2 channels). (converts resistance change at probe tip to a voltage change)

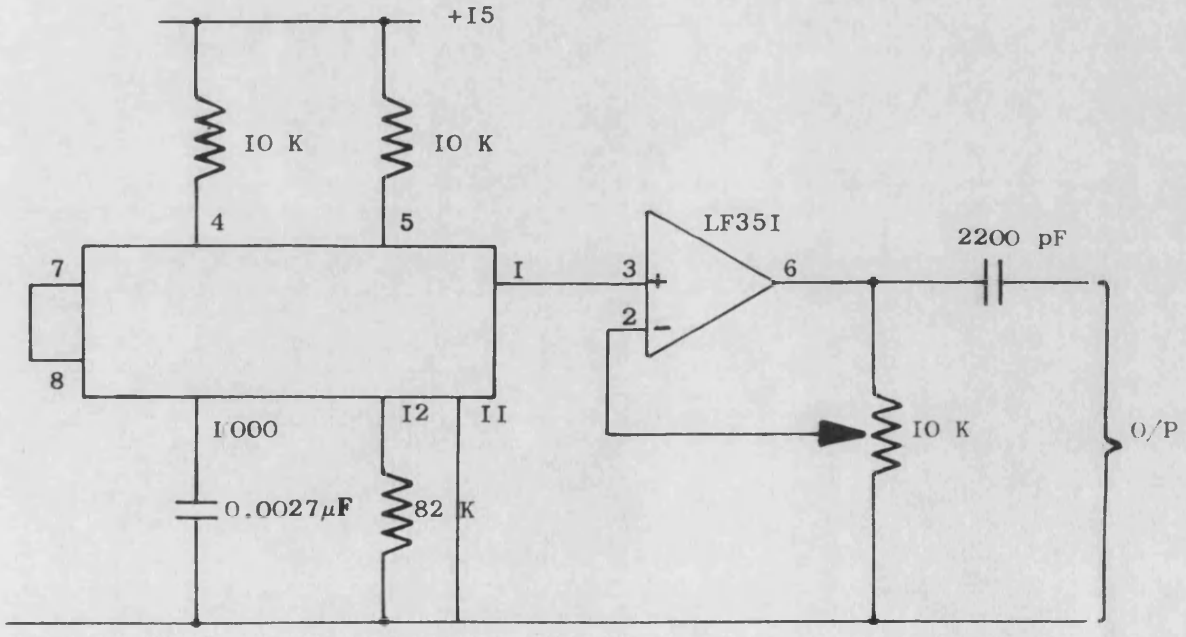

Fig 6.3 Conductivity probe excitation oscillator.

be a much more intricate and time consuming task than first anticipated. Hence, This feature was postponed for future work.

A 12 KHz sinusoidal current supply was used to excite the electrode. The excitation oscillator circuit is depicted in Fig 6.3. When the sensor tip is in air, the resistive bridge is balanced and none of the 12 KHz excitation signal appears at the output. With the probe in water, the resistance of one arm of the bridge is reduced, unbalancing the bridge and causing a 12 KHz waveform to appear at the output. The bridge output is connected to a first conditioning unit. As shown in Fig 6.4, the AC signal is first amplified and then passed to an active full wave rectifier and smoother circuit, and finally to an additional RC filter. The net result is a DC level proportional to the amplitude of the input signal. The DC signal is then connected via an opto coupler arrangement to the same conditioner used for the capillary suction probe (see Section 4.3.2.2).

The sensor electrode was coated with a thin layer of Epoxy resin except for the tip end. The wet Epoxy coating on the exposed length of the stainless-steel wire was sprayed with a PTFE type spray (Sprayflon-82 available from Pampus Fluorplast Ltd.) and was left to set for 24 hours. When dry, this gave a good hydrophobic property to the sensor tip, which resulted in a fast signal response. A typical pulse generated by a bubble hitting the probe tip is shown in Fig 6.5. The excellent stable nature of the signal allowed the threshold to be set fairly close to the liquid line, in order to minimise the error in the measurement of the pulse width, arising from the relatively slow rise of the signal from liquid to gas. This is due to the finite liquid film drainage rate at the probe tip.

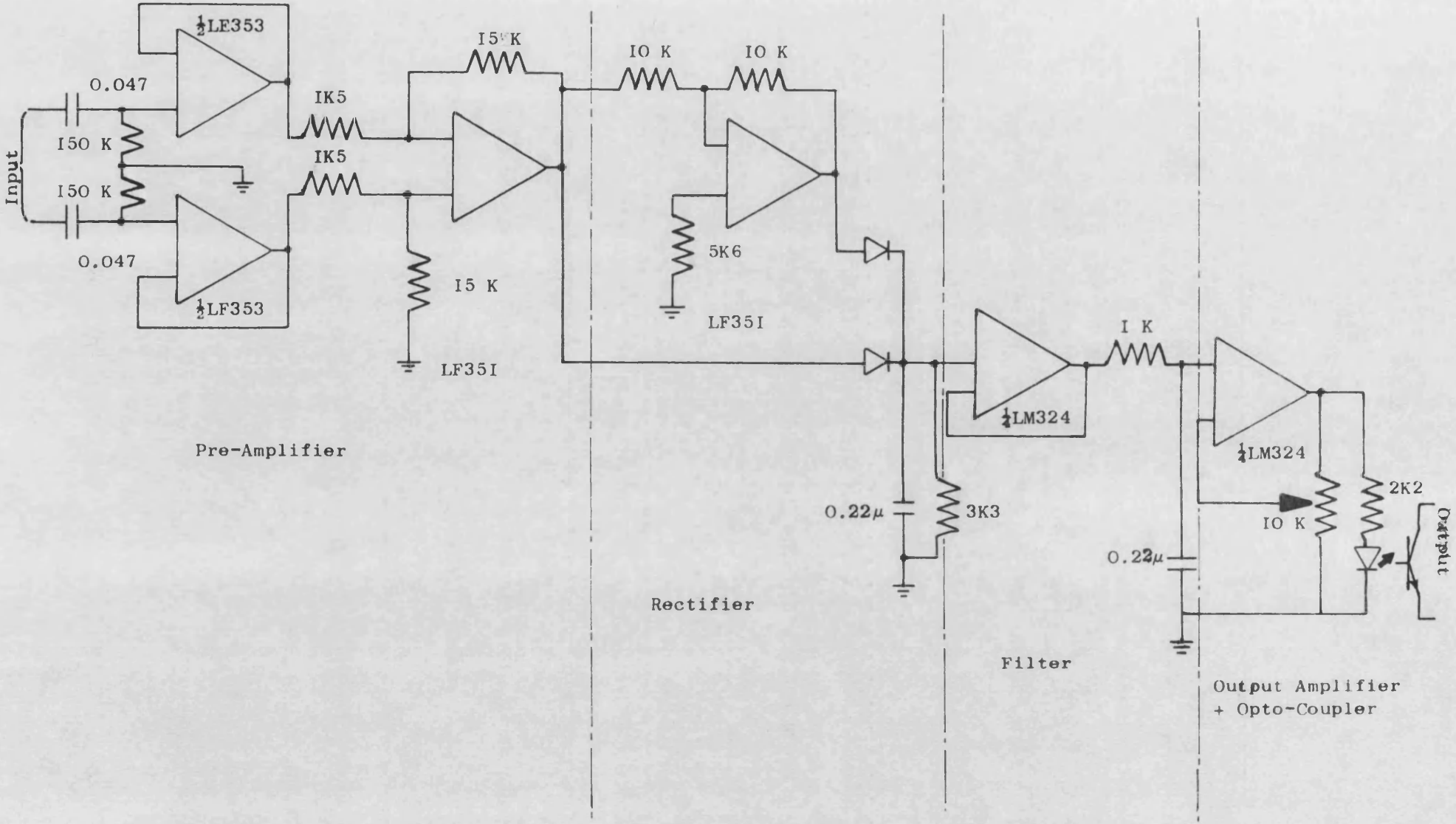

Fig 6.4 Conductivity probe signal conditioning.
(one channel only shown)

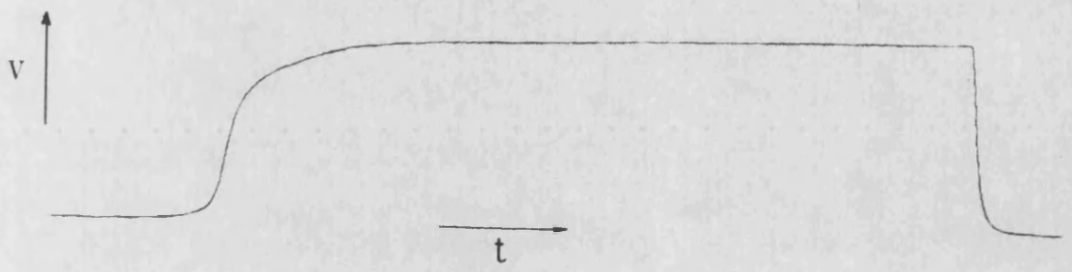

Fig 6.5 Typical recorded signal pulse generated by a bubble hitting probe tip.

The operation of the probe was controlled by a BBC microcomputer through fast machine code software. The data acquisition system used with the resistivity probe was the same system as that employed for the bubble suction probe, (described in Section 4.4). The software used for controlling the sampling process and analysing the acquired data is given in Appendix B.

The local holdup was calculated from the time average quantity ϵ_p given by:

$$\epsilon_p = \frac{\sum_{i=1}^{i=n_b} t_{g\,i}}{T} \tag{6.1}$$

where,

t_{gi} = bubble passage time

n_b = number of bubbles in sample

T = total sampling period

The local mean bubble passage frequency was obtained from:

$$n_f = \frac{n_b}{T} \tag{6.2}$$

The sampling time used was at least 3 minutes, which was sufficiently long to obtain a statistically representative sample of bubbles, typically 500 to 1000, depending on the local bubble frequency. The reproducibility of results was better than 5%.

6.2.3 Results and discussion

Using the resistivity probe described above, 22 points were explored in the 1.0 m tank, in the median plane between two adjacent baffles, as shown in Fig 5.9. The two-phase system investigated was air-

water. Measurements were performed for the loaded impeller flow regime, using the 0.333 m Rushton turbine, rotated at three different speeds for three air flow rates.

6.2.3.1 Bubble passage frequency

The bubble frequency maps generated by the resistivity probe are depicted in Fig 6.6, for the conditions investigated. There, the highest passage frequencies are always found in the impeller region. This is expected since bubbles are first generated from the dispersion zone of the gas cavities, behind the blades. They are then carried and dispersed into the vessel volume by the combined effect of buoyancy and the turbulent jet momentum. It is known [95] that liquid in the neighbourhood of the impeller discharge stream is entrained by momentum transfer and turbulence vertically into the radial stream and becomes part of the flowing 'jet', bringing more bubbles with it. This increases the bubble density in the impeller stream. The frequency is highest near the impeller periphery where bubble formation takes place, and decreases in the radial direction towards the wall. This reduction with radial distance could be due to the combination of three effects:

(i) Coalescence of bubbles as they move towards the wall, which results in larger but fewer bubbles.

(ii) Disengagement of bubbles from the impeller discharge stream ie., bubbles leave the radial stream and either rise upwards or are entrained by the circulating liquid towards the base of the tank. As bubbles move away from the impeller, their radial velocity decreases and hence their resultant velocity vector shifts in an axial direction. The increase in bubble size due to coalescence favours upward disengagement, because of the increase in bubble rise velocities.

Fig 6.6 Spatial distributions of bubble passage frequency (s^{-1}).

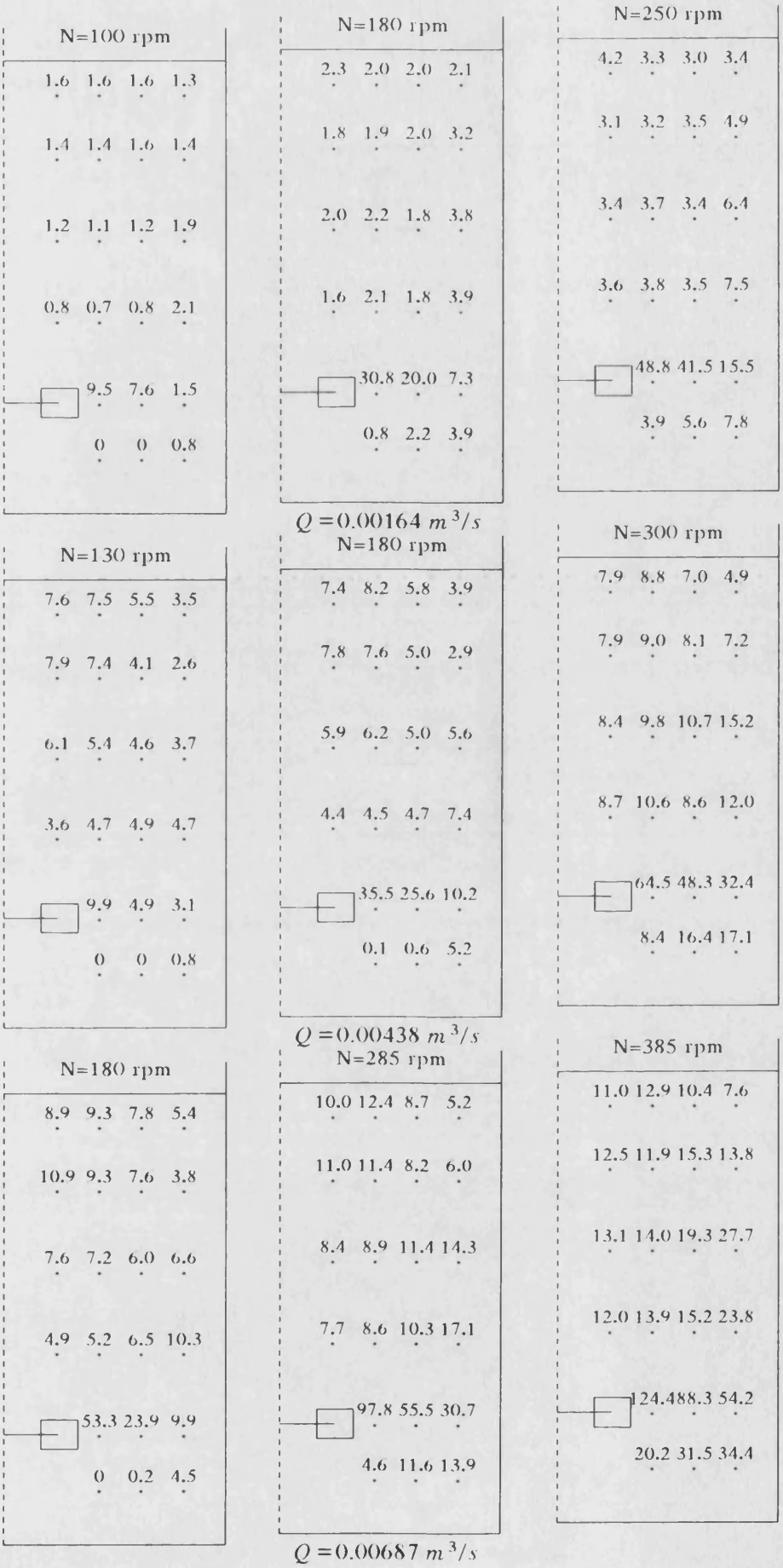

(iii) The radial velocity of the discharge liquid reduces with radial distance and therefore, the entrainment of bubbles from adjacent regions, as explained above, diminishes. In fact Sachs and Rushton [96] found that at a distance approximately 2/3 the vessel radius, the liquid induced flow becomes zero.

Below the impeller, the bubble concentration rises with radial distance, as would be expected, since the flow is from the wall towards the centre of the vessel. No bubbles are present in the central region at low speeds, but more and more bubbles are transported there as the speed of agitation increases. For example, at N=385 rpm and $Q = 0.00687\, m^3/s$, circulation in the lower half of the tank was seen to have practically obscured the whole impeller region.

It is remarkable to note that, except for the lowest speed which corresponds to the start of gas dispersion below the impeller level, at each gas flow rate the sum of the frequencies at positions 16 and 22 is close to the frequency at position 19. This suggests that position 19 coincides approximately with the point of separation of the two circulation loops in the upper and lower parts of the vessel. This also implies that the flow at this point is essentially axial, which is to be expected since this position is only about one baffle-width away from the wall.

The variation of n_f with height in the vessel is shown in Fig 6.7, for the highest value of Q. Similar profiles were observed for the other two gas rates. As N increases, the frequency at position 12 increases with respect to the adjacent positions, above and below, causing the vertical profile to bend inwards. This indicates the presence of a circulation loop at N=285 rpm, which is supported by the similar profile linking points 3 to 15. In this case, the circulation loop is more emphasised at N=385

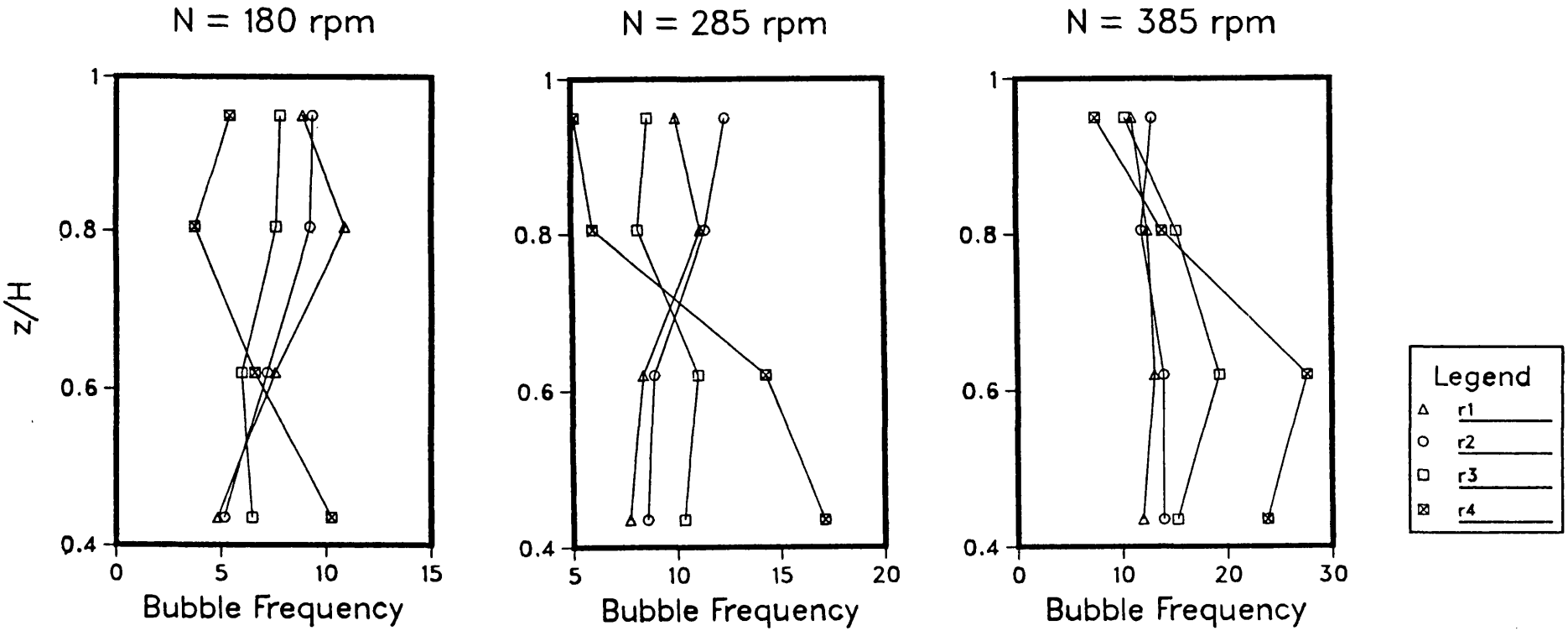

Fig 6.7 Vertical profiles of bubble passage frequency in upper part of vessel. ($Q=0.00687\ m^3/s$)

rpm.

The radial profiles of n_f in the upper region of the tank are shown in Fig 6.8, for the highest gas input rate. For z3 and z4, the levels immediately above the impeller, n_f exhibits an increasing trend towards the tank wall, indicating the formation of a circulating loop. For the higher levels the general trend is a decreasing frequency towards the wall. This decline is sharp at the lowest speed, leveling off as N increases, thus indicating an enlargement in the circulation loop. Until, at 385 rpm, it can be seen that the loop has reached level z5. However, the impeller is still not able to circulate bubbles above z5 as can be deduced from the still significant drop in n_f with radial distance. Essentially similar trends were observed for the other two gas flow rates, except that, for the lowest Q and agitation speed of 180 and 250 rpm, the circulation loop has exceeded level z5. This is reflected in a near uniform n_f distribution at z6.

As N increases, n_f is seen to increase at virtually every position in the tank, signifying an increase in gas holdup. Relatively, the most significant increase takes place below the impeller plane, where, as agitation is increased, more and more bubbles are entrained in the lower region of the vessel. This is due to their smaller size and lower rise velocities in the presence of a higher downward liquid velocity.

For the constant impeller speed of 180 rpm (Fig 6.6), it can be seen that n_f increases with Q at almost every point in the vessel except in the region below the impeller, where the effect is reversed. Position 22, however, first shows an increase with Q followed by a decline. This decline in frequency is due to the different hydrodynamic conditions in the impeller vicinity. At fixed N, and as Q increases, the impeller is less able to circulate bubbles in the lower half of the tank, the flow around it

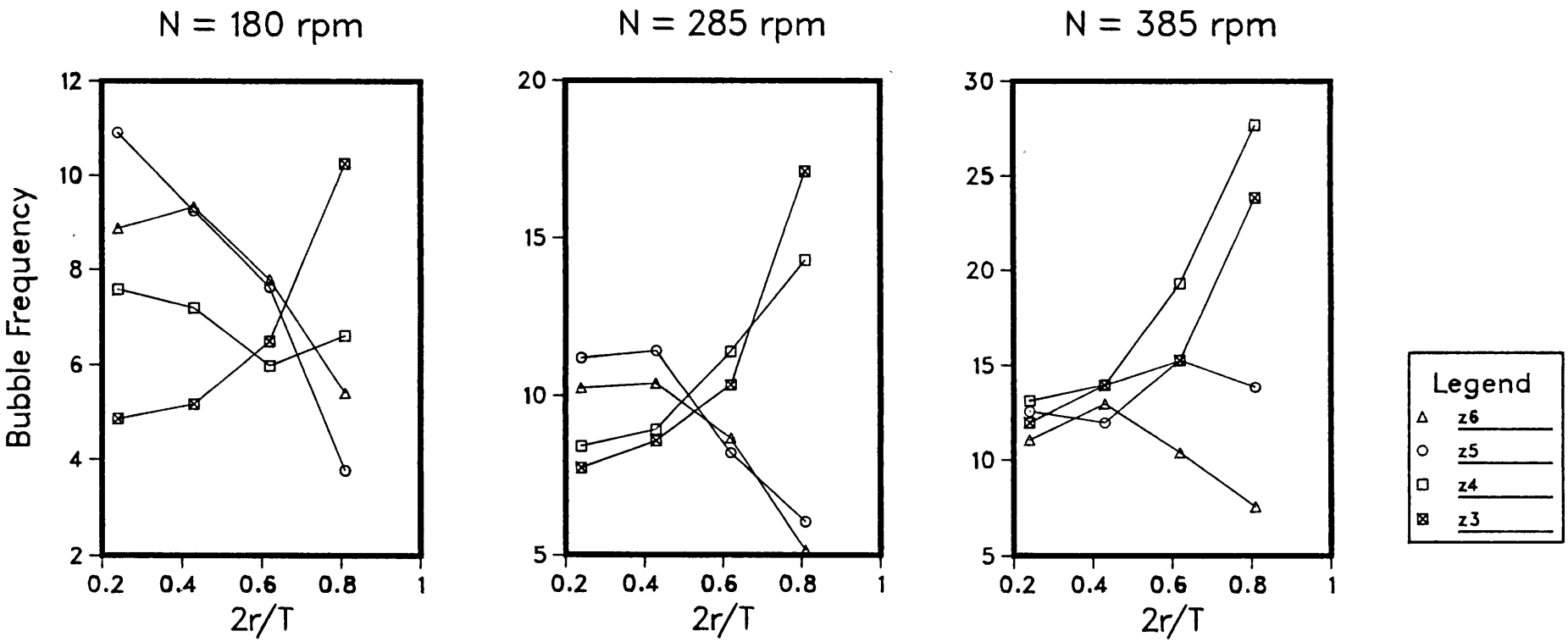

Fig 6.8 Radial profiles of bubble passage frequency in upper part of vessel. ($Q=0.00687\ m^3/s$)

being closer to the flooding regime.

Although at the location near the impeller tip n_f increases significantly with Q, the other two positions in the impeller plane first witness an increase followed by a slight drop. This drop is considered to be due to the decrease in the liquid pumping capacity of the agitator, which results in a reduction in the bubble velocity radial component. Therefore, there is a tendency for the bubbles to rise and leave the discharge stream at a shorter radial distance, evidencing a shift towards flooding. This is also helped by the increase in the bubble rise velocity of larger bubbles, as a result of higher gas loading.

The degree of dispersion of the bubbles inside the vessel, as represented by the coefficient of variation, $(\sigma/\bar{n}_f)$, for each bubble frequency map obtained, is plotted against the impeller speed in Fig 6.9. There, it can be observed that the coefficients of variation are high, signifying high levels of dispersion in the spatial distribution of the bubbles inside the tank. For each gas load, the degree of dispersion first rises with stirring speed, but then declines as agitation becomes very intense, in each case exceeding the recirculation speed. Thus, further enhancement in agitation is expected to bring about more uniformity in the distribution of the bubble population. At the common speed of 180 rpm, reducing the gas flow rate from $0.00687\ m^3/s$ to $0.00438\ m^3/s$ diminishes the spread in the distribution of n_f values. By the time the gas rate has reached $0.00164\ m^3/s$, however, the coefficient of variation has risen again considerably.

6.2.3.2 Local gas holdup

The local gas holdup maps generated by the conductivity probe are exhibited in Fig 6.10. In the absence of a second local measurement

Fig6·9 Degree of Dispersion of Bubble Frequency

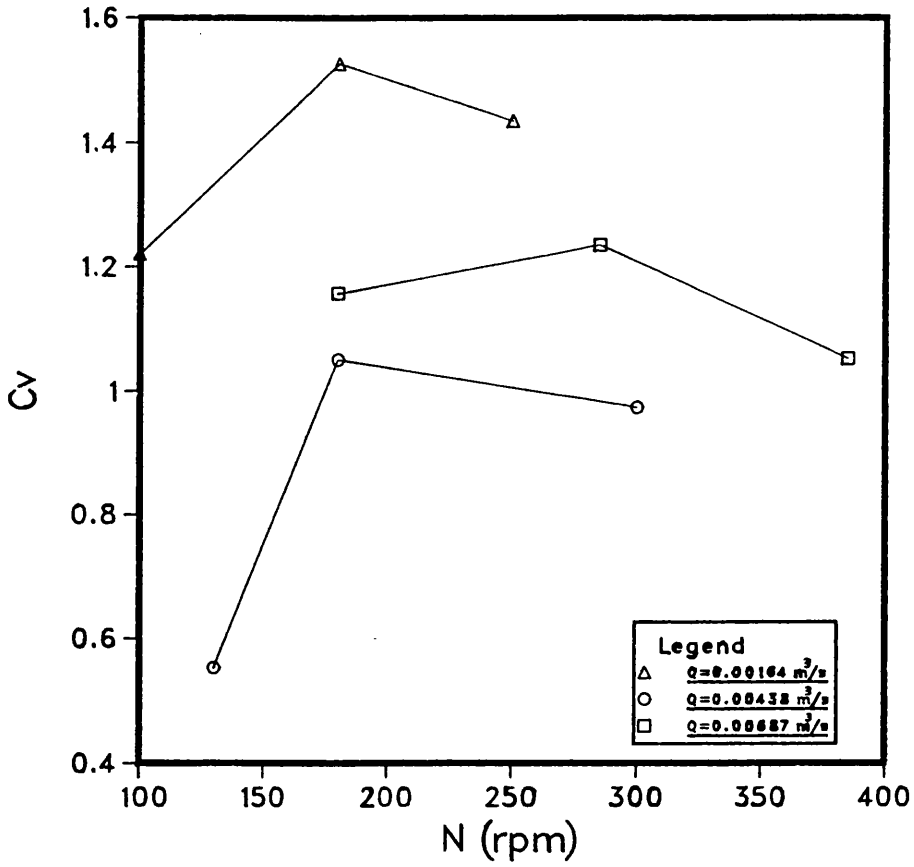

Fig 6.10 Spatial distributions of gas holdup (%).

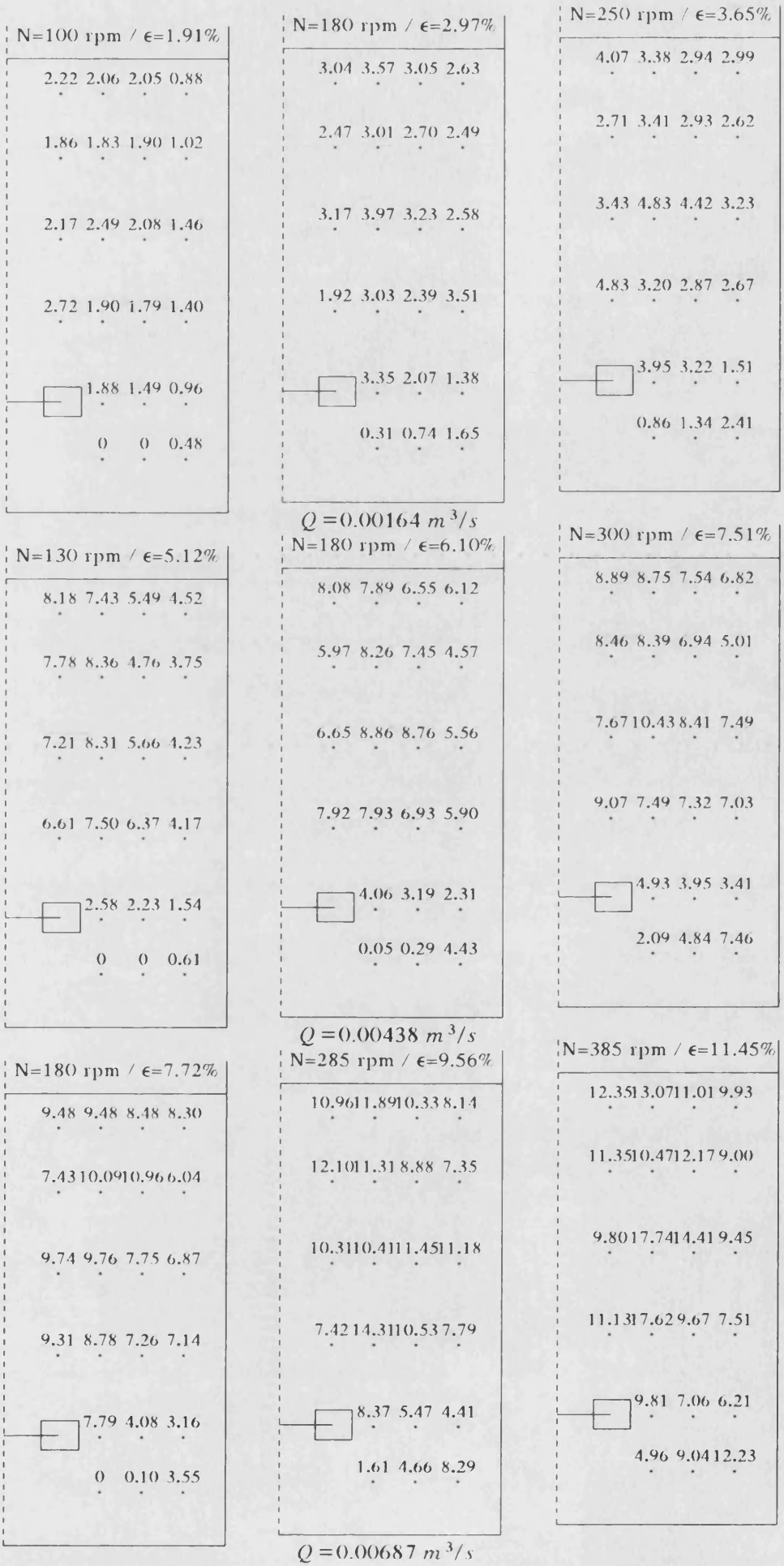

technique, the accuracy of the point holdup values was checked independently by comparing the mean integral holdup value, obtained for each matrix through two-dimensional integration, with the corresponding overall mean value, obtained by the level detection method described in Section 3.3.4. This comparison revealed that the resistivity probe underestimated ϵ_p under all conditions employed. The margin of error, however, remained within a reasonable range of 9 to 21%. This fact was also reported by Figueiredo [38], although the deviation in her case was slightly higher, probably because of the thicker sensor tip and lower quality of her probe signal. This feature is the result of a combined effect. First, the significance of any comparison test between the mean integral of local holdup values and the overall average holdup value is function of how well the two-dimensional matrix of measured values is representative of the three-dimensional point-to-point variations in the reactor. Also, some underestimations of the local holdup could arise from the difficulty in measuring the exact time length of the signal pulses because of the instrument finite response, especially at the time of piercing of a bubble. The response can only be improved by enhancing the water repellent properties of the sensor tip. A possible solution would be to fuse the wire in, say, a hydrophobic glass, although this would require considerably more expertise and would probably make the sensor more fragile. An increase in the sharpness of the tip is also desirable in order to improve its interaction with the bubbles. Very small bubbles may simply be deviated instead of being pierced by the probe tip. Further miniaturisation of the tip to solve this problem would obviously make its construction more complex. Being more delicate, would also significantly increase its sensitivity to mechanical stress. Alternatively, this phenomenon might be quantified, for example, by employing high speed photography. This effect, however, should reduce

with increasing bubble impact velocity, as observed by Nassos and Bankoff [57] for forced circulation in an air-water loop as compared with natural circulation. This may explain the reduction in the difference between the integral and the total holdup values observed in Fig 6.11, with increasing agitation speed.

The overall bias caused by all these effects, however, remains within acceptable limits, which makes the measurement technique very useful. Other advantages of this method reside in its low development cost and its very high speed of operation. A sample size of 1000 bubble time pulses is processed in approximately 105 seconds.

The point holdup maps (Fig 6.10) indicate a wide variation in the spatial distribution of ϵ_p inside the stirred vessel. The flow field in the tank can be divided into three principal regions; The circulation region below the impeller, the circulation region above it and the impeller discharge stream. The radial and vertical holdup profiles are plotted in Figures 6.12 and 6.13, respectively, for all conditions investigated. In the lower part of the vessel the holdup always shows an increasing trend towards the wall, with values near the centre being, in general, very low. It is only at the highest combination of agitation speed and gas flow rate that significant gas recirculation seems to have been achieved in the central area below the impeller. A photograph taken below the impeller showed the agitator to be almost completely obscured by gas bubbles. Overall, the holdup in the region below the impeller is appreciably lower than that in the upper part of the vessel, except at the position near the tank wall where the circulation starts from. The natural tendency of the gas bubbles to rise under buoyancy forces makes it difficult to disperse great amounts of gas in the lower part of the vessel. This fact demonstrates that high impeller clearances are not desirable from the

Fig 6.11 Measurement Error of Resistivity Probe

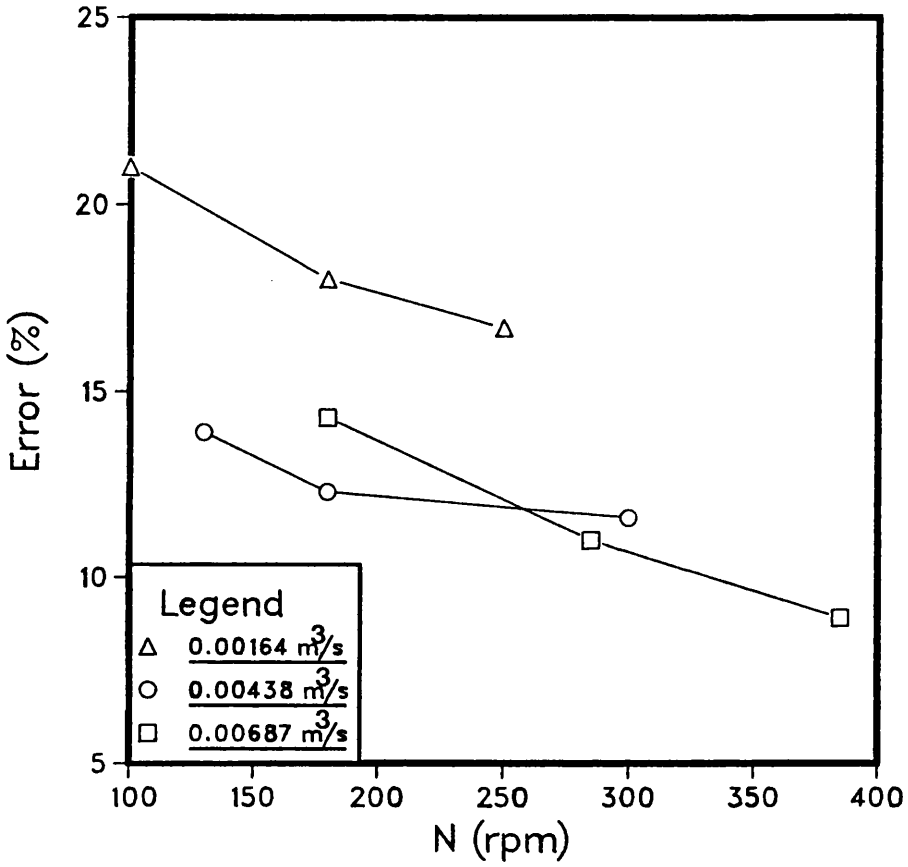

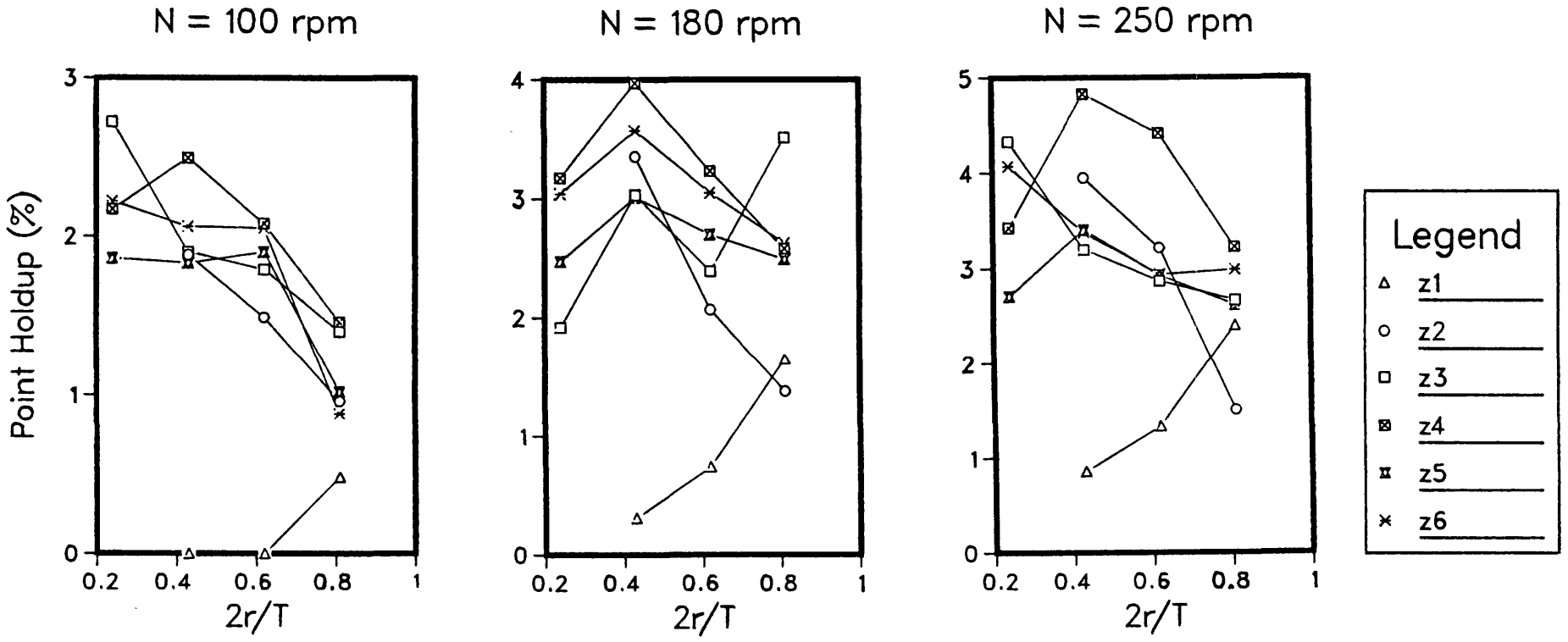

Fig 6.I2 (a) Q=0.00I64 m^3/s.

Fig 6.I2 Radial profiles of local gas holdup in vessel.

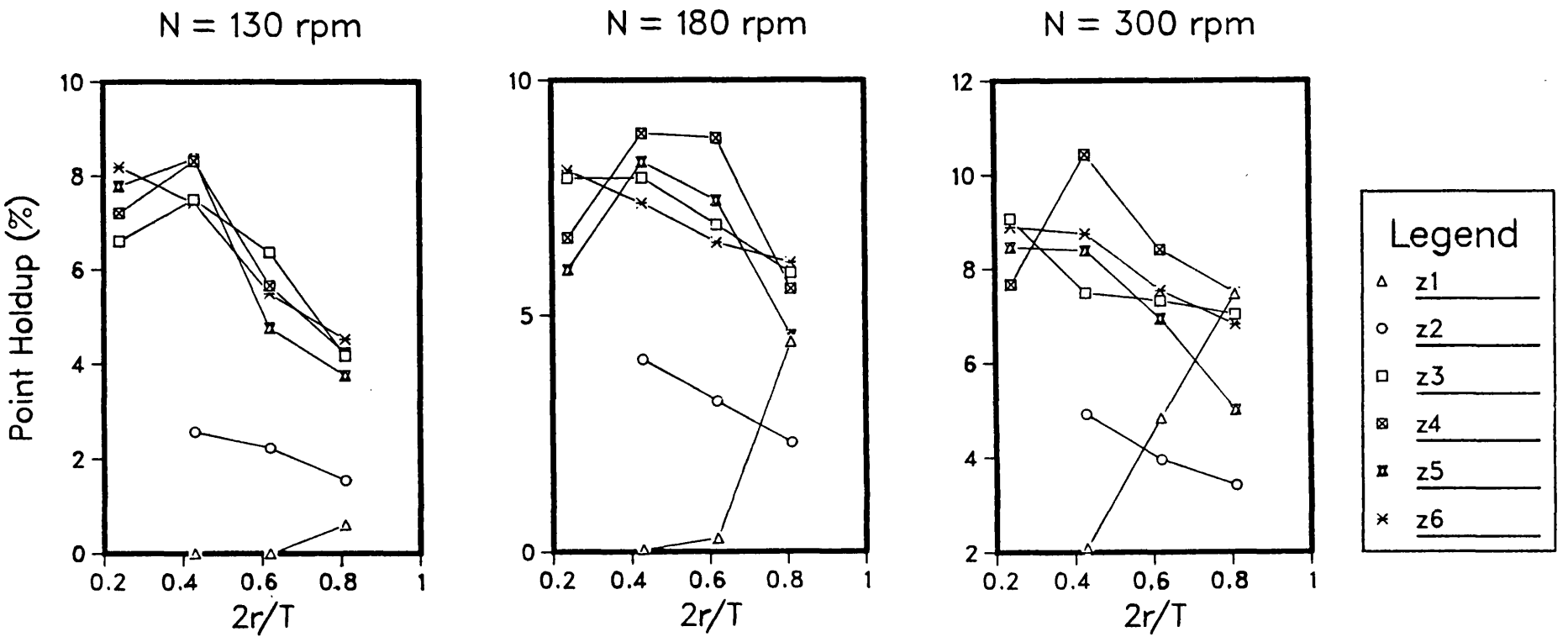

Fig 6.I2 (b) Q=0.00438 m^3/s.

Fig 6.I2 Radial profiles of local gas holdup in vessel.

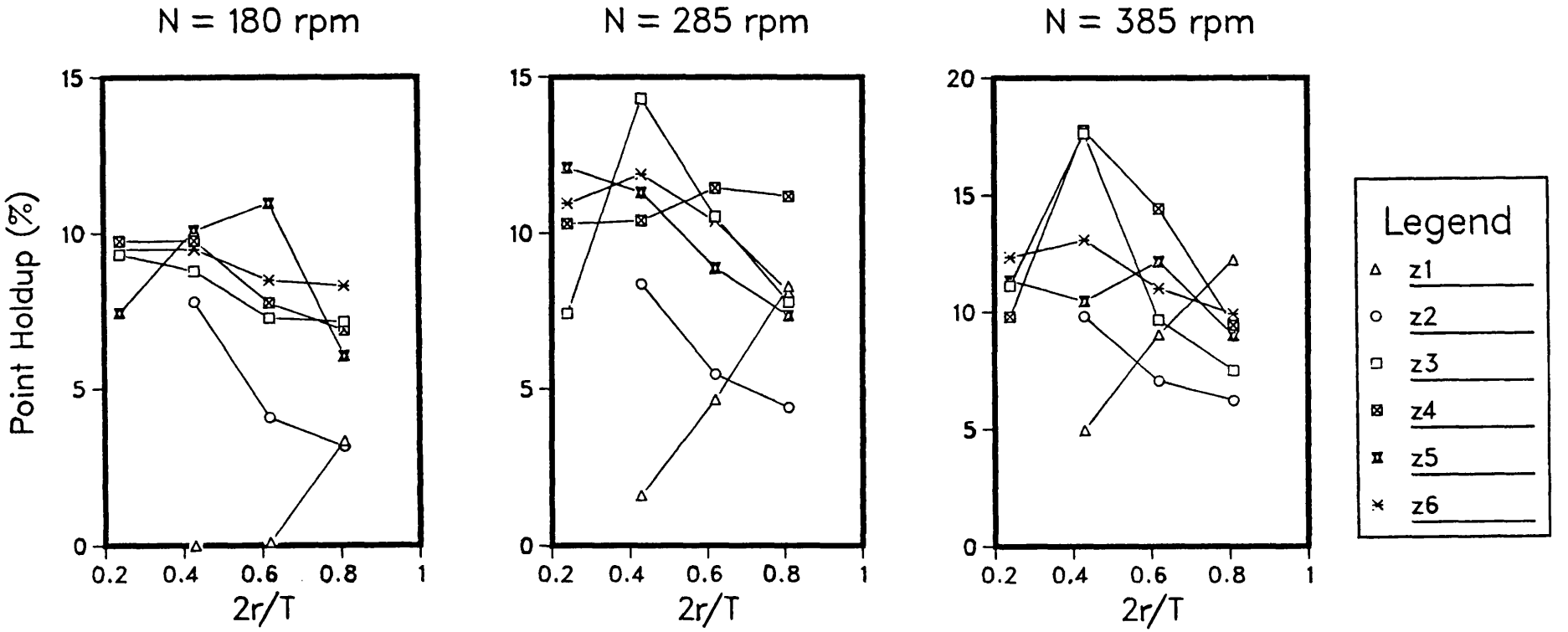

Fig 6.I2 (c) Q=0.00687 m^3/s.

Fig 6.I2 Radial profiles of local gas holdup in vessel.

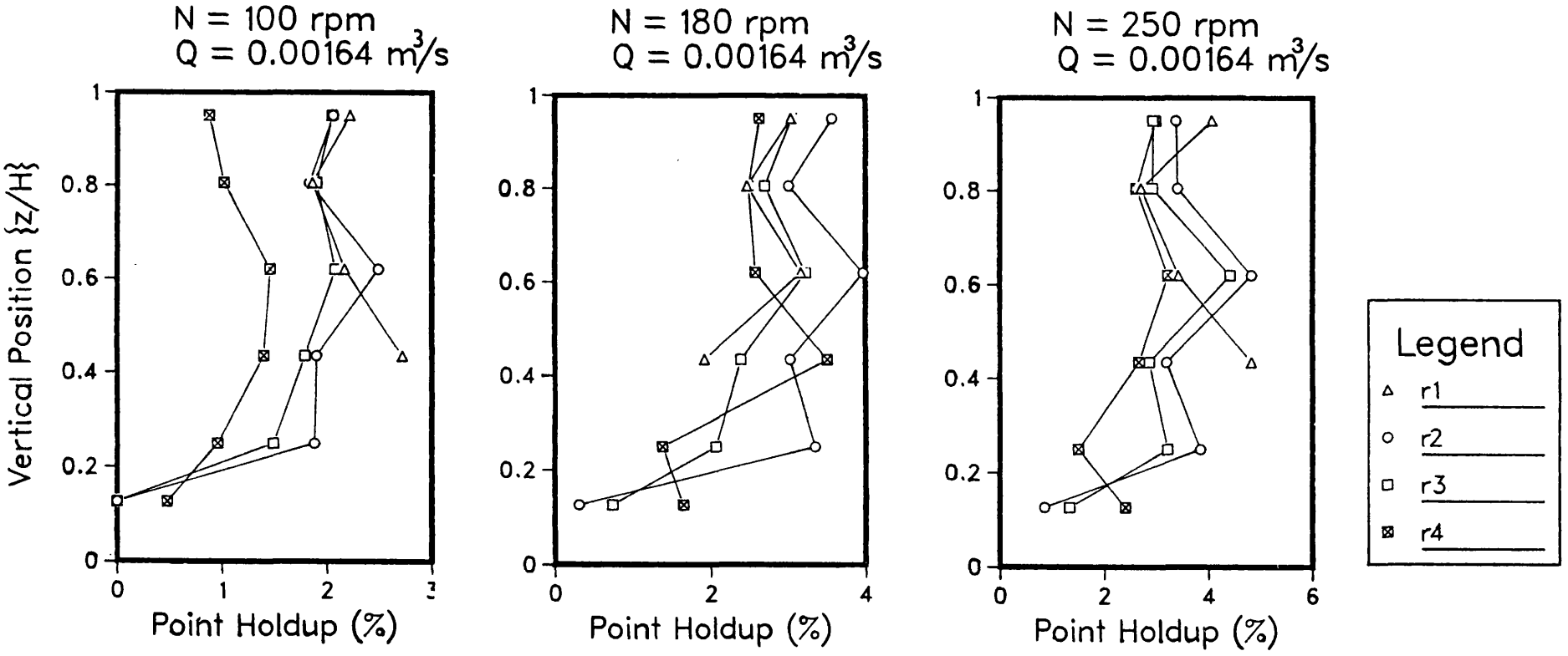

Fig 6.I3 (a) Vertical profiles of local gas holdup in vessel.

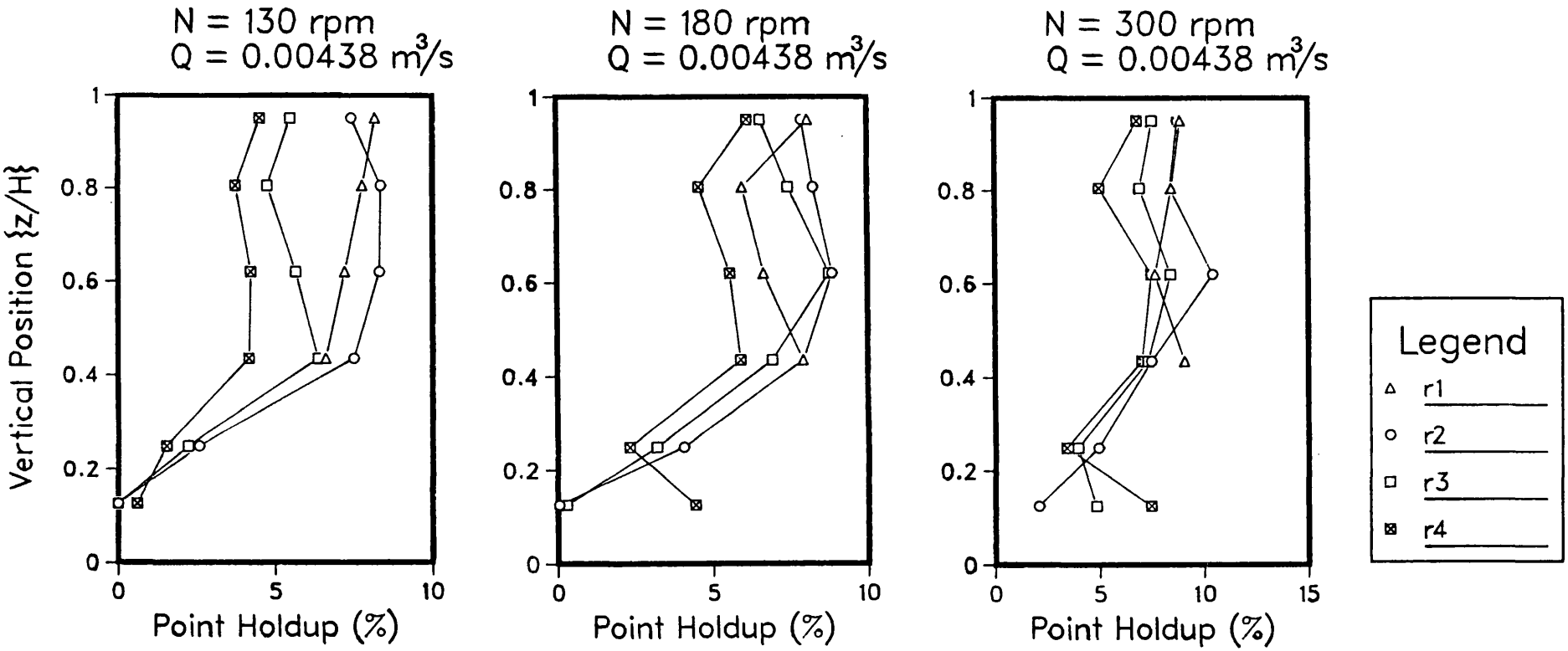

Fig 6.I3 (b) Vertical profiles of local gas holdup in vessel.

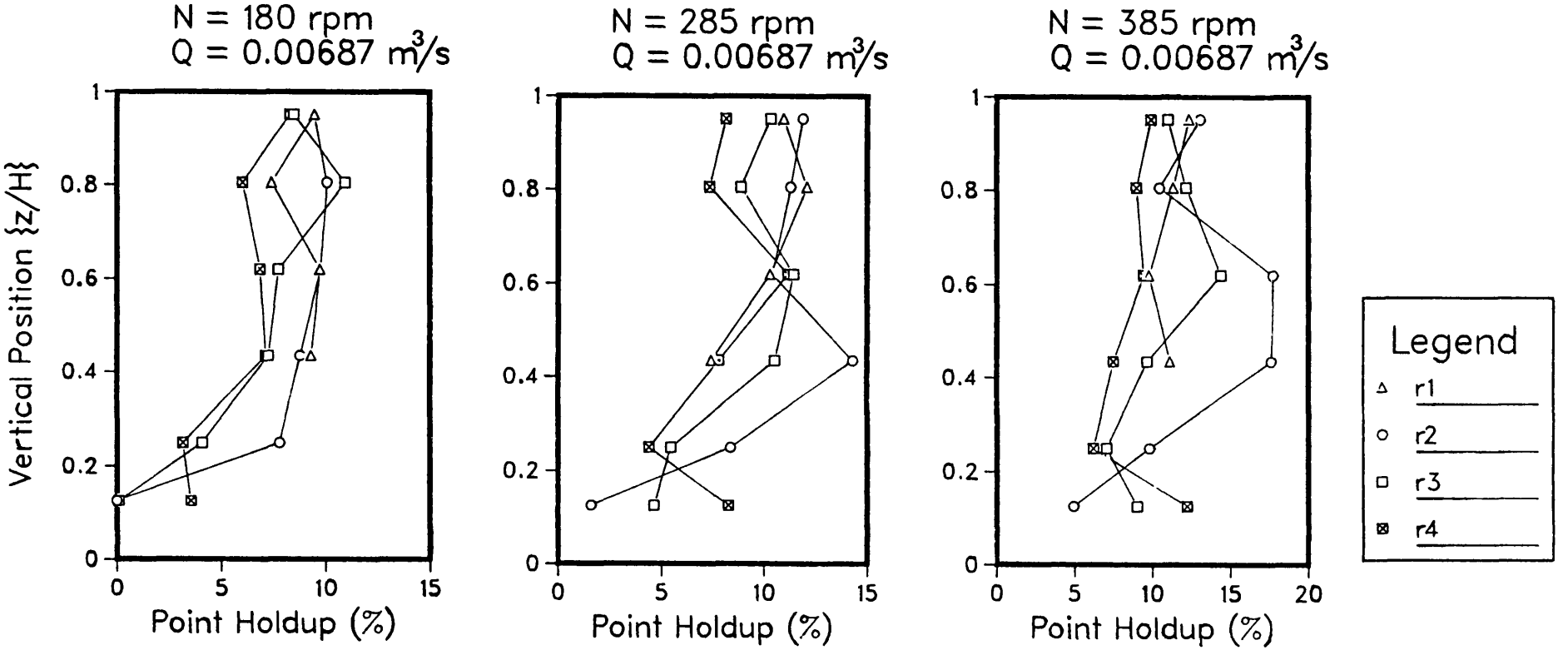

Fig 6.I3 (c) Vertical profiles of local gas holdup in vessel.

view point of gas liquid mixing.

The holdup in the impeller stream decreases monotonically, and quite sharply, away from the agitator. The level of holdup in the vicinity of the vessel wall is dependent on the radial velocity of the liquid stream from the turbine, which in turn is a direct function of N. At low speeds the buoyancy forces are effective in driving the gas quickly out of the stream, but, with increasing agitation, the buoyancy effect is overcome by the radial liquid flow, which transports more and more gas towards the boundary of the tank.

The upper part of the tank, which contains the bulk of the two-phase flow, is a region of complete gas dispersion, so long as the reactor is operated above flooding. The holdup in this region exhibits, almost invariably, sharp declining trends towards the contactor boundary, with relatively important values near the agitator shaft. The trend is principally non-monotonic with a maximum around the centre of the measurement plane. The gas in the vicinity of the wall flows upwards, concurrently with the circulating liquid at high velocities, whereas near the centre of the vessel, the buoyancy of the gas acts in an opposite direction to the downward flowing liquid. This is the reason for the difference in holdup between the two branches of the circulation loop. Close to the surface of the dispersion, the holdup is distributed radially in a fairly uniform fashion.

The effect of increasing N is to increase ϵ_p at every point in the impeller plane as well as the zone below it. In the bulk region of the vessel, however, the holdup fluctuates with impeller speed at certain locations, but the majority of positions show a monotonic increase. The overall effect of increasing N is to increase the uniformity of ϵ_p in the whole reactor under all conditions. This fact is represented by the

decreasing values of the coefficients of variation of the spatial holdup distributions in Fig 6.14.

At the constant speed of 180 rpm, the increase of Q produces an increase in ϵ_p at every point in the bulk, with the spatial distribution there remaining at approximately the same state of dispersion (C_v = 0.177,0.176,0.187) for the three gas rates employed. Also, the amount of gas dispersed in the central region of the lower volume of the vessel decreases considerably until at the highest gas load, no gas is detected at the innermost sampling position below the agitator. The reduction in the impeller pumping capacity, and therefore circulation capacity, which is due to the growth in gas cavities behind the blades (see Chapter 8), causes the flow pattern to move gradually in the direction of flooding.

6.2.3.3 Comparison with the literature

(i) Measurement methods

Despite the importance of local gas holdup, very few experimental studies are available in the literature. This is mainly due to the lack of appropriate measurement techniques. Calderbank [30] was the first researcher to tackle this problem. He made measurements in a stirred tank by sampling the air-water dispersion through a 1/4 inch diameter tube attached to an evacuated 500 cm^3 glass bulb, the latter having a gas burette attached to it. Sampling was performed by opening and closing a stopcock. The gas and liquid volumes, thus collected, were evaluated to yield the gas holdup. Loiseau [97] obtained measurements in a small reactor by means of a conductivity type probe with a 2 mm stainless-steel electrode. Figueiredo [38] also used a conductivity probe to acquire point holdup data in a stirred vessel. She found that the probe underestimated the holdup with respect to the overall measured value.

Nienow et al [76] employed a peristaltic pump to withdraw air-water dispersions from a reactor through a 0.33 mm capillary. Although they used a very short length of capillary (3 mm), which means that the suction rate through it must have been very high, the validity of the results should be considered with some scepticism because of some apparently high values detected (see also Section 6.2.1). Nonetheless, from a qualitative point of view their results are still useful. Nagase and Yasui [98], performed measurements by means of a 0.3 mm Nickel-wire electrode mounted inside a 3 mm glass suction tube. The authors claim that the holdup measurements obtained using both this technique and an independent needle-type probe agreed with each other within 20%. This method, although it uses a tube to sample the two-phase flow, it does not rely on the measurement of the gas and liquid volumes collected, like for instance, the method of Nienow et al [76]. Instead, it can be pictured as a resistivity probe inside a tube, and therefore does not come under the usual category of suction techniques. Most recently, Greaves et al [99] have tested a more sophisticated version of the early technique of Calderbank [30]. The procedure is based on the pressure change which arises when an intermittent series of gas-liquid samples is introduced through a glass tube into an isolated vacuum chamber. Each sample is acquired over a period of 6 seconds. A series of solenoid valves was used to control the intermittent sampling sequence. A host microcomputer was programmed to supervise the automatic procedure of holdup measurement. A single measurement requires 20 minutes. The technique was tested in a 0.75 m tank, and was found to give good reproducibility and good agreement with the overall holdup.

(ii) Literature results

-Calderbank [30]: His measurements relate to a 0.50 m tank. He presented the variations with vertical distance of the point holdup measured at the centre of the radius equidistant from two baffles, shown in Fig 6.15. These plots bear a lot of resemblance to the vertical profiles of the mean radial holdup obtained in this work, which are displayed in Figs 6.16(a-c) for all of the conditions investigated. Both sets of plots show significant dependence of the holdup on depth, and exhibit a peak mid-way between the impeller plane and the surface. This peak becomes sharper as the speed of agitation increases. The characteristic feature of Calderbank's distributions is the second peak at the impeller level, which is independent of stirrer speed. The effect of increasing N, in his case, is to shift the distributions towards high values, but only in the upper part of the vessel. In our case, the whole distributions are, invariably, displaced.

-Loiseau [97]: This author is the only researcher who has produced results for an electrolyte solution. His experiments relate to an air-0.8M Na_2SO_3 system in a 0.19 m reactor. He presented distributions of the local holdup in the central segment of the median plane between two baffles. Typical profiles have been drawn in Fig 6.17. Their great similarity with the trends in Figs 6.16(a-c) is evident. He found that below the minimum agitation speed required for full gas dispersion, the holdup increased monotonically with height, and for higher speeds the gas occupies the whole volume of the vessel and the holdup exhibits a maximum at the centre of the reactor. The level of gas holdup below the impeller plane is generally low, except at very high speeds. The small sizes of the bubbles, in this case, and their low rise velocities contribute towards establishing a more significant holdup in the lower part of the tank as compared with 'coalescing' systems.

Fig6·14 Degree of Dispersion of Point Holdup Distributions

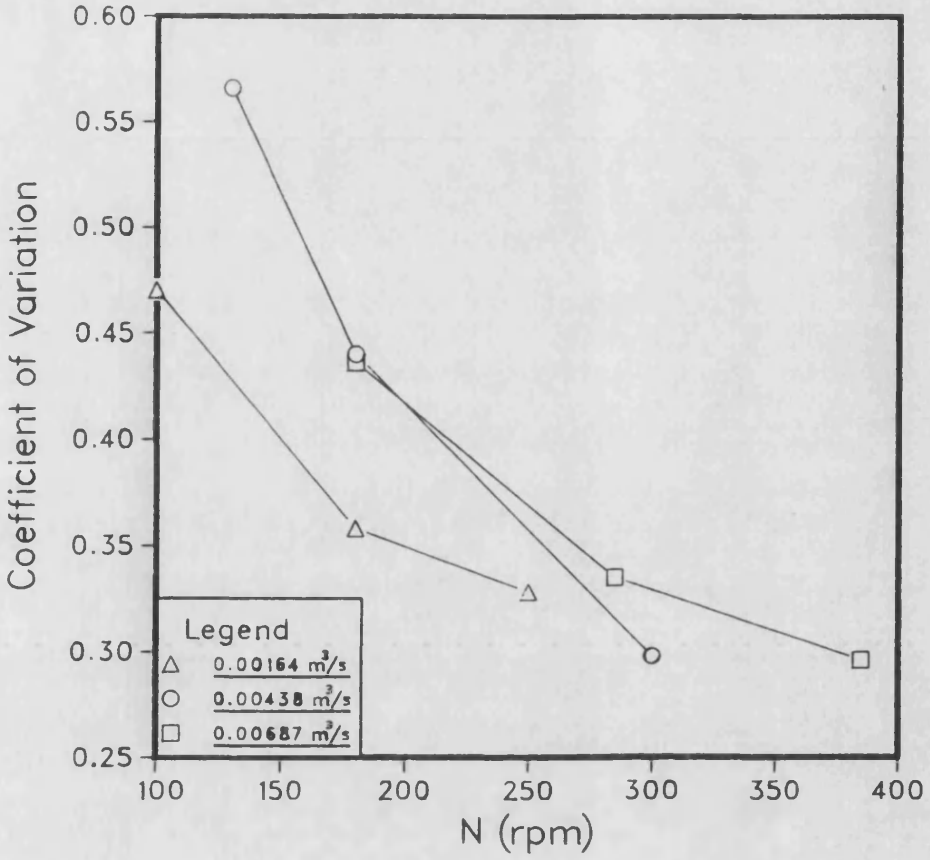

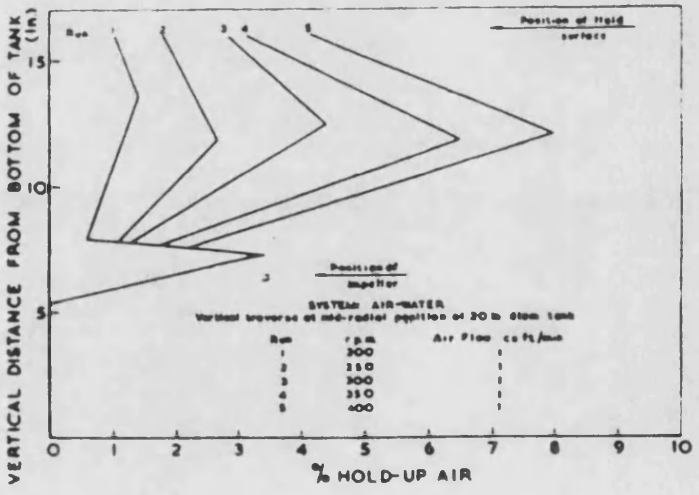

Fig 6.15 Typical vertical distribution of gas holdup in a 0.50 m tank, after Calderbank (30).

Fig 6.16 (a) Point Holdup Distributions
$Q = 0.00164\ m^3/s$

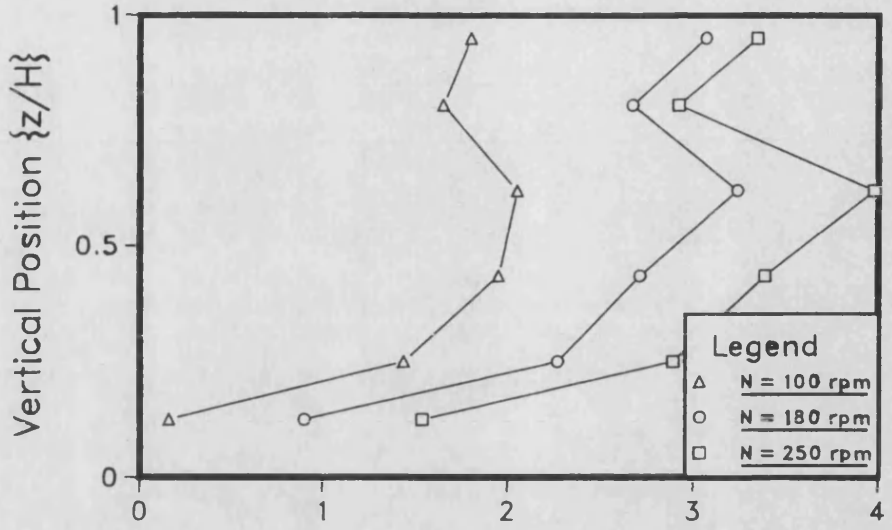

Fig 6.16 (b) Point Holdup Distributions
$Q = 0.00438\ m^3/s$

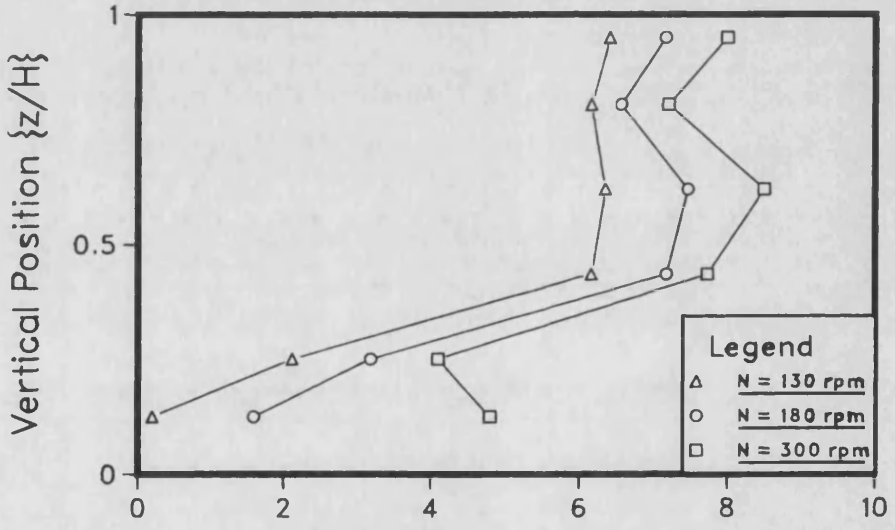

Fig 6.16 (c) Point Holdup Distributions
$Q = 0.00687\ m^3/s$

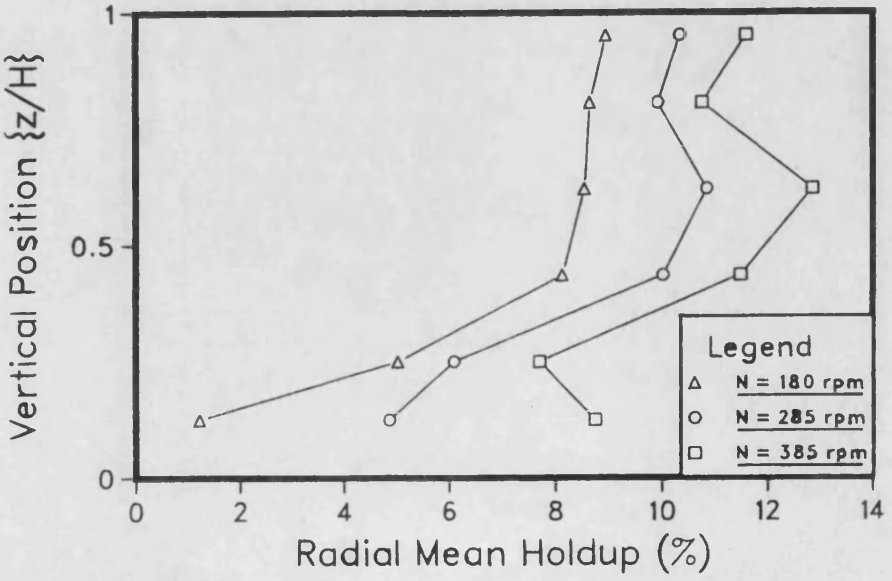

Fig6-17 Point Holdup Distributions of Loiseau [97]
$Q = 0.00018\ m^3/s$

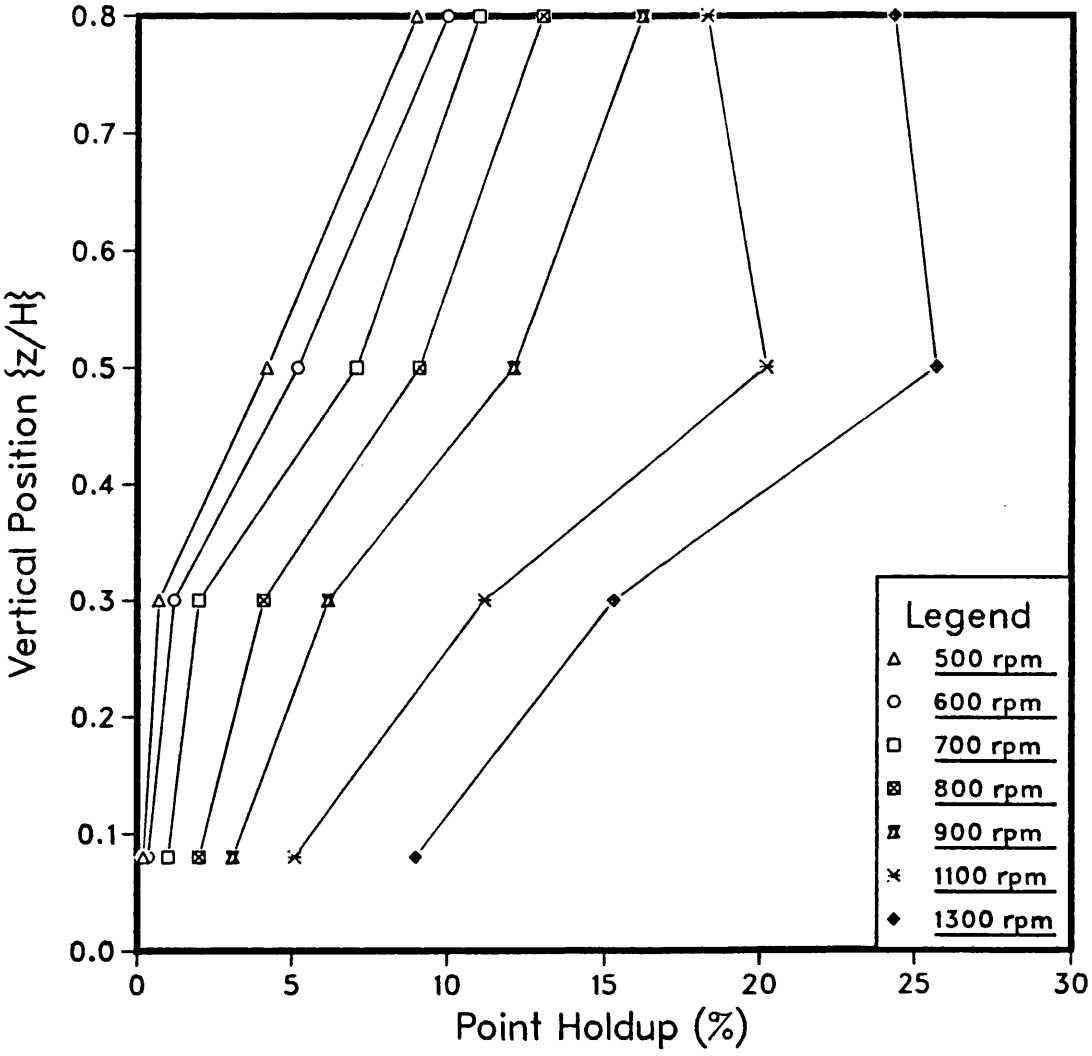

-Nienow et al [76]: They produced measurements in a 0.29 m vessel. In agreement with the radial distributions obtained here, they found that their distributions also peaked mid-way between the centre of the vessel and the wall, with high holdup values near the shaft and low values near the wall. Close to the surface their radial profiles also became flatter. The holdup in the lower part of the tank showed a decreasing trend from the wall towards the central region too, with very low values in the central zone. The vertical distributions of the authors' data have been plotted in Fig 6.18. The bulk section of these curves peaks above the impeller plane, in agreement with the curves in Figs 16(a-c). The minimum observed in the impeller plane, in their case, contradicts the maximum found by Calderbank at that position.

-Nagase and Yasui [98]: Their data was obtained in a 0.25 m reactor. The holdups near the impeller shaft were found to be higher than those near the tank wall, with a gentle maximum around the central position. This radial profile becomes fairly uniform at high levels. The vertical distributions produced by these workers are presented in Fig 6.19. They indicate a monotonic increase of holdup in the upper section of the dispersion, which is contradictory to all literature results except those of Loiseau [97], above, which were obtained at speeds below that for complete dispersion of the gas. Calculations showed that whereas for the lowest gas flow rate, the reactor was run just above the N_{CD} value, for the higher gas loads, it was in fact operated at a speed below this criterion. From these trends it is apparent that the holdup below the impeller is very low, which is consistent with the present findings.

-Greaves et al [99]: Their measurements which relate to a 0.75 m dished bottom tank, also revealed that the maximum holdup occurs at a

Fig6·18 Point Holdup Distributions of Nienow et al [76]

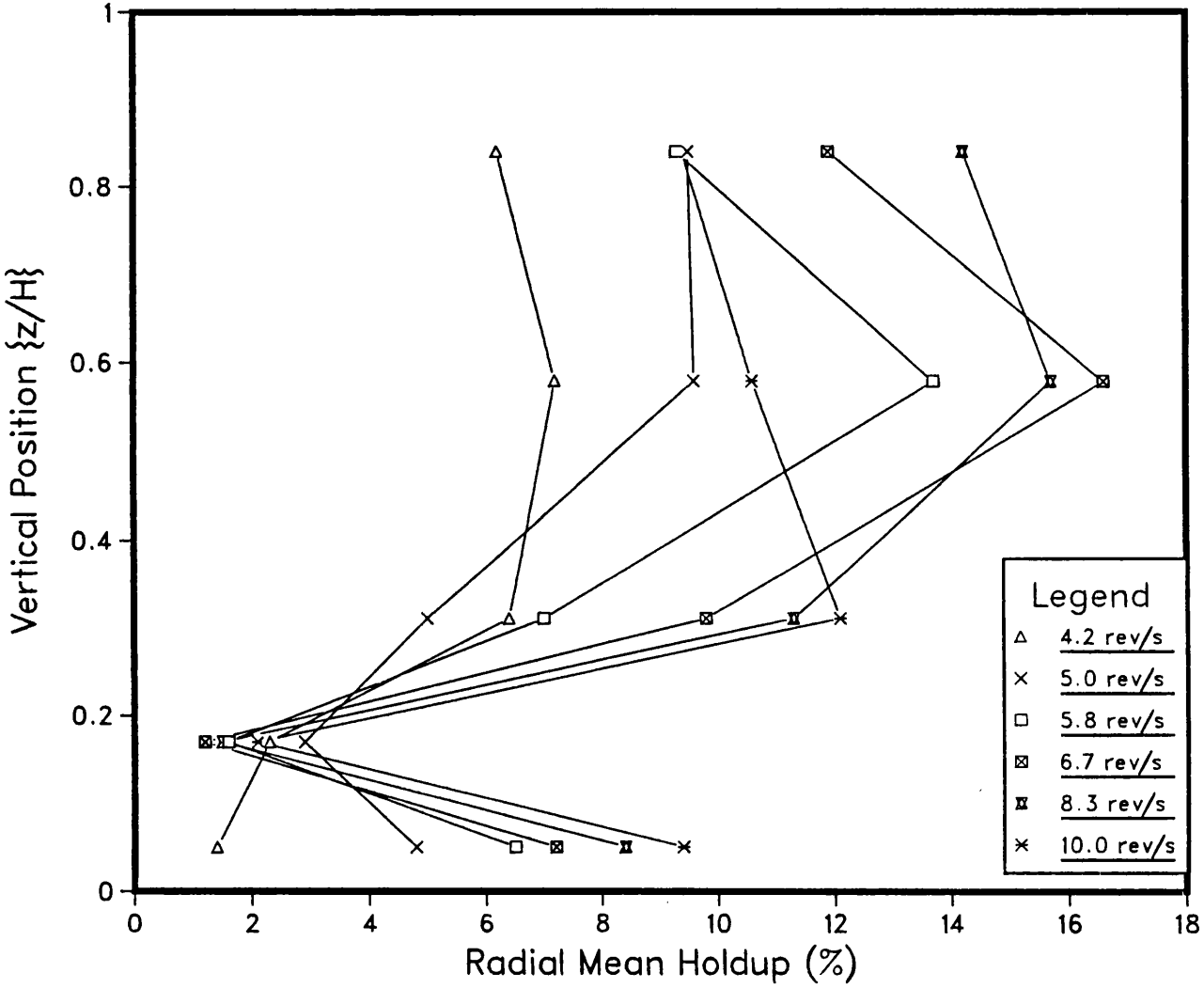

level between the impeller plane and the surface, as shown in Fig 6.20. The holdup generally decreased radially towards the tank wall, but no measurements were made in the segment near the shaft. The central region below the impeller contained low holdup values, and also in agreement with the findings of this work the location near the wall has a high gas content. Similar to present results, the effect of increasing N is seen to produce an increase in holdup at all sections in the tank.

-Figueiredo [38]: The author produced only a limited number of data points (9 points) in a 0.91 m tank, with no measurements taken below the agitator level. Although detailed comparison of the results is not possible, her measurements showed, consistently with present data, that an increase in speed causes the point holdup to increase at virtually all locations and enhances uniformity in the spatial holdup distribution.

6.3 Gas-liquid interfacial area

6.3.1 Interfacial area distributions

The point interfacial area distributions, shown in Fig 6.21, were derived from the point bubble Sauter diameter values of Fig 5.10, and the point holdup distributions of Fig 6.10, through the relationship:

$$a_p = 6\epsilon_p / d_{32_p} \qquad (6.3)$$

In the region below the impeller, the interfacial area decreases away from the wall. Towards the central zone, as discussed in the previous sections, the bubble density is generally low. Values at the impeller plane are remarkably high close to the agitator periphery because of the high local holdup and small bubble size. This trend, however, falls sharply towards the vessel boundary. In the bulk of the reactor, typically, as shown in Fig 6.22, the radial distributions of a_p,

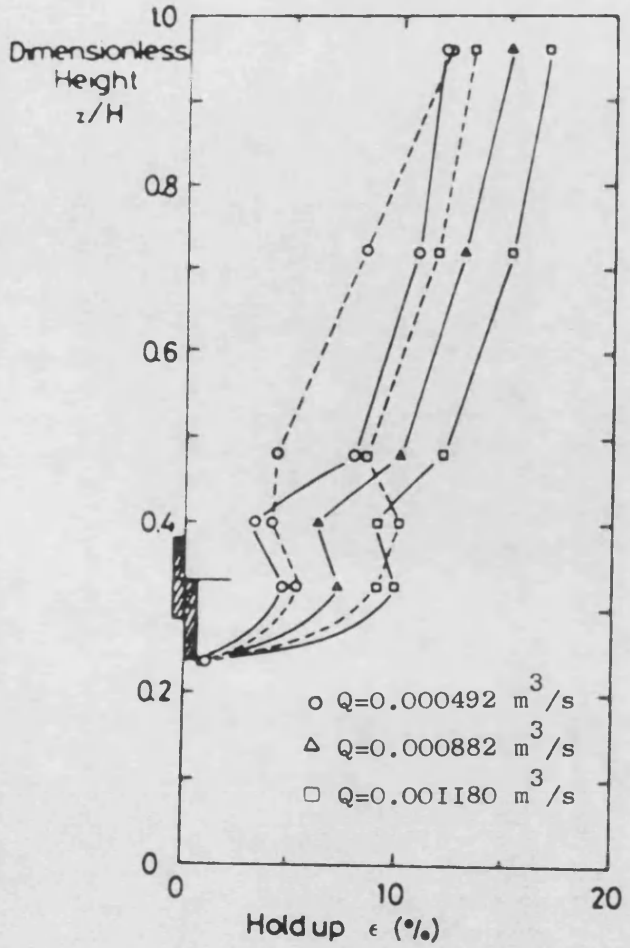

Fig 6.19 Radially averaged gas holdup as a function of height (98).

___ Disc turbine

- - - Vaned disc turbine

Fig6.20 Point Holdup Distributions of Greaves et al [99]

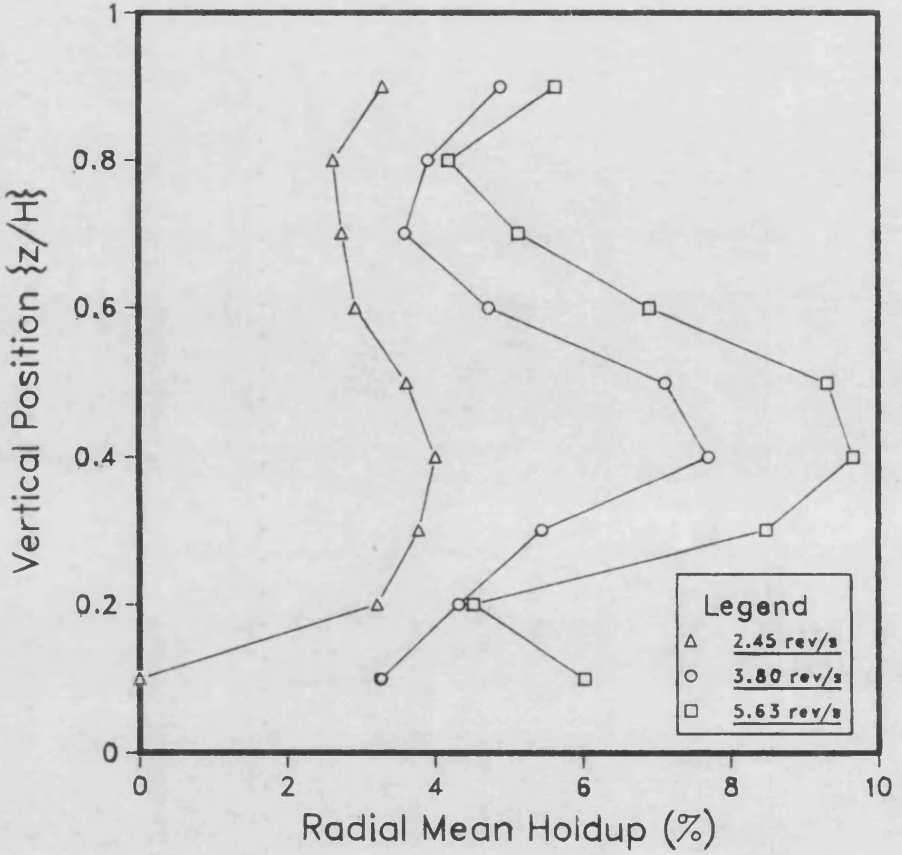

Fig 6.21 Spatial disributions of interfacial area (m^{-1}).

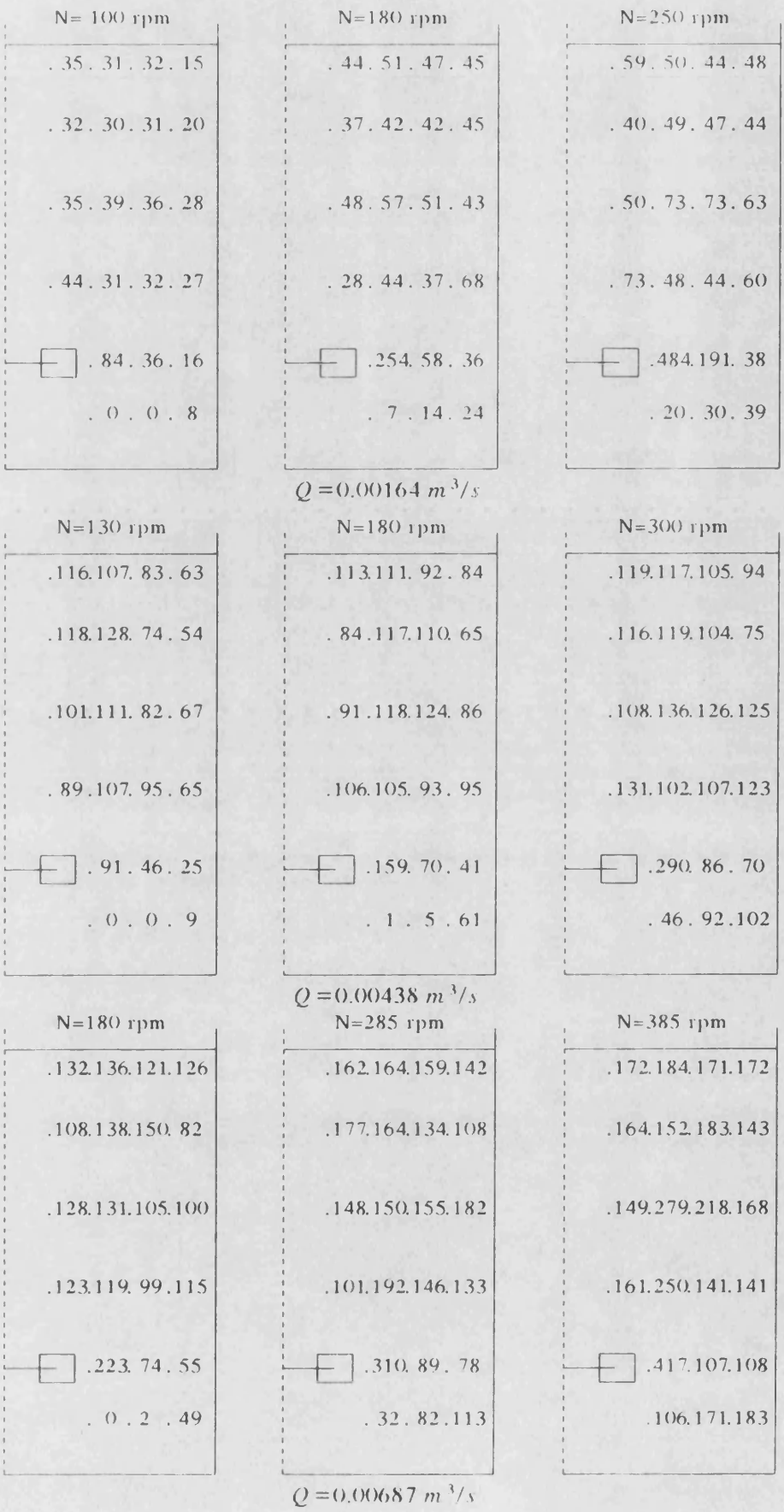

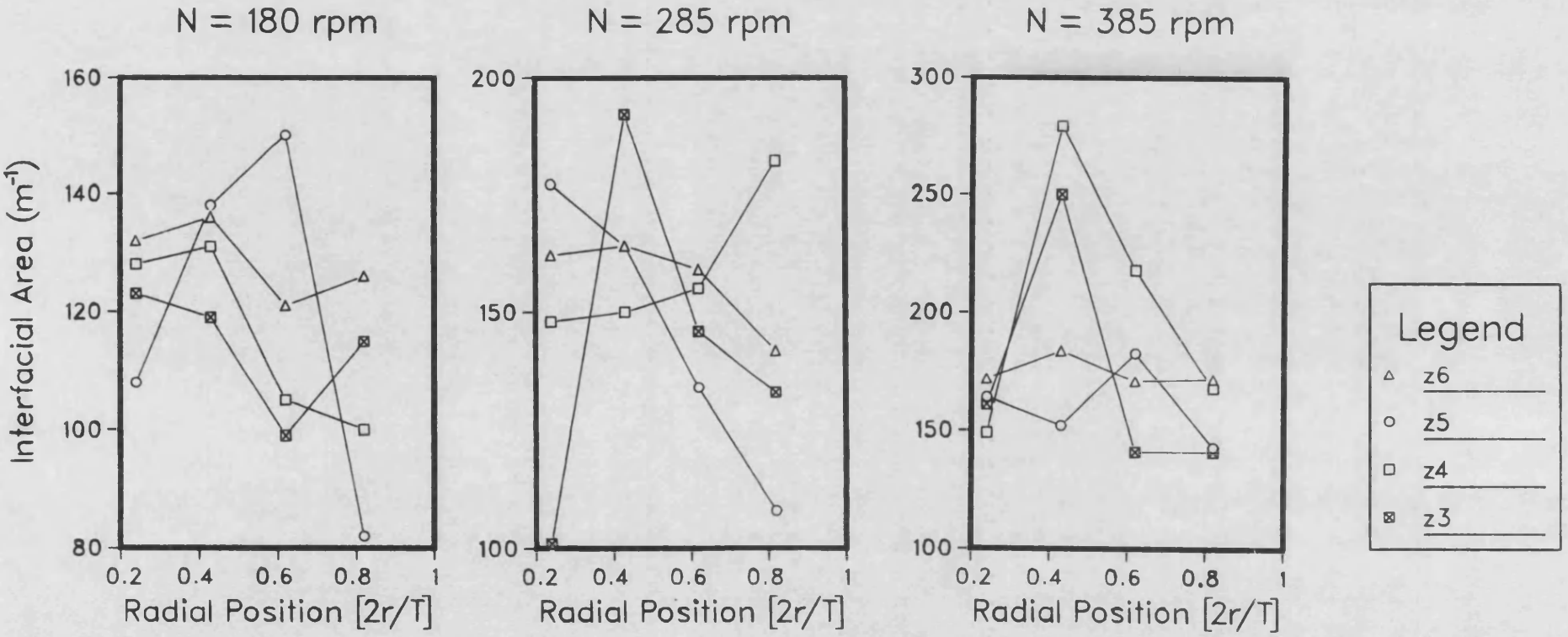

Fig 6.22 Radial profiles of local interfacial area in upper part of vessel.
(Q=0.00687 m^3/s)

present a maximum between the centre and the wall of the vessel, with a declining trend towards the wall. The least spread in these distributions is found near the surface of the dispersion. The vertical distributions corresponding to these same agitation conditions, are presented in Fig 6.23. At low rotational speeds the profiles fluctuate in a complicated manner and no generally distinct trend can be observed. But, at the highest speed, the curves exhibit a distinct peak near the middle of the tank depth.

The variations of the interfacial area, averaged radially, with liquid depth are also presented in Fig 6.24 for the conditions investigated. These profiles are characterised by two peaks, at the agitator level and between the free surface and the turbine. This is consistent with the earlier distributions produced by Calderbank [30] from measurements in a 0.50 m tank using a light obscuration technique, as described in Section 2.2.2. These peaks become sharper as agitation is enhanced. A relatively large proportion of the total gas-liquid interfacial area in the tank is contained in the impeller discharge stream, which shows the important contribution of the impeller region to mass transfer, by virtue of the intense turbulence which is generated.

The radial distributions of interfacial area, averaged over the height of the tank, are plotted in Fig 6.25, for the agitation conditions used. They exhibit a steeply rising trend from the centre of the reactor towards a maximum value at a radial position near the middle of the measurement plane, followed by a sharp fall and subsequently by a gradual decline towards the wall. These trends are similar to a typical radial distribution presented by Calderbank [30].

Mean integral interfacial area values, a, were obtained through a two-dimensional integration of the spatial surface area distributions, for

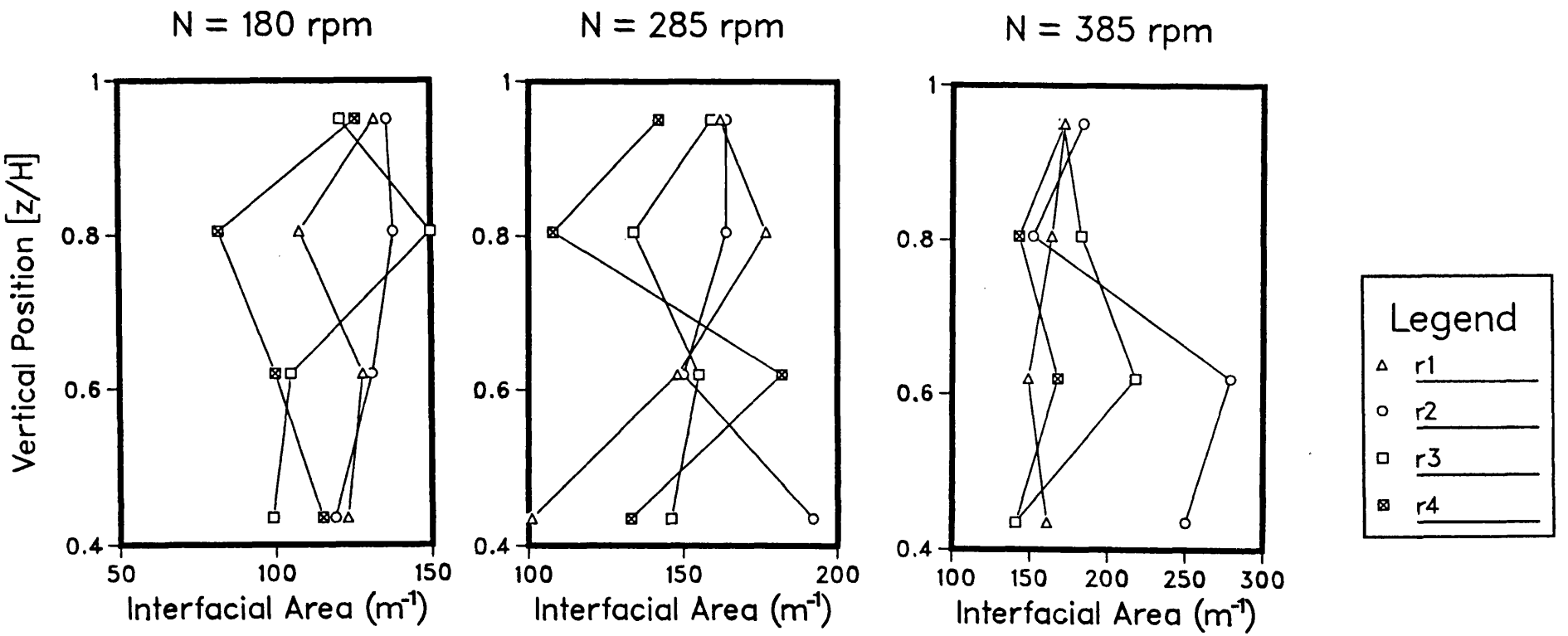

Fig 6.23 Vertical profiles of local interfacial area in upper part of vessel.
(Q=0.00687 m^3/s)

Fig 6.24 Vertical Profiles of Radial Mean Interfacial Area

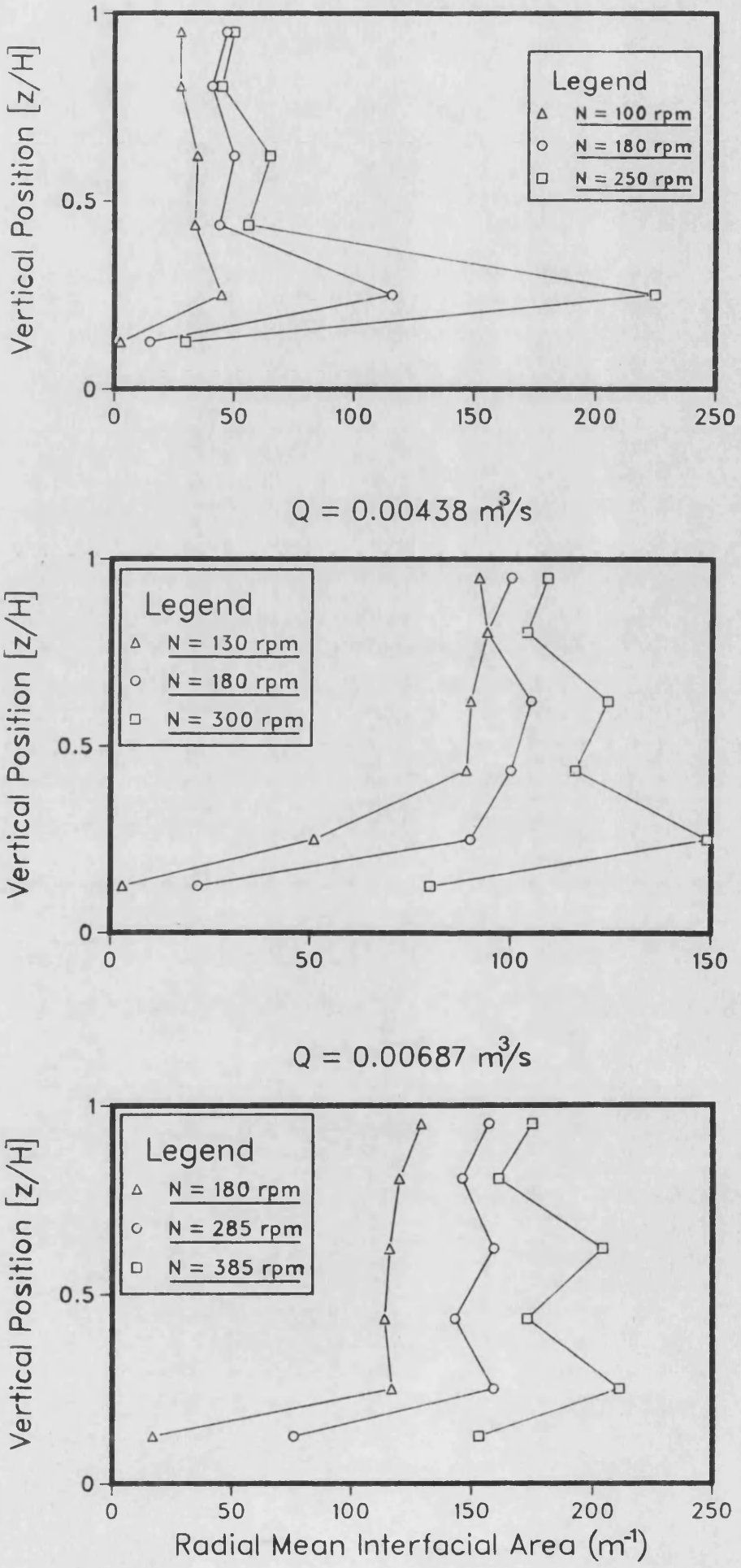

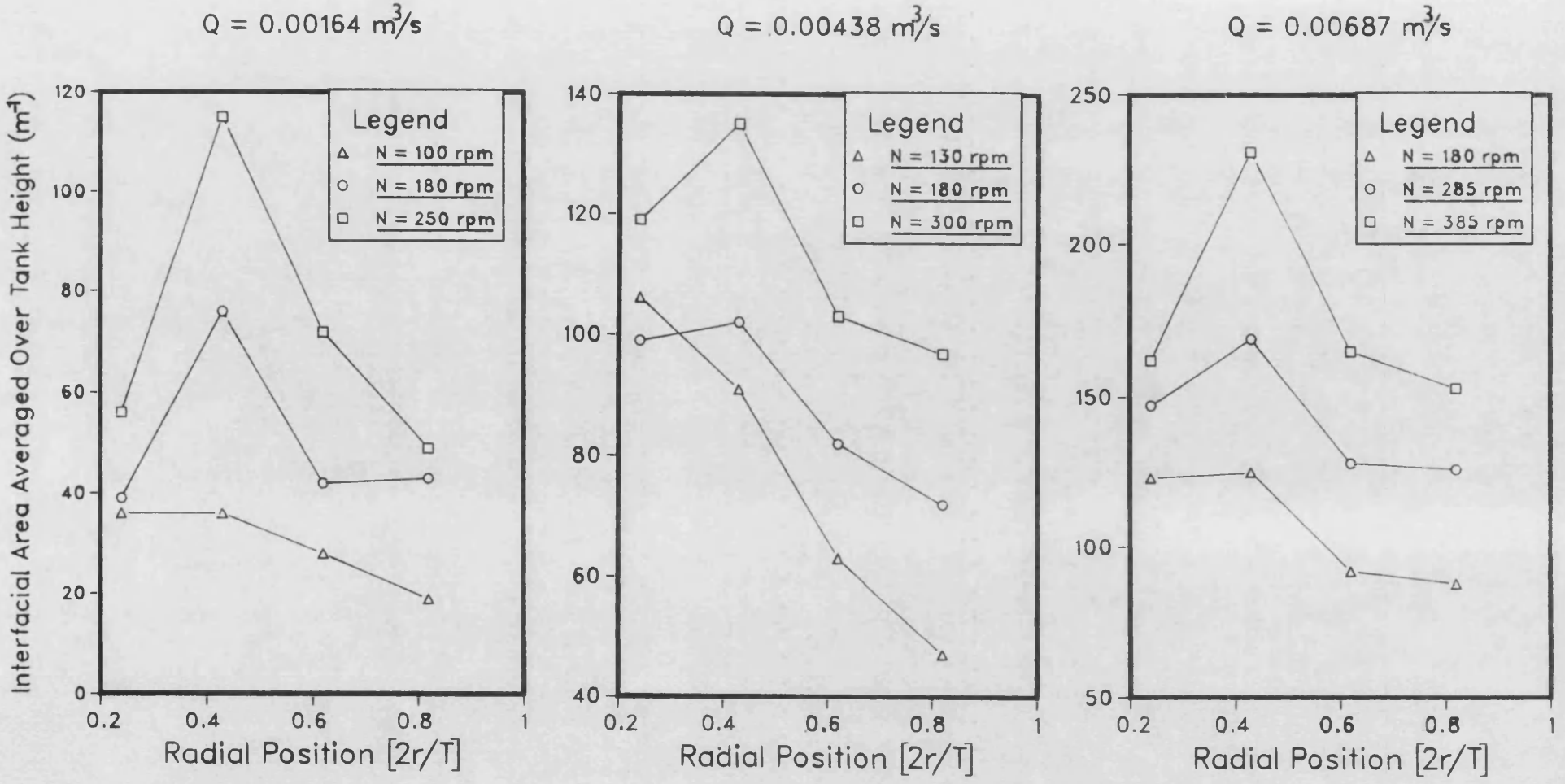

Fig 6.25 Radial profiles of interfacial area averaged over height of tank.

all of the agitation conditions investigated. The effect of stirrer speed on the mean integral surface area is illustrated in Fig 6.26. Although the number of data points is limited, a appears to increase with N in a consistently quasi-linear fashion for all gas flow rates used. The trends for the three gas loads are almost parallel. The effect of varying Q at constant speed (N=180 rpm) leads to a considerable enhancement (50%) in interfacial area at low gas feeds, but the rate of increase declines at higher values of Q (20%), leading to a situation of diminishing returns.

The data obtained was correlated by non-linear least squares regression, to yield the following equation:

$$a = 250N^{0.85}Q^{0.38} \tag{6.4}$$

where, r=0.954 and s=0.1137. As shown in Fig 6.27, this correlation fitted the experimental data, quite reasonably with an uncertainty range of ±15%.

The common way of predicting interfacial area uses the specific power and the superficial gas velocity. On this basis, the results are correlated by:

$$a = 186\left[\frac{P_{gt}}{V}\right]^{0.30} U_s^{0.51} \tag{6.5}$$

with, r=0.960 and s=0.1063. This equation is plotted in Fig 6.28, where the scatter of the data is within ±15%.

6.3.2 Effect of ionic solution

Since no point holdup distributions were available for the air-0.15M NaCl solution, the bubble size distributions produced for this gas-liquid system were used to obtain an overall representative bubble

Fig6·26 Mean Integral Interfacial Area vs Impeller Speed

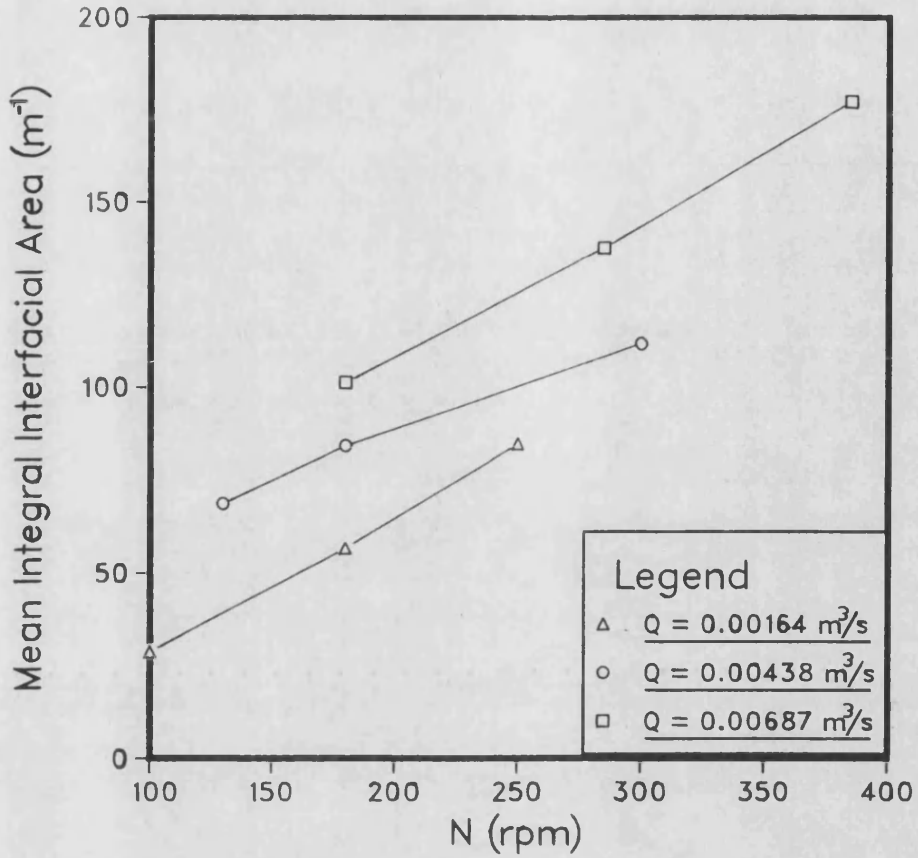

Fig6·27 Correlation of Interfacial Area

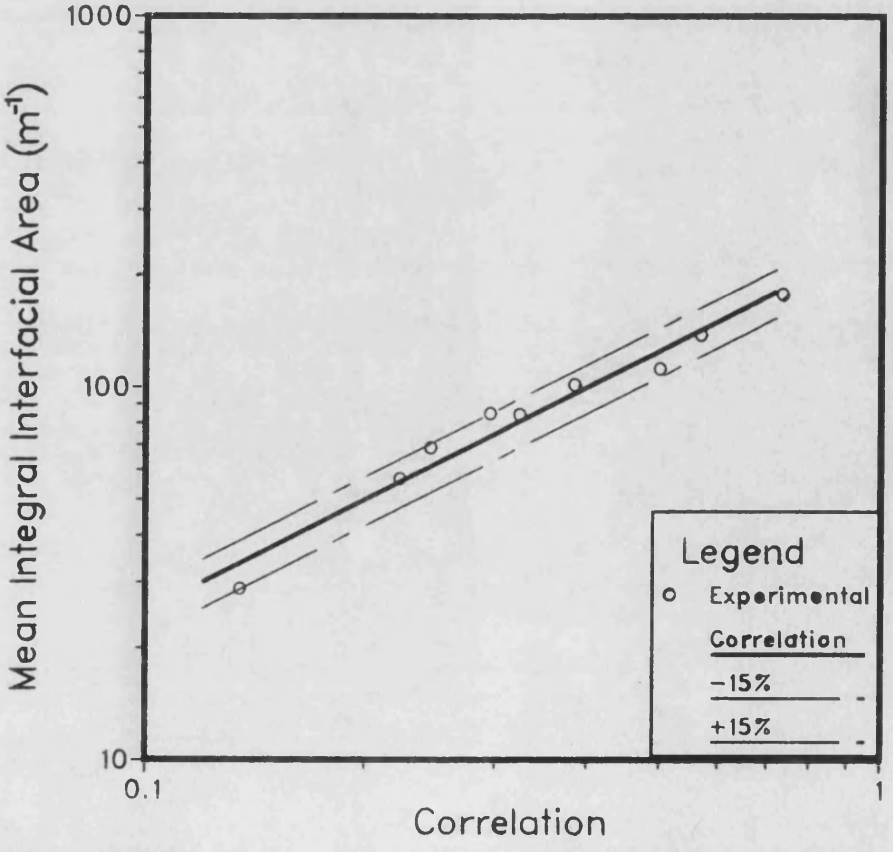

Sauter diameter value in each case which, in conjunction with the measured overall gas holdup, allowed the total interfacial area to be predicted from:

$$a = 6\epsilon/\bar{d}_{32} \tag{6.6}$$

The interfacial areas for the ionic system are compared with the interfacial areas for the air-water system, relating to the same agitation conditions, in Fig 6.29. There, it can be seen that the electrolyte concentration used generated a substantial increase in a, under all conditions, in a range of 52 to 111%.

Two separate correlations were obtained for a:

$$a = 206N^{1.02}Q^{0.28} \tag{6.7}$$

where, r=0.998 and s=0.0193.

$$a = 178\left[\frac{P_g}{V}\right]^{0.36} U_s^{0.45} \tag{6.8}$$

where, r=0.999 and s=0.01752. Both correlations fitted the data within ±8%, as shown in Figs 6.30 and 6.31.

Few correlations for predicting interfacial area are available in the literature. The majority were derived from chemical reaction measurements and are, therefore, unreliable. This point is substantiated in Section 2.2.1. The best correlation produced thus far, is that of Calderbank [30]:

$$a = 1.44\left[\frac{(P_g/V)^{0.4}\rho^{0.2}}{\sigma^{0.6}}\right]\left[\frac{U_s}{U_t}\right]^{0.5} \tag{6.9}$$

This equation was based on the integrated local interfacial area measurements acquired directly by the well known light transmission

Fig6·29 Effect of Ionic Solution on Interfacial Area

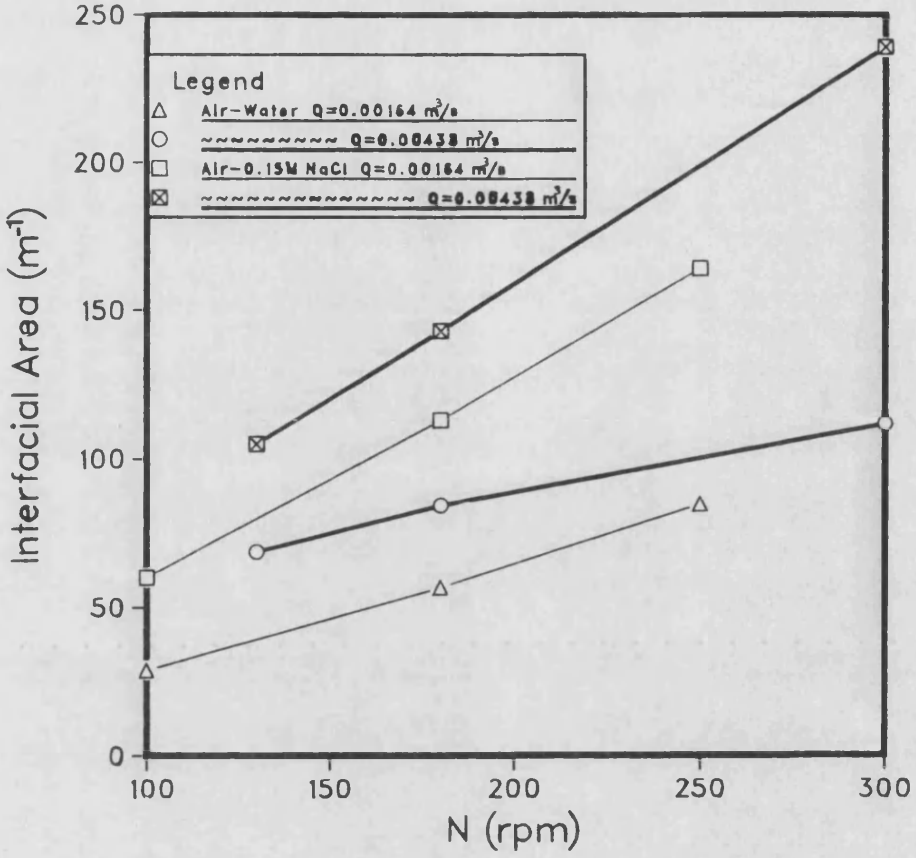

Fig6·28 Correlation of Interfacial Area

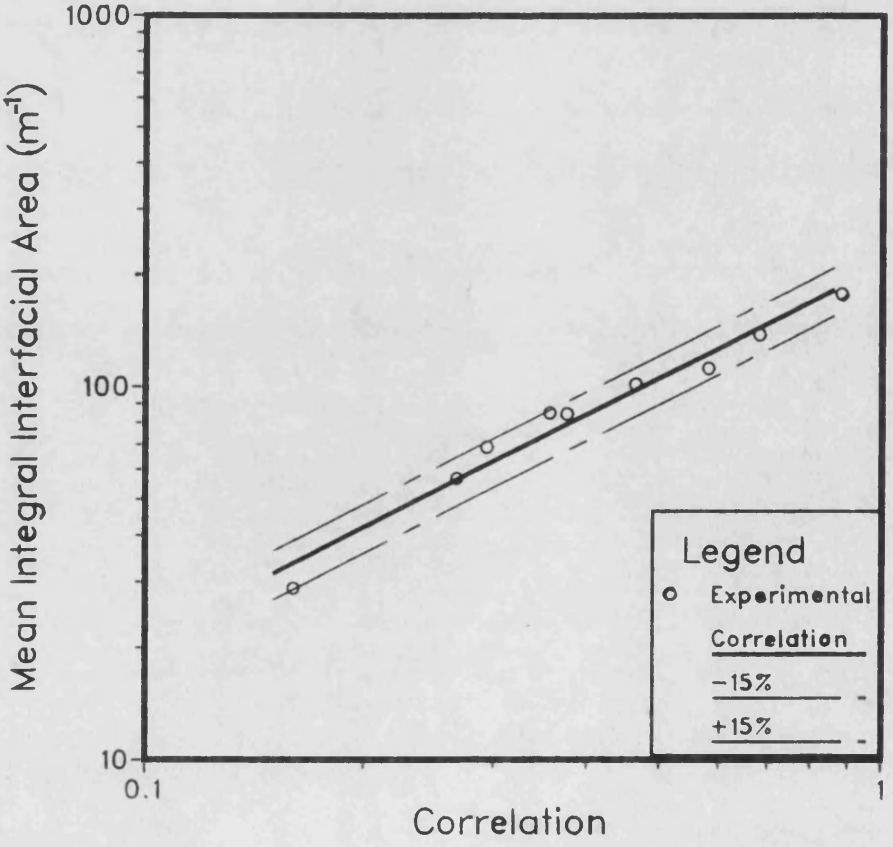

Fig6·30 Correlation of Interfacial Area Air–0.15M NaCl

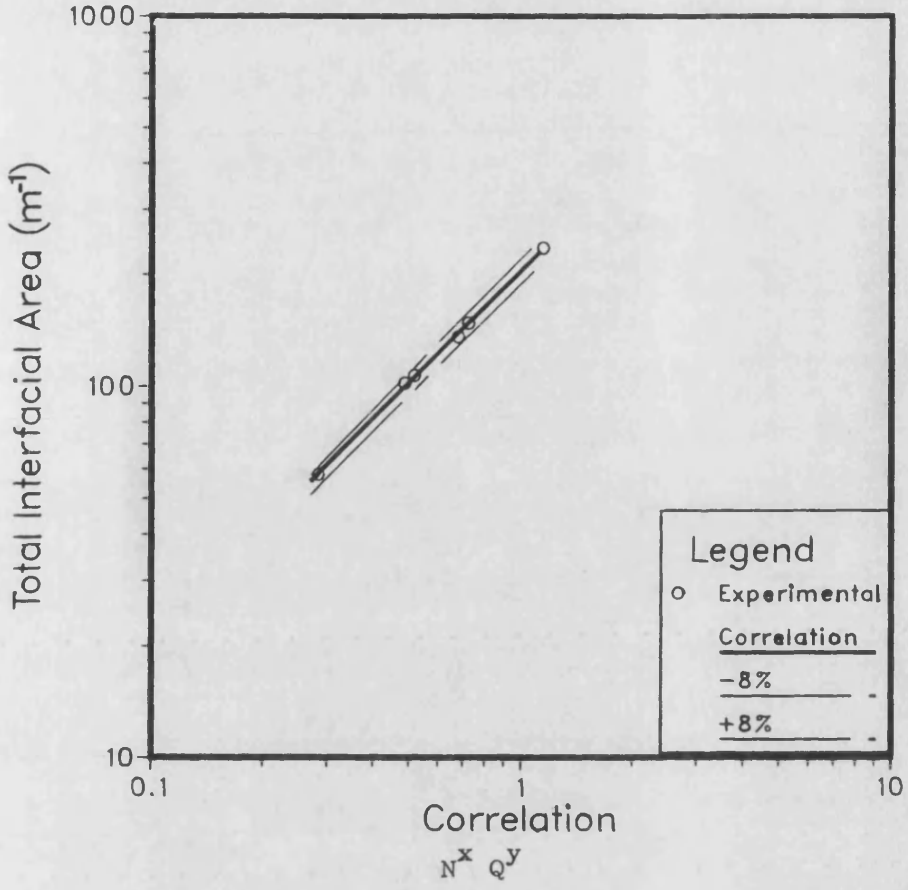

Fig6·31 Correlation of Interfacial Area Air–0.15M NaCl

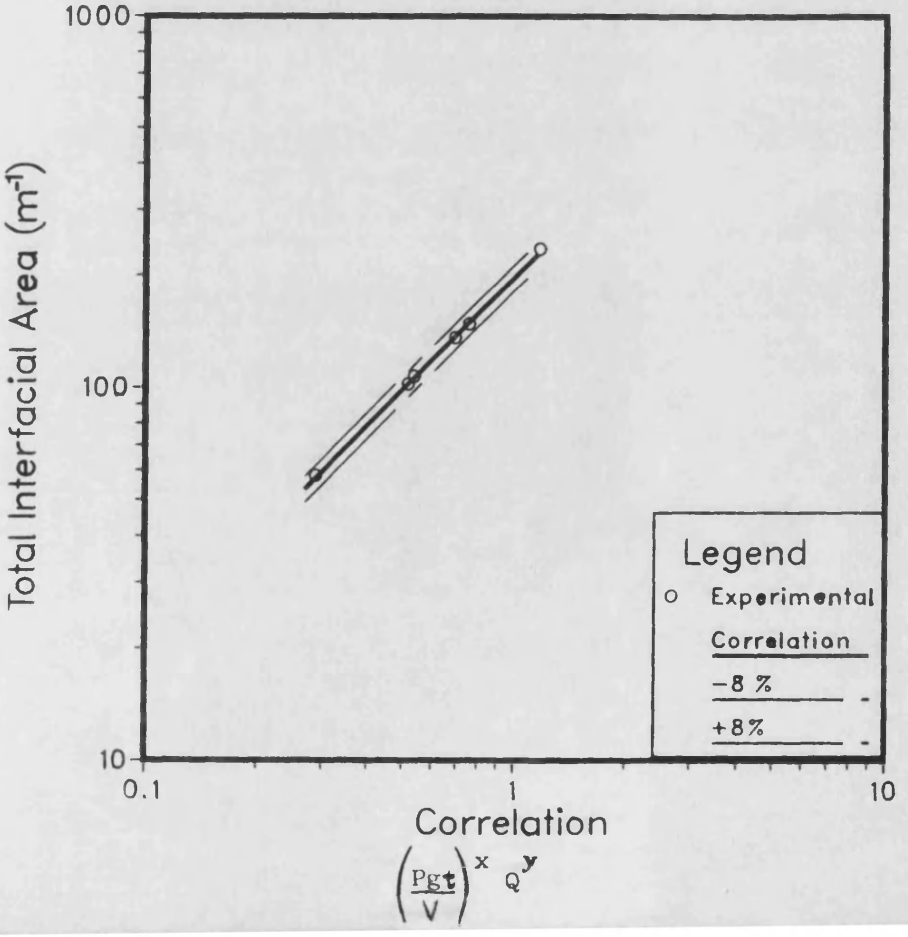

technique, in two reactors (0.19 and 0.50 m), using ten different liquids. Later, Sridhar and Potter [3] improved on the technique and extended Calderbank's original correlation to pressures higher than atmospheric. Substituting for the values of the physical properties of the solution used here (ie., $\rho=999\ Kg/m^3$ and $\sigma=70.99\times10^{-3}\ N/m$), and noting that $U_t=0.0265\ m/s$ [30], Calderbank's equation becomes:

$$a = 172\left[\frac{P_g}{V}\right]^{0.4} U_s^{0.5} \qquad (6.10)$$

Comparison of Equation (6.10) with Equation (6.8) shows that the power and superficial velocity exponents are close to each other and are certainly identical to one decimal place. The proportionality constants are also in excellent agreement.

6.4 Conclusions

- The spatial distribution of the bubble population inside the vessel is highly uneven. The degree of dispersion of the distribution varies in a non-monotonic fashion with stirrer speed and gas flow rate. The effects of the two variables N and Q, being opposite.

- The point holdup was found to change appreciably with position in the tank. Most of the gas is retained in the bulk of the dispersion. It is generally difficult to establish useful amounts of gas circulation in the region below the impeller plane and hence, from this stand point, high impeller clearances should be avoided.

- The general radial profiles of ϵ_g in the upper part of the vessel reveal high holdup values near the centre of the reactor, low values near the wall and a maximum at the mid-radial distance. Close to the surface the dispersion is fairly uniform. The mean vertical profiles exhibit a peak mid-way between the agitator and the dispersion surface.

- The effect of increasing the agitation speed is to increase the holdup at most positions in the tank, and to enhance uniformity in its spatial distribution.

- Increasing the gas flow rate at constant speed causes an almost uniform increase in ϵ_g in the bulk. However, it reduces gas circulation in the lower region of the vessel.

- Results presented in the literature show significant resemblance to the data obtained in this work. Complete similarity, however, cannot be expected because of the wide difference in the measuring techniques employed, in reactor size and in the flow regimes investigated.

- The resistivity probe proved to be a very fast measurement technique capable of revealing detailed aspects of the internal holdup structure in a stirred reactor. The overall bias caused by this technique is within reasonably acceptable limits. However, further miniaturisation and improved coating of the sensor tip should improve the accuracy of measurements.

- The spatial interfacial area distributions exhibit wide variations, with the impeller region containing a relatively large proportion of the total surface area in the tank.

- The air-0.15M NaCl system generated integral interfacial areas which were 52 to 111% greater than those produced by the air-water system for identical agitation conditions.

- Although the amount of interfacial area data obtained was limited, correlations for both air-water and air-NaCl systems were derived. The latter system correlation showed very good agreement with the correlation of Calderbank [30].

Chapter 7

PREDICTION OF TOTAL GAS HOLDUP AND AGITATION GASSED POWER

7.1 Introduction

Accurate predictions of total gas holdup and impeller gassed power demand are both important requirements in the design of mixing processes. A number of correlations are available in the literature for this purpose. Following a review of some of the main correlations, gas holdup and power measurements are discussed and analysed with the view to improving the accuracy of the prediction of these two parameters.

7.2 Gas holdup

7.2.1 Literature review

The overall gas holdup fraction usually serves as an index for the performance of the gas-liquid contactor. This has led researchers to try and develop mathematical models suitable for gas holdup prediction. Unfortunately, there is so far no universal correlation that can be used to predict this important parameter with sufficient accuracy. Generally, there is lack of agreement between measurements obtained by different investigators. This discrepancy can be largely explained by the difference in the measurement techniques employed and the experimental errors associated with each one of them, and also the different degree of cleanliness of the fluid phases, achieved by each investigator. In addition, there is also lack of agreement on the correlating parameters used by different authors in formulating their mathematical models. This point is strongly highlighted in Table 7.1, where some of the correlations developed over the past four decades are presented. Some details about the equipment used and the range of experiments are also given.

From Table 7.1 it can be seen that a common model for correlating gas holdup measurements combines the specific gassed power and the gas

Table 7.1 Gas holdup correlations

Authors	Two-Phase System: Liquid	Two-Phase System: Gas	Agitator	Sparger	Range of Experiments: T (m)	D/T	C/T	H/T	N (s^{-1})	U_s (mm/s)	ϵ (%)	P_g ($KW m^{-3}$)	Correlation
Foust et al [102] (1944)	Water	Air	6-10FBT (Curved)	4 Orifices	0.32 2.44	0.20 0.33	0.33 0.50	0.78 1.04	1.4-14.2	5.1-25.4	2-10	0.18-0.53	$\epsilon \propto \left\lvert \frac{P_g}{V} \right\rvert^{0.47} U_s^{0.53}$
Calderbank [30] (1958)	Water Glycerol EtOH EtAc	Air	6 FBT	Orifice	0.20 0.50	0.33	0.33	1.0	3-50	0.3-1.8	0-8	0-4.0	$\epsilon \propto \left\lvert \frac{P_g}{V} \right\rvert^{0.40} U_s^{0.50}$
Yoshida & Miura [103] (1963)	Water NaOH Glycerol	CO_2	12FBT	Orifice	0.25-0.59	0.40	0.30	1.0	1-5.83	1.7-7.6	0.4-5	-	$\epsilon \propto N^{0.80} U_s^{0.75} D^{1.2}$ based on liquid volume
Clark & Vermeulen [104] (1963)	Water Glycol CCl_4 Alcohol	Air	4 FBT	Ring	0.25	0.30-0.60	0.30	1.0	1.6-6.6	3-22	0-22	0.04-2.8	$\epsilon \propto \left\lvert \frac{P_g}{V} \right\rvert^{0.5} U_s^{1.0}$
Rushton & Bimbinet [105] (1968)	Water Corn Syrup	Air	6 FBT	Orifice	0.23-0.91	0.18-0.53	0.33	1.0		3-30	0-35	0.2-6.0	$\frac{\epsilon}{1-\epsilon} = a \left\lvert \frac{P_{gt}}{V} \right\rvert^{b} U_s^{0.60}$ a=0.18-0.31 b=0.17-0.39
Van Dierendonck et al [106] (1968)	Water Org. Liqs.	Air N_2 H_2	6 FBT	Ring & tubes	0.17-0.45	0.31-0.55	0.1-0.6	1.0	$N > N_0^*$	0-50	0-20	2.0-20.0	$\epsilon = 0.31 \left\lvert \frac{\mu U_s}{\sigma} \right\rvert^{2/3} \left\lvert \frac{\rho\sigma^3}{g\mu^4} \right\rvert^{1/6} + 0.45 \frac{(N-N^*)D^2}{T(gT)^{1/2}}$
	Ionic Solts.								$N > N_0$	3-30	0-30		$\epsilon = 0.075 \left\lvert \frac{\mu}{\sigma}(N-N_0)\frac{D^2}{T} \right\rvert \times \left\lvert \frac{\rho\sigma^3}{g\mu^4} \right\rvert^{1/4}$
Miller [107] (1974)	Different Liquids	Air	4 FBP	Ring	0.15-0.69	0.67	-	1.0	0.42-7.0	7.6-152.4	2.5-50	-	$\epsilon = \left\lvert \frac{U_s \epsilon}{U_s + U_t} \right\rvert^{0.5} + 2.16\times10^{-4} \times \left\lvert \frac{(P_{gt}/V)^{0.4}\rho^{0.2}}{\sigma^{0.6}} \right\rvert \times \left\lvert \frac{U_s}{U_s + U_t} \right\rvert^{0.5}$
Sterbacek & Sachova [108] (1976)	Water Glycerol	Air	4 FBT	-	0.16	0.57	-	1.0	5.3-15	7.2-21.6	1.7-16.2	-	$\epsilon = 9.0\times10^{-5} \left\lvert \frac{\rho U_s D}{\mu} \right\rvert^{0.77} \times \left\lvert \frac{\rho N^2 D^3}{\sigma} \right\rvert^{0.5}$

Cont...

Table 7.1 (cont'd) Gas holdup correlations

Authors	Two-Phase System: Liquid	Gas	Agitator	Sparger	Range of Experiments: T (m)	D/T	C/T	H/T	N (s^{-1})	U_s (mm/s)	ϵ (%)	P_g (KWm^{-3})	Correlation
Loiseau et al [109] (1977)	Organic & Ionic Solts.	Air	6 FBT	Orifice	0.22	0.33	0.33	1.0	5-27.5	6.4-47	0-60	0.18-20	$\epsilon = \frac{0.011}{\mu^{0.056}}\left\lvert\frac{P_{gt}}{V}\right\rvert^{0.27} \times \left\lvert\frac{U_s}{\sigma}\right\rvert^{0.36}$
Hassan & Robinson [110] (1977)	Water Non-ionic Solts.	Air	6 FBT	2 Orifices	0.15	0.33	0.33	1.0	3.3-35	3.5-6.8	3-50	0.03-16.2	$\epsilon \propto N^{1.14} Q^{0.57} \sigma^{-0.57}$
	Na_2SO_4 (0.4M)				0.29								$\epsilon \propto N^{0.88} Q^{0.44} \sigma^{-0.44}$
Joshi & Sharma [111] (1977)	Sodium Dithiorite	Air	Gas Inducing Agitator	-	0.41 0.57 1.0	0.35-0.75	D/6	1.0	3-12	0.3-32	4-15	1-15	$\epsilon \propto 1.12\times10^{-3}\left\lvert\frac{P_g}{V}\right\rvert^{0.5}$
Smith et al [112] (1977)	Water K_2SO_4	Air	6 FBT	Ring	0.91 1.83	0.33-0.50	0.35	1.0	1.1-5.0	4-20	3-25	0.1-5.0	$\epsilon \propto \left\lvert\frac{P_g}{V}\right\rvert^{0.47} U_s^{0.40}$
Roustan et al [113] (1978)	Water	Air	6 FBT	Plate	1.0	0.33	0.33	1.0				0-1.5	$\frac{\epsilon}{1-\epsilon} = 4.0U_s + 1.75Q^{0.6} \times \left\lvert\frac{D}{T}\right\rvert (N - N_R)$
Figuereido & Calderbank [114] (1978)	Water	Air	6 FBT	Orifice	0.91	0.33	0.33	1.0	4.16-8.33	6.34-12.7	4.3-10.0	0.41-4.8	$\epsilon = 0.23\left\lvert\frac{P_g}{V}\right\rvert^{0.26} U_s^{0.68}$
Yung et al [115] (1979)	Water Glycol Acetone	Air	6 FBT	Orifice	0.40	0.23-0.45	0.23-0.45	1.0	3.33-23.3	1-21	1-20	0.08-5.0	$\epsilon = 0.52 F_l^{0.5} W_e^{0.65}\left\lvert\frac{D}{T}\right\rvert^{1.4}$
	$NaCl$ (0.2,0.4M) Na_2SO_4 (0.03,0.31M)												$\epsilon \propto Q^{0.5} N^{0.8} D^{1.4}$
Hughmark [116] (1980)	Water	Air	6 FBT	Orifice	0.17-0.46	0.36	0.18-0.55	1.0	-	1.2-36 (vvm)	2-17	-	$\epsilon \propto \left\lvert\frac{Q}{NV}\right\rvert^{1/2}\left\lvert\frac{N^2D^4}{gWV^{2/3}}\right\rvert \times \left\lvert\frac{d_b N^2 D^4}{\sigma V^{2/3}}\right\rvert^{1/4}$
	Cyclohexane	N_2 H_2	6 FBT	Ring									
Kobbacy [118] (1981)	water	Air	6 FBT	Perforated	0.20	0.38	0.25	1.0	6-20	2.4-11.6	3-20	0.2-9.0	$\epsilon = 0.051\left\lvert\frac{P_{gt}}{V}\right\rvert^{0.36} U_s^{0.27} \times \left\lvert\frac{D}{T}\right\rvert^{0.85}$
	0.11M K_2SO_4			U-Tube	0.50	0.67							$\epsilon = 0.045\left\lvert\frac{P_{gt}}{V}\right\rvert^{0.475} U_s^{0.40}$
Chapman et al [117] (1983)	Water	Air	Various Types	Orifice	0.56	0.50	0.25	1.0		2.3-9.3	4-8	0.1-2.5	$\epsilon = 17.9\left\lvert\frac{P_g}{V}\right\rvert^{0.31} U_s^{0.67}$

FBT: Flat Blade Turbine
FBP: Flat Blade Paddle

superficial velocity in the form:

$$\epsilon \propto \left| \frac{P_{gt}}{V} \right|^{x} U_s^{y} \qquad (7.1)$$

where, P_{gt} includes the gas power input, which is now a generally accepted requirement. Although this model is useful in that it shows that power is a major quantity in achieving a desired amount of gas holdup in the vessel, and mathematically it may prove to be a good correlation for the data, there is now increasing awareness [100, 101] that from a practical point of view it is an unsatisfactory model. This is because it is not directly predictive. The gassed power is itself a dependent parameter which is not always easy to determine because of its complicated relationship with the gas superficial velocity.

The correlation of Hughmark [116] which is based on results obtained by five different workers and derived from dimensional analysis is also not directly predictive since it includes the Weber number, which is based on an arbitrary average bubble diameter. The remaining relationships are all directly predictive since they involve only purely independent variables. However, these correlations are subject to a relatively high margin of uncertainty [110, 115], usually $\pm 30\%$. This scatter is only partly accounted for by experimental error. Significantly, the data is usually correlated in a 'black-box' manner, without due regard to the different gas-liquid flow regimes which are established in the vessel. By considering the two phase flow hydrodynamics of disc turbine impellers Warmoeskerken and Smith [119] have depicted three main flow fields:

(i) loaded impeller with six vortex or clinging gas cavities,

(ii) loaded impeller with a 3-3 structure of large cavities,

(iii) flooded impeller with six ragged cavities.

These cavity structures are discussed in more detail in Chapter 8 where cavity formation is considered in relation to power dynamics.

Smith and Warmoeskerken [120] and Nienow et al [86] established relationships for determining the transitions between the above flow regimes. Recently, Smith and Warmoeskerken [120] suggested, although no details were given, that by systematising mass transfer coefficient and gas holdup data on the basis of the impeller hydrodynamics, the scatter of the correlations could be improved. The large amount of gas holdup data obtained in this study is analysed from this viewpoint.

7.2.2 Results and discussion

The procedure for measuring total gas holdup by means of a conductivity level probe is described in Section 3.3.4. Measurements were carried out in the 1.0 m tank for an air-water system at several rotational speeds (0.67-8.33 rev/s) and four gas flow rates (0.00164-0.00833 m^3/s), using three impeller sizes (D/T=1/4, 1/3, 1/2). Similar experiments were made with a 0.15M solution of Sodium Chloride using two impeller sizes (D/T=1/4, 1/3). A total of 82 data points was obtained for the air-water system and 54 points for the air-NaCl system.

The effect of the impeller speed, gas flow rate and impeller size on ϵ is illustrated in Fig 7.1, for the air-water system. On a log-log plot, as shown in Fig 7.2, for a given value of D/T the lines obtained for the four gas flow rates are almost parallel, with slopes less than unity. Similar trends were observed for the electrolyte solution.

As discussed above, because of the practical inadequacy of using the model of Equation (7.1), the measurements acquired were correlated using only the three truly independent variables, which are the impeller

Fig 7.1 Total Holdup vs Impeller Speed

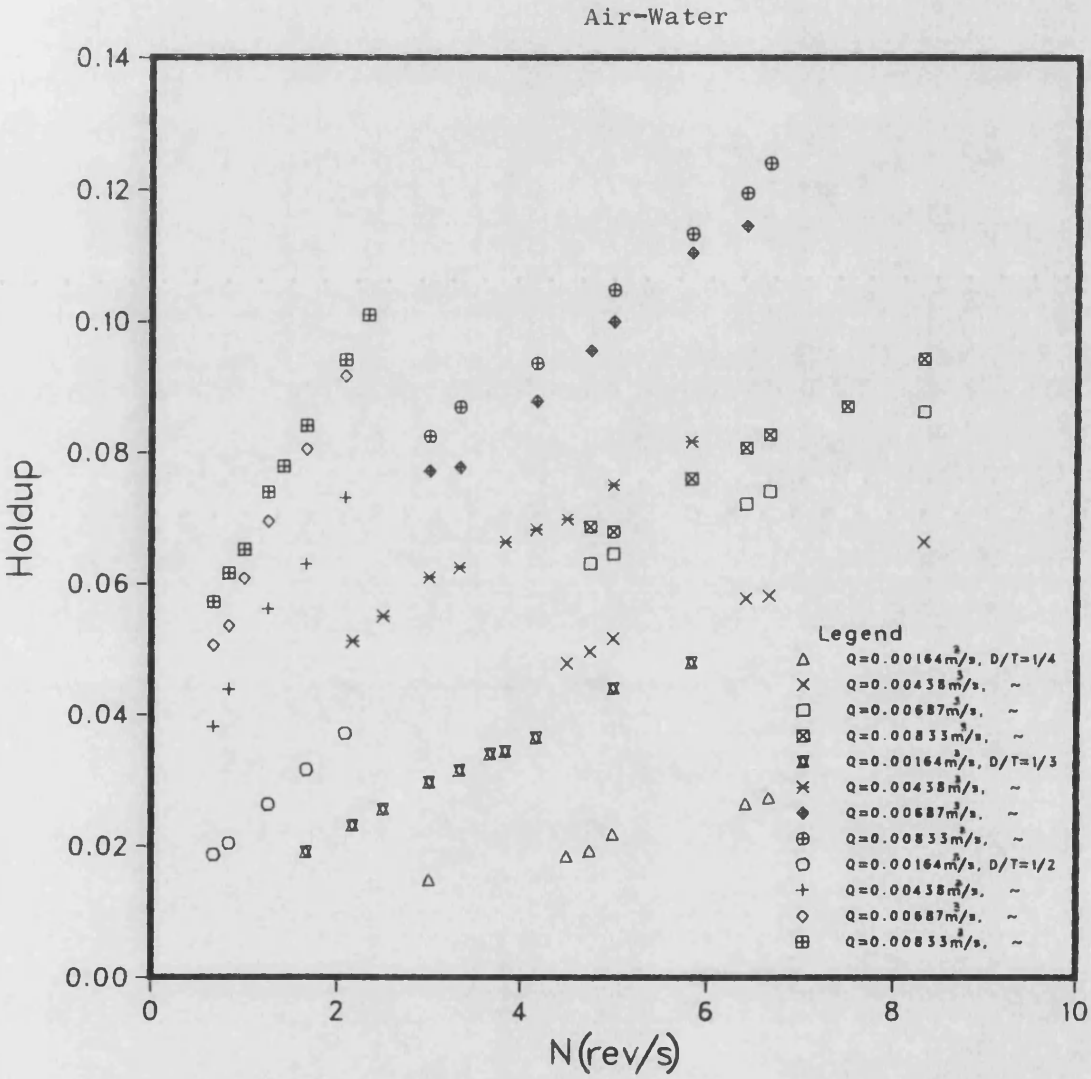

Fig 7.2 Total Holdup vs Impeller Speed

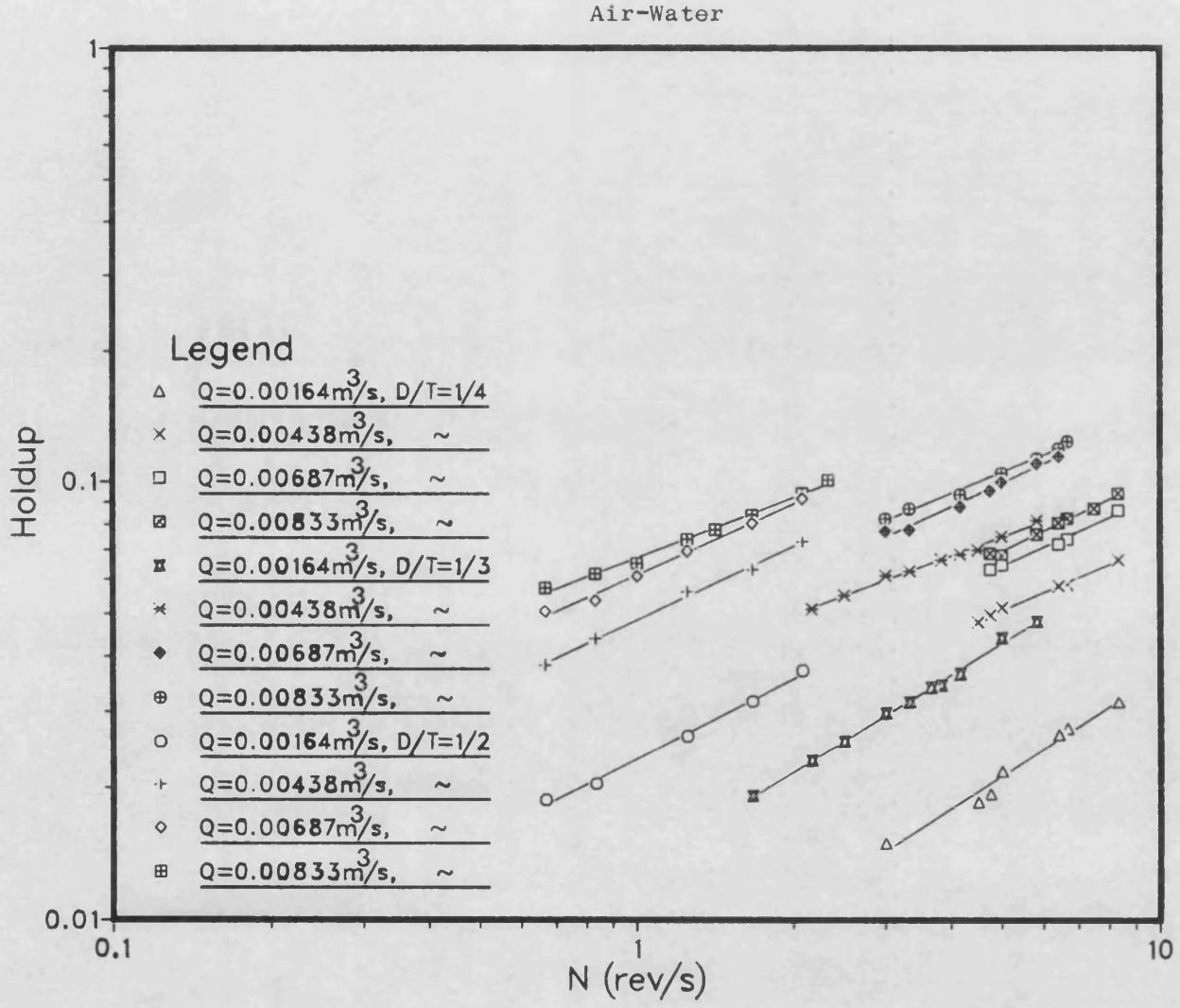

speed, N, the gas flow rate, Q, and the impeller-to-tank diameter ratio, D/T, in the form:

$$\epsilon = KN^{a}Q^{b}\left[\frac{D}{T}\right]^{c} \qquad (7.2)$$

using non-linear least square regression analysis. The coefficient of determination, r, of the fit is 0.966 and the standard deviation, s, of ϵ about the regression line is 0.1230, for the air-water dispersion. The values of the model parameters are:

$$K = 4.07,\quad a = 0.62,\quad b = 0.64,\quad c = 1.39.$$

and are all highly significant. Fig 7.3 shows a plot of ϵ against $N^{0.62}Q^{0.64}\left[\frac{D}{T}\right]^{1.39}$. The data falls within a 22% range either side of the regression line.

The same model was used to correlate the air-NaCl solution results. The values of the model parameters obtained are highly significant and equal to:

$$K = 4.20,\quad a = 0.79,\quad b = 0.52,\quad c = 1.92.$$

with r=0.985 and s=0.0618. This correlation is plotted in Fig 7.4 with the data lying in an uncertainty band of $\pm 15\%$. The scatter in this case is lower than that for air-water. This is due to the reduced disturbances at the bulk liquid surface in the case of the electrolyte solution, which allowed a more accurate determination of the dispersion level.

The data was then classified into a vortex-clinging cavity regime, hereafter called V-C regime, and a large cavity regime, hereafter called L regime. Measurements of gas holdup in the flooding regime were not possible because of the large disturbances occurring at the bulk

Fig 7.3 Total Holdup Air–Water

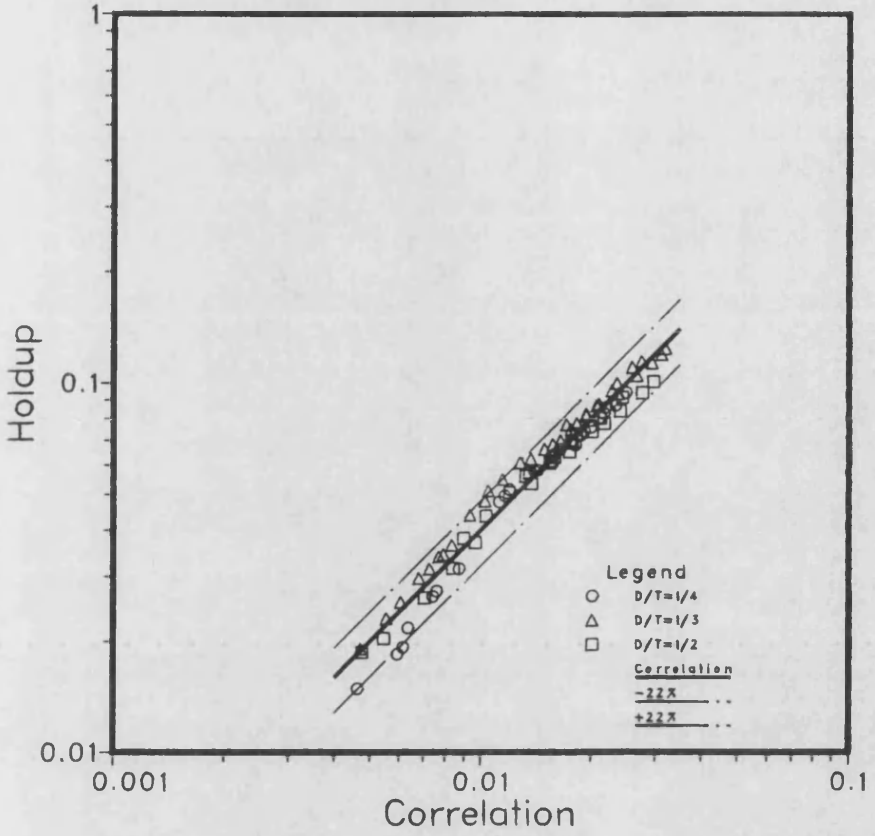

Fig 7.4 Total Holdup Air–0.15M NaCl

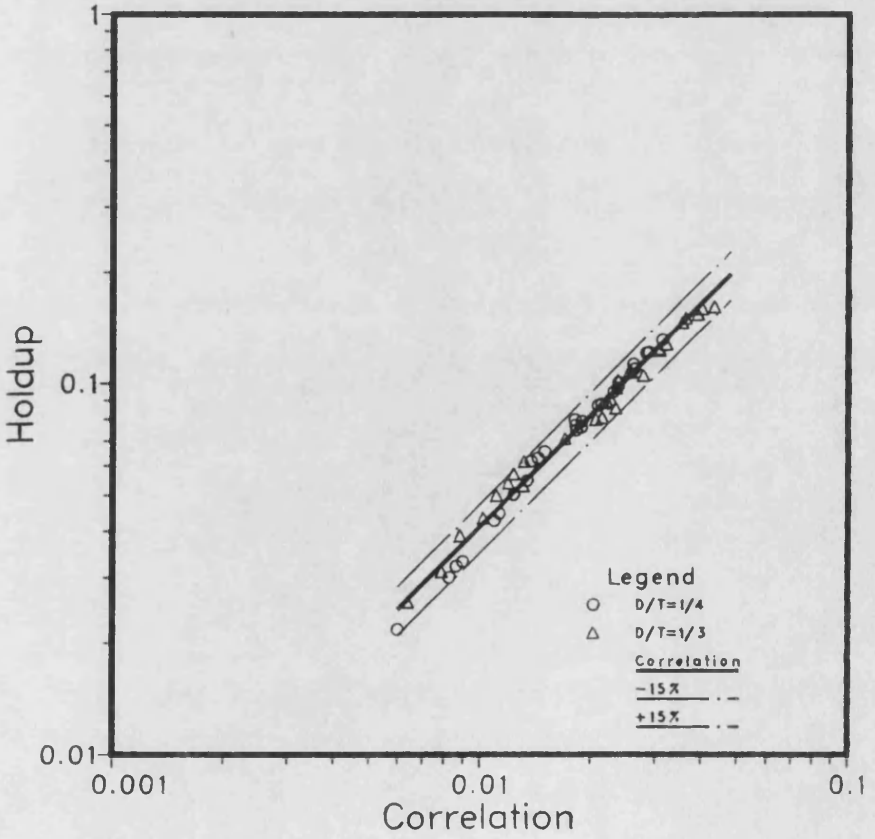

dispersion surface. For the air-water system 47 points were found to lie in the V-C regime and 35 in the L regime. Using the same model (Equation (7.2)) the two data sets were correlated separately and the following two relationships were obtained:

(i) V-C regime:

$$\epsilon = 3.851 N^{0.73} Q^{0.62} \left| \frac{D}{T} \right|^{1.64} \tag{7.3}$$

with r=0.978 and s=0.0676. The data for this regime is plotted in Fig 7.5 and it can be seen that the scatter around the regression line has reduced to about ±15%, which represents an improvement of some 30% compared with the scatter of the total grouped data correlation.

(ii) L regime:

$$\epsilon = 1.334 N^{0.60} Q^{0.44} \left| \frac{D}{T} \right|^{1.31} \tag{7.4}$$

where r=0.980 and s=0.0536. This correlation is plotted in Fig 7.6. The scatter of the points has reduced in this case to approximately ±10%, an improvement of 55% over the overall correlation.

In order to determine the statistical significance of the improvement achieved in the gas holdup model by classifying the data in the two flow regimes, a variance analysis of the above correlations was carried out. Table 7.2 summarises this analysis and gives the result of the F-distribution test of significance. The procedure involves calculating for each of the three correlations its residual sum of squares, which is simply the sum of squares of deviations of the experimental data points about the regression line. Then, the mean squares are calculated as the ratio of the residual sum of squares and the number of degrees of freedom. The number of degrees of freedom is equal to the total number of data points less the number of constraints which are established by

Fig 7.5 Total Holdup
(vortex–clinging cavity regime)

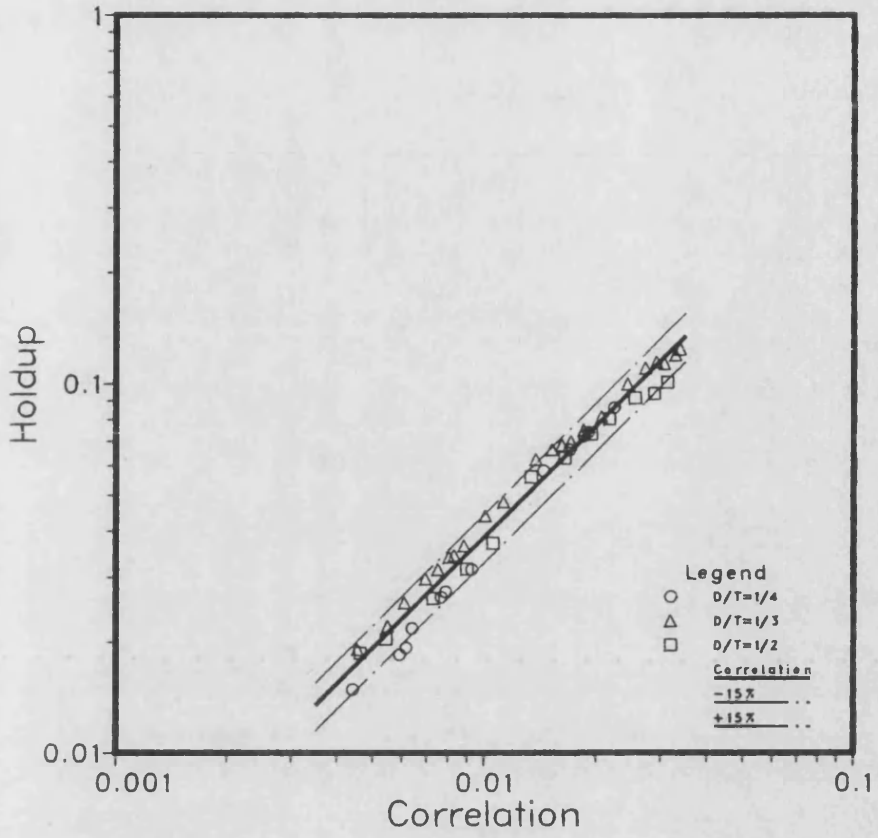

Fig 7.6 Total Holdup
(large–cavity regime)

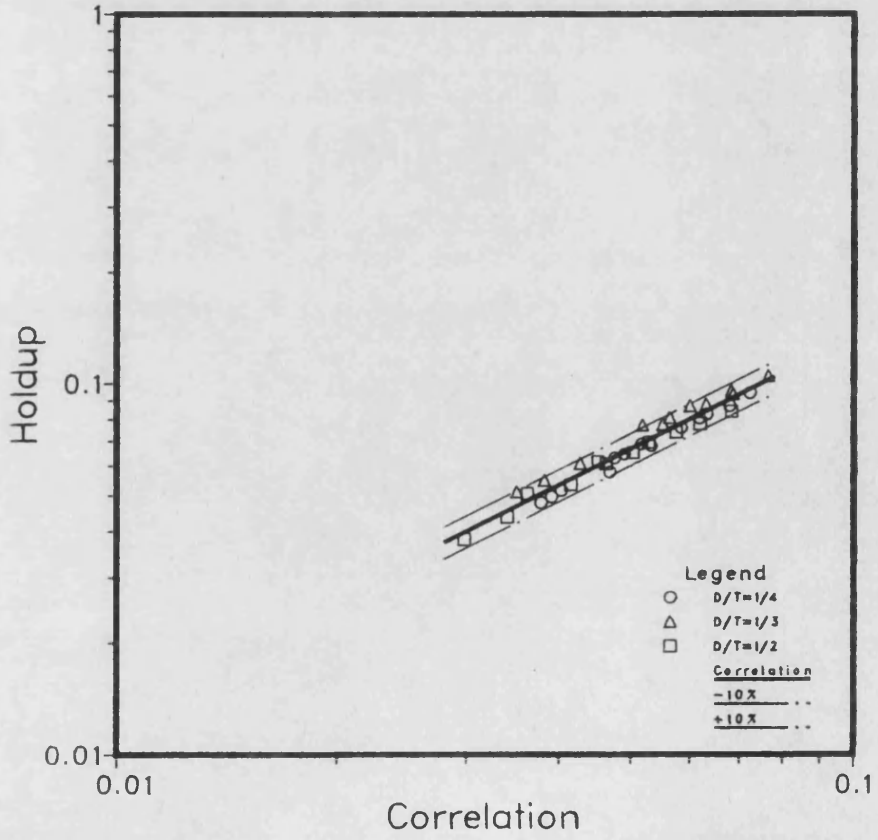

the least squares method of curve fitting. Fitting an equation with four parameters ie., K, N, Q and D/T, introduces four constraints. Two mean squares are obtained; One for the equation based on all data grouped together and the other is a combined mean squares obtained by summing the residual sum of squares of Equations (7.3) and (7.4), and dividing by the sum of their numbers of degrees of freedom. The ratio of the two mean squares, thus obtained, is computed and called the 'ms ratio'. The F-test consists in comparing the ms ratio with the F-ratio extracted from the statistical F-distribution tables [141] at the desired levels of significance, as shown in Table 7.2. Since the ms ratio, 2.163, is greater than 1.962 and less than 2.252, the improvement in accuracy achieved by using the two-separate-regime correlations is therefore strongly significant at the 0.5% level.

The same data grouping technique was applied to the measurements of the air-electrolyte solution system. Each flow regime contained 27 data points. The models obtained are:

(i) V-C regime:

$$\epsilon = 3.857 N^{0.92} Q^{0.41} \left[\frac{D}{T}\right]^{2.56} \tag{7.5}$$

with r=0.995 and s=0.0414. Fig 7.7 represents a plot of this correlation with an uncertainty band of ±10%, ie., more than 30% improvement on the overall correlation.

(ii) L regime:

$$\epsilon = 2.858 N^{0.76} Q^{0.51} \left[\frac{D}{T}\right]^{1.64} \tag{7.6}$$

with r=0.990 and s=0.0373. This correlation is plotted in Fig 7.8. The scatter of the data is within ±8%, which represents a reduction of 47%.

Table 7.2 Significance test for Air-Water gas-holdup correlations

Correlation	Degrees of Freedom (ν)	Residual Sum of Squares (ss)	Mean Squares ($ms = ss/\nu$)	ms Ratio	F-Ratio	Level of Significance
Overall	78	0.6750	0.00865		1.534	5%
V-C Regime	42	0.2028			1.836	1%
	+	+		2.163		
L Regime	31	0.0891			1.962	0.5%
	73	0.2919	0.00400		2.252	0.1%

Table 7.3 Significance test for Air-0.15M NaCl solution gas holdup correlations

Correlation	Degrees of Freedom (ν)	Residual Sum of Squares	Mean Squares ($ms = ss/\nu$)	ms ratio	F-Ratio	Level of significance
Overall	50	0.1907	0.00381		1.693	5%
V-C Regime	23	0.0394			2.114	1%
	+	+		2.458		
L Regime	23	0.0319			2.296	0.5%
	46	0.0713	0.00155		2.727	0.1%

Fig 7.7 Total Holdup Air–0.15M NaCl
(vortex–clinging cavity regime)

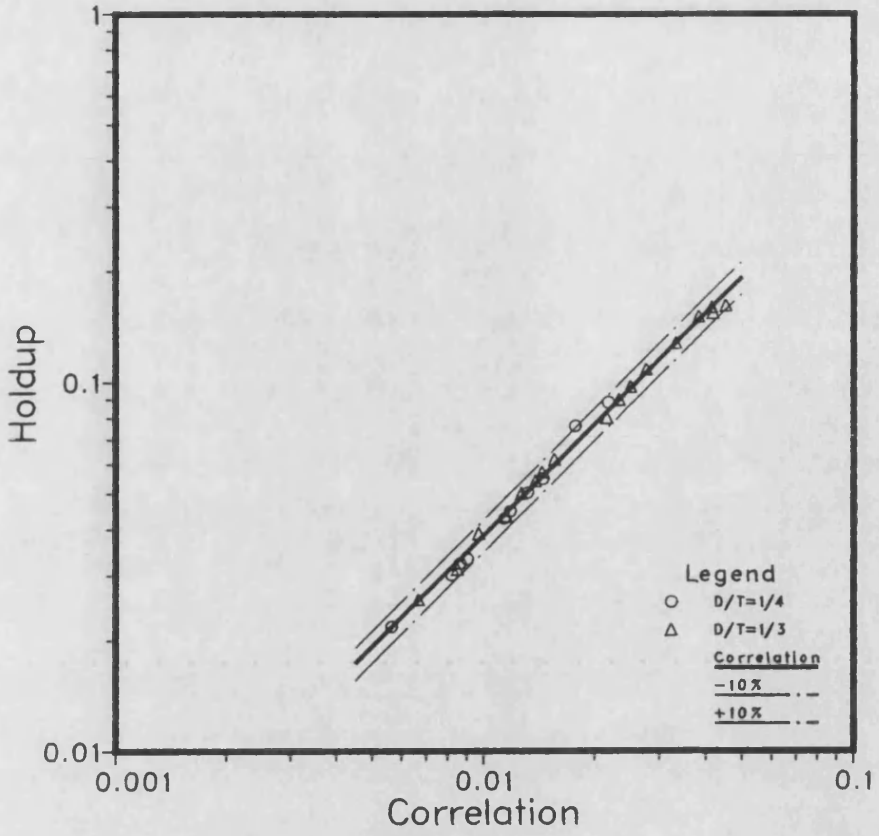

Fig 7.8 Total Holdup Air–0.15M NaCl
(large cavity regime)

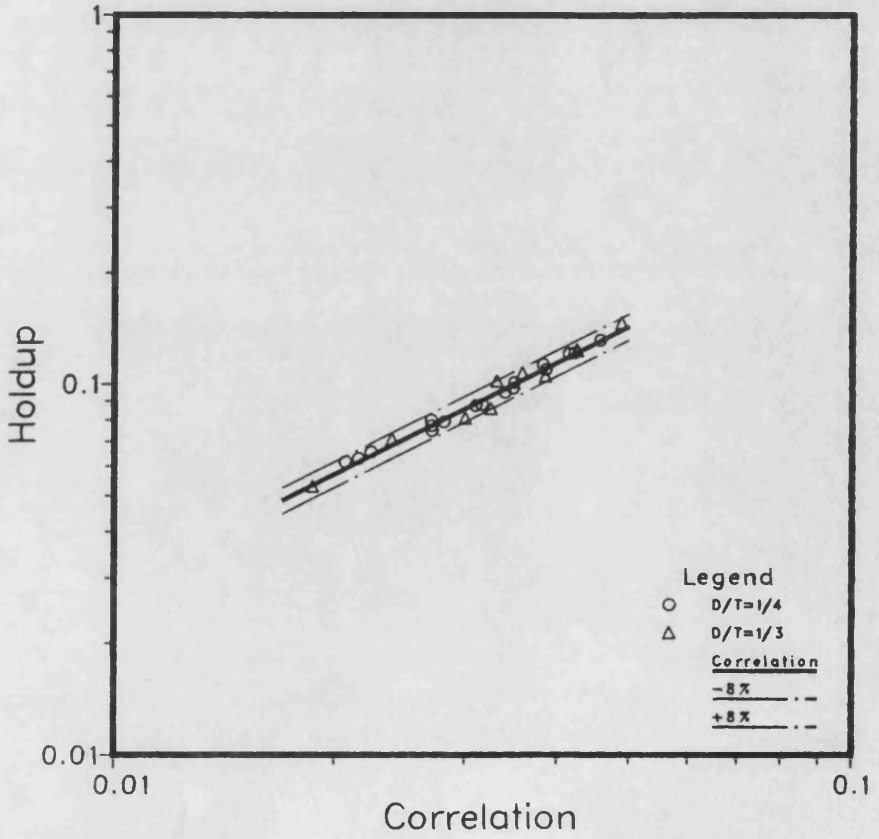

Table 7.3 exhibits the F-test of significance for the above two equations with respect to the overall air-NaCl correlation. The improvement achieved in the accuracy of prediction by using the two-separate-regime models is strongly significant at the 0.5% level.

The gas holdup relationships obtained for both air-water and air-NaCl are summarised in Table 7.4. From the literature correlations presented in Table 7.1, the ones which are amenable to direct comparison with the models established here are those which are based on independent parameters, bearing in mind that these equations donot distinguish between the different flow regimes:

- Yoshida and Miura [103]:

Their gas holdup fraction is based on the clear liquid volume and not on the dispersion volume. However, since the maximum holdup in their case is only 5% the effect should be small. Their equation can be rearranged in the form:

$$\epsilon \propto N^{0.80} Q^{0.75} \left[\frac{D}{T}\right]^{1.50} D^{-0.30} \qquad (7.7)$$

The exponents of N, Q, and D/T in this relationship are all higher than the ones in the overall air-water correlation in Table 7.4. They used 12 blade turbines, this makes the impeller gas handling capacity higher and therefore the exponents of the variables would be expected to be more significant.

- Sterbacek and Sachova [108]:

Their measurements relate to a very small tank where surface aeration may be important. This in addition to their different impeller geometry may explain the difference in the exponents of the parameters.

Table 7.4 Summary of gas holdup correlations		
Cavity Regime	Air-water	Air-0.15M NaCl solution
Overall	$\epsilon = 4.070N^{0.62}Q^{0.64}\left(\frac{D}{T}\right)^{1.39}$	$\epsilon = 4.200N^{0.79}Q^{0.52}\left(\frac{D}{T}\right)^{1.92}$
Vortex-Clinging	$\epsilon = 3.851N^{0.73}Q^{0.62}\left(\frac{D}{T}\right)^{1.64}$	$\epsilon = 3.857N^{0.92}Q^{0.41}\left(\frac{D}{T}\right)^{2.56}$
Large	$\epsilon = 1.334N^{0.60}Q^{0.44}\left(\frac{D}{T}\right)^{1.31}$	$\epsilon = 2.858N^{0.76}Q^{0.51}\left(\frac{D}{T}\right)^{1.64}$

- Hassan and Robinson [110]:

Considering their correlation which relates to non-electrolyte solutions, whereas their Q exponent of 0.57 is reasonably close to the one obtained here, 0.64, their N exponent is significantly higher than ours. Again, because of the small scale of their vessels surface aeration is thought to be the reason for this discrepancy together with the effect of the different liquid properties. Their equation for the air-Na_2SO_4 system, on the other hand, bears speed and flow rate exponents (0.88, 0.44) which are in reasonable agreement with the ones obtained here (0.79, 0.52) despite the fact that they used a different salt and a much higher molar concentration.

- Yung et al [115]:

The exponent of D/T (1.40) in their non-electrolyte system correlation is in excellent agreement with the one obtained in this work (1.39). However, the exponents of the other variables are discrepant. This may be due to the difference in the properties of the liquids used. Also, the data scatter of their correlation is greater than ±30%, which is significantly higher than the ±22% incurred here. On the other hand, the exponents of N and Q (0.80 , 0.50) in their equation which represents data for electrolyte solutions, are in very good agreement with the respective values of 0.79 and 0.52 in Table 7.4. The lower significance of their impeller diameter exponent could be due to a scale effect.

Higher gas holdups are achieved under the vortex-clinging cavity regime than under the large cavity regime. This is due to the blanketing of the impeller blades caused by the large cavities and therefore the ensuing decrease in liquid pumping capacity of the agitator, which results in a weaker circulation capacity and hence lower gas retainment

in the bulk of the vessel. The ultimate case would be a state of complete cavity growth which then leads to the flooding of the impeller, with a simple axial stream of gas.

For the air-water system, the gas holdup is significantly more sensitive to the three variables N, Q and D/T in the V-C regime than in the L regime. This means that a variation in any one of these parameters under the former regime will have a more pronounced effect on ϵ than under the latter, in other words, relatively more improvement in ϵ can be brought about by the same increase in either of the three variables under the V-C regime. This fact is also true for air-NaCl except that the case is reversed as far as the gas flow rate is concerned. Other discrepancies also exist between the two fluid systems. In addition to the gas holdup being higher for the ionic system, comparison of the equations in Table 7.4 reveals that the sensitivity of ϵ to N and D/T is appreciably higher for the electrolyte solution. This exists under both flow regimes considered, and hence it is also reflected in the overall correlations. In Section 5.5.7 it was found that recirculation of bubbles in the lower half of the vessel starts at lower speeds in the air-NaCl solution than in air-water. An increase in D/T enhances this recirculation and the resulting effect will therefore be higher for the ionic system. These two reasons may explain the higher sensitivity of gas holdup to N and D/T in the case of the electrolyte solution. The exponent of Q in the overall correlations is higher for the air-water dispersion. However, when the individual regime equations are considered, this observation is found to hold only for the V-C regime, the opposite being true for the L regime. This inconsistency is à-priori difficult to explain.

It has already been pointed out in the above discussion that greater gas holdup can be achieved by switching the operation of the stirred

vessel from the L regime to the V-C regime. This change of regime can be effected by an alteration in either of the three operational variables ie., N, Q or D/T. It was found that the relative effect on ϵ was significantly different between the two fluid systems considered. The result of increasing either N or D/T was a relatively higher increase in ϵ for air-NaCl. On the other hand, a reduction in Q to change the gas cavity structure from that of large to that of vortex-clinging produced a relatively higher increase in ϵ for air-water. This shows that not only is the overall two-phase flow different between the ionic and non-ionic fluid media, but also the amount of physical discrepancy between vortex-clinging cavity flow regime and large cavity flow regime is dependent on the fluid system used.

7.3 Impeller gassed power

7.3.1 Literature review

Many correlations for predicting impeller gassed power demand can be found in the literature. Some of these relationships are presented in Table 7.5 together with details pertaining to the range of experiments from which they were obtained. A good discussion of gassed power correlations can be found in Midoux [127] and in Mann [74]. Almost invariably, all of the correlations involve the ungassed power consumption P_{ug}. This makes them indirectly predictive since the usual assumption that the ungassed power number is constant for $R_e \geq 2\times10^4$ is not always true. Large falls in the power number can be expected at high rates of surface aeration as shown by Greaves and Kobbacy [126]. Also, recently Nienow et al [128] have found that the ungassed power number is a function of turbine disc thickness and scale.

Table 7.5 Impeller gassed power correlations

Authors	Two-Phase System: Liquid	Gas	Agitator	Sparger	Range of Experiments: T (m)	D (m)	C/T	U_s (mm/s)	R_e ($\times 10^{-4}$)	Correlation
Calderbank [30] (1958)	Water	Air	6 FBT	Orifice	0.20 0.50	0.33	0.33 0.55	0.3–1.8	1.3–136	$\frac{P_g}{P_o}=1-1.26\frac{Q}{ND^3}$, $F_l<0.035$ $\frac{P_g}{P_o}=0.62-1.85\frac{Q}{ND^3}$, $F_l>0.035$
Michel & Miller [121] (1962)	CCl_4 Al_2O_3 Glycerol	Air	6 FBT	orifice Ring	0.17 0.31	0.46 0.25 0.33	0.61 0.25 0.25	0.44–10.4		$P_g \propto \left\lvert \frac{P_o^2 N D^3}{Q^{0.56}} \right\rvert^{0.45}$ $(0.9<\mu<100cp)$
Nienow & Wisdom [123] (1974)	-	-	-	-	-	-	-	-	-	$\frac{P_g}{P_o}=1-8.5\frac{Q}{ND^3}$ $N_{FI}<N<N_R$
Pharamond et al [122] (1975)	Water	Air	6 FBT	Plate	0.29 0.48 1.00	0.33	0.19	0.84–5.0 1.5–6.1 0.88–14.1	6.4–13.6 10.0–20.1 16.3–45.7	$1-\frac{P_g}{P_o}=1.6\frac{QD^{0.63}}{V}$, $\frac{QD^{0.63}}{V}<3$ $\frac{P_g}{P_o}=0.5-0.55$, $\frac{QD^{0.63}}{V}>3$
Hassan & Robinson [110] (1977)	Aqueous Solts.	Air	6 FBT 6 FBP 4 FBP	2 Orifices	0.15 0.29	0.33 0.66	0.33 0.66	3.5–68 5–22.1	11.5–14.1	$\frac{P_g}{P_o}\propto\left\lvert\frac{N^2D^3\rho}{\sigma}\right\rvert^m\left\lvert\frac{Q}{ND^3}\right\rvert^{-0.38}\left\lvert\frac{\rho}{\rho_L}\right\rvert$ m = 0.22 4 FBP-6 FBP m = 0.25 6 FBT
Loiseau et al [109] (1977)	Glycol Ethanol H_2O+HCl $+CuCl$	Air	6 FBT	Orifice Plate	0.23 0.19	0.33	0.33	0.75–85	3–14.8	$P_g=0.83\left\lvert\frac{P_o^2ND^3}{Q^{0.56}}\right\rvert^{0.45}$ Non-Foaming Systems
Luong & Volesky [124] (1979)	Glycol CMC Solt.	Air	6 FBT	Orifice	0.22	0.33	0.33	0–6.7 0–5.8	40–65 45–69	$\frac{P_g}{P_o}\propto\left\lvert\frac{N^2D^3\rho}{\sigma}\right\rvert^m\left\lvert\frac{Q}{ND^3}\right\rvert^{-0.38}$ m = 0.18 Newtonian m = 0.194 Non-Newtonian
Yung et al [115] (1979)	Water Glycol Acetone $NaCl$ Na_2SO_4	Air	6 FBT 4 FBP	Orifice	0.40	0.225 0.325 0.45	0.225 0.325 0.45	0.97–21.6	53.3–372.8	$P_g=0.812\left\lvert\frac{P_o^2ND^3}{Q^{0.56}}\right\rvert^{0.45}$
Hughmark [116] (1980)	Water CCl_4 Al_2O_3 Glycol Glycerol CMC Solt.	Air	6 FBT	Orifice Ring Plate	0.17–1.00	0.25–0.46	-	0.2–1.8 (vvm)	-	$\frac{P_g}{P_o}=0.10\left\lvert\frac{Q}{NV}\right\rvert^{-1/4}\left\lvert\frac{N^2D^4}{gD_tV^{2/3}}\right\rvert^{-1/5}$
Greaves & Kobbacy [125] (1981)	Water 0.11M K_2SO_4	Air	6 FBT	Perforated U-Tube	0.20	0.375 0.500 0.665	0.25	2.6–12.3	2.6–13.4	$P_g=1007\left\lvert\frac{N^{3.33}D^{6.33}}{(\eta Q)^{0.4}}\right\rvert$

FBT: Flat Blade Turbine
FBP: Flat Blade Paddle

One of the most successful models is that of Michel and Miller [121]. A number of other workers have used the same type of model to correlate their experimental data. However, even with this type of correlation the accuracy of prediction cannot be expected to be better than ±30%. Nienow et al [76] described it as a 'catch-all' correlation referring to the fact that data was correlated regardless of the prevailing flow regimes. As a significant step forward towards a more rational approach which discriminates between the different flow patterns when predicting impeller gassed power requirements, Greaves and Kobbacy [125] incorporated in their model a dispersion efficiency η which depends upon the regime of mixing, although the approach behind the determination of η can be described as somewhat qualitative.

Because the gassed power is chiefly determined by the condition of the impeller gas cavities, a more rigorous way of accounting for the nature of the dispersion would be to correlate data according to the different gas cavity regimes. This method was employed in the previous section to improve the accuracy of gas holdup correlations and is used in the same way to treat gassed power measurements.

7.3.2 Results and discussion

Gassed power measurements were obtained in the 1.0 m tank for the three impellers (D/T=1/4, 1/3, 1/2), for a range of rotational speeds (0.67-8.33 rev/s) at gas flow rates (0.00164-0.00833 m^3/s), using the measuring procedure described in Section 3.3. The fluid systems investigated were air-water and air-0.15M NaCl solution.

In agreement with other workers [37, 104, 115, 121], no significant effect of the ionic properties of the salt solution was found. Consequently, the measurements of the two fluid systems were

combined and correlated together. A total of 136 data points were obtained. The model used involved only the fundamental variables N, Q and D/T.

When the data was correlated without due consideration to the different gas cavity regimes the relationship arrived at was:

$$P_r = 706.3N^{3.01}Q^{-0.45}\left(\frac{D}{T}\right)^{5.83} \tag{7.8}$$

where r=0.990, s=0.1028, and with all the parameters being highly significant. Fig 7.9 shows a plot of the above relationship. The data fits the model with an error interval of approximately ±25%, which is usually considered to be a reasonable spread. The data was subsequently sorted into a vortex-clinging cavity regime and a large cavity regime. Sixty nine data points belonged to the former regime while sixty seven points belonged to the latter. The equations derived for these two flow conditions are:

(i) V-C regime:

$$P_r = 441.4N^{3.13}Q^{-0.50}\left(\frac{D}{T}\right)^{5.82} \tag{7.9}$$

where r=0.994 and s=0.0747.

(ii) L regime:

$$P_r = 1737.1N^{2.99}Q^{-0.31}\left(\frac{D}{T}\right)^{5.98} \tag{7.10}$$

with r=0.991 and s=0.0810.

The above two correlations are plotted in Fig 7.10 and 7.11 respectively. The scatter for both fits is about ±15%, which represents an improvement of 40% over the overall correlation. A variance analysis

Fig 7.9 Gassed Power

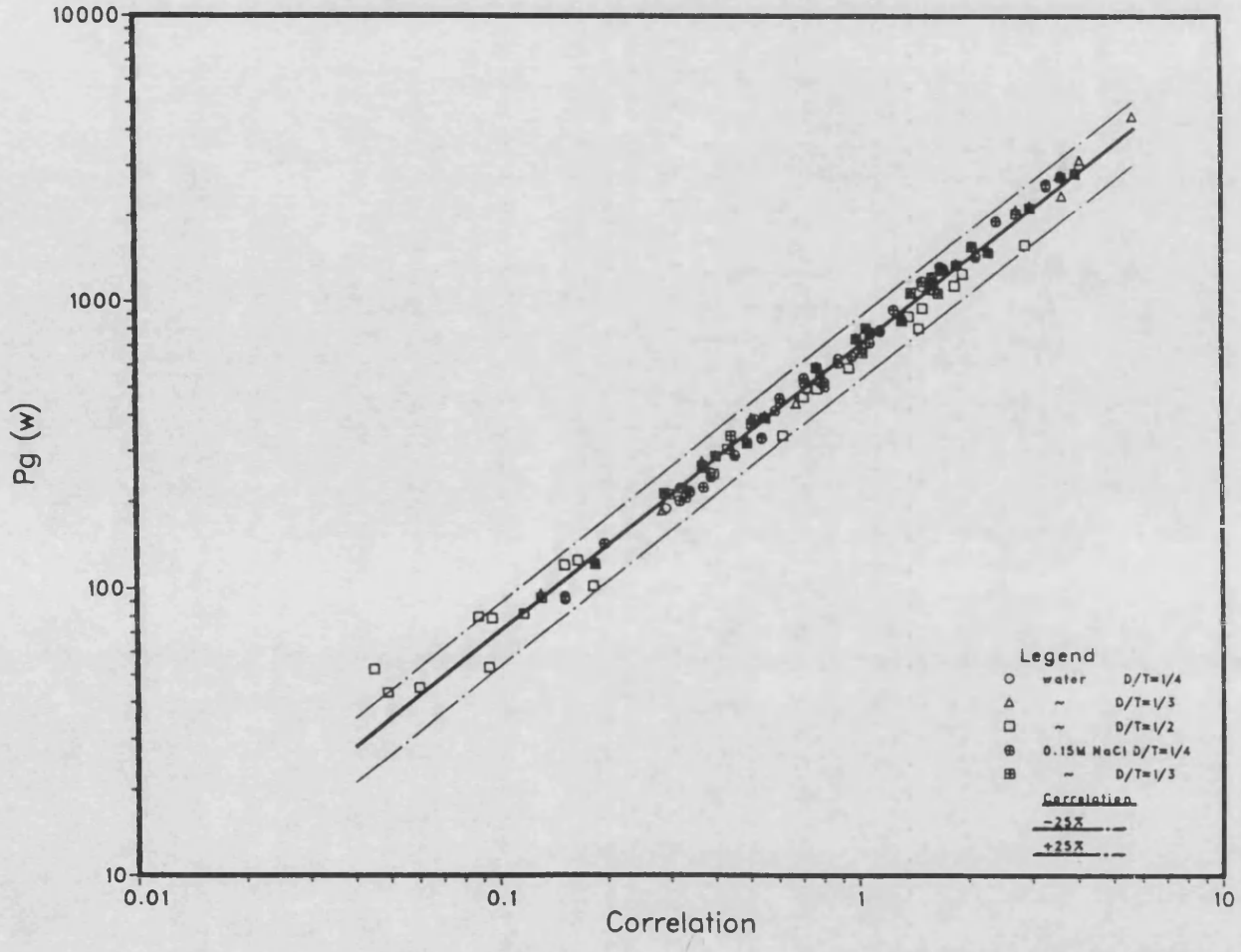

Fig7.10 Gassed Power
(vortex–clinging cavity regime)

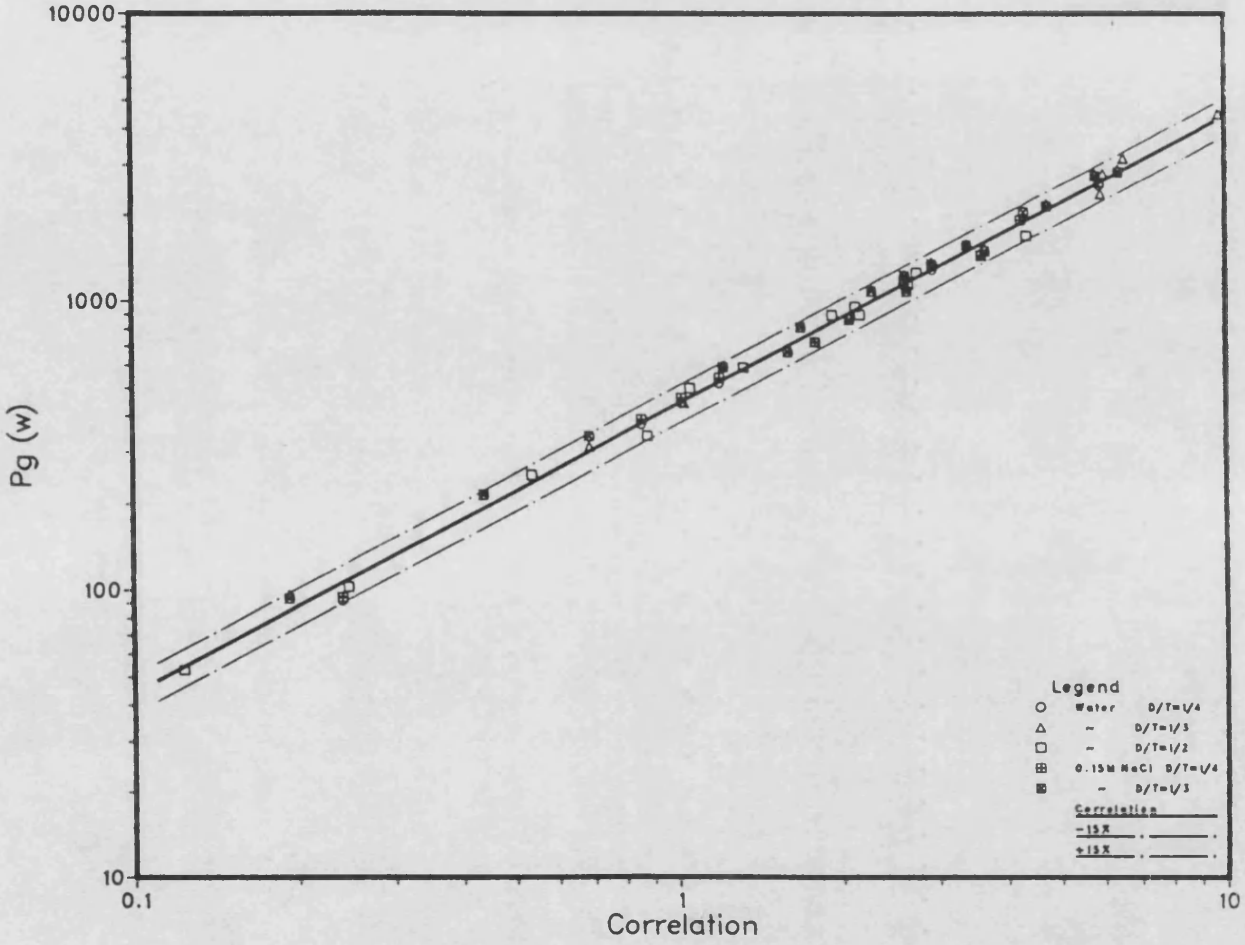

Fig7.11 Gassed Power
(large cavity regime)

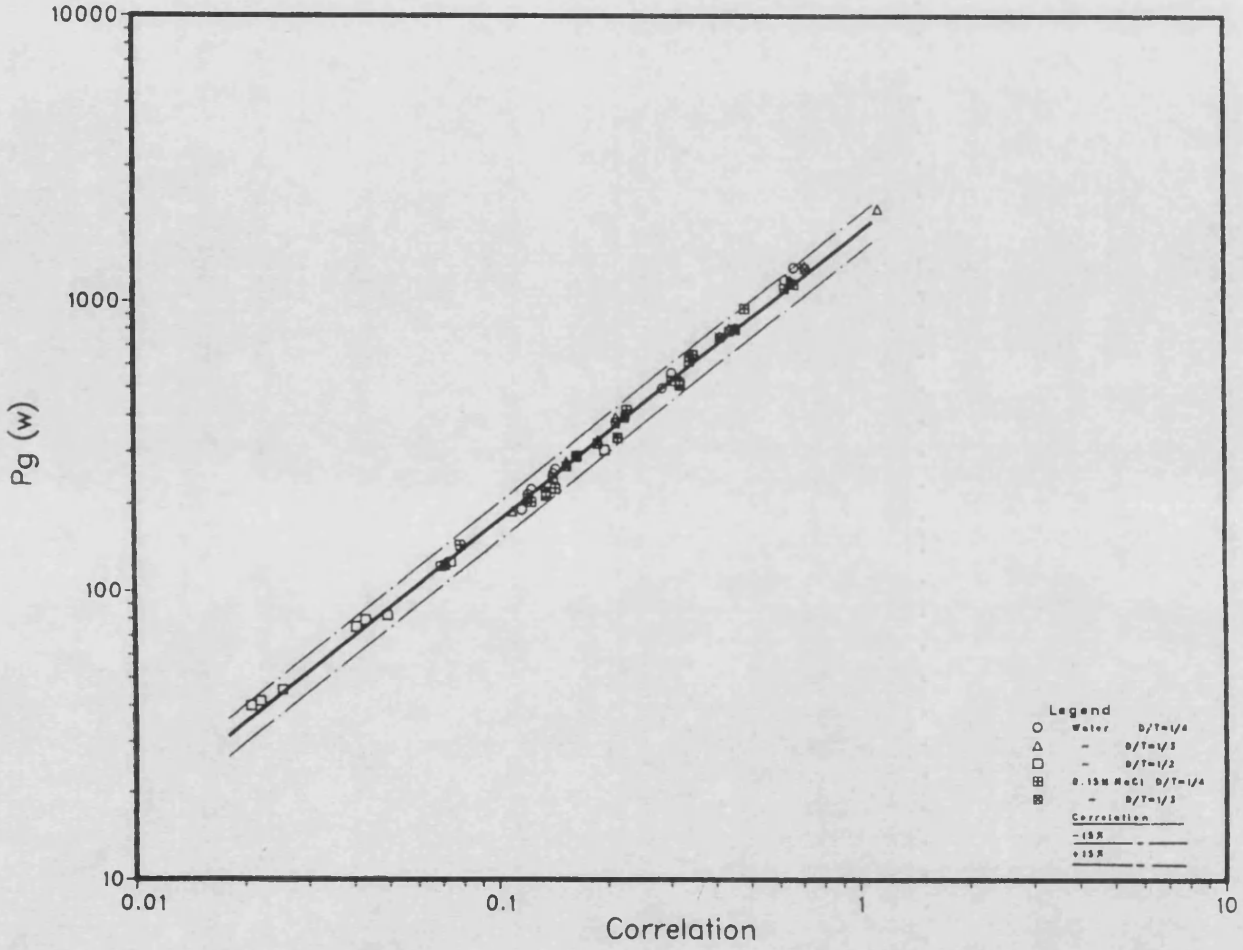

was conducted to test the statistical significance of this amelioration. Table 7.6 indicates that the improvement in accuracy achieved by the two separate models is highly significant at the 0.5% level.

Comparing Equations (7.9) and (7.10), it can be seen that the difference in the exponents of the parameters N and D/T is small. This implies that the effects of agitator speed and size variations on the power drawn are similar regardless of the gas cavity structure. However, significant difference exists between the respective exponents of Q. Gassed power is more sensitive to changes in gas flow rate under the vortex-clinging cavity regime than under the large cavity regime. This fact is in-line with the shape of the well known gassed power demand curve at constant N and varying Q, where the vortex-clinging cavity region is characterised by a relatively steep slope whereas the large-cavity-region part of the curve has a flatter slope, the point of inflection corresponding to the formation of the first three large cavities, as shown by Warmoeskerken and Smith [119].

The only correlation in Table 7.5 which uses only purely independent variables is that of Greaves and Kobbacy [125]. For η=1, their relationship relates to the 'efficient mixing regime' contained between flooding and gas recirculation. In gas-cavity structure terms this regime spreads over both the V-C and the L regimes. Despite the large difference in reactor scale the exponents of the variables are close to the ones of Equation (7.8) which correlates all the measurements acquired here.

In the model used, as Q approaches extremely low values outside the range explored ie., Q→0, the gassed power will be overestimated since $P_g \rightarrow \infty$ whereas in principle it should tend towards the ungassed power value. Also, at extremely high values of Q ie., Q→∞, the power

Table 7.6 Significance test for gassed power correlations

Correlation	Degrees of Freedom (ν)	Residual Sum of Squares (ss)	Mean Squares ($ms = ss/\nu$)	ms Ratio	F-Ratio	Level of Significance
Overall	132	1.39400	0.01056		1.352	5%
V-C Regime	65	0.36308			1.533	1%
	+	+		1.746		
L Regime	63	0.41338			1.606	0.5%
	128	07765	0.00607		1.767	0.1%

will be underestimated since $P_g \rightarrow 0$ whereas ideally it should tend towards the value of power needed to agitate the gas only. However, both of these extreme situations may not represent practical cases for the use of the gas-liquid stirred vessel.

7.4 Conclusions

- Predictive correlations have been obtained for the total gas holdup and gassed power demand, which use only the independent variables for the system ie., N, Q, and D/T. This is advantageous for practical design purposes. The overall correlations, without due regard to hydrodynamic regimes are, however, subject to a relatively high degree of data scatter.

- Systematisation of the experimental data into groups according to the two principal gas cavity structure regimes ie., vortex-clinging and large cavity regimes, enabled separate correlations for each regime to be obtained. In this way, the degree of scatter in the correlations was significantly reduced, thereby permitting more accurate prediction of gas holdup and power requirement.

- The analysis of the data with regard to different flow regimes provided insight into the sensitivity of the various parameters affecting gas holdup and gassed power.

Chapter 8

POWER DYNAMICS AND GAS CAVITY FORMATION

8.1 Introduction

The process of inflow and outflow of gas from a disc turbine impeller, under non-recirculation conditions, is described by a linear dynamic model. Transient power tests were carried out by making step changes in the sparged gas flow rate. The time constants of the measured power transients, together with the final steady-state gas outflow rate enable the size of the impeller gas cavities to be predicted. The model predictions are compared with estimates of cavity size made from photographs taken from below the impeller. These were at the same steady state conditions as for the transient power measurements.

8.2 Literature review

The shedding of roll vortices downstream from the blades of a turbine impeller in an ungassed reactor is a well recognised phenomenon [129]. The rotating action of the blade-trailing vortices creates a very low pressure inside the core of each vortex, and when gas is sparged into the vessel, these soon become filled with gas. An early photographic study by Rennie and Valentin (1968) [93] provided visual evidence of gas migration to these low pressure zones behind the six blades of a disc turbine. Since then much effort has been devoted to the investigation of these gas filled cavities. With increasing gas loads, they have been found to change in form and grow in size. The cavity shape is a function of the impeller speed and gas flow rate for a given agitator geometry system. At a fixed rotational speed and a low gas flow rate, 'vortex' cavities are formed by the process described above. On increasing the gas rate they evolve into 'clinging' cavities. If the gas rate is further increased three 'large' smoothly contoured cavities are formed behind alternate blades, the other three blades still being trailed by clinging cavities. At higher gassing rates six large cavities, but of two different alternating sizes

develop giving rise to the so-called '3-3' structure. This is the most stable configuration, in that their size does not fluctuate significantly and the cavities donot change their respective blades. At still higher gas rates 'bridging' cavities can form so that the space between the blades is completely filled with gas. Ultimately, a configuration of six large irregular and oscillating 'ragged' cavities is achieved. Not all of these configurations always occur. Some steps can be missing depending on the agitator speed. Van't Riet and Smith [129] first showed that the power consumption of a turbine agitator in an aerated vessel is related to the development of these gas-filled cavities behind the impeller blades. The formation of stable cavities reduces the form drag, due to a streamlining effect, and hence the mechanical power requirement is diminished.

Bruijn et al [130], and, Nienow and Wisdom [131] studied the cavity shape in more detail and put forward suggestions on how the cavities change with gas flow rate and impeller speed. The important role played by these gas cavities in the vessel hydrodynamics and, in turn, their influence on the overall performance of the contactor has become increasingly apparent through recent research [117, 132, 133]. Recent reviews by Smith and Warmoeskerken [101, 120] (1985), and by Nienow et al [86] (1985), have discussed the phenomena involved in gas cavity formation. The importance of studying cavity formation processes has been further evidenced in Chapter 7 where classification of experimental data on gas holdup and power demand, on the basis of the different impeller cavity structures established, led to more accurate correlations for these important mixing parameters.

Research on the development of streamlined impellers has also been evident in recent years. De Marteleire and Hendrickx [134, 135] attached artificial solid 'cavities' to the blades of a Rushton turbine.

Using 'cavities' of elliptical shape made of a synthetic material, they found that the power drawn by the agitator dropped to almost one third of the ungassed value and became independent of the gas flow rate. This gas-flow-rate independence of the power, they claim, would make scale-up rules for design of equipment more reliable. It must be remembered, however, that the gas cavities control the process of bubble generation by the impeller. Bubbles are dispersed into the bulk fluid from the outer edges of these cavities. The hydrodynamic of gas inflow and bubble dispersion is fundamental to operations of mixing and mass transfer [136]. Thus, all the gas that recirculates through the impeller is thoroughly mixed with the fresh gas flowing into the cavities. On balance, therefore, suppressing these gas cavities and replacing them by artificial solid 'cavities' will streamline the impeller blades, but will also seriously interfere with the gas mixing and bubble generation process. Although economy of mechanical power input is desirable, it should not be achieved at the expense of a poorer mixing performance. As a matter of fact, The same authors [134] have also observed a reduction in Nusselt numbers when using this new type of impeller.

8.3 Power dynamics

When a sudden variation in the gas flow rate ie., a step change, is applied to the system, the power consumption goes through a transient, after which it reaches a new stable condition. If we assume, as seems reasonable, that the instantaneous value of power drawn by the impeller is mainly determined by cavity size and shape, then it should be possible to obtain information about the process of formation and growth from the transient power response. Previous work on dynamic power response has shown that, following a pulse change in gas flow rate, the response is characterised by a single 'high' or 'low' frequency component, depending

on the extent of the gas recirculation inside the vessel [137]. The overall characteristics of the transient curves obtained for positive as well as negative step change have been discussed by Greaves et al [138], who also pointed to the suitability of a simple first order dynamic model to represent the experimental response.

Here, a simple model of the cavity formation is investigated, based on the gas inflow and outflow from the region of the impeller. The gas cavity sizes predicted by the model are compared with those obtained experimentally from photographs and the suitability of the model is discussed.

8.4 Simple dynamic model

Fig 8.1 is a simplified representation of the complex hydrodynamics occurring in the impeller region. The process of cavity formation is viewed in terms of gas inflow and gas outflow from the turbine impeller region under conditions of no gas recirculation. At a given impeller speed, the instantaneous cavity size is related to these gas flow rates. It is reasonable to assume, therefore, that the gas outflow $Q_0(t)$ from the control volume surrounding the impeller is proportional to the total volume of the cavities $V_c(t)$ as given by:

$$Q_0(t) = AV_c(t) \tag{8.1}$$

where A is a constant for a given impeller diameter and speed.

In order to arrive at a model which describes the agitator power transients, we need to define a relation for the change in impeller power resulting from a sudden change in gas flow rate, in terms of total cavity volume. In a low viscosity gas-liquid system the power response is very rapid [138], so the process of cavity growth must also be very fast. In

the absence of any detailed mechanistic understanding, the simplest approach is to assume a linear dependency of the power change on cavity volume, as follows:

$$P_g(0) - P'(t) = BV_c(t) \tag{8.2}$$

where, $P_g(0)$ is the impeller power at time 0 ie., the ungassed power value at the same rotational speed, P_0, and $P'(t)$ is the new steady state power value reached after time t from applying the change in gas load. Assuming constant gas density, the mass balance for the gas phase over the control volume enclosing the agitator can be written as:

$$\frac{dV_c(t)}{dt} = Q_i(t) - Q_0(t)$$

and substituting for $Q_0(t)$ from Equation (8.1) gives:

$$\frac{dV_c(t)}{dt} = Q_i(t) - AV_c(t)$$

For a steady state gas inflow $Q_i(t)$ equal to Q_g:

$$\frac{d(Q_g - AV_c(t))}{Q_g - AV_c(t)} = -Adt \tag{8.3}$$

Noting that at time t=0 the initial conditions are:

$$V_c(0) = 0 \quad Q_g = 0 \quad Q_0(0) = 0,$$

the integration of Equation (8.3) between times 0 and t gives:

$$\ln\left[\frac{Q_g - AV_c(t)}{Q_g}\right] = -At$$

whence,

$$1 - \frac{A}{Q_g} V_c(t) = e^{-At}$$

and,

$$V_c(t) = \frac{Q_g}{A}(1-e^{-At}) \tag{8.4}$$

Combining Equations (8.2) and (8.4) yields:

$$P_0 - P'(t) = \frac{B}{A} Q_g (1-e^{-At}) \tag{8.5}$$

The transient response is, therefore, expressed as an exponential time function characterised by a time constant $\tau_f = 1/A$. Hence, the steady state of Equation (8.1) becomes:

$$Q_0 = Q_g = \frac{1}{\tau_f} V_{cp}$$

where, V_{cp} is the model-predicted total cavity volume and is calculated by:

$$V_{cp} = \tau_f Q_g \tag{8.6}$$

8.5 Experimental procedure

Experiments were carried out in the 1.0 m mixing vessel which is fully described in Chapter 3. Relevant features of the equipment are also depicted in Fig 8.2. The Rushton turbines used had D/T ratios of 1/4, 1/3 and 1/2, and were placed at a clearance of T/4. The tank was filled to a height of 1.0 m with filtered softened water and the gaseous phase was filtered air. Prior to initiating a dynamic experiment, the system was first allowed to reach steady state. The input disturbance applied to the system was, in each case, a positive step change in the air flow rate starting from an ungassed condition, enabling the maximum power drop to be obtained. This eased the analysis of the transient curves somewhat.

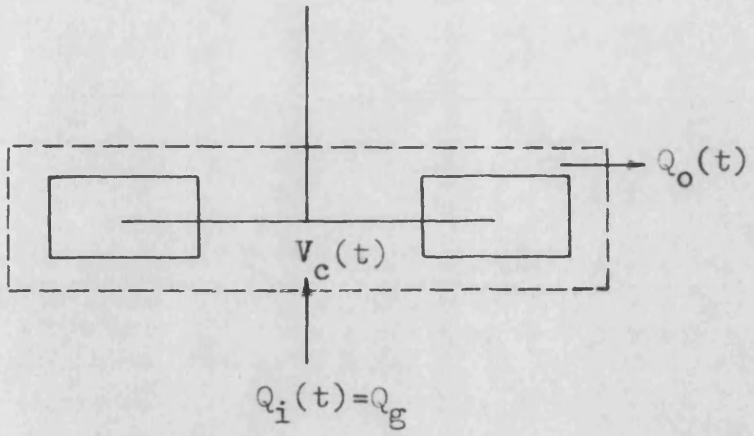

Fig 8.1 Flow of gas through impeller cavities (no gas recirculation).

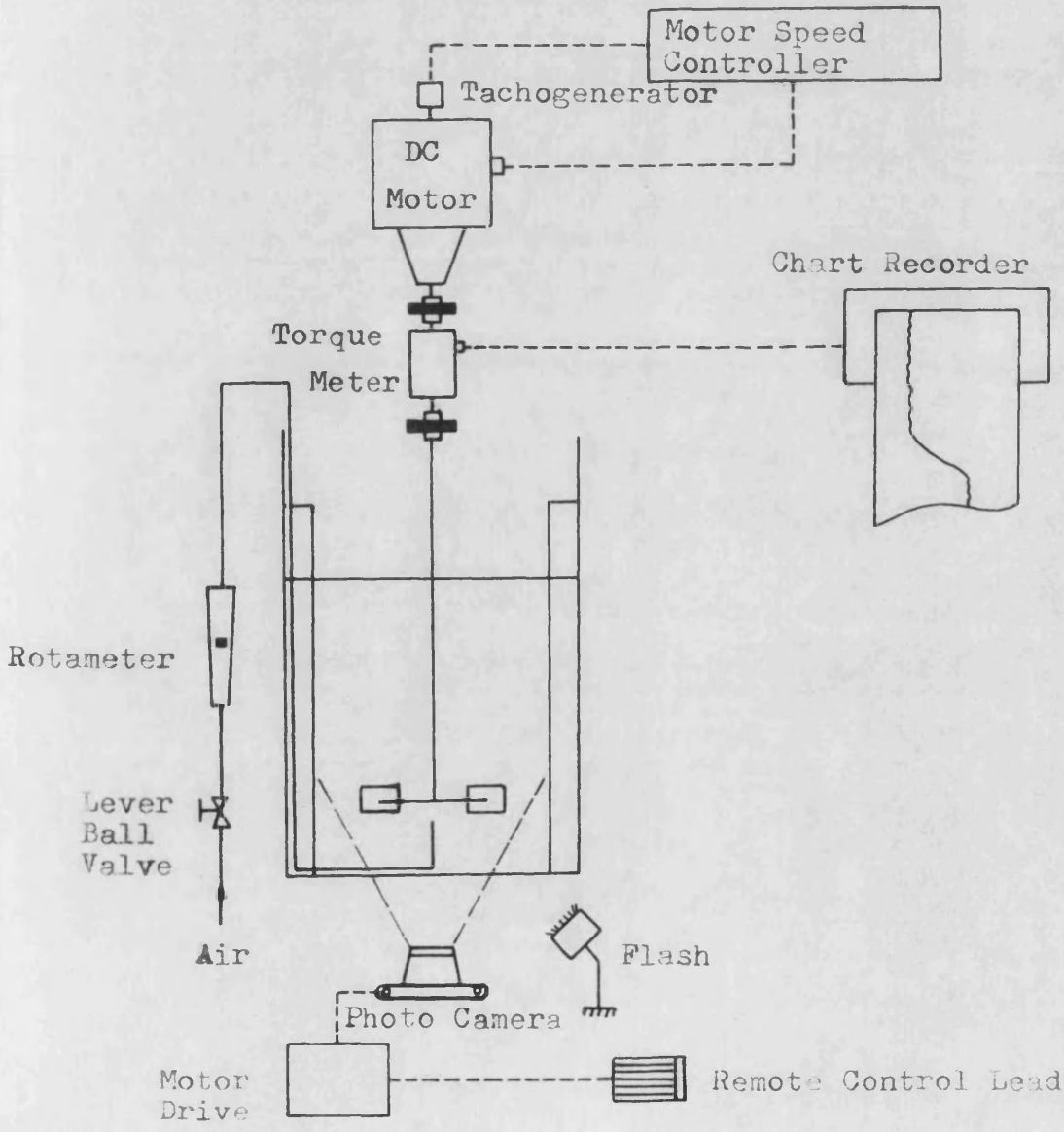

Fig 8.2 Set-up for power dynamic tests.

The step change in gas flow rate was achieved manually by suddenly opening a ball valve inserted in the gas line. The step changes used had magnitudes of 4.38, 6.87 and $8.33\times10^{-3}\ m^3/s$. The agitation speed ranged from 1.00 to 8.33 rev/s and its value was held constant during the dynamic tests by the Fenner speed controller described in Section 3.3. The transient impeller torque was measured by the BHC torque transducer mounted integrally with the impeller shaft (Section 3.3.1). The torque transient curves were recorded on a chart recorder for subsequent analysis. Any error in torque measurement was eliminated since the steady state component was subtracted from the output.

In order to check the validity of the dynamic model proposed, photographs of the impeller region were taken through the transparent base of the tank. The camera used was a Nikon-F2 35 mm single lens reflex with 28 mm wide angle lens, supplied with a remote control lead and motor drive. The camera was accurately aligned with the impeller centre and by using flash illumination (1/60 sec.) a steady image was obtained. The correct exposure was found by trial tests. The Pan-F film used was later developed for high contrast. Additional flow visualisation aid was provided by a stroboscope. The projected area of the cavities was measured by a planimeter and the total volume of the six cavities was then estimated by assuming a constant cavity depth equal to the depth of the blade, D/5, less the disc thickness.

8.6 Results and discussion

8.6.1 Power transients

A typical power transient curve is shown in Fig 8.3. The fast response reported by Greaves et al [138] in a 0.20 m vessel is confirmed here for this much larger scale reactor. The transient curves also

revealed that there are in fact two response regions, designated I and II in Fig 8.4. The very fast drop in power in Region I (a fraction of a second), which accounts for the major portion of the total power reduction, is mainly associated with the growth of the gas cavities. After reaching a pseudo steady state, corresponding to the value P', the power begins to fall again, eventually reaching its final steady state at P_g. The Region II response is much slower, typically extending over a period of a few seconds. This effect is attributed to the gradually developing pattern of gas holdup in the bulk of the vessel, as well as some gas recirculation into the impeller, causing a further increase in cavity size.

Qualitatively, the higher the gas holdup and the greater the extent of gas recirculation, the more the intermediate steady state P' will be separated from the final steady state P_g. This effect can be described approximately by the ratio $\frac{(P'-P_g)}{(P_0-P')}$. In the following discussion, attention is focused primarily on the process of the transient cavity growth as typified mainly by the response of Region I of the dynamic power curves.

The dynamic model (Equation (8.5)) predicts that the transient power response should have an exponential shape. It was in fact possible to fit an exponential curve to all the experimental transients. For this purpose, the curve fitting procedure was performed using a set of 'templates', selecting the best fit in each case. The time constant values, τ_f, obtained in this way are displayed in Table 8.1, for the three turbines used. For a given impeller size and speed some scattering in the values of the time constant can be noticed. This is due to the relatively large torque fluctuations in the signals as well as a certain degree of arbitrariness in the choice of the best exponential function fit. It can also be noted that, with the exception of some outlier values, for a given step

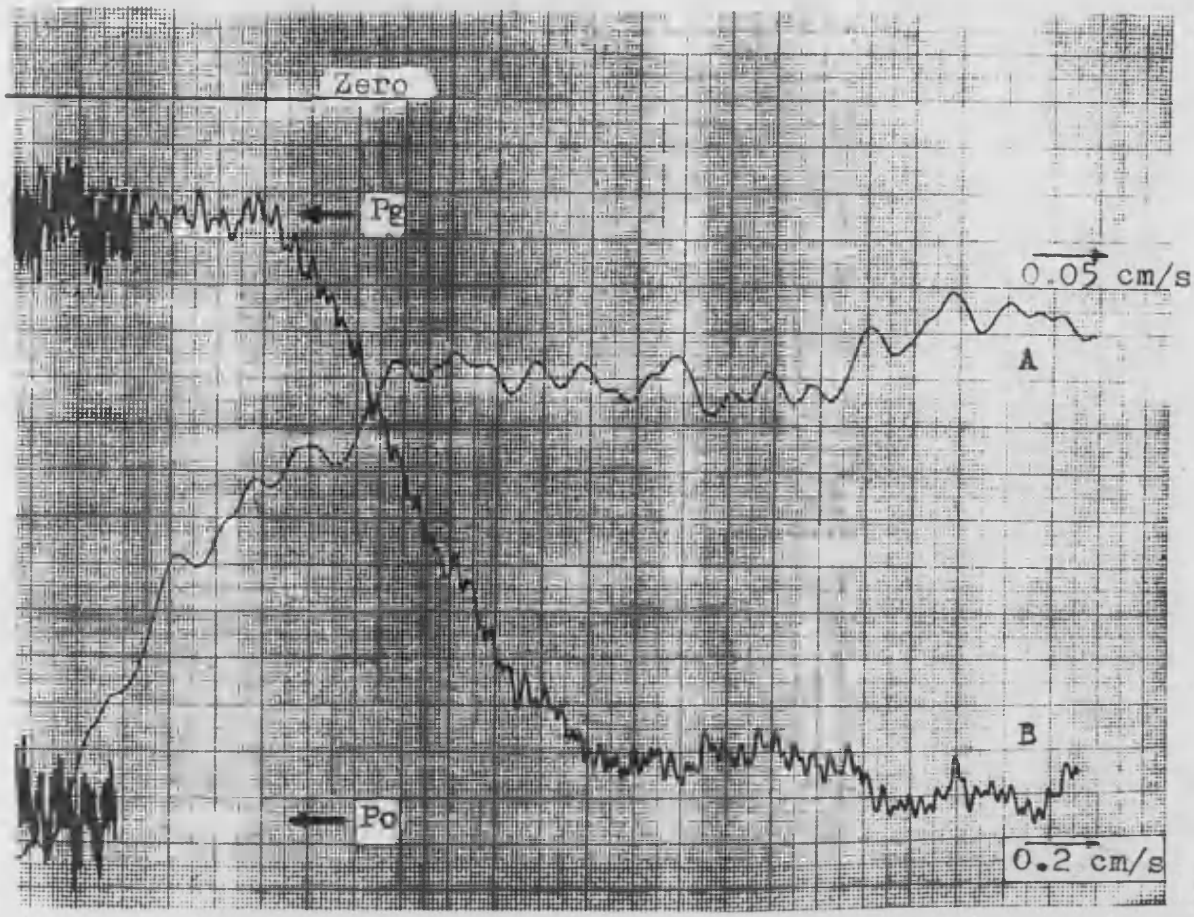

Fig 8.3 Typical transient power response
Curve A: Cavity formation
Curve B: Cavity stripping.

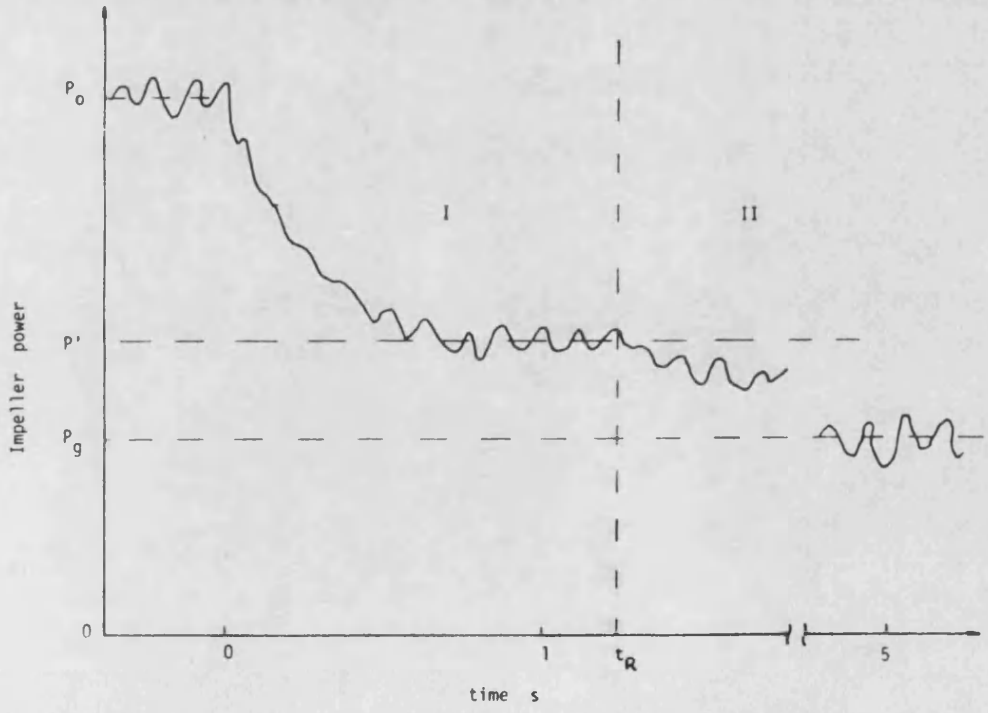

Fig 8.4 Interpretation of a transient power curve.

Table 8.1 Experimental time constants and cavity sizes

D/T		1/4							1/3							1/2			
N (rev/s)		4.75	5.33	5.83	6.42	6.67	7.50	8.33	2.42	3.00	3.33	4.17	4.50	4.75	5.00	1.00	1.25	1.67	2.08
4.38×10^{-3} (m^3/s)	V_{cc} ($10^{-3}m^3$)	-	-	-	0.88	0.78	-	0.88p	1.46	1.66	-	1.66	1.66p	1.66p	1.56p	-	-	r	r
	τ_F (s)	0.10	0.10	0.15	0.08	0.10	0.11	0.10	0.25	0.30	0.15	0.28	0.22	0.15	0.20	0.35	0.30	0.28	0.50
	τ_s (s)	0.80	0.78	0.90	0.86	0.82	1.06	1.30	0.34	0.33	0.28	0.43	0.36	0.42	0.38	0.31	0.62	0.41	0.57
6.87×10^{-3} (m^3/s)	V_{cc} ($10^{-3}m^3$)	0.68	0.88	-	-	1.07	-	r	1.66	1.76	1.95	1.85	1.85p	2.15p	r	-	3.39	3.58	r
	τ_F (s)	0.09	0.09	0.08	0.06	0.07	0.08	0.08	0.17	0.18	0.16	0.20	0.14	0.15	0.10	0.30	0.40	0.35	0.33
	τ_s (s)	1.14	0.90	1.08	0.98	1.04	1.00	1.02	0.22	0.25	0.23	0.27	0.21	0.21	0.19	0.42	0.54	0.56	0.38
8.33×10^{-3} (m^3/s)	V_{cc} ($10^{-3}m^3$)	-	-	1.17	-	1.07	-	0.88p	1.37	1.95	1.76	2.34	2.34p	2.34p	1.9p	-	-	3.39	r
	τ_F (s)	0.08	0.06	0.08	0.09	0.08	0.06	0.09	0.11	0.14	0.12	0.15	0.20	0.14	0.11	0.15	0.34	0.35	0.50
	τ_s (s)	0.90	0.92	0.94	0.86	1.00	1.20	1.26	0.16	0.22	0.21	0.21	0.25	0.22	0.19	0.15	0.28	0.39	0.33

p: partially obscured by recirculation

r: totally obscured by recirculation

input, Q, and a given impeller size, τ_f does not vary significantly with N. This means that N has a negligible effect on the speed of cavity formation. On the other hand, τ_f increases appreciably with increasing turbine diameter. This is simply due to the important relative increase in cavity size ($\propto D^2$). The time constants obtained were used to predict the total volume of the gas cavities from Equation (8.6).

8.6.2 Cavity size measurements

The photographs taken confirmed all of the cavity configurations described in Section 8.2 above ie., vortex, clinging, 3 clinging-3 large, '3-3' structure of large cavities, bridging and ragged cavities. Sample photographs of these configurations are shown in Figures 8.5 (a-f). The film negatives were mounted on slides and projected on a screen. From the magnified projections, the cavity contours were carefully traced onto transparent paper for subsequent measurements. The cavities considered were mostly of the '3-3' structure.

Unfortunately, not all of the photographs were useful because the cavities were obscured due to gas recirculation below the impeller. At high agitation speeds the impeller region became either partially or completely obscured by the dispersion. This effect was particularly restrictive with the largest turbine (D/T=1/2). The cavity volumes estimated from the photographic projections are plotted against those predicted by the dynamic model in Fig 8.6. There is a fair degree of agreement over the operating range. In the absence of any three-dimensional information on cavity shape, the volume of a cavity was calculated on the assumption of a constant cavity depth from the blade surface to the rear of the cavity. This is likely to overestimate substantially the actual volume of the cavity as its vertical profile would be reducing towards the rear of the cavity. It is not surprising therefore,

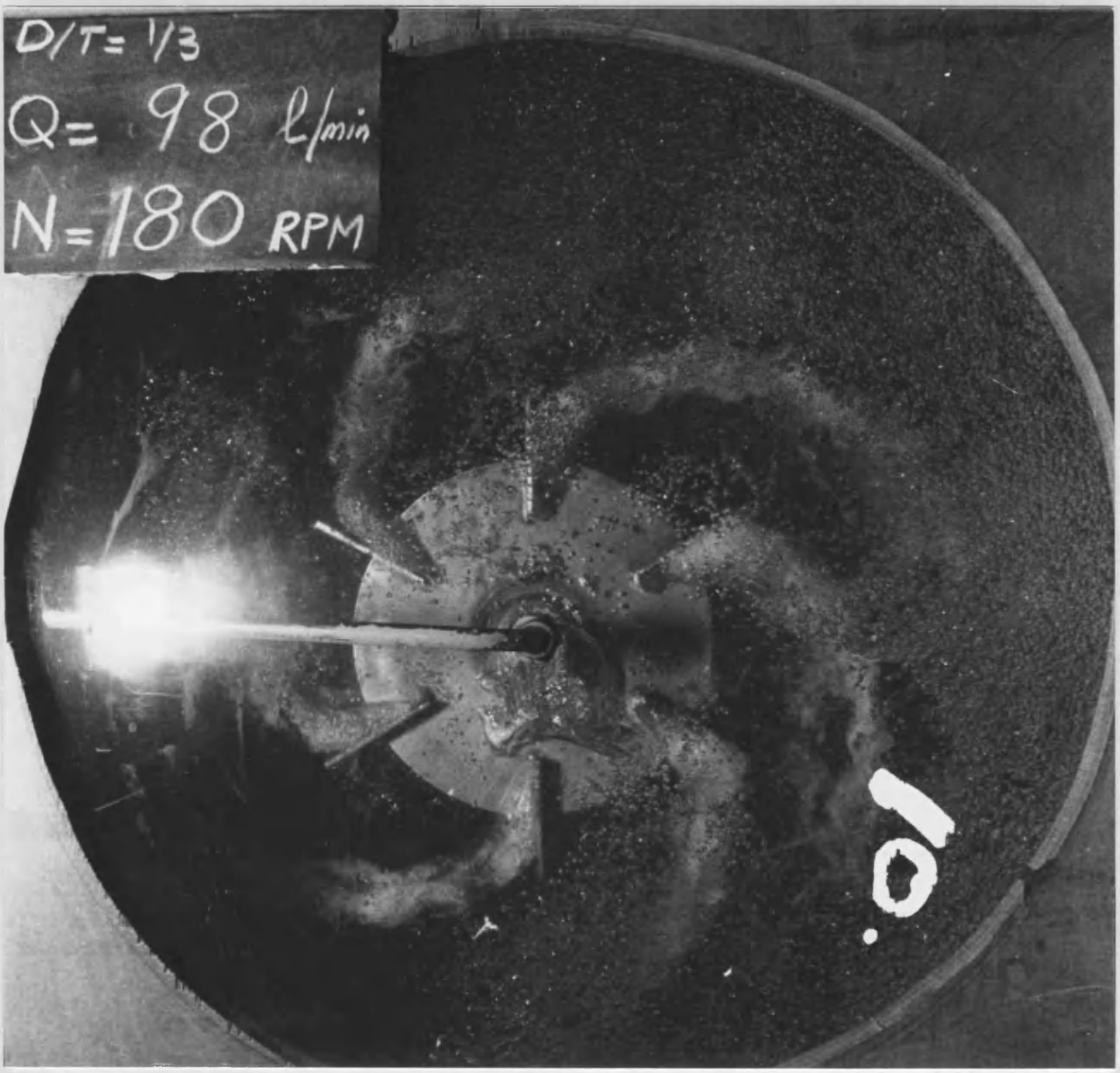

Fig 8.5 (a) Vortex cavities

D/T=I/3

N=3 rev/s

Q=0.00I64 m^3/s

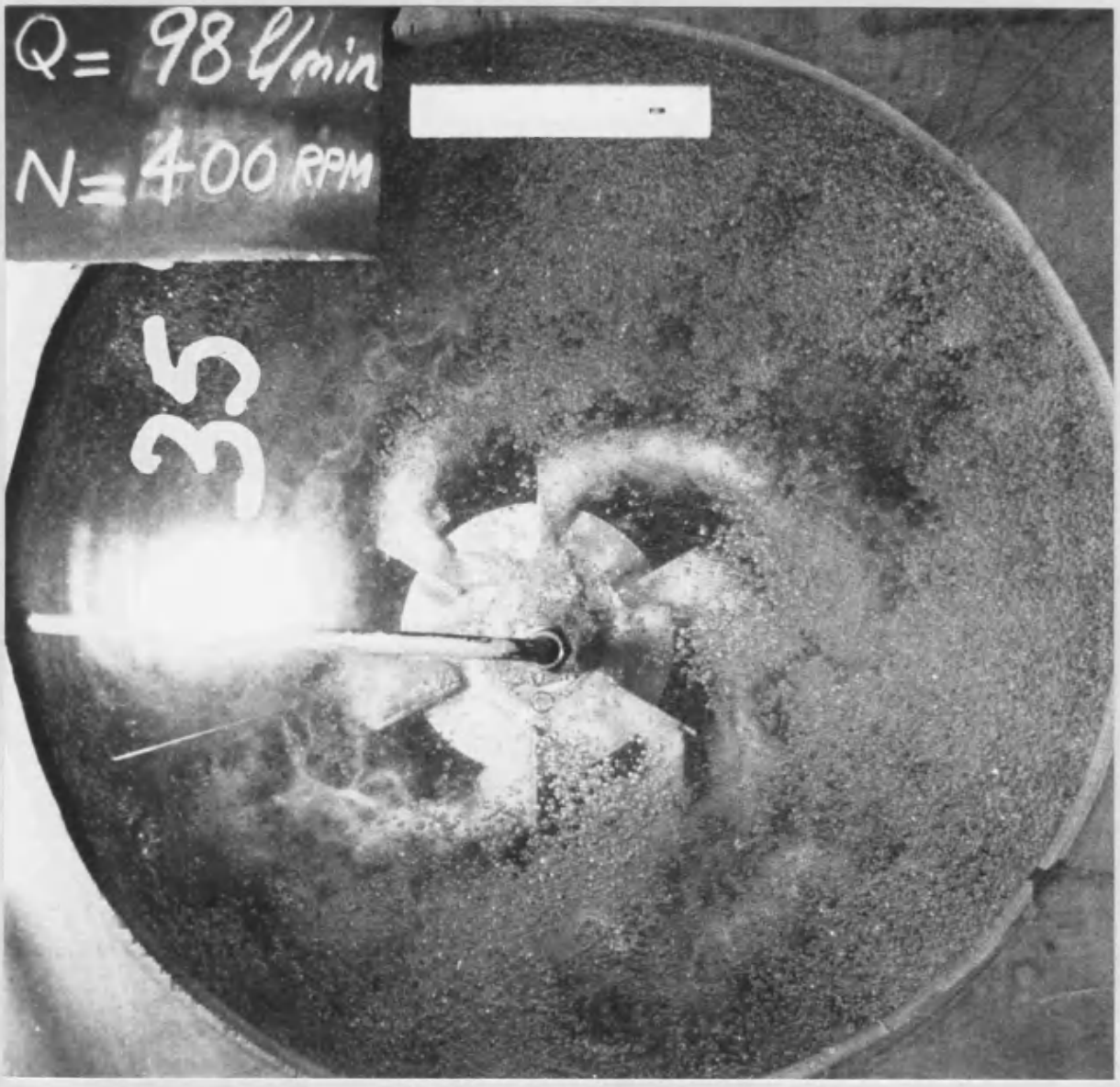

Fig 8.5 (b) Clinging cavities

D/T=I/4

N=6.67 rev/s

Q=0.00I64 m^3/s

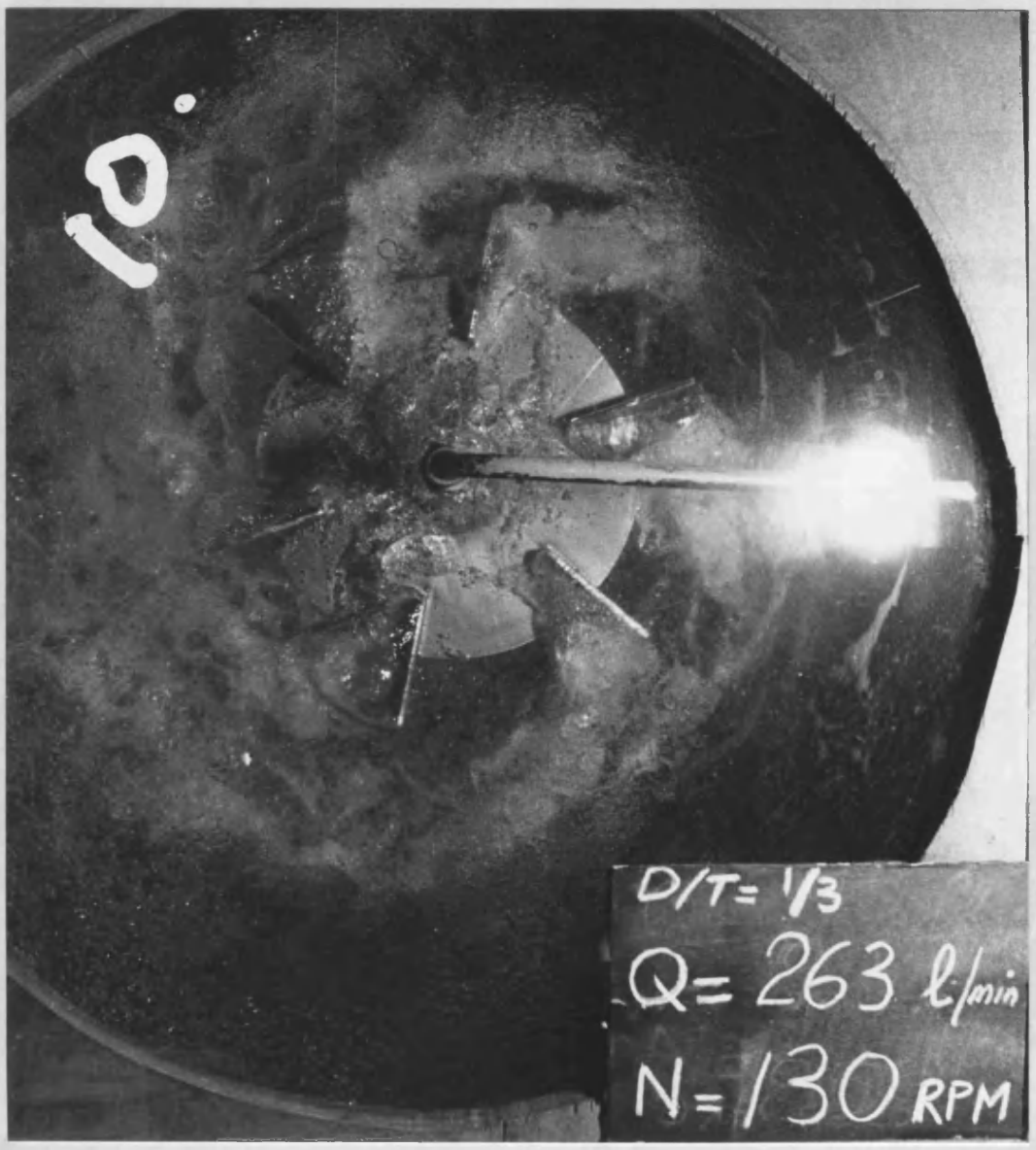

Fig 8.5 (c) 3 Clinging and 3 Large cavities

D/T=I/3

N=2.I7 rev/s

Q=0.00438 m^3/s

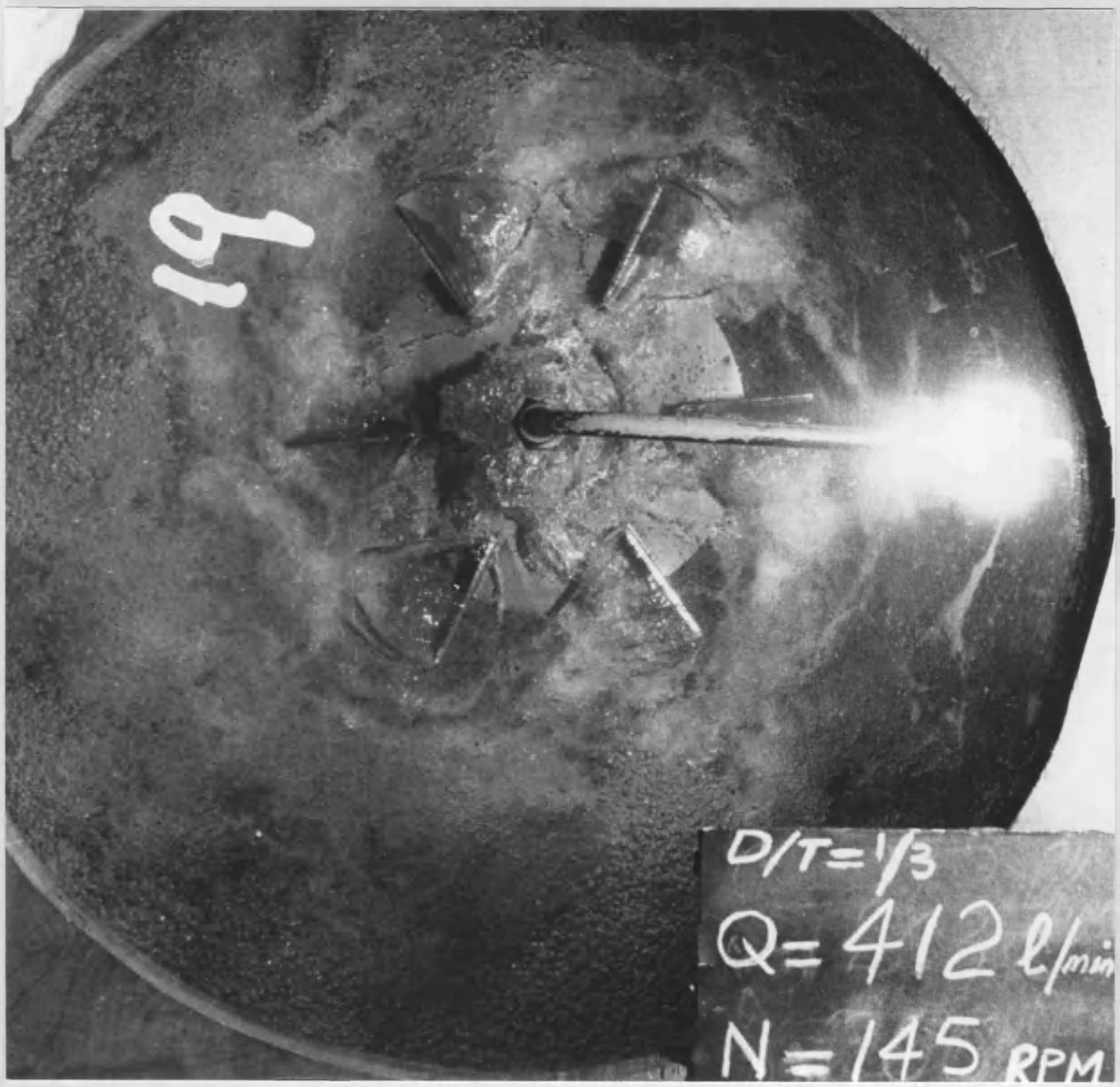

Fig 8.5 (d) '3-3' Structure (6 Large cavities of different size)

D/T=I/3

N=2.42 rev/s

Q=0.00687 m^3/s

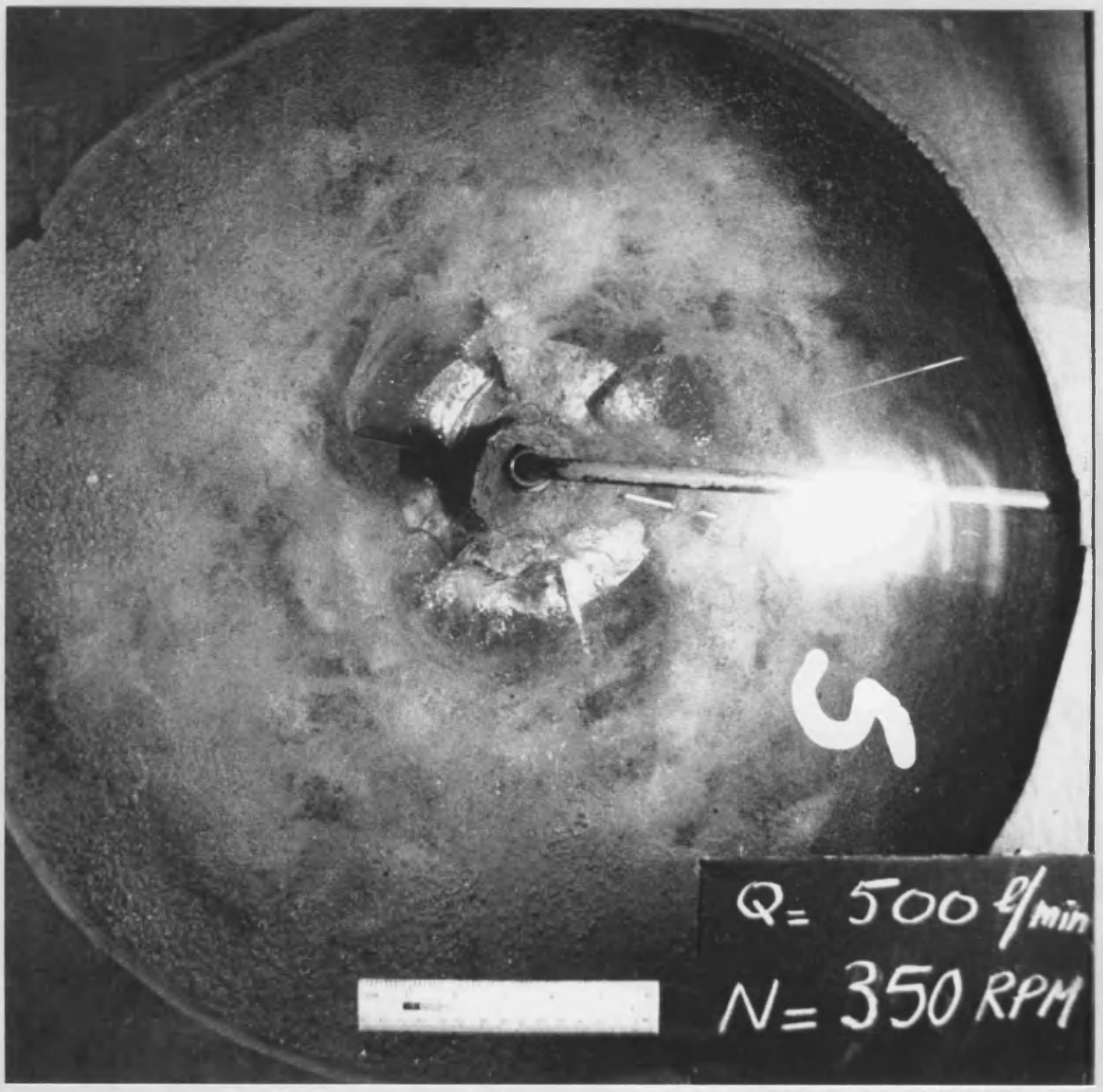

Fig 8.5 (e) Bridging cavities

D/T=I/4

N=5.83 rev/s

Q=0.00833 m^3/s

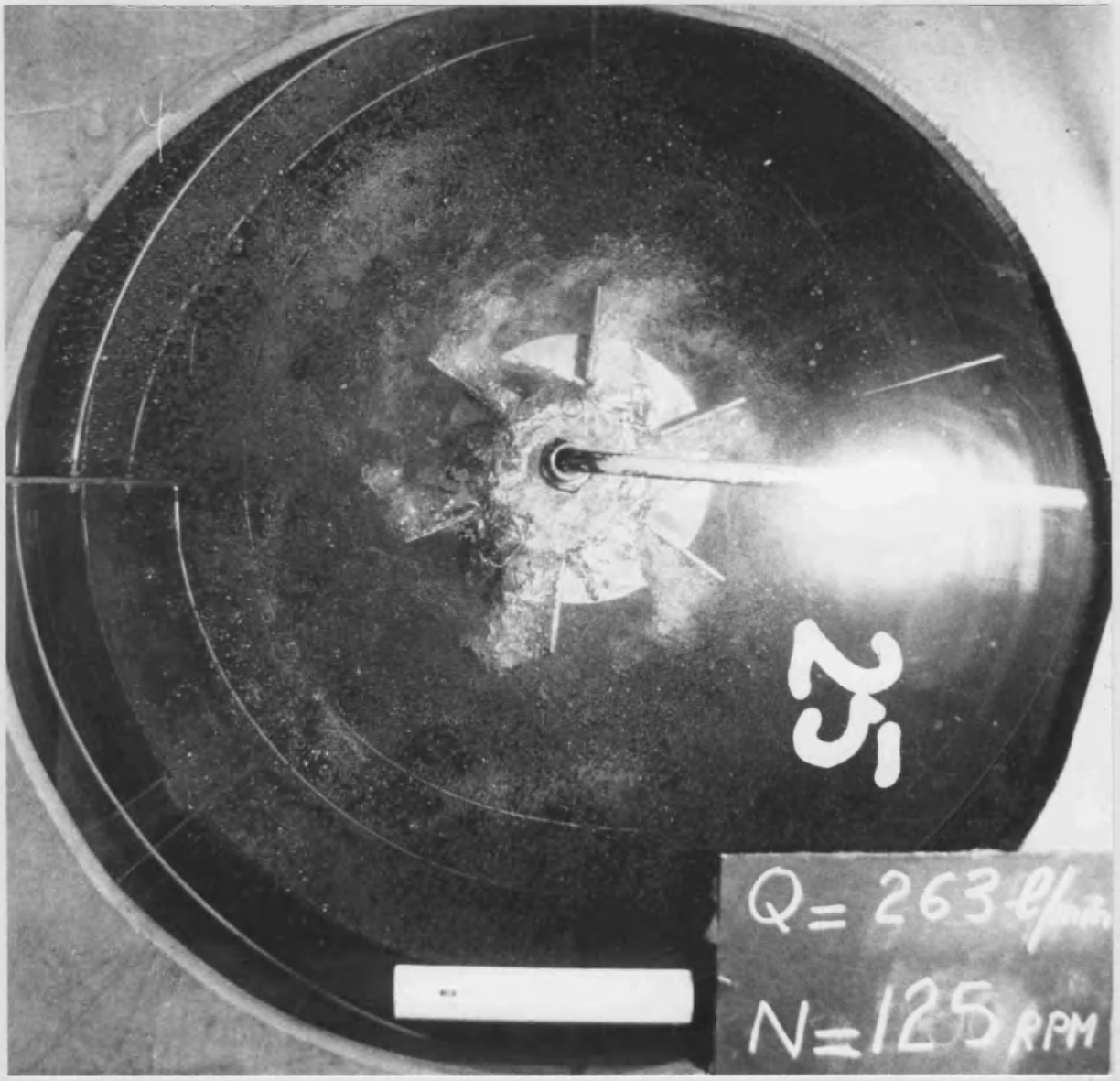

Fig 8.5 (f) Ragged cavities

D/T=I/4

N=2.IO rev/s

Q=0.00438 m^3/s

Fig 8.6 Measured Cavity Size vs Model Prediction

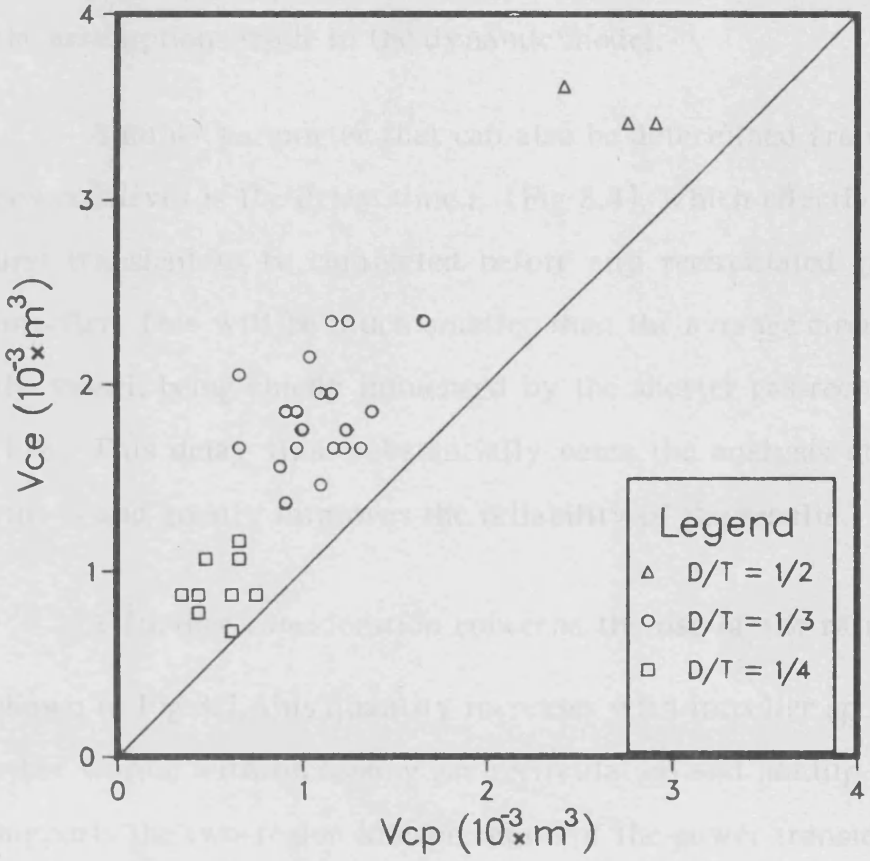

that the observed volume values generally lie above the diagonal. The overall percentage error of the predicted values is -36%. Moreover, the cavity size predicted from the power transient does not account for the later increase in cavity volume that may occur due to gas recirculation into the impeller, whereas the photographs obviously show the steady-state cavity size, which includes this latter contribution. Consequently, the agreement between the observed and the model predicted cavity volumes is judged to be satisfactory, broadly confirming the validity of the assumptions made in the dynamic model.

Another parameter that can also be determined from the transient power curves is the delay time t_r (Fig 8.4), which effectively allows the first transient to be completed before any recirculated gas reaches the impeller. This will be much smaller than the average circulation time in the vessel, being chiefly influenced by the shorter gas recirculation loops [118]. This delay time substantially eases the analysis of the transient curves and greatly improves the reliability of the results.

A further consideration concerns the use of the ratio $\frac{(P'-P_g)}{(P_0-P')}$. As shown in Fig 8.7, this quantity increases with impeller speed and size, in other words, with increasing gas recirculation and holdup. This not only supports the two-region interpretation of the power transient curves, but could also provide a useful basis for analysing gas recirculation effects, allowing the present cavity model to be extended to conditions of recirculation.

While all these results encourage further work on transient response measurements, it is evident that improvement of the measurement and data processing of results is desirable in order to improve the precision. This can be achieved through computer control of

Fig 8.7 [P'−Pg]/[Po−P'] vs Impeller Speed, Showing Recirculation Trend

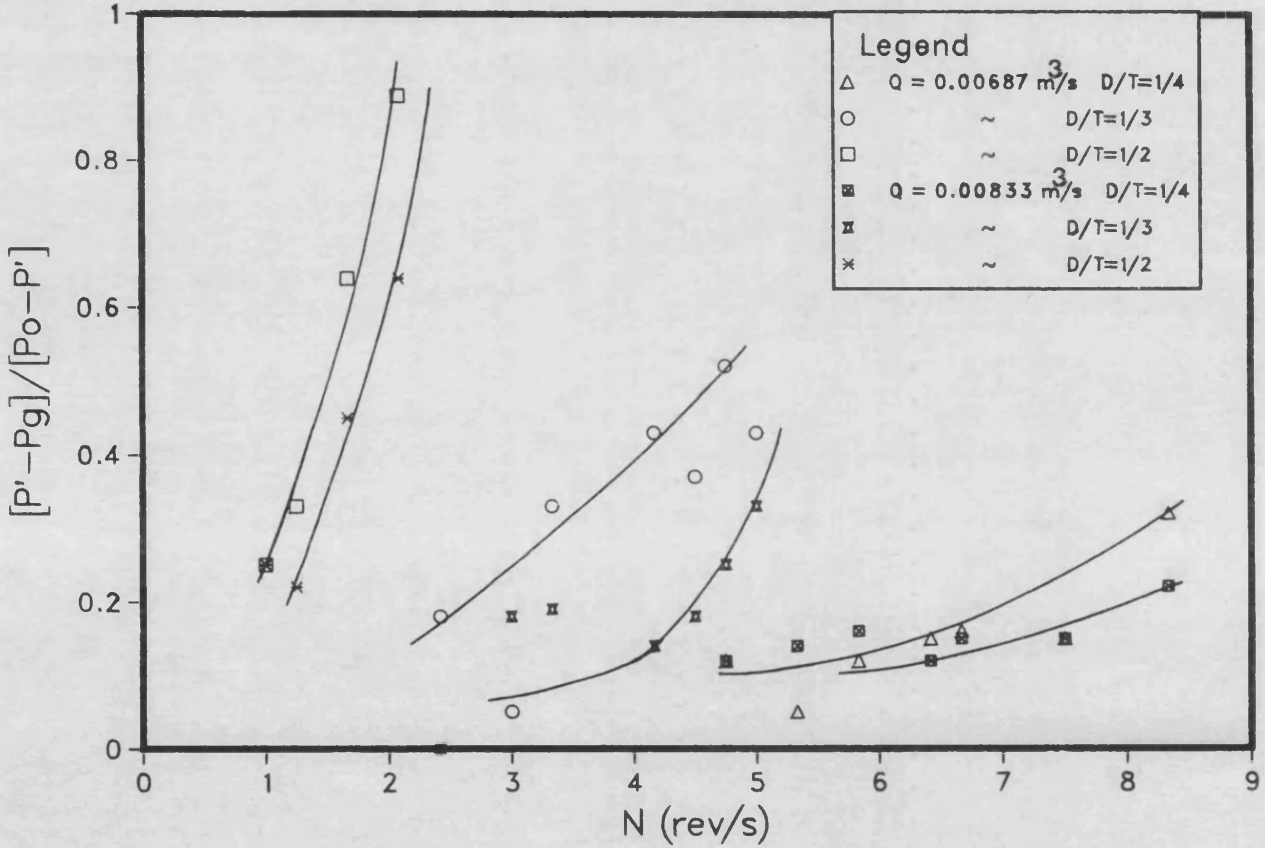

the measurement process, enabling repetitive sets of experimental results to be smoothed and subsequently correlated by numerical least squares fitting procedures. The use of a fast automatic on-off valve to introduce the step changes in gas flow rate would also be advantageous.

8.6.3 Cávity stripping process

The process of cavity formation which follows the sudden opening of the air valve was generally found to be much faster than the reverse process of cavity stripping which results from the instant shut down of the air flow into the vessel. A typical transient curve representing the latter process is compared with the corresponding dynamic curve of cavity formation in Fig 8.3. The difference between the fall and rise of the two transients, respectively, is remarkable. Bruijn et al [130] found that with large cavities the pressure behind the impeller blades rises to almost the static pressure in the flow. In the instance of cavity development, the low pressure field behind the blades provides a high attraction force for the gas. At steady state, gas is dispersed from the outer edges of the cavities and this is made up for by the inflowing sparged and recirculated gas into the impeller. When the sparged gas flow is interrupted gas continues to disengage from the cavities. Consequently, the decreasing pressure behind the blades acts to delay this process of gas disengagement by resisting the gas outflow from the impeller and by capturing more of the still recirculating bubbles.

The values of the time constant τ_s, extracted from the cavity stripping transients, are displayed in Table 8.1. In this case also, the agitation speed does not have any notable effect on τ_s, for a given gas rate and impeller diameter. The interesting difference, here, between the two time constants τ_f and τ_s, is that whilst on average τ_f increases monotonically with D/T for a constant Q, τ_s decreases sharply between

D/T=1/4 and 1/3, but then recovers at D/T=1/2. Therefore, it seems that there exists a critical value for D/T between 1/4 and 1/2, which is a turning point for the trend of τ_s. Given that data has only been obtained for three impeller sizes and that no quantitative or qualitative information is available on the transitory states of the process, it is, at first hand, difficult to speculate about the causes behind this phenomenon. From Table 8.1, it can be seen that the difference between the speeds of cavity formation and stripping is very high for the smallest turbine, but reduces in magnitude as D/T increases. In fact, for the largest ratio the time constants of the two transients become more or less of the same order. This is a result of the basically adverse effects that the increase in impeller size has on the speeds of the two processes.

By comparing the general behaviour of the two transients in Fig 8.3, it can be noted that the reverse process of cavity stripping seems to follow the same trend as the forward formation process, although much more slowly. In fact, the stripping transient also shows a two-region response behaviour. The first region accounting for most of the power increase, is considered to be governed by the stripping of the cavities, whereas the second region represents the subsequent slow disengagement of the gas holdup. Visual observation showed this second mechanism to be relatively slow, typically occurring over a period of approximatey 10 seconds, as also found by Mann et al [140] in their dynamic gas disengagement experiments. This is due to the slow release of the gas bubbles entrapped in the liquid circulation loops.

8.6.4 Cavity structure maps

A cavity structure map for each of the three D/T ratios used has been constructed (Fig 8.8 (a,b,c)) using established correlations from the literature. On each map three principal regimes can be distinguished:

(i) A stable regime with six vortex or clinging cavities.

(ii) A stable regime with either 3 large-3 clinging or '3-3' large cavity structure.

(iii) An unstable regime with six oscillating ragged cavities.

The transition from loading regime (i) to loading regime (ii) was correlated by Smith and Warmoeskerken [120] as:

$$F_l = 3.8\times10^{-3}\left[\frac{R_e^2}{F_r}\right]^{0.067}\left[\frac{T}{D}\right]^{0.5} \tag{8.7}$$

The transition from loading regime (ii) to flooding regime (iii) was correlated by Nienow et al [86] as:

$$F_l = 30F_r\left[\frac{D}{T}\right]^{3.5} \tag{8.8}$$

Two other transitions have been added on the maps. The first one corresponds to the start of gas recirculation in the lower part of the vessel. This is characterised by the N_{CD} speed correlated by Nienow et al [76] as:

$$F_{l_{CD}} = 0.2\left[\frac{D}{T}\right]^{0.5} F_{r_{CD}}{}^{0.5} \tag{8.9}$$

The N_{CD} line corresponds to a minimum in the power consumption as the speed is increased at constant gas flow rate. In terms of gas dispersion, it denotes the condition of full gas distribution in the upper part of the vessel and initiation of bubble deflection below the impeller plane. Originally, N_{CD} was interpreted as the transition to flooding by Nienow et al [139]. This speed is in fact significantly higher than the value given by Equation (8.8).

The second transition line also identified by Nienow et al [76, 86], corresponds to a maximum in the power demand when the speed is

Fig 8.8 (a) Cavity Structure Map for D/T=1/4

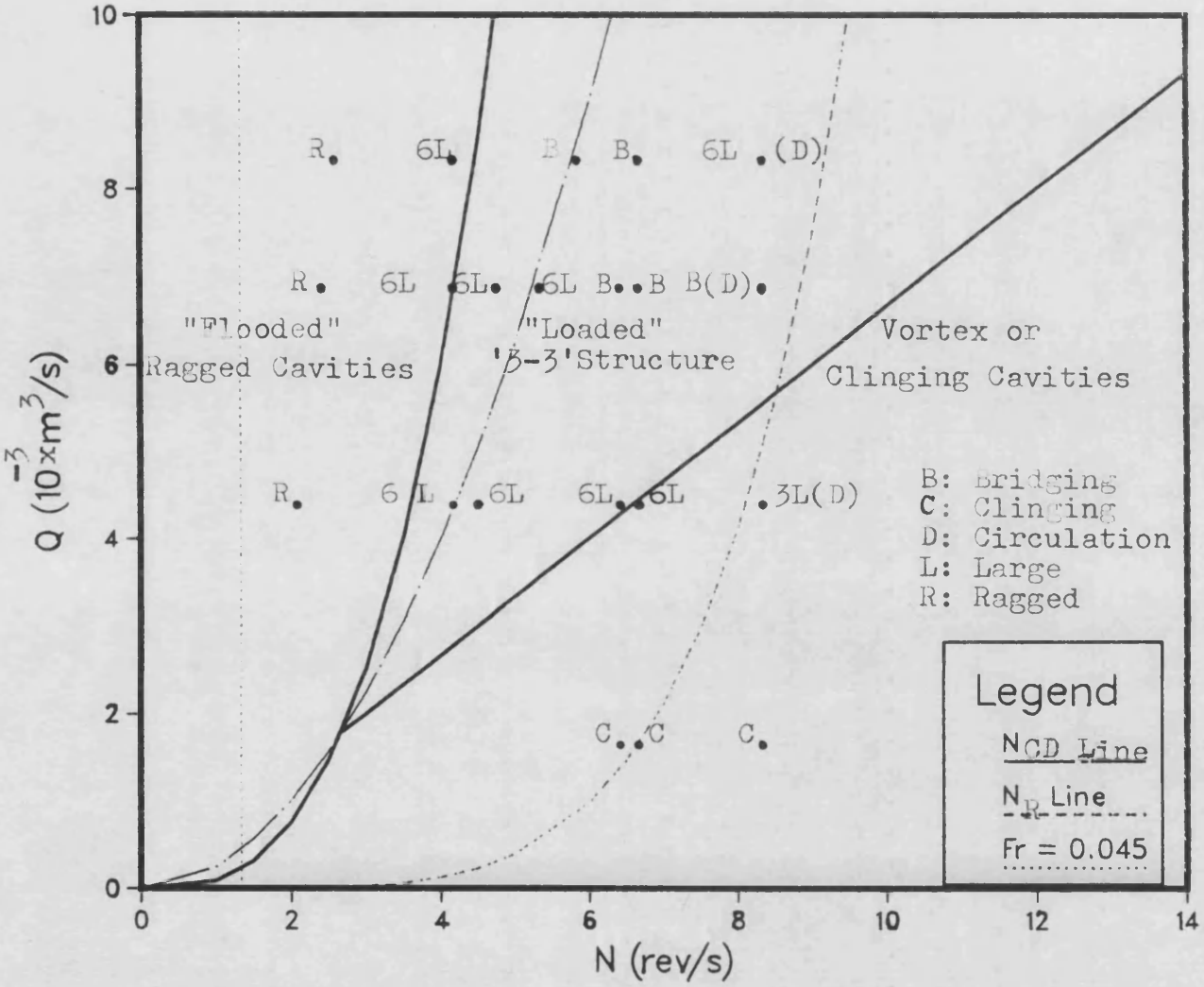

Fig 8.8 (b) Cavity Structure Map for D/T=1/3

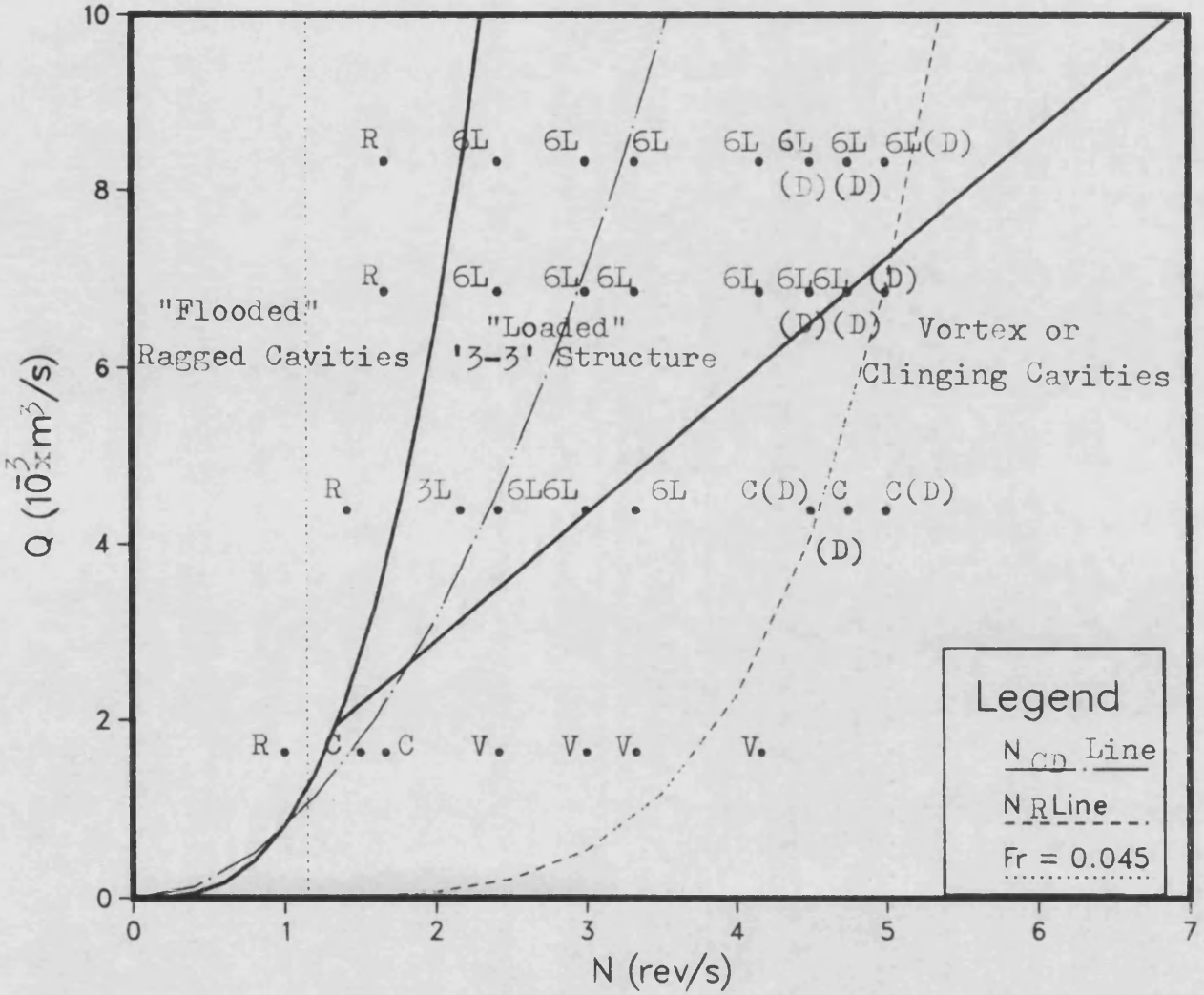

Fig 8.8 (c) Cavity Structure Map for D/T=1/2

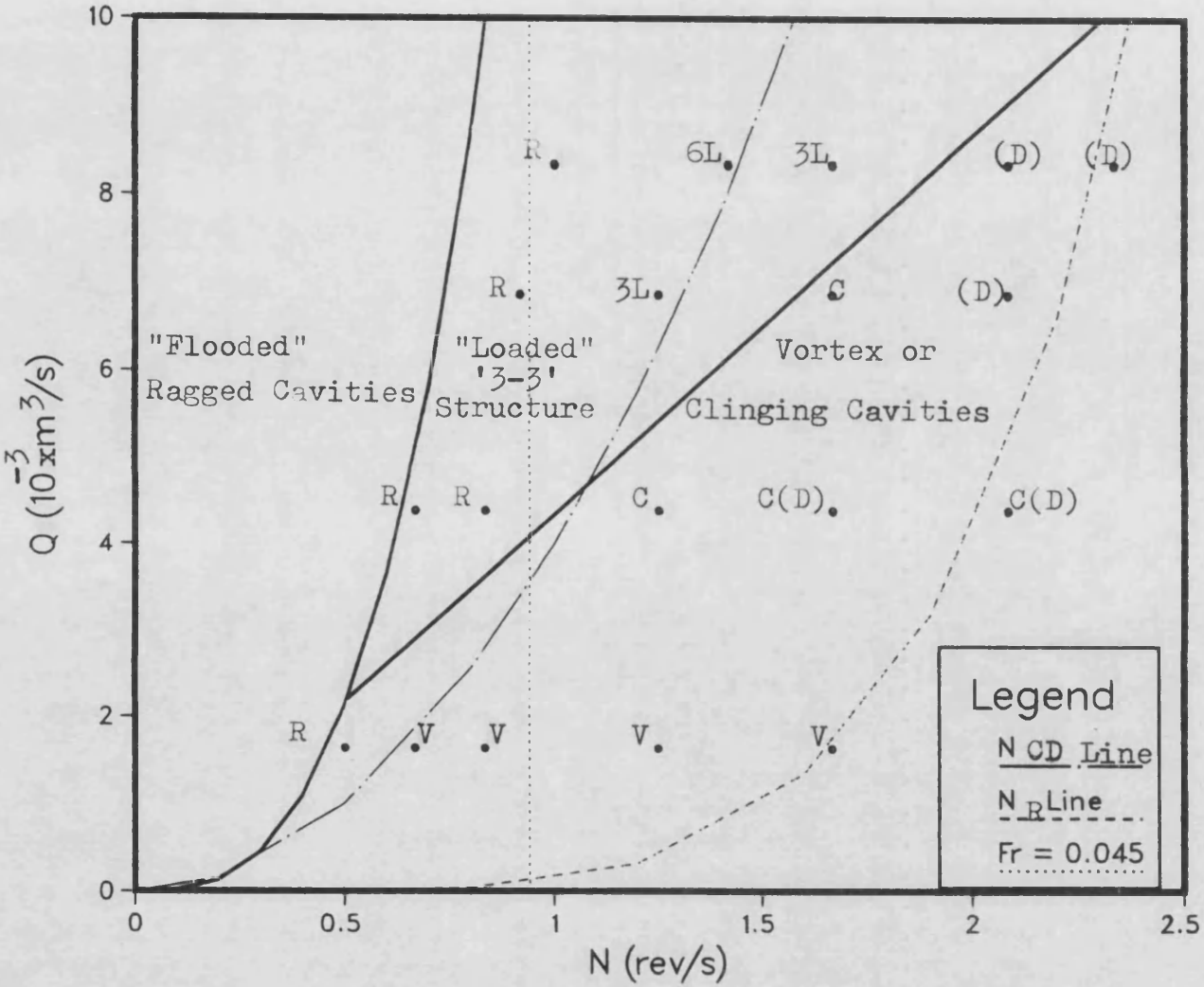

increased at constant gas flow rate, above N_{CD} to a value N_R. This speed, N_R, marks the establishment of intensive gas recirculation to the impeller, causing an increase in the cavity size and hence the power drops slightly again. It is expressed as:

$$N_R' = 1.5\frac{Q^{0.2}T}{D^2} \tag{8.10}$$

The cavity configurations observed photographically at different agitation speeds and air flow rates are indicated on the cavity maps for the three D/T ratios. They generally confirm the validity of the correlations for cavity structure transition, except for D/T=1/2 where some ragged cavities were detected to the right of the flooding regime boundary ie., inside the '3-3' structure zone. This indicates a possible scale-up limitation for equation (8.8), bearing in mind that this correlation was derived from experimental data obtained in vessels having a maximum size of 0.61 m only [86].

Warmoeskerken et al [119, 132] reported that large cavities could not form at Froude numbers less than 0.045. On their cavity maps the lines corresponding to F_l=0.045 are situated outside the '3-3' structure region ie., in the area of vortex-clinging cavities at low gas flow rates, and lying therefore, in the zone of ragged cavities at high gas flow rates. This is also the case for the D/T=1/4 and 1/3, as shown in Figs 8.8 (a,b). For D/T=1/2, however, the line is seen to cross the '3-3' structure region for an important range of gas flow rates, à priori, suggesting the possibility of large cavity formation at Froude numbers below the value of 0.045. On the other hand, the cavities observed in this vicinity of this Froude number value, were of the ragged type, as indicated in Fig 8.8 (c). Although this seems to support the finding of Warmoeskerken et al that large cavities should not form below a Froude number of 0.045, it

also appears to support the remark made above that the flooding-loading transition should be shifted to the right, therefore, bringing the Froude number line out of the '3-3' structure region, inside the flooding zone.

8.7 Conclusions

- The impeller transient power response resulting from an input disturbance in sparged gas flow rate demonstrates two response regions. A very fast drop in power in Region I, which accounts for the major part of the total power reduction, mainly associated with the growth of gas cavities behind the impeller blades, and a much slower response in Region II, marking the subsequent contribution to power drop due to the build-up of gas holdup and recirculation.

- A simple first order dynamic model is proposed to describe the interaction between the inflow and outflow of gas from the cavities which form behind the agitator blades when gas is sparged into the reactor. The experimental time constants can be used to estimate the size of these gas cavities. The model is able to predict to a reasonable degree the first part (Region I) of the power transient response.

- In general, the cavity formation process is much faster than the reverse process of cavity stripping, but however, the difference between the two diminishes significantly with increasing D/T ratios.

- There is increasing interest in the optimisation of impeller profiles in relation to mixing performance, justifying the need of searching for more understanding of the impeller hydrodynamics, because only through complete appreciation of the complex phenomena involved can significant progress be achieved in this domain. In this respect, a detailed knowledge of the gas cavity formation, size and shape is important if performance parameters (eg. ϵ, P_g, $K_L a$ etc.) are to be

accurately predicted and optimised for particular geometries. The transient technique described is useful for studies of impeller hydrodynamics in stirred vessels, especially in those cases where visual observation of the agitator is obscured eg. three phase reactors, intensive recirculation below the impeller, or is not possible for other reasons. Furthermore, the simplicity of the measurement technique makes it possible to apply it straightforwardly to full plant scale operations.

Chapter 9

RECOMMENDATIONS FOR FUTURE RESEARCH

- The potential of the data acquisition system of the capillary suction probe and the conductivity probe techniques can be greatly enhanced by extending the present two-channel binary waveform store to an external FIFO (fist-in-first-out) buffer system. The essential features of such a system are described in Appendix C. Instead of data being analysed after the whole bubble sample has been collected, this facility will allow data analysis to occur in between bubble detections and therefore will reduce the experimental time to virtually just the time needed to detect the sample of bubbles. In addition, such a buffer can be made large enough so that in practice sampling periods can be of unlimited length.

- It would be interesting to arrange for the application of the capillary suction probe technique to bubble size measurements in an industrial stirred reactor because of the need for data from actual industrial scale operations. The compactness of the probe and the associated data acquisition system makes such an experiment quite feasible. In an industrial environment an increase in the robustness of the probe would be desirable. In this respect the use of a glass lined stainless-steel capillary tube would be advantageous.

- Measurements of bubble size in the presence of a third solid phase are rare, and the effect of solids on the bubble coalescence and breakage processes are not well known. The capillary probe technique was tested, although no detailed measurements were made, in a small stirred vessel using glass particles for the solid phase. The method was found to work provided the solid particles were larger than the capillary diameter, otherwise probe blockage problems would arise.

- An other undeveloped area in gas liquid mixing is the bubble behaviour in viscous systems. No knowledge is available on bubble size

distributions in these systems. The capillary probe technique could be useful in providing a contribution in this field. It must however be borne in mind that because of the limited pressure available for suction through the capillary, the method may not work with highly viscous liquids. Nonetheless, the technique will still be useful for an appreciable viscosity range. For high viscosities the development of alternative techniques is needed. In this respect fibre optical probes have great potential. The basic frame work for developing one of such instruments has been established in the present research study but more work is needed in order to complete its development.

- The extension of the conductivity probe to a two-electrode instrument would be valuable in providing information on local bubble velocity. The signal treatment and data acquisition systems are in their present form already able to cater for such an instrument. Further miniaturisation and improved coating of the electrodes would be desirable in order to increase the accuracy of measurements.

NOMENCLATURE

a	Total specific interfacial area	(m^{-1})
a_p	Point specific interfacial area	(m^{-1})
C_v	Coefficient of variation	
d	Impeller disc diameter	(m)
d_b	Bubble equivalent spherical diameter	(mm)
d_i	Internal hub diameter	(m)
d_{10}	Number mean bubble diameter	(mm)
$\bar{d}_{10}$	Overall value of mean bubble diameter	(mm)
d_{32}	Sauter mean bubble diameter	(mm)
$\bar{d}_{32}$	Overall value of Sauter bubble diameter	(mm)
$\bar{d}_{32p}$	Point Sauter bubble diameter	(mm)
d_o	Outer hub diameter	(m)
D	Impeller diameter	(m)
DT	Time interval between detectors	(s)
F_l	Flow number (Q/ND^3)	(-)
F_r	Froude number (DN^2/g)	(-)
g	Acceleration of gravity	(m/s^2)
H	Liquid height in tank	(m)
I_0	Incident light intensity	(photons $m^{-2}s$)
I	Transmitted light intensity	(photons $m^{-2}s$)
l	Optical path length	(m)
L_b	Impeller blade length	(m)
L_h	Hub length	(m)
n_b	Number of bubbles in a sample	
n_f	Bubble passage frequency	(s^{-1})
N	Impeller speed	(rev/s)
N_{CD}	Stirrer speed for start of gas dispersion below impeller	(rev/s)
N_0	Minimum stirrer speed for gas dispersion	(rev/s)
N_{Fl}	Flooding speed	(rev/s)

N_R	Recirculation speed	(rev/s)
P_g	Impeller gassed power	(W)
$P_{g'}$	Total gassed power	(W)
P_0	Ungassed impeller power	(W)
P'	Intermediate pseudo steady state value of power	(W)
Q	Gas flow rate	(m^3/s)
Q_0	Gas outflow rate from impeller	(m^3/s)
Q_i	Gas inflow rate to impeller	(m^3/s)
r	Coefficient of determination or radial coordinate	
R_e	Reynolds number ($\rho ND^2/\mu$)	(-)
s	Standard deviation of correlated variable about regression line	
t_b	Impeller blade thickness	(mm)
t_g	Bubble passage time	(s)
T_b	Bubble detection time	(s)
T	Tank diameter (m) or total sampling period (s)	
T_d	Impeller disc thickness	(mm)
T_i	Impeller torque	(Nm)
T_s	Shaft torque	(Nm)
U_s	Gas superficial velocity	(m/s)
U_t	Bubble terminal velocity	(m/s)
v_b	Bubble velocity	(m/s)
V	Liquid volume	(m^3)
V_c	Total volume of gas cavities	(m^3)
V_{cp}	Total volume of gas cavities predicted by dynamic model	(m^3)
V_{cv}	Total measured volume of gas cavities	(m^3)
W	Impeller blade width	(m)
z	Vertical coordinate	
ϵ	Total gas holdup	(%)
ϵ_p	Point gas holdup	(%)

μ	Liquid viscosity	(Ns/m^2)
ρ	Liquid density	(Kg/m^3)
ρ_v	Gas density	(Kg/m^3)
σ	Surface tension (N/m) or Standard deviation	
τ_f	Time constant for cavity formation transient	(s)
τ_s	Time constant for cavity stripping transient	(s)
η	Dispersion efficiency	(-)

REFERENCES

1. Reith, T., "Physical Aspects of Bubble Dispersions in Liquids", PhD Thesis, Technical University, Delft, Holland, 1968.

2. Landau, J., Boyle, J., Gomaa, H.G. and Al Taweel, A.M., Can. J. of Chem. Eng., vol 55, 1977, p13-.

3. Sridhar, T. and Potter, O.E., Chem. Eng. Sci., Vol 55, 1977, p13-.

4. Langlois, G.E., Gullberg, J.E. and Vermeulen, T., Rev. Sci. Inst., Vol 25 (4), 1954, p360-.

5. Trice, V.G. Jr and Rodger, W.A., AIChemE J., Vol 2 (2), 1956, p205-.

6. Ohba, K. and Itoh, T., "Light attenuation technique for void fraction measurement in two-phase bubbly flow", Part II experiment, Technology reports of the Osaka University, Vol 28, 1449, 1978, p495-.

7. Topiwala, H.H. and Hammer, G., Trans. Inst. Chem. Engrs., Vol 52, 1974, p113-.

8. Buchholz, R. and Schugerl, K., Euro. J. Appl. Microbiol. and Biotechnol., Vol 6, 1979, p301-.

9. Veteau, J.M., "Contribution a L'Etude des Techniques de Mesure de L'Aire Interfaciale Dans Les Ecoulements a Bulles", These de Docteur Es-Sciences Physiques, Universite Scientifique et Medicale de Grenoble, France, 1981.

10. Calderbank, P.H. and Rennie, J., Trans. Inst. Chem. Engrs., Vol 40, 1962, p3-.

11. Porter, K.E., Davies, B.T. and Wong, P.F.Y., Trans. Inst. Chem. Engrs., Vol 45, 1967, pT265-.

12. Ashley, M.J. and Haselden, G.G., Trans. Inst. Chem. Engrs., Vol 50, 1972, p119-.

13. Yamashita, F., Mori, Y. and Fujita, S., J. of Chem. Eng. of Japan, Vol 12 (1), 1979, p5-.

14. Burgess, J.M. and Calderbank, P.H., Chem. Eng. Sci., Vol 30, 1975, p.743-.

15. Burgess, J.M. and Calderbank, P.H., Chem. Eng. Sci., Vol 30, 1975, p1107-.

16. Hsu, Y.Y., Simoneau, R.J., Simon, F.F. and Graham, R.W., 11th Nat. ASME/AIChemE Heat Transfer Conference, Minneapolis, Aug., 1969, p5-.

17. Holmes, T.L. and Russel, T.W.F., Int. J. of Multiphase Flow, Vol 2, 1975, p51-.

18. Veteau, J.M., "Mesure Des Aires Interfaciales Dans Les Ecoulements Diphasiques", Rapport CEA-R-5005, Centre d'Etudes Nucleaires de Grenoble, France, 1979.

19. Clift, R., Grace, J.R. and Weber, M.E., "Bubbles Drops and Particles", Academic Press, 1978.

20. Underwood, E.E., "Quantitative Stereology", Addisson-Wesley Publishing Co., London, 1970.

21. Takahashi, K., McManamey, W.J. and Nienow, A.W., Actes, Colloque "Agitation Mecanique", Toulouse, France, 11-12 June, 1986.

22. Westerterp, K.R., Van Dierendonck, L.L. and Kraa, J.A., Chem. Eng. Sci., Vol 18,

1963, p157-.

23. Sharma, M.M. and Danckwerts, P.V., Brit. Chem. Eng., Vol 15 (4), 1970, p522-.

24. Sridharan, K. and Sharma, M.M., Chem. Eng. Sci., Vol 31, 1976, p767-.

25. Hofer, H. and Mersmann, A., Ger. Chem. Eng., Vol 3, 1980, p347-.

26. Dankwerts, P.V., "Gas-Liquid Reactions", McGraw-Hill Co., London, 1970.

27. Shumpe, A. and Deckwer, W.D., Chem. Eng. Sci., Vol 35, 1980, p2221-.

28. Midoux, A. Laurent, A. and Charpentier, J.C., AIChemE J., Vol 26 (26), 1980, p157-.

29. Reith, T., Brit. Chem. Eng., Vol 15 (12), 1970, p1559-.

30. Calderbank, P.H., Trans. Inst. Chem. Engrs., Vol 36, 1958, p443-.

31. McLaughlin, C.M. and Rushton, J.H., AIChemE J., Vol 19 (4), 1973, p 817-.

32. Curl, R.L., AIChemE J., Vol 20, 1974, p184-.

33. Vermeulen, T., Williams, G.M. and Langlois, G.E., Chem. Eng. Prog., Vol 15 (2), 1955, p85F-.

34. Lockett, M.J. and Safekourdi, A.A., AIChemE J., Vol 23, 1977, p395-.

35. Sridhar, T. and Potter, O.E., Chem. Eng. Sci., Vol 35, 1980, p683-.

36. Al Taweel, A.M., Divakarla, R. and Gomaa, H.G., Can. J. of Chem. Eng., Vol 62, Feb., 1984, p73-.

37. Lee, J.C. and Meyrick, D.L., Trans. Inst. Chem. Engrs., Vol 48, 1970, pT37-.

38. De Figueiredo, M.M.L., PhD Thesis, University of Edinburgh, UK, 1978.

39. Calderbank, P.H., Evans, F. and Rennie, J., Intern. Symp. on Distillation, Inst. Chem. Engrs., Brighton, England, 1960, p51-.

40. Calderbank, P.H., Evans, F. and Rennie, J., Intern. Symp. on Distillation, London, 1965, p51-.

41. Danel, F. and Delhaye, J-M., Mesures Regulation et Automatisme, Aug.-Sept., 1971, p99-.

42. Galaup, J-P. and Delhaye, J-M., La Houille Blanche, 1, 1976, p17-.

43. Miller, N. and Mitchie, R.E., 11th Nat. ASME/AIChemE Heat Transfer Conference, Minneapolis, Aug., 1969, p82-.

44. Miller, N. and Mitchie,R.E, J. British Nucl. Energy Soc., Vol 9, 1970, p94-.

45. Hinata, S., Bulletin of the JSME, Vol 15 (88), 1972, p1228-.

46. Galaup, J-P., "Contribution a L'Etude Des Ecoulements Diphasiques Eau-Air et Eau-Vapeur", These de Docteur Ingenieur, Universite Scientifique et Medicale de Grenoble, Institut National Polytechnique de Grenoble, 1975.

47. Mann, R. and Hackett, L.A., 2nd Int. Conf. on Multiphase Flow, London, England, 19-21 June, 1985, p345-.

48. Abuaf, N., Jones, O.C., Zimmer, G.A., Leonhardt, W.J. and Saha, P., CNSI Meeting on Transient Two-Phase Flow, Paris, June, 1978, p715-.

49. Abuaf, N., Zimmer, G.A. and Jones, O.C., Two-Phase Instrumentation Review Group Meeting, Troy, New York, March 13-14, 1978, p1-.

50. Hayes, E.I., Proc. 5th Biennial Symposium on Turbulence, Oct., 1977, p1427-.

51. Calderbank, P.H. and Pereira, J., Chem. Eng. Sci., Vol 32, 1977, p1427-.

52. De Lasa, H., Lee, S.L.P. and Bergougnou, M.A., Can. J. of Chem. Eng., Vol 62, April, 1984, p165-.

53. Akagawa, K., Trans. of the JSME, 1963, p924-.

54. Lecroart, H. and Porte, R., Symposium on Two-Phase Systems, Haifa, 1971.

55. Sekogushi, K., Fukui, H., Matsuoka, T. and Nishikawa, K., Bulletin of the JSME, Vol 18 (118), April, 1975, p391-.

56. Serizawa, A., Kataoka, I. and Michiyoshi, I., Int. J. of Multiphase Flow, Vol 2, 1975, p221-.

57. Nassos, G.P. and Bankoff, S.G., Can. J. of Chem. Eng., Vol 45, 1967, p271-.

58. Herringe, R.A. and Davis, M.R., J. Phys. E.; Scient. Instrum., Vol 7, 1974, p807-.

59. Herringe, R.A. and Davis, M.R., J. Fluid Mechanics, Vol 73 (1), 1976, p97-.

60. Thang, N.T. and Davis, M.R., Int. J. of Multiphase Flow, Vol 5, 1979, p17-.

61. Lewis, D.A. and Davidson, J.F., Chem. Eng. Sci., Vol 38 (1), 1983, p161-.

62. Buchholz, R. and Schugerl, K., Euro. J. Appl. Microbiol. and Biotechnol., Vol 6, 1979, p301-.

63. Steinemann, J. and Buchholz, R., Part. Charact., Vol 3, 1984, p102-.

64. Lewis, D.A., Nicol, R.S. and Thompson, J.W., Chem. Eng. Res. Des., Vol 62, 1984, p334-.

65. Hewitt, G.F., "Measurement of Two-Phase Flow Parameters", Academic Press, 1978.

66. Hewitt, G.F., "Handbook of Multiphase Systems", Chapter 10, Hemisphere Publishing Corporation, 1982.

67. Jones, O.C. and Delhaye, J-M., Int. J. of Multiphase Flow, Vol 3, 1976, p89-.

68. Smith, A.V., J. British Nucl. Energy Soc., Vol 14, 1975, p227-.

69. Lottes, P.A., PWR Reactor Technol., Vol 10, 1967, p148-.

70. Semiat, R. and Duckler, A.E., AIChemE J., Vol 27 (1), 1981, p148-.

71. Lee, S.L. and Srinivisan, J., Int. J. of Multiphase Flow, Vol 4, p141-.

72. Mahalingam, R., Limaye, R.S. and Brink, J.A., AIChemE J., Vol 22, 1976, p1152-.

73. Lee, S.L. and Srinivisan, J., Int. J. of Multiphase Flow, Vol 8 (1), 1982, 47-.

74. Mann, R., "Gas-Liquid Contacting in Mixing Vessels", IChemE Industrial Research Fellowship Report, 1983.

75. Azzopardi, B.J., Int. J. of Heat and Mas Transfer, Vol 22, 1979, p1245-.

76. Nienow A.W., Wisdom, D.J. and Middleton, J.C., Proc. 2nd Euro. Conf. on Mixing, BHRA, Cambridge, England, 1977, paper F1, p1-.

77. Holland, F.A. and Chapman, F.S., "Liquid Mixing and Processing in Stirred Tanks", Reinhold Publishing Co., New York, 1966.

78. Advani, L.T., "Horsepower Tables for Agitator Impellers, Gulf Publishing Co., 1976.

79. Uhl, V.W. and Gray, J.B., "Mixing- Theory Related to Practice", Vol 2, Academic Press Inc., 1967.

80. Roark, R.J. and Young, W.C., "Formulas for Stress and Strain", McGraw Hill Book Co..

81. Kipke, K.D., 3rd Euro. Conf. on Mixing, BHRA, York, England, April, 1979, paper E1, p241-.

82. Kipke, K.D., 4th Euro. Conf. on Mixing, BHRA, The Netherlands, April, 1982, paper K1, p335-.

83. Pollard, G.J., 4th Euro. Conf. on Mixing, BHRA, The Netherlands, April, 1982, paper K3, p383-.

84. Ramsey, W.D. and Gerald, C.Z., Chemineer Inc., Dayton, Ohio, Chem. Eng. J., Aug., 1976.

85. Hannah, J. and Stephens, C., "Mechanics of Machines- Advanced Theory and Examples", E. Arnold, 2nd Edition, 1976.

86. Nienow, A.W. and Warmoeskerken, M.M.C.G., Smith, J.M. and Konno, M., Proc. 5th Euro. Conf. on Mixing, BHRA, Cranfield, England, June, 1985, paper 15.

87. Lehrer, I.H., Ind. Eng. Chem. Process Des. Dev., Vol 7 (2), 1968, p226-.

88. Bretherton, F.P., J. of Fluid Mechanics, Vol 10, part 2, March, 1961, p166-.

89. Taylor, G.I., J. of Fluid Mechanics, Vol 10, part 2, March, 1961, p161-.

90. Suo, M. and Griffith, P., Trans. of the ASME, J. of Basic Engineering, Sept., 1964, p576-.

91. Suo, M., "Two-Phase Flow in Capillary Tubes", DSc Thesis, M.I.T, USA, March, 1963.

92. Greaves, M. and Kobbacy, K.A.H., Chem. Eng. Res. Des., Vol 61, 1984, p3-.

93. Rennie, J. and Valentin, F.H.H., Chem. Eng. Sci., Vol 23, 1968, p663-.

94. Glass, D.H. and Mojtahedi, W., Chem. Eng. Res. Des., Vol 61, Jan., 1983, p37-.

95. Rushton, J.H. and Oldshue, J.Y., Chem. Eng. Prog., Vol 49 (4), April, 1953, p161-.

96. Sachs, J.P. and Rushton, J.H., Chem. Eng. Prog., Vol 50 (12), Dec., 1954, p597-.

97. Loiseau, B., "Contribution a L'Etude de L'Hydrodynamique et du Transfert de Matiere Dans Les Reacteurs a Cuve Agitee Mecaniquement", These de Docteur Ingenieur, Institut Nationale Polytechnique de Lorraine, Toulouse, France, CNRS A012906, 1976.

98. Nagase, Y. and Yasui, H., Chem. Eng. J., Vol 27, 1983, p37-.

99. Greaves, M., Patel, A.G. and Karmarker, M., Actes, Colloque "Agitation Mecanique", Toulouse, France, June 1986, p5.33-.

100. Mann, R., Chem. Eng. Res. Des., Vol 64, Jan., 1986, p23-.

101. Warmoeskerken, M.M.C.G. and Smith, J.M., Actes, Colloque "Agitation Mecanique", Toulouse, France, June, 1986, p4.4-.

102. Foust, H.C., Mack, D.E. and Rushton, J.H., Ind. Eng. Chem., Vol 36, 1944, p517-.

103. Yoshida, F. and Miura, Y., Ind. Eng. Chem., Vol 2 (4), 1963, p263-.

104. Clark, M.W. and Vermeulen, T., LRL Report, UCRL-10996, Berkely, California, Aug., 1963.

105. Rushton, J.H. and Bimbinet, J.J., Can. J. of Chem. Eng., Vol 46, Feb., 1968, p16-.

106. Van Dierendonck, L.L., Fortuin, J.M.H. and Venderbos, D., Euro. Symposium on Chem. Reaction Eng., Brussels, 1968, p205-.

107. Miller, D.N., AIChemE J., Vol 20 (3), May, 1974, p445-.

108. Sterbacek, Z. and Sachova, M., Int. Chem. Eng., Vol 16 (1), Jan., 1976.

109. Loiseau, B., Midoux, N. and Charpentier, J.C., AIChemE J., Vol 23 (6), 1977, p931-.

110. Hassan, I.T.M. and Robinson, C.W., AIChemE J., Vol 23 (1), 1977, p48-.

111. Joshi, J.B. and Sharma, M.M., Can. J. of Chem. Eng., Vol 55, Dec., 1977, p683-.

112. Smith, J.M., Van't Riet, K. and Middleton, J.C., 2nd Euro. Conf. on Mixing, BHRA, Cambridge, England, 1977, paper F4, p4-.

113. Roustan, M., "Contribution a L'Etude Des Phenomenes D'Agitation et de Transfert de Matiere Dans Les Reacteurs Gaz-Liquide", These de Docteur D'Etat, Universite Paul Sabatier de Toulouse, Toulouse, France, 1978.

114. De Figueiredo, M.M.L. and Calderbank, P.H., Chem. Eng. Sci., Vol 34, 1979, p1333-.

115. Yung, C.N., Wong, C.W. and Chang, C.L., Can. J. of Chem. Eng., Vol 57, 1979, p672-.

116. Hughmark, G.A., Ind. Eng. Chem. Process Des. Dev., Vol 19 (4), 1980, p638-.

117. Chapman, C.M., Nienow, A.W., Cooke, M. and Middleton, J.C., Chem. Eng. Res. Des. Dev., Vol 61, March, 1983, p82-.

118. Kobbacy, K.A.H., "Power Consumption and Gas Dispersion in Agitated Vessels", PhD Thesis, University of Bath, Bath, UK, 1981.

119. Warmoeskerken, M.M.C.G. and Smith, J.M., Chem. Eng. Sci., Vol 40 (11), 1985, p2063-.

120. Smith, J.M. and Warmoeskerken, M.M.C.G., Proc. 5th Euro. Conf. on Mixing, June, 1985, paper 13, p115-.

121. Michel, B.J. and Miller, S.A., AIChemE J., Vol 8 (2), 1962, p262-.

122. Pharamond, J.C., Roustan, M. and Roques, H., Chem. Eng. Sci., Vol 30, 1975, p907-.

123. Nienow, A.W. and Wisdom, D.J., Inst. Chem. Engrs., 3rd Annual Research Meeting, Salford, 1976.

124. Luong, H.T. and Volesky, B., AIChemE J., Vol 25, 1979, p893-.

125. Greaves, M. and Kobbacy, K.A.H., Fluid Mixing, IChemE Symposium Series, 64, 1981, paper L.

126. Greaves, M. and Kobbacy, K.A.H., Fluid Mixing, IChemE Symposium Series, 64, 1981, paper H.

127. Midoux, N., "les Reacteurs Gaz-liquide a Cuve Agitee", These de Docteur Es-Sciences Physiques, Insitut National Polytechnique de Lorraine, Toulouse, France, 1978.

128. Nienow, A.W, Bujalski, W., Chatwin, S. and Cooke, M., Colloque "Agitation Mecanique", PROJEC, Toulouse, France, June, 1986, p1.1-.

129. Van't Riet, K. and Smith, J.M., Chem. Eng. Sci., Vol 28, 1973, p1031-.

130. Bruijn, W., Van't Riet, K. and Smith, J.M., Trans. Inst. Chem. Engrs., Vol 52 (1), 1974, p88-.

131. Nienow, A.W. and Wisdom, D.J., Chem. Eng. Sci., Vol 29, 1974, p1994-.

132. Warmoeskerken, M.M.C.G., Freijen, J. and Smith, J.M., Inst. Chem. Engrs., Symposium Series 64, 1981, paper J.

133. Warmoeskerken, M.M.C.G. and Smith, J.M., Proc. 4th Euro. Conf. on Mixing, BHRA, The Netherlands, 1982, p237-.

134. De Marteleire, E. and Heyndrickx, G.V., Med. Fac. Landbroww. Rijksuniv., Gent, 50/4, 1985.

135. De Marteleire, E., Doctoral Dissertation, State University of Gent, 1980.

136. Van't Riet, K., PhD Thesis, Delft University of Technology, 1975.

137. Greaves, M. and Economides, C.A., Proc. 3rd Euro. Conf. on Mixing, BHRA, York, England, 1979, p357-.

138. Greaves, M., Kobbacy, K.A.H. and Millington, G.C., Chem. Eng. Sci., Vol 38, 1983, p1909-.

139. Middleton, J.C., Edwards, M.F. and Stewart, I., "Recommended Standard Terminology and Nomenclature for Mixing", IChemE, Rugby, Reprinted for Chemical Enginneer, Aug/Sept, 1980, p557-.

140. Mann, R., Mavros, P. and Middleton, J.C., IChemE Symposium Series, 64, paper G, 1981.

141. Himmelblau, D.M., "Process Analysis by Statistical Methods", John Wiley & Sons Inc., New York , London.

142. Valentin, F.H.H., "Absorption in Gas-Liquid Dispersions", E. & F.N. Spon Ltd., London, 1967.

143. Okamoto, Y., Nishikawa, M. and Hashimoto, K., International Chem. Eng., Vol 21, 1981, p88-.

144. Nishikawa, M., Okamoto, Y., Hashimoto, K. and Nagata, S., J. Chem. Eng. of Japan, Vol 9, 1976, p489-.

145. Harvey, P.S. and Greaves, M., Trans. Inst. Chem. Engrs., Vol 60, 1982, p195-.

146. Harvey, P.S. and Greaves, M., Trans. Inst. Chem. Engrs., Vol 60, 1982, p201-.

147. Bertrand, J., Couderc, J.P. and Angelino, H., Chem. Eng. Sci., Vol 35, 1980, p2157-.

148. Kawecki, W., Reith, T., Van Heuven, J.W. and Beek, W.J., Chem. Eng. Sci., Vol 22, 1967, p1519-.

APPENDICES

Appendix A: Equipment specifications

Appendix B: Computer programmes

Appendix C: Data acquisition systems

APPENDIX A

A1 Motor and speed controller

The motor and speed controller were made by JH FENNER & Co. (Power Transmission) Ltd., and the following specifications were taken from 'Fenner Electrical Drives' manual 200/82.

A1.1 Motor

Model	Speed Ranger DC Gearmotor
Type	563 P2040
Speed range	0-2000 rpm
Gear ratio	3.8
Maximum torque	97 Nm
Power	5.5 Kw

A1.2 Controller

Model	Tacho Feedback Controller
Type	516 P5000
Regulation	better than ±0.1% of full motor speed throughout speed range

A2 Shaft couplings

Type	Fenaflex Tyre Couplings
Make	JH FENNER & Co. (Power Transmission) Ltd.
Max. parallel misalignment	2.1 mm
Max. end float	±2.1 mm
Max. angular misalignment	4°

Normal torque	253 Nm
Max. torque	759 Nm
Max. speed	3100 rpm
Assembly	by means of taper lock bushes

A3 Torque transducer

The instrument was supplied by British Hovercraft Corporation Ltd., East Cowes, Isle of Whight, England. The following specifications were taken from 'Transducers and Instrumentation' manual, SP4352 Issue 3, March 82.

Model	Type 2MK4
Size code	CC
Load range	0-135 Nm
Overload rating	1.5 times full working torque without loss of calibration accuracy. Transient loads to twice the full working torque without damage.
Bridge resistance	601 Ω at 20 °C
Bridge supply voltage	up to 20 V AC or DC
Sensitivity	2.2 mV ±5% per Volt applied at full working torque
No-load output	+0.014 mV/V
Performance	maximum error from calibration due to non-linearity hysteresis and repeatability ±0.1% of full working torque from 0 rpm to maximum speed quoted below.
Operating Temperature	0 to 45 °C
Rotation	suitable for rotation in either direction
Speed range	0-6000 rpm
Maximum speed	6000 rpm

A4 Level transmitter

(Source: Installation and Operating Instructions, 909-605-176D, 1977) It is a two wire capacitance to current transmitter which produces a standard 4-20 mA DC output signal directly proportional to the input capacitance.

Make	Robertshaw Skil Ltd.,
Model	160
Linearity	±0.25% for 10 to 500 p.f. span
Temperature effect	
Span	0.018%/°C
Zero	0.018%/°C
Max. output ripple	0.25% peak to peak
Response time	100 ms
Stability	1% max/30 days, non cumulative

A5 BBC microcomputer

(Source: BBC System Manual)

Make	Acorn Computers
Model	B

Central Processing Unit (CPU)

Word length	8 bits
Memory	32 Kbytes
Clock speed	2 MHz

A/D Converter

Type	ICL 7109 (made by Intersil)
Resolution	12 bit + sign bit

Gain	fixed, 2 V full scale
Conversion time	40 ms
Gain/Temp. coefficient	±80 ppm/°C
Non-linearity error	±0.2 lsb

A6 Macsym II microprocessor

(Source: Macsym II System Manual)

Make	Analog Devices Ltd.
Model	Macsym II

ADIO Controller

A/D converter

Non-linearity error	±0.5 lsb
Gain temperature	±15 ppm°C max.
A/D conversion time	25 μs max.

Central Processing Unit (CPU)

Word length	16 bits
Memory	64 Kwords
Execution speed	
Arith./logic instructions	1.2 μs
Memory ref. instructions	1.8 μs

Analog Input Card

Number of inputs	32 single ended or 16 true differential
Gain	1, 16, 256
Gain accuracy	±0.02%
Gain/Temp. coefficient	±30 ppm/°C

Linearity	±0.001%
Settling time	25 μs: G = 1, 16
	50 μs: G = 256

APPENDIX B

B1 Programme for power measurement

B1.1 Description of principal routines

1. PROCassemble: Assembles machine code routines concerned with speed measurement (lines 260-850).

2. Setup: machine code routine which initialises speed measurement system:

(i) The VIA (Versatile Interface Adaptor) is set up to provide the 50 KHz time base for rotational period measurement (lines 520-580).

(ii) Interrupt service vectors are changed to point to the new interrupt service routine INTIN (lines 590-700).

3. PROCsetupanalog: programs the VIA to interface with the A/D converter (lines 1130-1240).

4. FNanalog: function which returns the current value of the analog input (lines 960-1020).

5. FNvalue: function which reads the output of the A/D converter after a conversion has been performed (lines 1540-1610)

6. FNready: function which tests whether the A/D has finished conversion in progress (lines 1630-1650).

7. FNspeed: function which returns last measured value of motor shaft speed in RPM (shaft speed is measured and stored continually as a background task, whether or not FNspeed is invoked. This contrasts with FNanalog), (lines 870-940).

8. getspeed: machine code routine which reads the last measured speed value from temporary store and returns it in the microprocessor's internal registers. A flag is also returned which indicates whether an attempt has been made to read the same value twice in succession. This is tested by FNspeed in line 890 (line 800).

9. Intin: the interrupt service routine for speed measurement. Contents of the VIA counter (representing 65536-period of input pulse in 20 μs units) are transferred to temporary memory store. VIA is set up to measure next pulse (line 720).

Other routines and functions are briefly described where they are defined in the source code.

BI.2 Source code

```
 10  REM program for power measurements
 20  PROCassemble
 30  CALL setup
 40  PROCsetupanalog
 50  TIME=0
 60  REPEAT:PRINT FNanalog:UNTIL TIME>=500
 70  SOUND 1,-15,53,8
 80  INPUT XX
 90  I%=0:N=0:F=0
100  REPEAT
110    IF I%<10 GOTO 140
120    N=N+FNspeed
130    F=F+VAL(FNanalog)
140    I%=I%+1
150    UNTIL I%=110
160  N=N/((I%-11)*3.8):PRINT "N  = ";N;" RPM":REM shaft speed in rpm
170  F=F/(I%-11)
180  Vin=(F*XX)/4000
190  SOUND 1,-15,53,8
200  T=(339*Vin)/22.0078:PRINT "T  = ";T;" Nm" :REM torque in Nm
210  N1=N/60:D=0.25
220  P=2*PI*N1*T:PRINT "P  = ";P;" W":REMpower in watts
230  Np=P/(1000*(N1^3)*(D^5)):PRINT "Np = ";Np :REM power nbre
240  Re=1000*N1*(D^2)/1E-3:PRINT "Re = ";Re :REM reynolds nbre
250  END
260
270  DEF PROCassemble
280
290     V=&FCC0 : REM base address for VIA board
300
310
320    IOB=V      : IOA=V+1        : DDRB=V+2       : DDRA=V+3
330    T1C_L=V+4 : T1C_H=V+5      : T1L_L=V+6      : T1L_H=V+7
340    T2C_L=V+8 : T2C_H=V+9      : SR=V+10        : ACR=V+11
350    PCR=V+12     : INFR=V+13      : IER=V+14       : IONA=V+15
360
370
380    IOB2=V+16     : IOA2=V+17      : DDRB2=V+18    : DDRA2=V+19
390    T1C_L2=V+20   : T1C_H2=V+21    : T1L_L2=V+22   : T1L_H2=V+23
400    T2C_L2=V+24   : T2C_H2=V+25     : SR2=V+26      : ACR2=V+27
410    PCR2=V+28     : INFR2=V+29     : IER2=V+30     : IONA2=V+31
420
430
440  IRQ2V=&206
450  oldvect=&70
460  newcount=&72
470  newanalog=&76
480  DIM X% 200
490  REM code block
500  FOR N%=0 TO 2 STEP 2
```

```
510  P%=X%
520  [ OPT N%
530   .setup SEI : LDA £&BF : STA DDRB2
540  STA IOB2 : LDA £&E0 : STA ACR2
550  LDA £8 : STA T1L_L2 : \ 20 microsec clock
560  LDA £0
570  STA T1L_H2
580  STA T1C_H2   \ counter starts now
590  LDA £&88 : STA PCR2
600  LDA £&7F : STA INFR2 : STA IER2
610  JSR change_vect
620  LDA £&90 : STA IER2 \  enable interrupts
630  CLI : RTS
640
650  .change_vect
660  LDA IRQ2V : STA oldvect
670  LDA IRQ2V+1 : STA oldvect+1
680  LDA £(intin MOD 256)
690  STA IRQ2V
700  LDA £(intin DIV 256)
710  STA IRQ2V+1
720  RTS
730
740  .intin PHA : PHP
750  LDA INFR2 : ROL A : LDA IOB2  :\ CLC : BCC intout
760  LDA T2C_L2 : STA newcount : LDA T2C_H2 : STA newcount+1
770   LDA £&FF : STA T2C_L2
780  STA T2C_H2 : STA newcount+2 \  this should clear the timer flag
790  LDA IOB2 \ clear the interrupt
800
810  .intout PLP : PLA : CLI : JMP (oldvect)
820
830  .getspeed SEI
840   LDA newcount : LDX newcount+1 : LDY newcount+2 : PHA : LDA £0
850  STA newcount+2 : PLA
860  CLI : RTS
870  ]
880  NEXT
890  ENDPROC
900
910  DEF FNspeed
920  LOCAL S%,P%,R%
930  REPEAT : R%=USR(getspeed) : UNTIL (R% AND &FF0000)=&FF0000
940  S%=(R% AND &FFFF)
950  S%=R% AND &FFFF
960  P%=65536-S%
970  =1600000/P%
980  ENDPROC
990
1000 DEF FNanalog
1010 PROCset(run_hold%) : REM start conversion
1020  REPEAT : UNTIL (NOT FNready) : REM wait for beginning of conversion
1030 REPEAT : UNTIL FNready : REM wait for end of conversion
>
```

```
1040  PROCreset(run_hold%) : REM END conversion (convert on demand)
1050  =FNvalue
1060  ENDPROC
1070
1080
1090  DEF PROCkeys : REM test purposes only
1100  *KEY0PROCpulse(reset_mem_ptr%,1)|M
1110  *KEY1PROCpulse(inc_mem_ptr%,0)|M
1120  *KEY2PROCpulse(load_sr%,1)|M
1130  *KEY3P.?SR|M
1140  ENDPROC
1150
1160
1170  DEF PROCsetupanalog
1180
1190  load_sr%=0
1200  run_hold%=1
1210  status%=2
1220
1230  ?DDRB=&FB : REM all outputs save 2 (end of conversion)
1240  ?IOB=0 : REM ALL low
1250  ?ACR =&C4 : REM shift in under T2
1260  ?T2C_L=&4   : REM safe shifting rate
1270  ?T1L_L=8 : ?T1L_H=0 : ?T1C_H=0
1280  ENDPROC
1290
1300
1310
1320
1330  DEF PROCpulse(sig%,pol%)
1340  IF pol%=1 PROCpospulse(sig%) ELSE PROCnegpulse(sig%)
1350  ENDPROC
1360
1370
1380  DEF PROCpospulse(sig%)
1390  LOCAL Y%
1400  Y%=2^sig%
1410  ?IOB=?IOB OR Y%
1420  ?IOB=?IOB AND NOT Y%
1430  ENDPROC
1440
1450
1460  DEF PROCnegpulse(sig%)
1470  LOCAL Y%
1480  Y%=2^sig%
1490  ?IOB=?IOB AND NOT Y%
1500  ?IOB=?IOB OR Y%
1510  ENDPROC
1520
1530
1540
1550
1560
>
```

```
1570
1580  DEF FNvalue
1590  LOCAL X%,pol$
1600  PROCpulse(load_sr%,1)
1610  X%=?SR   : REM discard first one
1620  ?newanalog=?SR : X%=?SR : newanalog?1=(X% AND &0F)
1630  IF (X% AND &40)=0 THEN pol$="+" ELSE pol$="-"
1640  IF (X% AND &80)<>0 THEN ="overrun" ELSE =(pol$+STR$(!newanalog AND &FFF))
1650  ENDPROC
1660
1670  DEF FNready   : REM is conversion over?
1680  IF (?IOB AND 2^status%) <>4 THEN =TRUE ELSE =FALSE
1690  ENDPROC
1700
1710  DEF PROCset(sig%)
1720  LOCAL Y%
1730  Y%=2^sig%
1740  ?IOB=?IOB OR Y%
1750  ENDPROC
1760
1770  DEF PROCreset(sig%)
1780  LOCAL Y%
1790  Y%=2^sig%
1800  ?IOB=?IOB AND NOT Y%
1810  ENDPROC
1820
1830  DEF PROCup(P%)
1840  LOCAL N%
1850  FOR N%=0 TO P% : ?IOB2=2 : ?IOB2=0 : NEXT
1860  ENDPROC
1870
1880  DEF PROCdown(P%)
1890  LOCAL N%
1900  FOR N%=0 TO P% : ?IOB2=1 : ?IOB2=0 : NEXT
1910  ENDPROC
```

B2 Programme for bubble size measurement

B2.1 Description of principal routines

1. PROCassemble: assembles machine code routines concerned with bubble sampling (lines 2910-3820).

2. PROCsetup: sets up the VIA to enable it to communicate with the event logger. Also, initialises the memory array and other variables.

3. incp: machine code routine which obtains the next recorded event from the logger memory and presents it in a form easily accessible by the Basic programme. After invoking incp, the integer variable T% contains the event time, and, R% and S% contain polarity information (see section 4.4.2) for channels 1 and 2 respectively. In addition, incp increments the memory pointer (P%) by one each time it is invoked.

4. FNfull: checks if memory is full.

5. PROCpulse (stop-bub%,1): turns off sampling process.

6. PROCpulse (rest-mem-ptr%,1): resets memory pointer to position zero.

B2.2 Source code

```
 10  PRINT "INPUT D/T RATIO:":INPUT DDD
 20  PRINT "INPUT IMPELLER SPEED IN RPM :":INPUT N
 30  PRINT"INPUT GAS-FLOW RATE IN L/MIN :":INPUT Q
 40  PRINT "INPUT POSITION Nbre :":INPUT  POSITION
 50  VDU2
 60   PRINT "D/T = ";DDD;TAB(0);"N    = ";N;" RPM"
 70   PRINT "Q    = ";Q*1E-3/60;" M3/SEC.
 80  PRINT "POSITION ";POSITION;TAB(0);"________"
 90  PRINT:PRINT
100  VDU3
110  PROCsetup
120  PROCpulse(start_bub%,1)
130  REPEAT : UNTIL FNfull
140  PROCpulse(reset_mem_ptr%,1)
150
160  SOUND 1,-15,53,8
170  PRINT "MEMORY FULL"
180  PRINT "INPUT MEMORY SIZE:":INPUT MEM%
190  @%=&20509
200  DIM A%(1450),B%(1450),X%(2),Y%(2)
210    J%=0:L%=0:W%=300:G1%=200:G2%=400:P%=0:I%=-1
220  K%=-1:H1%=-1:H2%=-1:STOREW1%=0:STOREW2%=0
230  PROCpulse(inc_mem_ptr%,0)
240  REPEAT
250    CALL incp
260    UNTIL R%=1
270
280  REPEAT
290    REPEAT
300      REPEAT
310        IF P%=MEM%-3 GOTO 570
320        IF R%<>0 THEN I%=I%+1 :X%(I%)=T%
330        IF S%<>0 THEN K%=K%+1 :Y%(K%)=T%
340        IF L%=0 THEN IF S%=2 AND K%=0 THEN K%=-1
350        CALL incp
360        UNTIL I%=2 OR K%=2
370      C%=X%(2)-X%(1)
380      D%=Y%(2)-Y%(1)
390      IF X%(2)<>0 AND C%<W% STOREW1%=STOREW1%+C%
400      IF Y%(2)<>0 AND D%<W% STOREW2%=STOREW2%+D%
410      S1%=X%(1):S2%=X%(2):R1%=Y%(1):R2%=Y%(2)
420      IF I%=2 THEN I%=0:X%(1)=0:X%(2)=0
430      IF K%=2 THEN K%=0:Y%(1)=0:Y%(2)=0
440      UNTIL C%>=W% OR D%>=W%
450    U%=X%(0):V%=Y%(0)
460    E%=S1%-U%
470    F%=R1%-V%
480    IF C%>=W% X%(0)=S2%
490    IF D%>=W% Y%(0)=R2%
500    UNTIL E%>=G1% OR F%>=G1%
```

```
  510    IF C%>=W% AND E%>=G1% THEN A%(J%)=U% :
  520  A%(J%+1)=S1%:J%=J%+2:H1%=H1%+1:X%(2)=0:X%(1)=0:I%=0
  530    IF D%>=W% AND F%>=G1% THEN B%(L%)=V%
  540  B%(L%+1)=R1%:L%=L%+2:H2%=H2%+1:Y%(2)=0:Y%(1)=0:K%=0
  550  IF J%>=1450 OR L%>=1450 GOTO 570
  560  GOTO 280
  570  ENDA%=J%-1 : ENDB%=L%-1
  580  I%=0:J%=0:L%=0:S1=0:S2=0:S3=0:GAS=0:Tg%=0:sTB%=0:TG=0
  590   A1%=0:A2%=0:A3%=0:A4%=0:A5%=0:A6%=0:A7%=0
  600  A8%=0:A9%=0:A10%=0:A11%=0:A12%=0:A13%=0:A14%=0
  610  A15%=0:A16%=0:A17%=0:A18%=0:A19%=0:A20%=0
  620  A21%=0:A22%=0:A23%=0:A24%=0:A25%=0:A26%=0:A27%=0
  630  A28%=0:A29%=0:A30%=0:A31%=0
  640  REPEAT
  650    TB11%=A%(J%+1)-A%(J%)
  660    TB21%=B%(L%+1)-B%(L%)
  670    X%=A%(J%) : Y%=B%(L%)
  680    R=0.04
  690    E=ABS((TB11%-TB21%)/TB11%)
  700    IF TB11%<=1000 AND TB21%<=1000 THEN R=0.10
  710    IF E<=R THEN GOTO 940
  720    IF J%+3>ENDA% OR L%+3>ENDB% THEN GOTO 1110
  730    TB12%=A%(J%+3)-A%(J%+2)
  740    TB22%=B%(L%+3)-B%(L%+2)
  750    E=ABS((TB12%-TB22%)/TB12%)
  760     IF E<=R THEN TB11%=TB12%:TB21%=TB22%
  770    J%=J%+2:L%=L%+2:GOTO 940
  780    E=ABS((TB12%-TB21%)/TB12%)
  790    IF E<=R TB11%=TB12%:J%=J%+2:GOTO 940
  800    E=ABS((TB11%-TB22%)/TB11%)
  810    IF E<=R TB21%=TB22%:L%=L%+2:GOTO 940
  820    IF TB11%<TB21% GOTO 840 ELSE GOTO 890
  830
  840    H%=J%+3
  850    TB11%=A%(H%)-X%
  860    E=ABS((TB11%-TB21%)/TB11%)
  870    IF E<=R THEN J%=H%-1:DT%=Y%-X%:GOTO 950
  880    ELSE IF TB11%<TB21% THEN H%=H%+2:GOTO 850
  890    H%=L%+3
  900    TB21%=B%(H%)-Y%
  910    E=ABS((TB11%-TB21%)/TB11%)
  920    IF E<=R THEN L%=H%-1:DT%=Y%-X%:GOTO 950
  930    ELSE IF TB21%<TB11% THEN H%=H%+2:GOTO 900
  940    DT%=B%(L%)-A%(J%)
  950    Ub=X/DT%
  960    m=Us-Ub/Us
  970     IF DT%<=0 OR TB11%<=0 THEN sTB%=sTB%+TB11%
  980    J%=J%+2:L%=L%+2:GOTO 1080
  990    r=TB11%/DT%
 1000    Vb=0.00147048*(r^3)
 1010    Db=(6*Vb/PI)^(1/3)
 1020    S1=S1+Db
 1030    S2=S2+Db^2
 1040    S3=S3+Db^3
 1050    GAS=GAS+Vb :REM total gas volume
>
```

```
1060  PROCclass(Db)
1070  I%=I%+1:J%=J%+2:L%=L%+2
1080  UNTIL J%+4>ENDA% OR L%+4>ENDB%
1090  REM printing results
1100  VDU2
1110  NB%=I% :PRINT"NB = ";NB%
1120  D10=S1/NB% :PRINT "D10 = ";D10;" mm" :REM MEAN DIAM. mm
1130   D32=S3/S2 :PRINT"S3  = ";S3;TAB(0);"S2  = ";S2
1140  PRINT "D32 = ";D32;" mm" :REM SAUTER DIAM. mm
1150   Tg%=Tg%-STOREW1% :PRINT"SW1 = ";STOREW1%*1E-2;" mSEC."
1160  PRINT "Tg  = ";Tg%*1E-5;" SEC.": REM TOTAL GAS TIME SEC.
1170   T%=A%(ENDA%)-A%(0)-sTB%:PRINT"sTB = ";sTB%*1E-5
1180  PRINT "T   = ";T%*1E-5;" SEC." :REM TOTAL SAMPLING TIME
1190  PRINT "GAS = ";GAS;" mm3"
1200  S=SQR((S2-(S1^2)/NB%)/(NB%-1)):PRINT"S   = ";S
1210  CV=S/D10 :PRINT"CV  = ";CV
1220  PRINT:PRINTTAB(15);"Nbre fraction"
1230  PRINTTAB(2)"0.1";:PROCstar(100*A1%/NB%)
1240  PROCstar(100*A2%/NB%)
1250  PROCstar(100*A3%/NB%)
1260  PROCstar(100*A4%/NB%)
1270  PROCstar(100*A5%/NB%)
1280  PRINTTAB(2)"1.1";:PROCstar(100*A6%/NB%)
1290  PROCstar(100*A7%/NB%)
1300  PROCstar(100*A8%/NB%)
1310  PROCstar(100*A9%/NB%)
1320  PROCstar(100*A10%/NB%)
1330  PRINTTAB(2)"2.1";:PROCstar(100*A11%/NB%)
1340  PROCstar(100*A12%/NB%)
1350  PROCstar(100*A13%/NB%)
1360  PROCstar(100*A14%/NB%)
1370  PROCstar(100*A15%/NB%)
1380  PRINTTAB(2)"3.1";:PROCstar(100*A16%/NB%)
1390  PROCstar(100*A17%/NB%)
1400  PROCstar(100*A18%/NB%)
1410  PROCstar(100*A19%/NB%)
1420  PROCstar(100*A20%/NB%)
1430  PRINTTAB(2)"4.1";:PROCstar(100*A21%/NB%)
1440  PROCstar(100*A22%/NB%)
1450  PROCstar(100*A23%/NB%)
1460  PROCstar(100*A24%/NB%)
1470  PROCstar(100*A25%/NB%)
1480  PRINTTAB(2)"5.1";:PROCstar(100*A26%/NB%)
1490  PROCstar(100*A27%/NB%)
1500  PROCstar(100*A28%/NB%)
1510  PROCstar(100*A29%/NB%)
1520  PROCstar(100*A30%/NB%)
1530  PRINTTAB(2)"6.1";:PROCstar(100*A31%/NB%)
1540  PRINTTAB(4);"D(mm)"
1550  PRINT :PRINT :PRINT"END OF RUN":PRINT"----------":PRINT:PRINT:PRINT
1560  @%=10
1570  VDU3
1580  END
1590  DEF PROCclass(X)
1600  IF X<=0.2 A1%=A1%+1
>
```

```
1610  IF X>0.2 AND X<=0.4 A2%=A2%+1
1620  IF X>0.4 AND X<=0.6 A3%=A3%+1
1630  IF X>0.6 AND X<=0.8 A4%=A4%+1
1640  IF X>0.8 AND X<=1.0 A5%=A5%+1
1650  IF X>1.0 AND X<=1.2 A6%=A6%+1
1660  IF X>1.2 AND X<=1.4 A7%=A7%+1
1670  IF X>1.4 AND X<=1.6 A8%=A8%+1
1680  IF X>1.6 AND X<=1.8 A9%=A9%+1
1690  IF X>1.8 AND X<=2.0 A10%=A10%+1
1700  IF X>2.0 AND X<=2.2 A11%=A11%+1
1710  IF X>2.2 AND X<=2.4 A12%=A12%+1
1720  IF X>2.4 AND X<=2.6 A13%=A13%+1
1730  IF X>2.6 AND X<=2.8 A14%=A14%+1
1740  IF X>2.8 AND X<=3.0 A15%=A15%+1
1750  IF X>3.0 AND X<=3.2 A16%=A16%+1
1760  IF X>3.2 AND X<=3.4 A17%=A17%+1
1770  IF X>3.4 AND X<=3.6 A18%=A18%+1
1780  IF X>3.6 AND X<=3.8 A19%=A19%+1
1790  IF X>3.8 AND X<=4.0 A20%=A20%+1
1800  IF X>4.0 AND X<=4.2 A21%=A21%+1
1810  IF X>4.2 AND X<=4.4 A22%=A22%+1
1820  IF X>4.4 AND X<=4.6 A23%=A23%+1
1830  IF X>4.6 AND X<=4.8 A24%=A24%+1
1840  IF X>4.8 AND X<=5.0 A25%=A25%+1
1850  IF X>5.0 AND X<=5.2 A26%=A26%+1
1860  IF X>5.2 AND X<=5.4 A27%=A27%+1
1870  IF X>5.4 AND X<=5.6 A28%=A28%+1
1880  IF X>5.6 AND X<=5.8 A29%=A29%+1
1890  IF X>5.8 AND X<=6.0 A30%=A30%+1
1900  IF X>6.0 A31%=A31%+1
1910  ENDPROC
1920  DEF PROCstar(Q)
1930  R%=Q
1940  IF Q=0 GOTO 1990
1950  PRINT TAB(5);" ";
1960  REPEAT PRINT "*";
1970    UNTIL COUNT=R%+7
1980  PRINT ;TAB(40)Q/100:GOTO 2000
1990  PRINT
2000  ENDPROC
2010  DEF PROCkeys : REM test purposes only
2020  *KEY0PROCpulse(reset_mem_ptr%,1)|M
2030  *KEY1PROCpulse(inc_mem_ptr%,0)|M
2040  *KEY2PROCpulse(load_sr%,1)|M
2050  *KEY3P.?SR|M
2060  ENDPROC
2070  DEF PROCsetup
2080  DDRB=&FE62
2090  IOB=&FE60
2100  SR=&FE6A
2110  ACR=&FE6B
2120  PCR=&FE6C
2130  T2L=&FE68
2140  T1L_L=&FE66
2150  T1L_H=&FE67
>
```

```
2160  T1C_H=&FE65
2170  start_bub%=0
2180  inc_mem_ptr%=1
2190  reset_mem_ptr%=2
2200  reset_tim_sampler%=3
2210  load_sr%=5
2220  stop_bub%=6
2230  full_up%=7
2240  ?DDRB=&7F : REM all outputs save 7 (buffer full)
2250  ?IOB=2 : REM ALL low
2260  ?ACR =&04 : REM shift in under T2
2270  ?T2L=&4   : REM safe shifting rate
2280  PROCpulse(stop_bub%,1)
2290  PROCpulse(reset_mem_ptr%,1)
2300  PROCpulse(reset_tim_sampler%,1)
2310  PROCassemble
2320  ENDPROC
2330  DEF PROCpulse(sig%,pol%)
2340  IF pol%=1 PROCpospulse(sig%) ELSE PROCnegpulse(sig%)
2350  ENDPROC
2360  DEF PROCpospulse(sig%)
2370  LOCAL Y%
2380  Y%=2^sig%
2390  ?IOB=?IOB OR Y%
2400  ?IOB=?IOB AND NOT Y%
2410  ENDPROC
2420  DEF PROCnegpulse(sig%)
2430  LOCAL Y%
2440  Y%=2^sig%
2450  ?IOB=?IOB AND NOT Y%
2460  ?IOB=?IOB OR Y%
2470  ENDPROC
2480  DEF FNchannel2
2490  LOCAL X%
2500  PROCpulse(load_sr%,1)
2510  X%=?SR   : REM discard first one
2520  X%=?SR : IF (X% AND &80) =0 THEN ="" ELSE IF (X% AND &40) =0 THEN ="-" ELSE ="
2530  ENDPROC
2540  DEF FNchannel1
2550  LOCAL X%
2560  PROCpulse(load_sr%,1)
2570  X%=?SR
2580  X%=?SR : IF (X% AND &20) =0 THEN ="" ELSE IF (X% AND &10) =0 THEN ="-" ELSE ="
2590  ENDPROC
2600  DEF FNread_time
2610  LOCAL X%
2620  PROCpulse(load_sr%,1)
2630  X%=?SR   : REM discard first one
2640  ?&73=(?SR AND &F) : ?&72=?SR : ?&71=?SR : ?&70=?SR
2650  =!&70
2660  ENDPROC
2670  DEF FNfull    : REM is buffer memory full?
2680  IF (?IOB AND 2^full_up%) <>0 THEN =TRUE ELSE =FALSE
2690  ENDPROC
2700  DEF PROCassemble
>
```

```
2710  DIM code 300
2720  LOCAL N%,P%
2730  FOR N%=0 TO 2 STEP 2
2740    P%=code
2750    [ OPT N%
2760    .incp LDX £0
2770    LDA £1
2780    CLC : ADC &440 : STA &440
2790    TXA : ADC &441 : STA &441
2800    TXA : ADC &442 : STA &442
2810    TXA : ADC &443 : STA &443
2820    \ increment memory pointer
2830    \ bit 1, negative pulse
2840    LDA &FE60
2850    TAX
2860    AND £253 \drop bit 1
2870    STA &FE60
2880    TXA
2890    ORA £2  \ bit 1 back
2900    STA &FE60
2910
2920    \ load shift register
2930    \ bit 5, positive pulse
2940
2950    LDA &FE60
2960    TAX
2970    ORA £32  \ bit 5 up
2980    STA &FE60
2990    TXA
3000    AND £223 \ drop bit 5
3010     STA &FE60
3020
3030    \ read the time into T%
3040
3050    LDA &FE6A  \ shift register
3060    JSR waitflag
3070    LDA &FE6A
3080    TAX
3090    AND £15
3100    STA &453
3110    JSR waitflag
3120    LDA &FE6A : STA &452 : JSR waitflag
3130    LDA &FE6A : STA &451 : JSR waitflag
3140    LDA &FE6A : STA &450
3150    \ set R% and S% to zero
3160    LDY £8
3170    LDA £0
3180     .again STA &447,Y
3190    DEY : BNE again
3200    \ sort out channel1
3210    TXA
3220    AND £&20
3230    BEQ riszero
3240    TXA
3250    AND £&10
```

```
3250  AND £&10
3260  BEQ ristwo
3270  LDA £1
3280  BNE riszero
3290  .ristwo LDA £2
3300  .riszero STA &448
3310  \ and for S%
3320  TXA
3330  AND £&80
3340  BEQ siszero
3350  TXA
3360  AND £&40
3370  BEQ sistwo
3380  LDA £1
3390  BNE siszero
3400  .sistwo LDA £2
3410  .siszero STA &44C
3420
3430  \ now back to basic
3440  RTS
3450  .waitflag LDA &FE6D \ ifr reg. 13
3460  AND £&4
3470  BEQ waitflag
3480  RTS
3490  ]
3500  NEXT
3510  ENDPROC
```

B3 Programme for local gas holdup measurement

```
 10  PRINT "INPUT Q":INPUT QQ
 20  PRINT "INPUT RPM":INPUT NN
 30  PRINT "INPUT POSITION":INPUT POSITION
 40  VDU2
 50   PRINT:PRINT
 60  PRINT"Q = ";QQ*1E-3/60;" M3/S"
 70  PRINT"N = ";NN;" RPM"
 80  PRINT"POSITION = ";POSITION;TAB(0);"________"
 90  PRINT: PRINT
100  VDU3
110  PROCsetup
120  PROCpulse(start_bub%,1) : REM commence sampling process
130  REPEAT : UNTIL FNfull : REM wait for memory to fill
140   PROCpulse(reset_mem_ptr%,1)
150  REM resets memory pointer to position zero
160  SOUND 1,-15,53,5
170  PRINT "MEMORY FULL"
180  MEM%=1024
190  @%=&20409
200  DIM X%(2)
210   S1=0:S2=0:A1%=0:A2%=0:A3%=0:A4%=0:A5%=0:A6%=0
220  A7%=0:A8%=0:A9%=0:A10%=0:A11%=0:A12%=0:A13%=0
230  A14%=0:A15%=0:A16%=0:A17%=0:A18%=0:A19%=0:A20%=0
240  A21%=0:A22%=0:A23%=0:A24%=0:A25%=0:A26%=0:A27%=0
250  A28%=0:A29%=0:A30%=0:A31%=0:A32%=0:A33%=0
260
270  P%=0:I%=-1:H1%=0:Tg%=0
280
290   PROCpulse(inc_mem_ptr%,0)
300  REM increments mem.pointer position from 0 to 1
310
320  REPEAT :REM identifies 1st liq._to_gas transition on ch1
330    CALL incp
340    UNTIL R%=2
350  T0%=T%
360
370
380
390  REPEAT
400       IF P%>MEM%-2 GOTO 520
410    REM stops aquiring data when end of memory
420    REM reached,and proceeds further
430     IF R%<>0 THEN I%=I%+1 :X%(I%)=T%
431    REM checks for change on ch1 and reads time value
440    CALL incp
450     UNTIL I%=1 :REM 2 time values must be retrieved from
460  memory on either channel before proceeding further
470  t%=X%(1)-X%(0)
480  H1%=H1%+1:Tg%=Tg%+t%:T1%=X%(1):I%=-1
490
500  GOTO 390 :REM search for next bubble
>
```

```
 510  REM printing results
 520  VDU2
 530  NB%=H1% :PRINT"NB = ";NB%
 540  Tg%=Tg%:PRINT"Tg  = ";Tg%*1E-5;" SEC.": REM TOTAL GAS TIME SEC.
 550  T%=T1%-T0%:PRINT"T   = ";T%*1E-5;" SEC." :REM TOTAL SAMPLING TIME
 560  TL%=T%-Tg% :PRINT"TL  = ";TL%*1E-5;" SEC." :REM TOTAL LIQUID TIME SEC.
 570  Hp =Tg%/T%:PRINT"Hp  = ";Hp
 580  Nf=NB%/T%*1E5 :PRINT"Nf  = ";Nf:REM frequency of bubble arrival
 590  Tm=Tg%*1E-2/NB%
 600  PRINT "Tm  = ";Tm;" mSEC.":REM MEAN GAS TIME IN mSEC.
 610  PRINT :PRINT :PRINT"END OF RUN":PRINT"----------"
 620  VDU3
 630  @%=10
 640  VDU3
 650  SOUND 1,-15,53,10
 660  END
 670
 680
 690  DEF PROCkeys : REM test purposes only
 700  *KEY0PROCpulse(reset_mem_ptr%,1)|M
 710  *KEY1PROCpulse(inc_mem_ptr%,0)|M
 720  *KEY2PROCpulse(load_sr%,1)|M
 730  *KEY3P.?SR|M
 740  ENDPROC
 750
 760
 770  DEF PROCsetup
 780  DDRB=&FE62
 790  IOB=&FE60
 800  SR=&FE6A
 810  ACR=&FE6B
 820  PCR=&FE6C
 830  T2L=&FE68
 840  T1L_L=&FE66
 850  T1L_H=&FE67
 860  T1C_H=&FE65
 870
 880  start_bub%=0
 890  inc_mem_ptr%=1
 900  reset_mem_ptr%=2
 910  reset_tim_sampler%=3
 920  load_sr%=5
 930  stop_bub%=6
 940  full_up%=7
 950
 960
 970  ?DDRB=&7F : REM all outputs save 7 (buffer full)
 980  ?IOB=2 : REM ALL low
 990  ?ACR =&04 : REM shift in under T2
1000  ?T2L=&4   : REM safe shifting rate
1010  PROCpulse(stop_bub%,1)
1020  PROCpulse(reset_mem_ptr%,1)
1030  PROCpulse(reset_tim_sampler%,1)
1040  PROCassemble
1050  ENDPROC
>
```

```
1060
1070
1080
1090  DEF PROCpulse(sig%,pol%)
1100  IF pol%=1 PROCpospulse(sig%) ELSE PROCnegpulse(sig%)
1110  ENDPROC
1120
1130
1140  DEF PROCpospulse(sig%)
1150  LOCAL Y%
1160  Y%=2^sig%
1170  ?IOB=?IOB OR Y%
1180  ?IOB=?IOB AND NOT Y%
1190  ENDPROC
1200
1210
1220  DEF PROCnegpulse(sig%)
1230  LOCAL Y%
1240  Y%=2^sig%
1250  ?IOB=?IOB AND NOT Y%
1260  ?IOB=?IOB OR Y%
1270  ENDPROC
1280
1290
1300
1310
1320  DEF FNchannel2
1330  LOCAL X%
1340  PROCpulse(load_sr%,1)
1350  X%=?SR   : REM discard first one
1360  X%=?SR : IF (X% AND &80) =0 THEN ="" ELSE IF (X% AND &40) =0 THEN ="-" ELSE ="
1370  ENDPROC
1380
1390
1400  DEF FNchannel1
1410  LOCAL X%
1420  PROCpulse(load_sr%,1)
1430  X%=?SR
1440  X%=?SR : IF (X% AND &20) =0 THEN ="" ELSE IF (X% AND &10) =0 THEN ="-" ELSE ="
1450  ENDPROC
1460
1470
1480  DEF FNread_time
1490  LOCAL X%
1500  PROCpulse(load_sr%,1)
1510  X%=?SR   : REM discard first one
1520  ?&73=(?SR AND &F) : ?&72=?SR : ?&71=?SR : ?&70=?SR
1530  =!&70
1540  ENDPROC
1550
1560
1570  DEF FNfull    : REM is buffer memory full?
1580  IF (?IOB AND 2^full_up%) <>0 THEN =TRUE ELSE =FALSE
1590  ENDPROC
1600  DEF PROCassemble
)
```

```
>
1610  IF (?IOB AND 2^full_up%) <>0 THEN =TRUE ELSE =FALSE
1620  ENDPROC
1630  DEF PROCassemble
1640  DIM code 300
1650  LOCAL N%,P%
1660  FOR N%=0 TO 2 STEP 2
1670    P%=code
1680    [ OPT N%
1690    .incp LDX £0
1700    LDA £1
1710    CLC : ADC &440 : STA &440
1720    TXA : ADC &441 : STA &441
1730    TXA : ADC &442 : STA &442
1740    TXA : ADC &443 : STA &443
1750
1760    \ increment memory pointer
1770    \ bit 1, negative pulse
1780
1790    LDA &FE60
1800    TAX
1810    AND £253 \drop bit 1
1820    STA &FE60
1830    TXA
1840    ORA £2  \ bit 1 back
1850    STA &FE60
1860
1870    \ load shift register
1880    \ bit 5, positive pulse
1890
1900    LDA &FE60
1910    TAX
1920    ORA £32  \ bit 5 up
1930    STA &FE60
1940    TXA
1950    AND £223 \ drop bit 5
1960     STA &FE60
1970
1980    \ read the time into T%
1990
2000    LDA &FE6A  \ shift register, hopefully
2010    JSR waitflag
2020    LDA &FE6A
2030    TAX
2040    AND £15
2050    STA &453
2060    JSR waitflag
2070    LDA &FE6A : STA &452 : JSR waitflag
2080    LDA &FE6A : STA &451 : JSR waitflag
2090    LDA &FE6A : STA &450
2100
2110    \ set R% and S% to zero
2120
2130    LDY £8
2140    LDA £0
2150     .again STA &447,Y
>
```

```
2160  DEY : BNE again
2170
2180  \ sort out channel1
2190
2200  TXA
2210  AND £&20
2220  BEQ riszero
2230  TXA
2240  AND £&10
2250  BEQ ristwo
2260  LDA £1
2270  BNE riszero
2280  .ristwo LDA £2
2290  .riszero STA &448
2300
2310  \ and for S%
2320
2330  TXA
2340  AND £&80
2350  BEQ siszero
2360  TXA
2370  AND £&40
2380  BEQ sistwo
2390  LDA £1
2400  BNE siszero
2410  .sistwo LDA £2
2420  .siszero STA &44C
2430
2440  \ now back to basic
2450
2460  RTS
2470
2480  .waitflag LDA &FE6D \ ifr reg. 13
2490  AND £&4
2500  BEQ waitflag
2510  RTS
2520  ]
2530  NEXT
2540  ENDPROC
>
```

APPENDIX C

C1 Interrupt driven system

A functional block diagram of this system is given in Fig C1. The system uses two type-6522 versatile interface adaptor integrated circuits connected directly to the BBC-computer processor bus.

Time counter

A 100 KHz time base is applied to the input of an 8 bit (Modulo 256) counter. The output of this counter can be read by the VIA digital input port when necessary. The overflow of the eight bit counter is connected via some logic, explained below, to a 16 bit binary counter internal to the VIA. Finally, each time the 16 bit counter overflows, an interrupt to the processor is generated which enables the contents of a memory location to be incremented. Thus the elapsed time is always available as a four byte number, with a resolution of 10 μs.

Sampling of the input signal

The binary waveform input signal is sampled every 10 μs. If the current sample differs from the preceding sample the pin CA1 is activated. This has the following effects:

(i) The 8 bit counter is prevented from incrementing the 16 bit VIA counter until the current elapsed time value has been stored.

(ii) The 8 bit counter output is latched into the VIA input/output register.

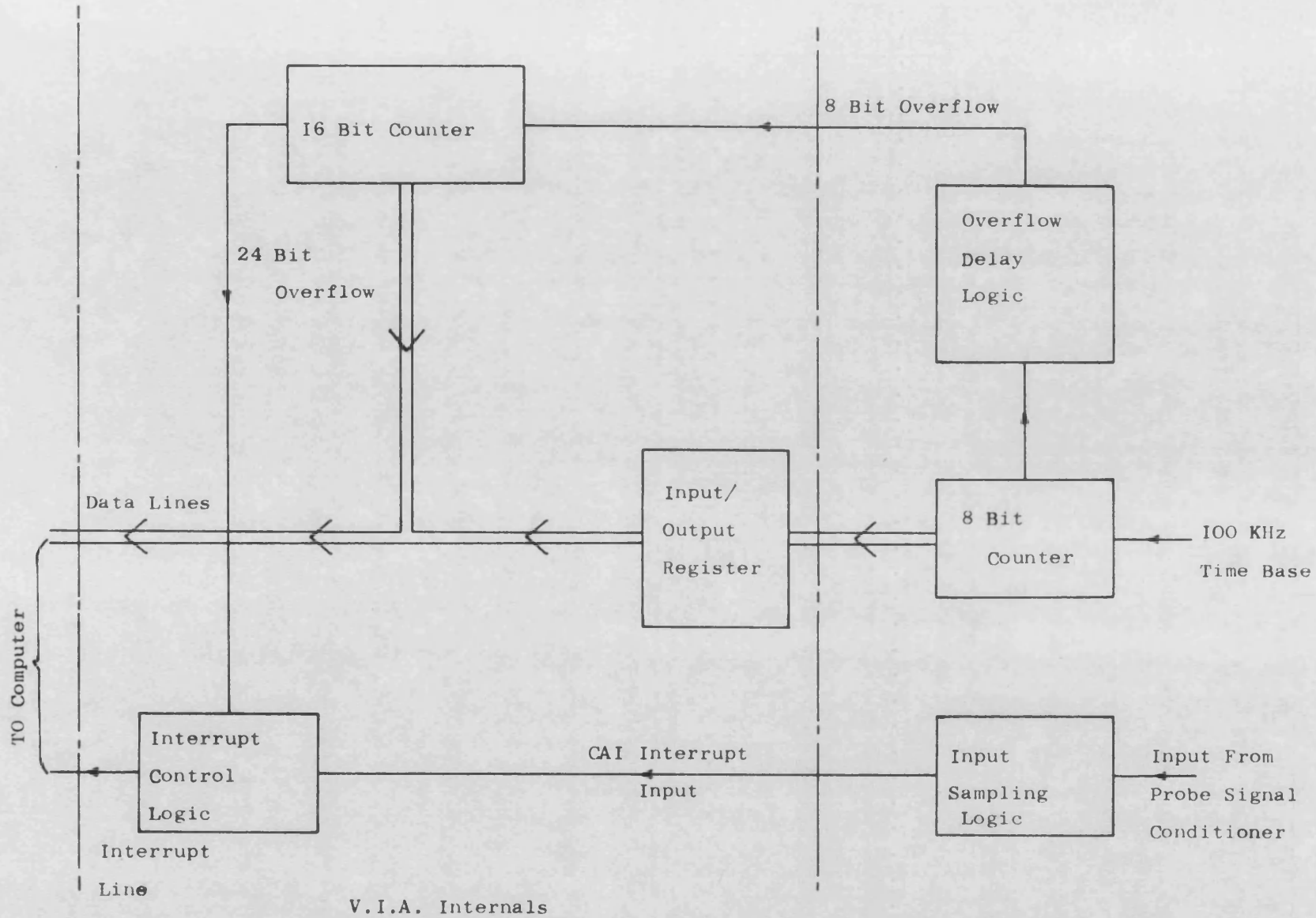

Fig CI Interrupt driven system.

(iii) An interrupt to the processor is generated. The interrupt output of the VIA is connected to the non maskable interrupt input (NMI) of the processor. This ensures that interrupts are serviced in the least possible time. The interrupt service routine carries out the following tasks:

(i) Checks if the 16 bit VIA counter has recently overflowed, and takes the necessary action.

(ii) The 4 byte elapsed time value (defined above) is stored in memory, together with information specifying whether the input level change was +ve or -ve going.

(iii) Overflows from the 8 bit low-order counter are re-enabled.

Software

The interrupt processing and system initialisation routines were committed to EPROM (read only memory) and permanently installed in the BBC computer. The routines were written so that by executing the command '*BUBBLE1' the initialising routines were invoked and sampling began. Following the execution of the command '*BUBBLE1', the BASIC variable storage space is searched to see if two integer arrays A% and B% have been previously defined by the BASIC control programme. If no such arrays exist, an error message is generated and the computer is returned to command level. Otherwise, the VIA's are initialised and interrupts enabled, ready for sampling.

Data storage

Arrays A% and B% are used to store the times of occurrence of events on channels 1 and 2 respectively. When storing the data, the following convention is adopted: If the input level is positive going, the time is stored as a positive 4 byte number, and if the change is negative going, the TWOs complement of the time is stored ie., -(+time). When either or both of the arrays are full, sampling is automatically terminated. Additionally, sampling may be terminated by executing a 'BUBBLE0' command.

C2 External FIFO system

The general scheme of operation of such a system is illustrated in Fig C2. The system requires two address counters, one to provide the address of the next location to be written to, the other providing the address of the next location to be read from. These addresses must be continuously compared to ensure that 'memory empty' and 'memory full' conditions are recognised when they occur, and that the appropriate action is taken. A multiplexer is required to switch the memory between the two address counters for read or write operations. A second multiplexer is required so that during a write operation, data from the elapsed time clock and the input logic is routed to the memory, and, during a read operation, data from the memory is routed to a temporary store, from which it can be retrieved by the computer. Additional control and timing logic is required to ensure that read and write operations donot clash, to perform the necessary switching etc..

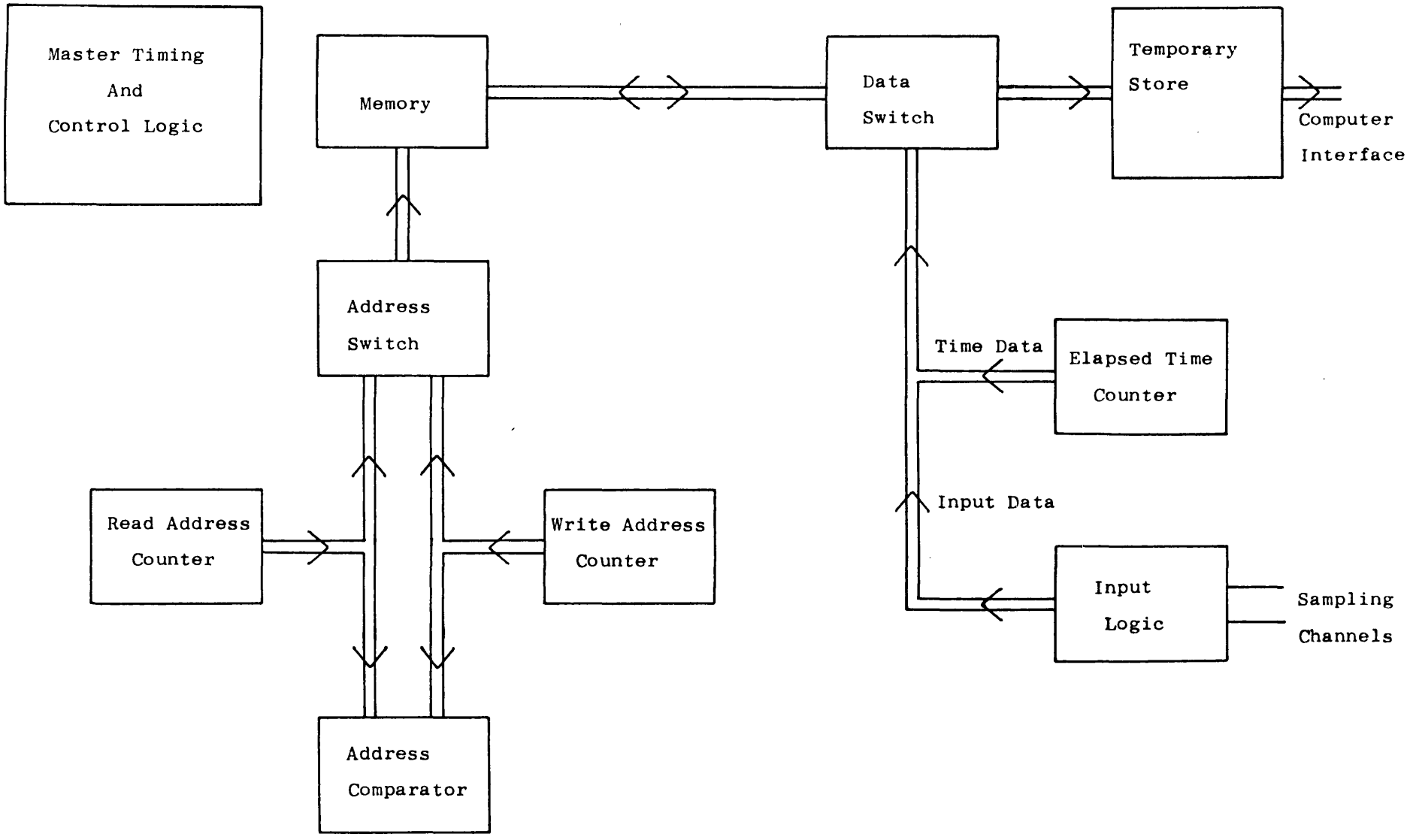

Fig C2 Proposed external FIFO system (simplified block diagram).